Department of Pure & Applied Chemistry

Nanoparticle Design for Drug Delivery to Atherosclerotic Plaques

By

Jennifer Gracie

A thesis presented to the Department of Pure and Applied Chemistry, University of Strathclyde, in fulfilment of the requirements for the degree of Doctor of Philosophy.

2020

This thesis is the result of the author's original research. It has been composed by the author and has not been previously submitted for examination which has led to the award of a degree.

The copyright of this thesis belongs to the author under the terms of the United Kingdom Copyright Acts as qualified by University of Strathclyde Regulation 3.50. Due acknowledgement must always be made of the use of any material contained in, or derived from, this thesis.

Signed: Date: 10th February 2020

Acknowledgements

To thank every person that helped along this PhD journey would result in a thesis twice the size this already is. To those that encouraged me to keep going, to those that took the time to help and to those that poured a glass of wine after a hard day, all of you helped in one way or another.

Prof Duncan Graham and Prof Karen Faulds thank you for allowing me to carry out this work and inspiring different research routes when results looked bleak. You also supported my ambition to do other activities during the PhD, and I think this will make me a more rounded Doctor in the end.

To the many postdocs that answered my never-ending questions and showed me the way around our labs, thank you. Your guidance and proof reading made this whole experience a little easier.

To all the PhD students in the group past and present, your banter lifted spirits on those bad days and I never felt alone in this journey. In particular, Kirsty, Emma, Iona, Sian, Craig, Amy, Alex and Anastasia you kept me sane! I hope the rants and 'office wines' helped you as much as they did me. Even though some of you have moved to other parts of the world, I hope our friendships last a lifetime.

To my friends outside of academia, you have zero idea what I do, but still you support me and act interested when I rambled on about nanoparticles, so thanks for that.

My family - Mum, Dad, Kirsty (and Bailey)...you nurtured my inquisitive/annoying nature from a young age, and look where it has lead. Your love and never wavering support is more than I could ever have asked for. I hope you are proud of me and I can't thank you enough for getting me to this point.

Finally, to the one that took the brunt of it all, Ruari. Without your level-headed reasoning, unfaltering belief and love I would not have made it across this finish line. Your motivational pep talks and dog memes kept me going. We can now enjoy a thesis free life together!

"That knowing is better than wondering, that waking is better than sleeping, and that even the biggest failure, even the worst, most intractable mistake, beats the hell out of never trying."

Meredith Grey

Abstract

Cardiovascular disease remains the main cause of death worldwide, and at the core of most cardiac problems is atherosclerosis. This progressive condition is characterised by the hardening and narrowing of the arteries. Often a cholesterol-lowering drug known as a statin is prescribed. Studies have shown these drugs to have many advantageous properties including an anti-inflammatory effect, the ability to improve endothelial function and the power to stabilise plaques. It was hypothesised that delivering the statin to the plaque could enhance these therapeutic effects since the disease is triggered from a local, rather than systemic, event.

Research focussed around the drug carrier design, with initial effort to investigate potential particles for the core. Nobel metal nanoparticles, such as gold and silver, are widely studied for use in medicine, owing to their plasmon resonance and facile surface chemistry. It is their interaction with light that makes the nanoparticles trackable via surface enhanced Raman spectroscopy (SERS) and capable of exchanging light to heat. In the literature, studies have shown that the heat generated during plasmonic interrogation can trigger drug release and hence could facilitate localised statin delivery. All these properties make metallic nanoparticles an appealing candidate for the core of the drug delivery design.

Iron oxide nanoparticles were synthesised and characterised as an initial vector for a drug carrier design. It was anticipated that a thin gold coating would facilitate the ability to functionalise and track the particles *in* vivo. As an alternative approach, hollow gold nanoparticles were investigated as the core nanoparticle, with their vacant centre allowing for higher drug payloads. Their synthesis, photothermal properties and enhancement of Raman scattering was investigated. An interesting relationship between the Raman signal and the plasmonic heating of the nanoparticles was observed. This phenomenon is not currently published in the literature, and this research theorises that an increase in 'adatom' density causes the signal enhancement.

This project validated a nanoparticle vehicle for the localised delivery of statins to atherosclerotic plaques. The combination of metallic nanoparticles with SERS was studied to better understand the possibility of such a treatment.

Abbreviations

2-MPY	2-mercaptopyridine
4-NTP	4-nitrothiolphenol
Ab	Antibody
AgNP	Silver nanoparticle
AuNP	Gold nanoparticle
BSA	Bovine serum albumin
BT	Benzenethiol
CRP	C-reactive protein
CVD	Cardiovascular disease
DHCA	3,4-dihydroxyhydrocinnamic acid
DLS	Dynamic light scattering
DMSO	Dimethyl sulfoxide
EDC	1-ethyl-3-(3-dimethylaminopropyl)-carbodiimide
EDTA	Ethylenediaminetetraacetic acid
EM	Electromagnetic
eNOS	Endothelial nitric oxide synthase
FC	Field cooling
FWHM	Full width half maximum
hCG	Human chorionic gonadotropin
HEPES	4-(2-Hydroxyethyl)piperazine-1-ethanesulfonic acid
HGN	Hollow gold nanoparticle
HMG-CoA	3-hydroxy-3-methylglutaryl-coenzyme A
ICAM-1	Intercellular adhesion molecule 1
ICP-MS	Inductively coupled plasma mass spectrometry
IONC	Iron oxide nanocage
LDL	Low-density lipoproteins
LSPR	Localised surface plasmon resonance
MES	2-(N-morpholino)ethanesulfonic acid

MGITC	Malachite green isothiocyanate
MMPs	Matrix metalloproteinases
MNP	Magnetic nanoparticles
MRI	Magnetic resonance imaging
NIR	Near-infrared
NO	Nitric oxide
NTA	Nanoparticle tracking analysis
PEG	Polyethylene glycol
PPY	4-(1H-pyrazol-4-yl)pyridine
rHDL	Reconstituted high-density lipoprotein
RRS	Resonance Raman scattering
SEM	Scanning electron microscopy
SERRS	Surface enhanced resonance Raman scattering
SERS	Surface enhanced Raman scattering
sNHS	N-hydroxysulfosuccinimide
SPR	Surface plasmon resonance
SQUID	Superconducting quantum interference device
TEM	Transmission electron microscopy
VCAM-1	Vascular cell adhesion molecule 1
ZFC	Zero-field cooling

Contents

1. General Introduction

1.1 Cardiovascular Disease

Cardiovascular disease (CVD) is a collective term for conditions that affect the structure and function of the heart and blood vessels. In their most recent report, the World Health Organisation announced that 17.9 million people die each year from CVD, representing an estimated 31% of all global fatalities.[1] This figure makes CVD the most likely cause of death worldwide, a statistic that could be lower considering that it is a non-communicable disease and often preventable through lifestyle choices and medication.

1.1.1 Atherosclerosis

At the core of almost all CVDs is atherosclerosis, a progressive disease which is characterised by the hardening and thickening of the artery walls. This is a result of lipids depositing in the innermost arterial layer, known as the intima. The plaques form through a cascade of biological events, and there are multiple theories surrounding the initial trigger, although most agree that damage to the endothelium is the underlying cause. Over time, and without any intervention, the plaques will intrude the artery lumen and cause an obstruction to the blood flow as shown in Figure 1.1.
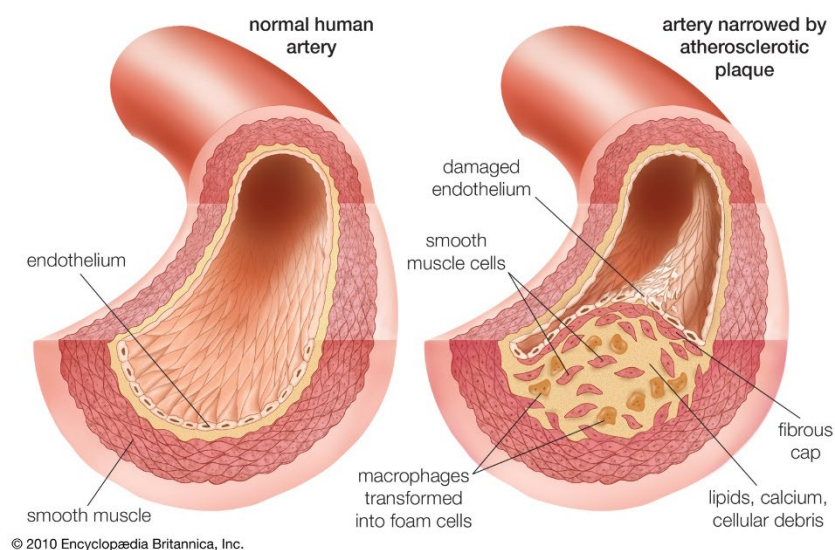
Figure 1.1 - Cross section of a healthy and diseased artery showing the intrusion of an atherosclerotic plaque. Figure reproduced with permission from Encyclopædia Britannica, Inc.

The events that lead to atherosclerotic plaques developing within the arteries are summarised in chronological order in Figure 1.2[2-3]

Endothelial Dysfunction
- Low density lipoproteins (LDL) permeate a defective endothelium
- Further degradation of endothelial cell layer occurs
- Inflammatory response is triggered

Cell Recruitment
- Upregulation of vascular cell adhesion molecules -VCAM-1, ICAM-1 and P-selectin.
- This recruits inflammatory response cells into the subendothelial space

Foam Cells
- Incoming monocytes differentiate into macrophages
- These internalise many LDL molecules until full, then they are termed foam cells
- Accumulation of foam cells, leads to 'fatty streaks', which is the first visible sign of atherosclerosis

Plaque Growth
- Smooth muscle cell migration and proliferation occurs
- Extracellular matrix begins to decompose, resulting in necrosis
- This process forms the core of the atheroma, with a fibrous cap acting as a protective barrier

Remodelling
- As the growing plaque invades the lumen space, the artery wall remodels to compensate
- Eventually it cannot remodel any more and begins to have clinical manifestations e.g. angina

Clinical Event
- Unstable plaques burst resulting in an occlusion in the artery
- The blockage of the arterial blood flow can lead to myocardial infarctions and strokes amongst other cardiac issues
- The clot can also travel away from the heart and cause circulatory problems of the limbs or other organs.

Figure 1.2 – Biological events that lead to the formation of an atherosclerotic plaque. This series of complex biological events has been simplified for the purpose of this figure.

1.1.2 Treatment of CVD

The disease is influenced by both modifiable factors, e.g. smoking, diabetes, high blood pressure, high cholesterol, body weight and physical inactivity, as well as non-modifiable factors such as age, gender, family history and ethnicity.[4] The latter cannot be changed, therefore the former list is the main target of treatment. In order to live a healthier life, lifestyle management is often the first step of any treatment. Many surgical options are also available, such as stents and bypasses, but due to the risk associated with operations, these are a more extreme solution. Most often, patients at risk of CVDs are prescribed a cholesterol-lowering drug called a statin.

1.1.3 Pharmalogical Intervention – Statins

Statins are a class of drug that are routinely prescribed for both the primary and secondary prevention of CVD. Their main function is to lower the level of circulating low-density lipoproteins (LDL), known colloquially as "bad cholesterol", which is an important risk factor established by The Framingham Heart Study.[5] Even though an individual's diet can contribute to the levels of circulating cholesterol, the liver actually produces over two thirds of the body's cholesterol.[6] As a result, most research is focused on the suppression of hepatic cholesterol synthesis in order to reduce serum cholesterol levels.[7]

Statins reversibly inhibit the pathway of enzyme 3-hydroxy-3-methylglutaryl-coenzyme A (HMG-CoA) reductase by competing with the endogenous substrate HMG-CoA.[8] Their antagonistic behaviour is a result of an analogous structure to the native HMG-CoA substrate, and therefore statins also bind to the enzyme active site. Figure 1.3 shows the molecular structure of the HMG-CoA substrate (in red) and a common statin called Rosuvastatin. This competition disrupts the normal mevalonate production pathway and reduces the biosynthesis of hepatic cholesterol. Consequently, liver cells express more LDL receptors, which in turn increases LDL clearance, causing serum levels to decrease.[9]
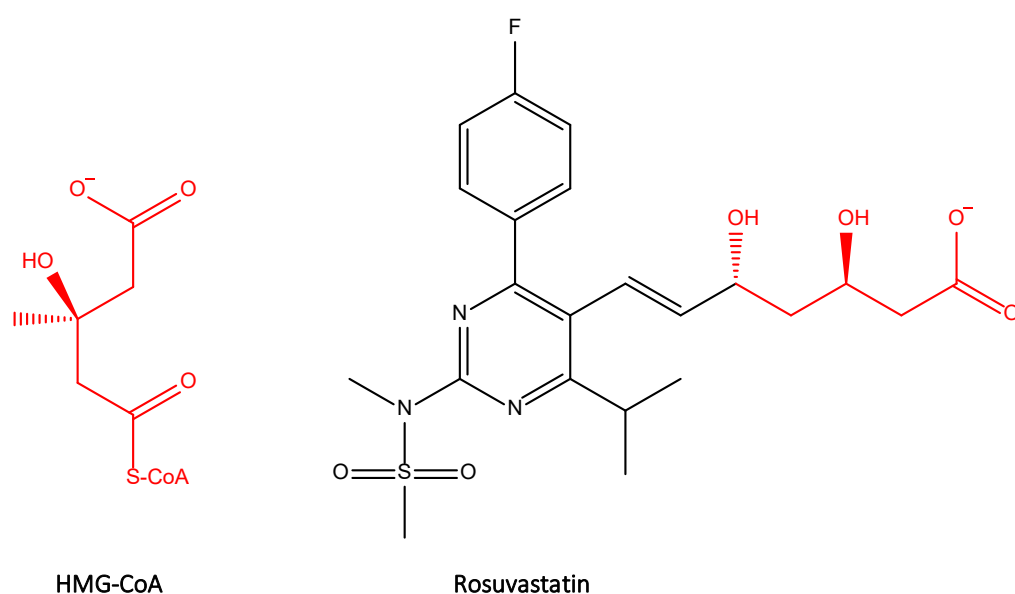
Figure 1.3 – Structure of HMG-CoA shown on the left and a commonly prescribed statin, Rosuvastatin, on the right. The structures highlighted in red show the portion of the molecules that bind to the pocket of the HMG-CoA reductase enzyme. It is the similarities in this structure that leads to the competition for binding sites.

1.1.4 Beneficial Pleiotropic Effects

Atherogenesis can be considered a local immune response and statins are understood to have a multifunctional role in reducing the development of plaques. 'Pleiotropic' comes from the Greek 'pleion' meaning more and 'tropos' meaning direction/way.[10] Statins are now being termed 'pleiotropic' as research suggests that they reduce atherosclerosis via multiple biological effects. [6,9,11,12] These additional effects are an attractive benefit to prescribing statins, as they can combat the progression of atherosclerosis in numerous ways. Some of the additional therapeutic characteristics that could be achieved through this therapy are described in Figure 1.4. [13,14,15,16]

4

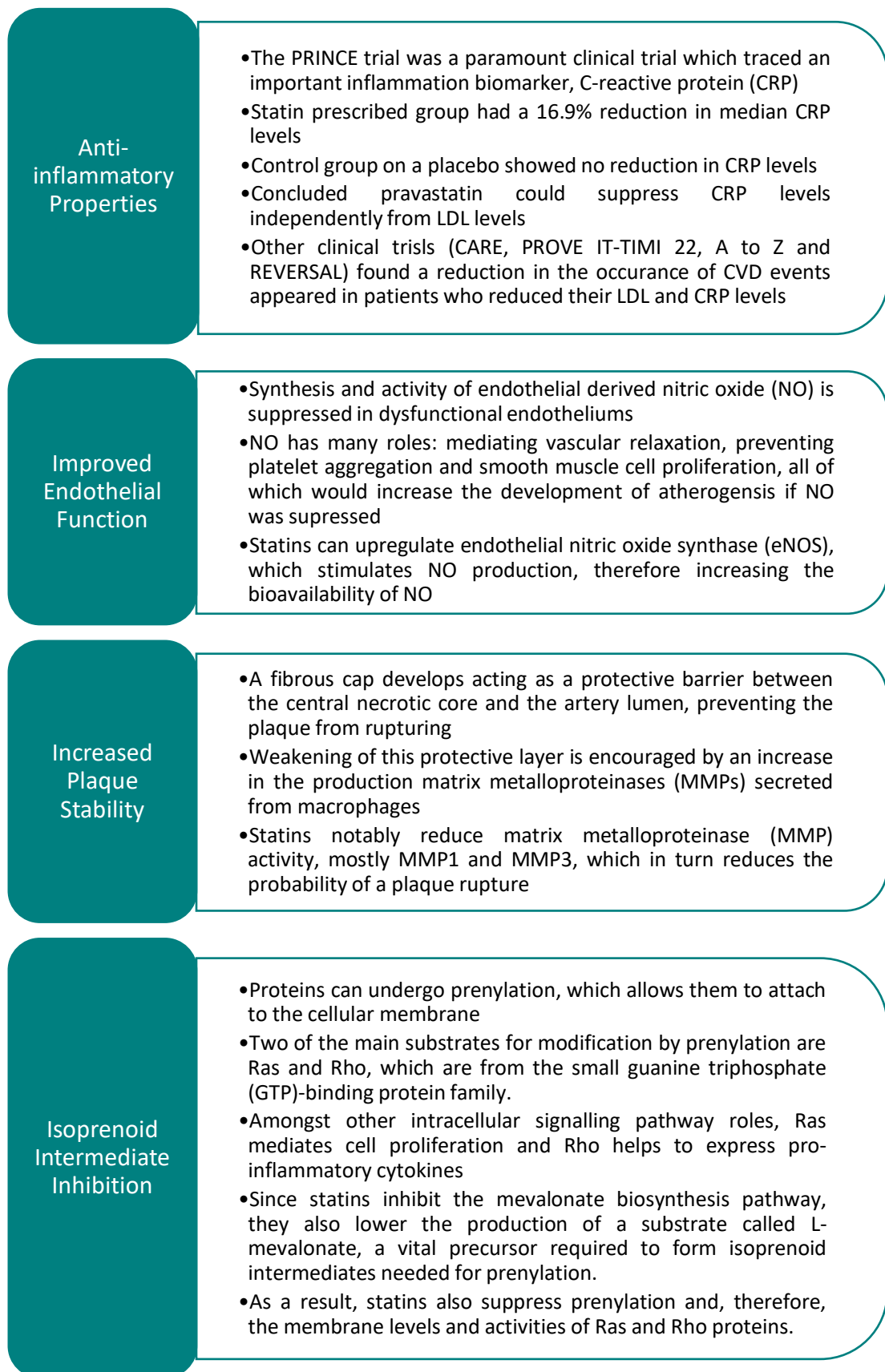| Anti-inflammatory Properties	• The PRINCE trial was a paramount clinical trial which traced an important inflammation biomarker, C-reactive protein (CRP) • Statin prescribed group had a 16.9% reduction in median CRP levels • Control group on a placebo showed no reduction in CRP levels • Concluded pravastatin could suppress CRP levels independently from LDL levels • Other clinical trisls (CARE, PROVE IT-TIMI 22, A to Z and REVERSAL) found a reduction in the occurance of CVD events appeared in patients who reduced their LDL and CRP levels
Improved Endothelial Function	• Synthesis and activity of endothelial derived nitric oxide (NO) is suppressed in dysfunctional endotheliums • NO has many roles: mediating vascular relaxation, preventing platelet aggregation and smooth muscle cell proliferation, all of which would increase the development of atherogensis if NO was supressed • Statins can upregulate endothelial nitric oxide synthase (eNOS), which stimulates NO production, therefore increasing the bioavailability of NO
Increased Plaque Stability	• A fibrous cap develops acting as a protective barrier between the central necrotic core and the artery lumen, preventing the plaque from rupturing • Weakening of this protective layer is encouraged by an increase in the production matrix metalloproteinases (MMPs) secreted from macrophages • Statins notably reduce matrix metalloproteinase (MMP) activity, mostly MMP1 and MMP3, which in turn reduces the probability of a plaque rupture
Isoprenoid Intermediate Inhibition	• Proteins can undergo prenylation, which allows them to attach to the cellular membrane • Two of the main substrates for modification by prenylation are Ras and Rho, which are from the small guanine triphosphate (GTP)-binding protein family. • Amongst other intracellular signalling pathway roles, Ras mediates cell proliferation and Rho helps to express pro-inflammatory cytokines • Since statins inhibit the mevalonate biosynthesis pathway, they also lower the production of a substrate called L-mevalonate, a vital precursor required to form isoprenoid intermediates needed for prenylation. • As a result, statins also suppress prenylation and, therefore, the membrane levels and activities of Ras and Rho proteins.

Figure 1.4 – A summary of the pleotropic effects that statins exhibit. These additional therapeutic effects are an attractive benefit to prescribing statins, as they can combat the progression of atherosclerosis in a multimodal way.

1.1.5 Statin Delivery via Nanoparticles

In 2011, the European Union adopted an updated definition of a nanoparticle, in short they are a particle with one or more dimension in the 1-100 nm size range.[17] Nanoparticle-based drug delivery systems have promise to expand the current therapeutic potential of statins, by increasing the drug bioavailability. The reformulation of statins into nanocarriers could help improve bioavailability, reduce dosage levels/frequency and supress drug toxicity.[18]

There are already examples of this in the literature, Soni *et al.* used poly(D,L-lactide-co-glycolide) copolymers loaded with Simvastatin to improve the absorption of the statin in the gastrointestinal tract.[19] The loaded nanoparticles showed better *in vivo* performance than Simvastatin alone in reducing the total cholesterol and triglyceride levels in blood. This result was attributed to the improved solubility of the statin-nanoparticle mixture, therefore increasing the statin concentration in the bloodstream. Pitavastatin was also incorporated into poly(lactic-co-glycolic) acid nanoparticles by Katsuki *et al.* and was shown to inhibit plaque destabilisation and rupture.[20]

Duivenvoorden *et al.* formulated a statin loaded reconstituted high density lipoprotein (rHDL) nanoparticle vehicle for delivering statins to the atherosclerotic plaque. They demonstrated the anti-inflammatory effects of statin-rHDL *in vitro* and showed the loaded nanoparticles accumulate in atherosclerotic lesions *in vivo*.[21]

In a more direct delivery, Tsukie *et al.* incorporated statins into the coating of stent devices, to promote vascular healing after surgery.[22] The inclusion of Pitavastatin in the stent coating showed endothelial healing effects in porcine coronary artery models.

Nanoparticle based delivery methods could offer additional benefits if targeted directly to the site of inflammation, i.e. atherosclerotic plaques in the heart. As a result of this interesting concept, the long term aim of this research was to design a nanoparticle vehicle with the prospect of delivering the statin directly to the affected cardiac tissue.

1.2 Nanotechnology

Nanotechnology can be defined as the understanding and manipulation of matter on the nano-scale. Physicist Richard Feynman is often credited for the conception of nanotechnology, when in 1959, he delivered his talk aptly named "There's Plenty of Room at the Bottom"[23]. Feynman proposed that there were no principles of physics that objected to the possibility of manoeuvring individual atoms, but it had simply not been achieved yet due to a lack of miniaturised technology. However, even though his 'prophecy' did come true, with major breakthroughs of early nanotechnology including the invention of the scanning tunnelling microscope, the atomic force microscope and the movement of 35 individual xenon atoms[24], many think his accreditation is a result of retroactive interest in the talk.[25] In the decades after the talk few papers actually cited Feynman, it wasn't until the early 2000's that citations increased, which lead to a snowball effect and the widely believed notion that Feynman is the father of nanotechnology. The actual term 'nanotechnology' was first used by Norio Taniguchi at a conference in Japan in 1974.[26] Regardless of the origin of nanotechnology, it is a field of research that is advancing at an exceptional pace.

The prefix 'nano' is derived from the Greek word '*nanos*' which indicates extreme smallness.[27] As a metric prefix, nano (10^{-9} or n), indicates the unit measurement being divided by one billion. These nano-scale materials often have unique size-related properties that differ from their bulk relatives. This presents the opportunity to advance science and engineering, especially in fields such as medicine and electronics, by utilising these novel materials.

1.2.1 A History of Inorganic Nanomaterials

Inorganic nanomaterials have been employed unknowingly for thousands of years by artisans creating beautiful ceramic and porcelain pieces. They would incorporate metallic nanoparticles into their materials for a lustrous glaze finish, or to include colour in the designs.[28] Nanoparticles have also been found in the colourful stain glass

designs often found in places of worship, where the nanoparticles have been trapped within the glass for centuries, retaining their vibrant colours.[29]

The most famous historical application of nanomaterials is in the creation of the 'Lycurgus Cup', dating back to the late Roman Empire (AD 300). The ornate cup appears opaque green in reflected light, but translucent red in transmitted light; an optical phenomena resulting from the dispersion of metallic nanoparticles throughout the glass.[29] Figure 1.5 shows the Lycurgus cup illuminated in both states.

Figure 1.5 - The Lycurgus Cup, shown in reflected light (left), transmitted light (right) and with an excited PhD student (middle). Outer images reproduced with permission from © Trustees of the British Museum.

Despite nanomaterials being inadvertently used for millennia, it was only in 1857 that Michael Faraday presented his research on the 'Experimental Relations of Gold (and other Metals) to Light', and so became the first scientist to document the properties of synthesised nanoparticles.[30] Using phosphorus to reduce an aqueous solution of gold chloroaurate, he produced a ruby-red solution containing diffuse gold nanoparticles, known today as a colloid.

Many synthesis methods have been published to produce a variety of sizes of gold nanoparticles. The most popular method was developed by Turkevich[31], where a gold salt is reduced in solution by citrate to form the spherical gold nanoparticles. The method was refined by Frens[32] decades later, and more recently by Ji[33], who investigated the influence of pH on the synthesis route.

1.2.2 Optical Properties of Nanoparticles

Within the field of nanomaterial research, noble metals, e.g. silver and gold, are often studied as a colloidal suspension. These nanoparticles convey unique optical properties that differ from their bulk material relatives, an effect which has a pronounced dependence on the particle size and shape.

1.2.3 Surface Plasmon Resonance

When the free electrons in a noble metal collectively oscillate, it is known as a plasmon.[34] Nanoparticles interact with electromagnetic waves (light), inducing an oscillating cloud of conductance band electrons on the particle surface, which is termed the surface plasmon resonance (SPR). The moving cloud of electrons couple with the incoming electromagnetic radiation and is displaced by the electric field in a wave-like motion, as shown in Figure 1.6. This interaction results in a net displacement of the negative charge from the positive core, causing a momentary dipole. This effect occurs through the bulk of the metal material and is called the localised surface plasmon resonance (LSPR) when it is restricted to the nanoscale.
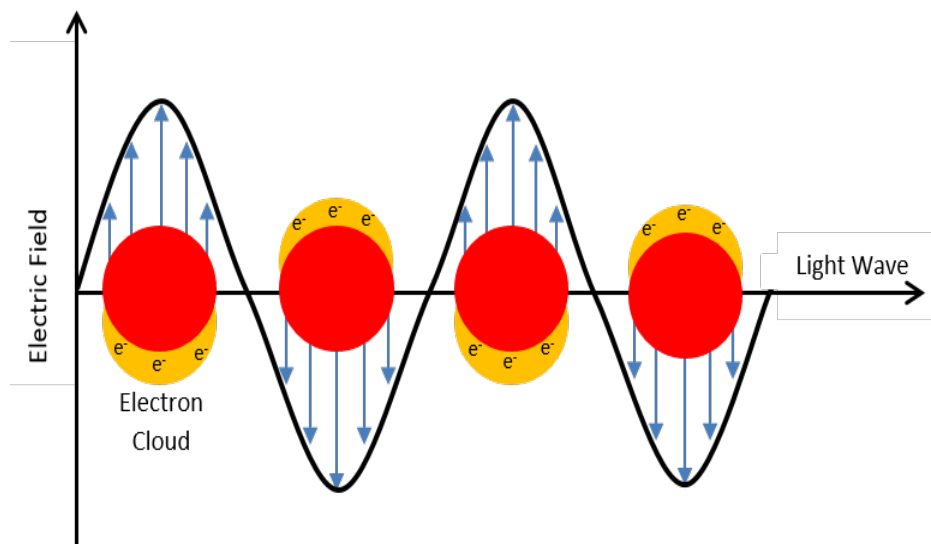

Figure 1.6 - Interaction between conductance band electrons (electron cloud) in a nanoparticle and the incident light. When confined the nanoscale, this is termed the Localised Surface Plasmon Resonance (LSPR).

The LSPR will produce a spectral extinction band (the combination of absorption and scattering events) with a maximum coinciding with the plasmon resonant frequency. Monodispersed spherical nanoparticles show one surface plasmon band in an

extinction spectrum, whereas rod shaped nanoparticles exhibit two plasmon bands. This results from the extra mode in which the rod nanoparticle can be polarised; a longitudinal plasmon band (oscillations from along the length of the nanorod) and another corresponding to the transverse plasmon band (oscillation along the width).[35]

The LSPR will also greatly enhance the electric fields near the particle surface; an effect which diminishes with increasing distance from the nanoparticle surface. This effect is the fundamental reason metal nanoparticles are used in Raman spectroscopy for signal enhancement, a method which is described in later sections. Many factors contribute to the LSPR position and even the slightest change in any of these components can cause an LSPR to shift in energy. These influential factors are summarised in Figure 1.7.
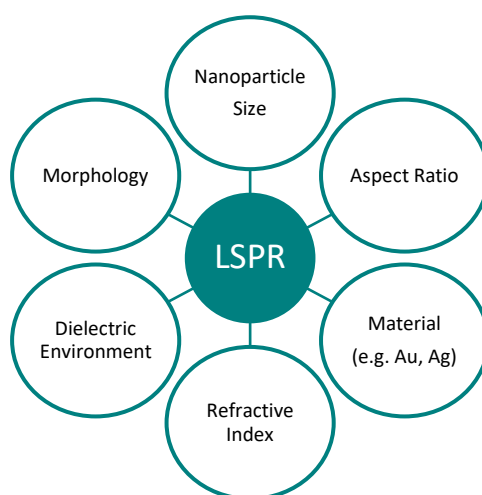

Figure 1.7 – Factors that influence the position of the LSPR. For example, larger nanoparticles will have a red-shifted LSPR compared to smaller particles of the same type. This is due to the larger contribution of scattering to the extinction that large nanoparticles exhibit.

The inter-particle distance between the nanoparticles, i.e. their state of aggregation, also influences the LSPR. When two nanoparticles come in close proximity to each other, their surface plasmons couple, and this results in a bathochromic shift. It shifts the plasmon band to a longer, lower energy, wavelength and is often referred to as a 'red shift'. This was first demonstrated by Mirkin *et al.* who used complimentary DNA strands to self-assemble nanoparticles in aggregates.[36] This controlled aggregation was reversible and was followed by extinction spectroscopy as the aggregate formation shifted the LSPR position.

1.3 Nanomedicine

There is significant potential for the application of nanoparticles within medicine, both diagnostically and therapeutically. As the literature covering this area is so extensive, discussion will be focussed to platforms which utilise metallic nanoparticles, and more specifically gold nanoparticles. Nanoparticles can be designed to actively target biomarkers *in vivo* and *ex vivo*, either to aid diagnosis or return a therapeutic effect.

Gold nanoparticles are frequently utilised for *ex vivo* diagnostic tests, by exploiting their unique optical properties, biomarker detection limits often exceed those currently established in routine blood tests. This feature of nanoparticle-based diagnostics results in earlier detection of disease, and therefore enables medical treatment to commence sooner leading to a better patient prognosis.

The most common diagnostic use of nanoparticles is within the assembly of paper based devices, such as a lateral flow assay. A widely known example of this is the pregnancy test, where nanoparticles are selectively immobilised if the target (human chorionic gonadotropin (hCG), a biomarker hormone indicating pregnancy) is present in the urine sample. The concentrated collection of gold nanoparticles in a line provides a visible indicator for pregnancy, which does not require medical expertise to interpret the results.

1.3.1 Drug Delivery

Publications of nanoparticle-assisted drug delivery has risen exponentially in the last few years as various combinations of materials and nanoparticle characteristics have been explored.[37,38,39] The inclusion of nanoparticles into a drug delivery system looks to improve on the low bioavailability of the drug, and also target the site of action more accurately.

In cancer treatment, the abnormal tumour vasculature can be targeted due to hypervascularisation and poor lymphatic drainage. This leads to an accumulation of nanoparticles in the tumour over time, this is known as the enhanced permeability

and retention (EPR) effect.[40] A damaged cardiac endothelium will also have leaky vasculature, and so nanoparticle targeting could be enhanced due to this structural defect.

Combining existing drugs with nanoparticles could lead to more efficient treatments, and if successful, the dosage level could be reduced, therefore suppressing the toxic side effects often associated with drugs. This section shall focus on gold nanoparticle based systems, and in particular of treatments targeted to the heart, since CVD is the primary target for this research.

Spivak *et al.* combined a clinically approved cardiac drug, Simdax, with gold nanoparticles to observe the effect in rats with induced heart failure.[41] They found the nanoparticle and drug combination had a cardio-protective effect when compared to the drug alone. In their study, they also found the nanoparticle system to be biologically safe (in cytotoxicity, genotoxicity and immunoreactivity).

One of the main issues surrounding nanoparticle use in vivo is knowing the distribution throughout the body. Many factors influence this, with nanoparticle size being the dominant factor. Studies have shown the accumulation of gold nanoparticles in the hearts of healthy rats and mice to be size dependent when injected intravenously. De Jong *et al.* found that when rats were injected with 10, 50, 100 and 250 nm gold nanoparticles, after 24hrs, the majority were present in the liver and spleen.[42] The 10 nm nanoparticles were also found in the blood, kidneys, testis, thymus, lungs, brain and heart, whereas the larger particles were only detected in blood, liver and spleen. A similar study by Sonavane *et al.* observed the same pattern in mice.[43] Where from the nanoparticle range (15-200 nm) injected, the 15 nm nanoparticles accumulated the most in various organs, including the heart. Both these studies looked at healthy animal models however, and may not correlate with the nanoparticle accumulation in a diseased heart.

Other studies have shown that larger nanoparticles accumulate in a diseased heart, with Lundy *et al.* finding particles with a size range between 20 and 200 nm accumulating in the heart after cardiac injury.[44] It is well established that tissue

vasculature becomes increasingly permeable following injury, therefore allowing larger particles to infiltrate from the blood stream into the cardiac tissue. However, it should be noted that the majority of nanoparticles were found in the spleen post injection, regardless of their size in the range investigated (20 nm – 2 µm). This is due to its key role in the immune system, acting as a filter for the blood. However, it should also be mentioned that these studies focussed on passive targeting, and that nanoparticle retention in specific tissues could be improved by actively targeting surface receptors in the tissue of interest.

Noonan *et al.* reported the targeted *in vivo* imaging of multiple vascular biomarkers using antibody-functionalised nanoparticles and surface-enhanced Raman scattering (SERS).[45] Their work was able to target intercellular adhesion molecule 1 (ICAM-1), vascular cell adhesion molecule 1 (VCAM-1) and P-selectin which were all overexpressed in atherosclerotic plaques in a humanised mouse model. This study showed promise for actively targeting the plaque sites in a nanoparticle-drug delivery system.

Very few studies have been published using gold nanoparticles to target the heart and deliver a therapeutic response, as such the toxicity to the heart is not fully understood. It is commonly accepted that despite the accumulation of gold nanoparticles in the filtering organs (kidneys or liver), there is no observable toxicity. A mini review article by Zhang *et al.* commented that nanoparticle size and administration (in terms of length and mode) would be the main factors influencing the toxicity of gold nanoparticles to the heart in vivo.[46] It is widely known that more studies on the efficacy and safety of drug loaded nanoparticles intended for the heart would need to be completed before presenting this treatment method in anything other than animal models.
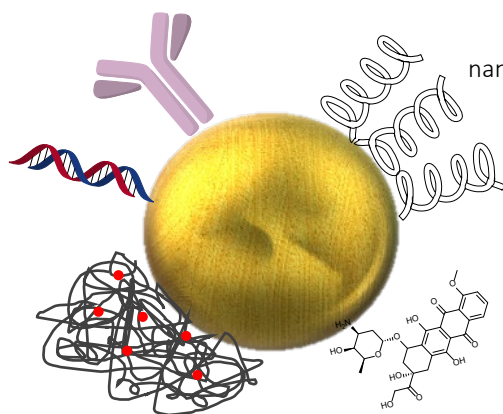
1.3.2 Surface Modification of Gold Nanoparticles for Drug Delivery

The versatility of gold nanoparticles as a surface makes them attractive vehicles for drug delivery designs. A plethora of functional molecules can be conjugated to the gold nanoparticle surface via an anchoring group with thiols and amines being the most popular.[47] This convenient method of attachment allows for almost any molecule to be modified for gold nanoparticle conjugation including, but not restricted to: drug molecules, DNA/RNA, proteins, peptides, lipids and stabilising polymers.[48]

Once in the bloodstream, nanoparticles are treated as invading particles and the immune system acts to remove the foreign particles from circulation. Proteins in the blood will adsorb around the particle forming a protein corona. The encapsulating proteins act as opsonins and mark the nanoparticles for clearance by phagocytes.[38] The mononuclear phagocytes system that operates in organs such as the lungs, liver and spleen is where most nanoparticles will be cleared from circulation.[49] To reduce the opsonisation and increase circulation time of nanoparticles in the bloodstream their surface should be made more hydrophilic.[50] This can be achieved by modifying with hydrophilic polymers or surfactants. Modified polymers such as thiolated polyethylene glycol (PEG-SH) can be used to accomplish the desired hydrophilic nature needed to produce the 'stealth' nanoparticles, and avoid the absorption of serum proteins, avoiding the formation of a protein corona.[47,51] Figure 1.8 shows a selection of the various molecules that can functionalise the gold nanoparticle surface for use in drug delivery.

Targeting Ligands - biomolecular recognition to bind to intended site e.g. antibodies, DNA

Hydrophilic Ligands –shields nanoparticles from the immune system e.g. PEG

Therapeutic Payload – Drug molecules, peptides, DNA, proteins etc. Can diffuse from nanoparticle surface or be released via a trigger e.g. light, heat, and pH

Polymer Matrix – can encapsulate 'cargo' and release over time in the body

Figure 1.8 - Gold nanoparticle functionalisation by a variety of molecules* for recognition, targeting, stability and delivery. *Molecules not drawn to scale compared to nanoparticle.

1.3.3 Photothermal Effect

Plasmonic nanoparticles such as AuNPs can convert incident photons into heat, this is known as the photothermal effect. The heat generated will dissipate through the nanoparticle-medium interface at a rate dependent on the medium, particle size, shape and excitation laser source, as the nanoparticles cool to their initial temperature.[52] Due to this intrinsic property, nanoparticles have the potential to change the landscape of disease treatment and their heating capabilities are being studied as a trigger for drug release and the localised hyperthermia.

The photothermal properties of gold nanoparticles have been studied by Link and El-Sayed using femtosecond transient absorption spectroscopy.[53] Their research has built the foundation for the understanding of the conversion of light to heat by metallic nanoparticles. The conversion of incident photons into thermal energy and the subsequent transfer to the surrounding medium occurs through a multi-step process.[53,54,55]

i. The interrogating photons excite the electrons at the nanoparticle surface, initiating electron-electron collisions, occurring within a few hundred femtoseconds. This produces hot electrons with temperatures as high as 1000 K.

ii. A heated electron gas is formed and transfers the energy to the nanoparticle lattice through electron-phonon* coupling.

*A phonon is a packet of vibrational energy that arises from oscillating atoms within a crystal. It is similar to how a photon is a quantum of electromagnetic radiation.[56]

iii. The hot lattice begins to cool off by transferring its heat to the surrounding medium via phonon-phonon interactions. Phonons relax on the time scale of a few hundred picoseconds.

It is this final stage in the conversion process that can be utilised to heat adsorbed molecules and release them to the local surroundings. Similarly if these nanoparticles

are located within a cancer tumour, the localised heating can be used to thermally ablate the cancerous cells, whilst protecting healthy surrounding tissue. Metallic nanoparticles are especially attractive for these applications since they have an abundance of mobile electrons and can be further enhanced when the excitation laser frequency matches that of the collective plasmon resonance of the nanoparticles.[57]

It should be noted the final step in the process can differ if the lattice energy is high enough. The lattice heating and cooling to surrounding medium is a competitive process, and if the cooling rate is below the heating rate, heat accumulates in the lattice. This can lead to morphological changes, such as the nanoparticle melting or fragmenting. This was demonstrated by Link *et al.* where they followed gold nanorods melting to spherical nanoparticles or fragmenting after irradiation; an adapted figure from the paper is shown in Figure 1.9.[58]
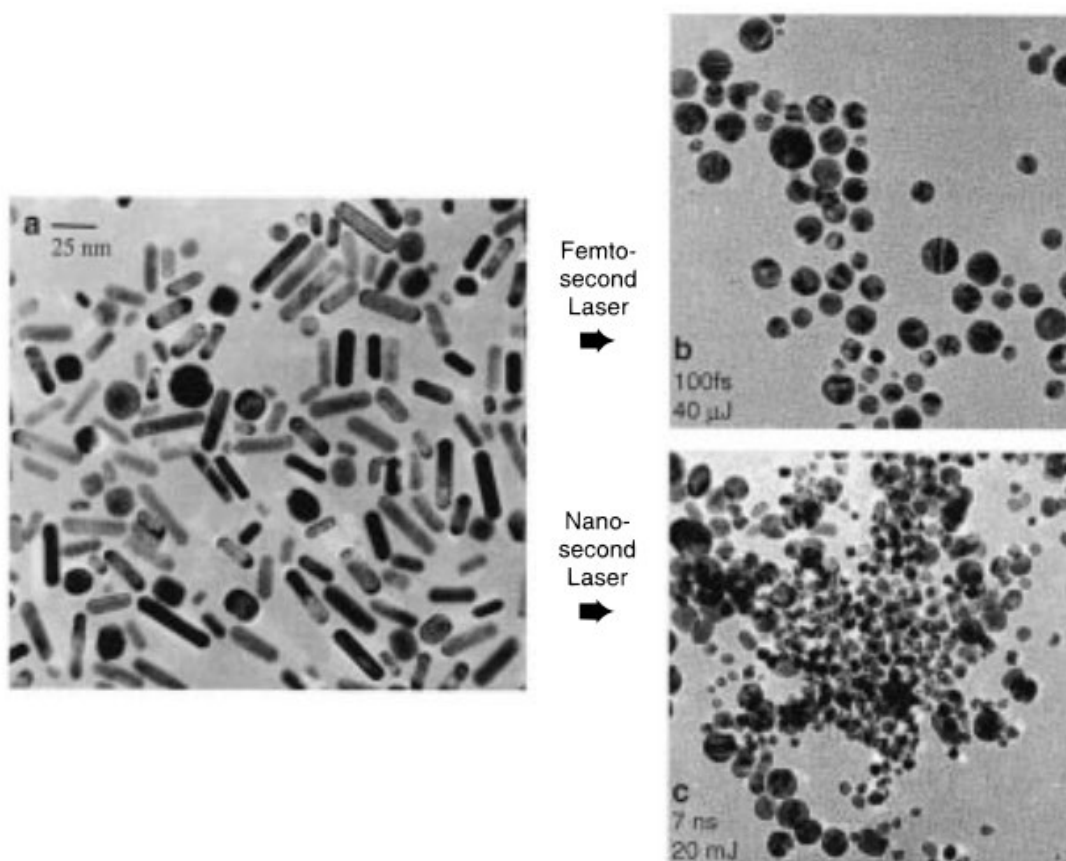

Figure 1.9 - (a) TEM image of the colloid prior to irradiation. (b) TEM image after exposure to 40 μJ femtosecond pulses (800 nm, 100 fs) for 7 min. (c) TEM image after exposure to 20 mJ nanosecond laser pulses (800 nm, 7 ns) for 1 min. (The scale bar in the upper left corner of (a) corresponds to 25 nm and also applies for b and c.) Adapted with permission from S. Link, C. Burda, M. B. Mohamed, B. Nikoobakht and M. A. El-Sayed, J. Phys. Chem. A, 1999, 103, 1165–1170. Copyright 1999 American Chemical Society.[58]

These outcomes can occur when high energy pulsed lasers deliver an intense burst of energy over a very short timeframe. When femtosecond pulsed laser excitation is used, the nanoparticles can be heated above the melting temperature of bulk gold, resulting in the reshaping and melting of the nanoparticle structure. This occurs due to the fast energy deposition and transfer rate to the nanoparticle lattice. In comparison, when a longer nanosecond pulsed laser is used, the absorption and relaxation processes overlap resulting in an increase in lattice energy which induces fragmentation of the nanoparticles. Both outcomes are not only based on the pulse width, but also the power of pulse delivered, meaning high energy femtosecond pulses can also produce fragmentation and low energy nanosecond pulses can produce nanoparticle melting.[59]

For most therapeutic applications, and for all experiments presented in this thesis, continuous wave lasers were employed to allow the less destructive heat transfer to the surrounding medium.

1.4 Raman Spectroscopy

In 1923, Adolf Smekal proposed that light could be inelastically scattered[60], however, it was not until 1928 that Chandrasekhara Venkata Raman and Kariamanickam Srinivasa Krishnan experimentally confirmed this phenomenom.[61] Landsberg and Mandelstam also independently observed this inelastic scattering effect and published their findings in the same year as Raman.[62] However it was Raman that was later recognised for this pioneering research when he was awarded the 1930 Nobel Prize in Physics. In honour of his research, the technique was subsequently named Raman spectroscopy. This vibrational technique can provide structural information about a molecule, through the unique 'fingerprint spectrum' obtained. Raman spectroscopy features heavily in this research, hence the separate introduction of the technique compared to other analytical techniques used.

1.4.1 Raman Scattering

Basic physics states that when a photon of light interacts with a molecule, it can either be absorbed, scattered or pass through with no interaction. The majority of scattered light is classified as 'Rayleigh' scattering; an elastic process that sees little to no energy transferred, resulting in the scattered and incident light having indistinguishable energies.

However, one in every 10^6-10^8 photons can be inelastically scattered and this inherently weak process is termed 'Raman scattering'.[63] It is a result of the incident electromagnetic radiation distorting the molecule's electron cloud, and therefore inducing a dipole. The molecule becomes momentarily polarised and exists in a virtual energy state. The energy of this virtual state is defined by the frequency of the laser used to excite the molecule. This state is not stable and so photons scatter as the distorted electron cloud relaxes. Inelastic scattering results in either a net loss or gain of energy between the photon and molecule, the energy is shifted by one vibrational unit.

This energy transfer can be categorised as either 'Stokes' or 'anti-Stokes' scattering depending on the direction of the energy transfer.[63] If energy passes from the incident photon to the molecule it is termed Stokes scattering, and the scattered light is of lower energy than the incident light. During this process, the excited molecule relaxes from the virtual state to an excited vibrational energy level of the ground electronic state. The Stokes bands in a Raman spectrum appears at a lower frequency as they are lower in energy.

In contrast, if the incident photon receives the energy transfer it is termed anti-Stokes scattering and results in scattered light of a higher energy than the incident light. This occurs when excitation initiates from a higher vibrational level than the ground vibrational state, after which relaxation and scattering occur. In a Raman spectrum, the anti-Stokes bands are less intense and occur at a higher frequency since they are higher in energy than the incident light. Figure 1.10 shows a schematic representation of the three scattering processes, known as a Jabłoński diagram.
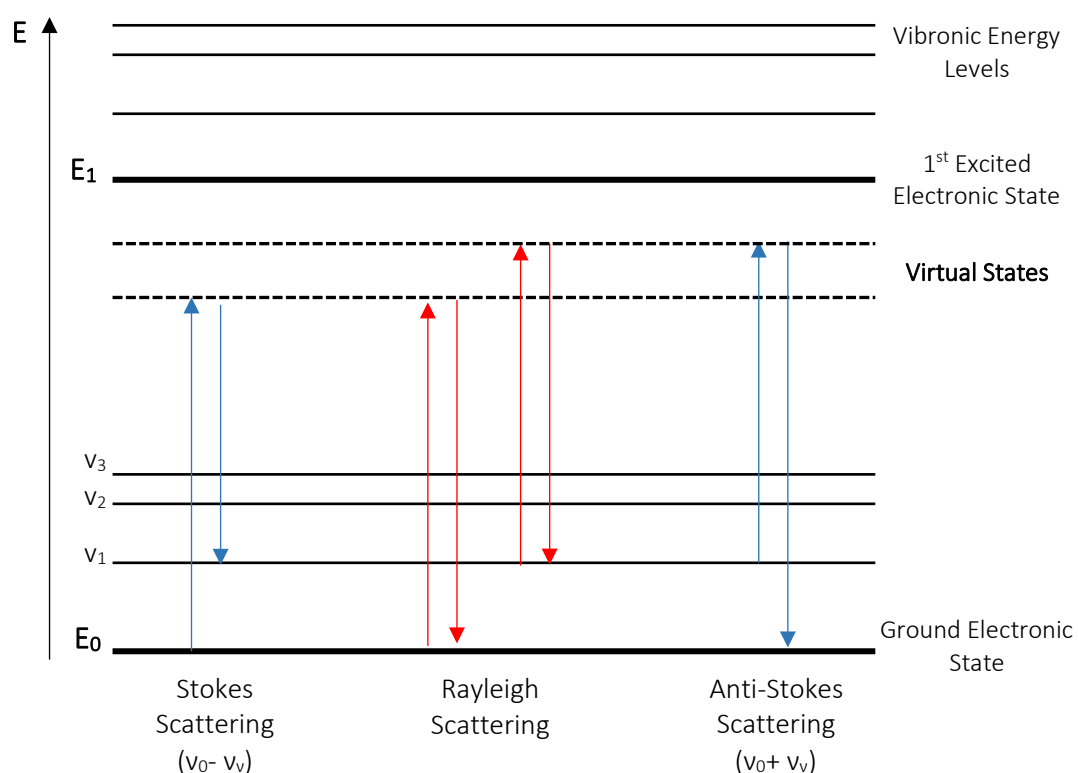

Figure 1.10 - A Jabłoński diagram showing the process of both elastic (Rayleigh) and inelastic (Raman) scattering of light. Rayleigh scattering results in no net gain/loss of energy during the scattering process. Stokes scattering occurs when energy is passed from the photon to the molecule, and the scattered light is lower in energy than the incident light. Anti-Stokes scattering is the reverse process, energy is passed from the molecule to the photon, resulting in scattered light of higher energy than the incident photon.

When using Raman spectroscopy, Stokes scattering occurs more intensely and frequently than anti-Stokes scattering at room temperature due to Boltzmann distribution. This is because more molecules are in the ground state at room temperature, but if temperatures were increased, more anti-stokes scattering would be observed. Predictions of the energy levels, and therefore the likelihood of Stoke/anti-Stokes scattering intensity can be calculated using the Boltzmann equation shown in Equation 1.1. N_1 denotes the number of molecules in the upper energy level, N_0 the number of molecules in their ground state, g is the degeneracy of the energy levels, E is the energy difference between the energy states, k is the Boltzmann constant (1.3807×10^{-23} J K^{-1}) and T is the temperature (K). The final term in the Boltzmann equation has the largest effect on the population distribution. Statistically most molecules are in their ground vibrational state at room temperature, and so will proceed to Stokes scattering over anti-Stokes scattering.[63]

Equation 1.1 - The Boltzmann Equation.

$$\frac{N_1}{N_0} = \frac{g_1}{g_0} \, exp \left[\frac{-(\Delta E)}{kT} \right]$$

Since Raman scattering is a measure of the shift in energy from the exciting radiation it should technically should be expressed as Δ cm^{-1}, but is more commonly recorded as cm^{-1}. It is these shifts that give structural information on the molecule under observation as they directly correspond to molecular vibrations. The intensity of the Raman scattering can be expressed as shown in Equation 1.2.

Equation 1.2 - Raman intensity dependence.

$$I = Kl\,\alpha^2 v^4$$

Where K consists of constants including the speed of light, l is the intensity of the laser, α is the polarisability (an intrinsic property of the molecule) and v is the excitation laser frequency. The intensity and frequency of the laser can be controlled by the spectroscopist, and given that the latter is to the fourth power, this has a large influence on the intensity of the resultant Raman spectrum. Shorter excitation wavelengths, e.g. UV region, result in higher Raman scattering but often molecules

absorb this radiation and sample degradation or burning can occur. Longer wavelengths, and therefore lower frequencies, result in weaker signals, but this is balanced by less interference from competing events such as fluorescence. Experimental parameters such as acquisition time can overcome this issue.

Raman scattering in general is an inherently weak process (one in every 10^6-10^8 photons), as such there has been development in the detecting instrumentation and other enhancement approaches (e.g. resonance Raman, surface enhanced Raman and surface enhanced resonance Raman). These approaches help improve the intensity of the otherwise weak signals obtained.

Enhancement of the Raman signal can be achieved by fine tuning the energy of the interrogating light to coincide with the energy of an electronic transition within the molecule, i.e. close to an absorbance maxima in the molecule. This is known as Resonance Raman scattering (RRS). This allows light to be both absorbed and scattered, however the timescale for scattering light is much faster than to absorb.[63] Scattering occurs before the nuclei has reached equilibrium positions in the excited state. Compared to normal Raman, the scattering efficiency of RRS can be increased by 10^4 orders of magnitude.[63] In addition to vibrational information, this technique can reveal electronic information about the molecule, and is observed when certain peaks in the spectrum are enhanced more than others.

1.4.2 Surface Enhanced Raman Scattering

Nearly half a century after the theoretical reasoning to Raman spectroscopy was published, Fleischmann *et al.* observed an enhancement of Raman intensity when the analyte was adsorbed onto a metal surface, schematic shown in Figure 1.11.[64] While detecting pyridine at a silver electrode, they noted that a roughened electrode surface produced a higher Raman scattering signal than a smooth silver electrode did, and suggested it was due to an enhanced surface area. In 1977, two independent papers proposed mechanisms for the enhancement effect. Jeanmaire and Van Duyne

proposed the electromagnetic enhancement[65], while Albrecht and Creighton proposed a charge transfer effect.[66]
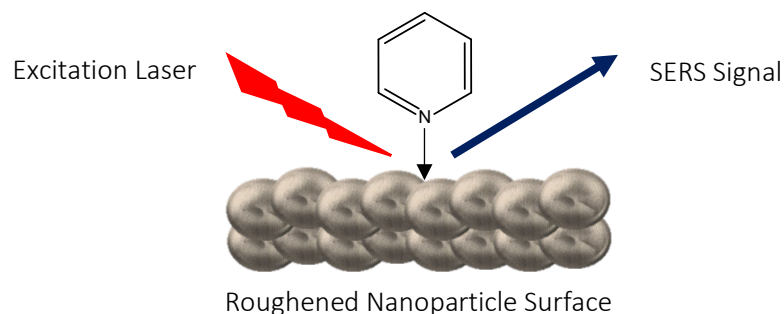

Figure 1.11 - Schematic of SERS. Pyridine binds to the metal surface via lone pair on nitrogen. The roughened surface increases the electromagnetic field the molecule experiences, leading to an increase in Raman scattering.

The electromagnetic effect is the dominating process and results from the incident light interacting with the nanoparticle surface electrons. By utilising a roughened metal surface, the surface plasmons are no longer tightly bound as is within a smooth metal surface. This means that they can radiate in directions both parallel and perpendicular to the nanoparticle surface.[67] When the incident radiation interacts with the rough surface, it causes the surface plasmon to oscillate and in turn the adsorbed molecule experiences an increase in the local electromagnetic field.[68] Consequently the polarisation of the adsorbed molecule intensifies, generating a greater Raman signal. If the plasmon frequency is in resonance with the interrogating laser and the plasmon oscillations are perpendicular to the nanoparticle surface, an even greater enhancement occurs. Even more signal enhancement is possible when nanoparticles touch or cluster together. This is because single particles oscillate over a narrow wavelength range, but when coupled to neighbouring nanoparticles, a wider range of wavelengths is achieveable.[63] This phenomena is known as 'hot spots' and can further increase the enhancement factor observed.

The lesser contributing effect is a result of a charge transfer between the nanoparticle surface and the molecule in question. When the molecule is bound to the metal surface, a charge-transfer complex is formed. The excitation radiation interacts with the metal to form an electron-hole pair, acting as a passage for energy transfer

between the molecule and metal, and then returned for scattering.[67] This interaction forms a new electronic state, which is close to or in resonance with the wavelength of the excitation laser.[68] This can cause a change in the intrinsic polarisability of the molecule and in turn increases the Raman scattering.[69]

1.4.3 Surface Enhanced Resonance Raman Scattering (SERRS)

In 1983, Stacy and Van Duyne combined both RRS and SERS to create a technique known as surface enhanced resonance Raman scattering (SERRS).[70] This hybrid technique combines the use of chromophores which are in resonance with the interrogating light, and the rough metal surface enhancement. The estimated SERRS enhancement factor for rhodamine lies between 10^{13}-10^{15}, a factor much higher than theories could predict from the addition of a surface enhancement and molecular resonance.[67] A primary advantage of SERRS is that most interfering fluorescence is quenched, as a result of the chromophore and metal surface being in close proximity. This significantly improves the detection of the Raman scattering, producing a clearer and more detailed spectrum.

In recent years, there has been focus on SERS techniques to reach single-molecule detection limits, and although proven to have high specificity, the sensitivity in such dilute solutions remains challenging. Yang *et al.* developed a SERS based technique which improves on the delivery of analytes into the SERS active sites, reaching a quantitative detection limit of 75 fM for Rhodamine 6G.[71] It is possible that even lower detection limits could be achieved by using a laser excitation wavelength in resonance with the Raman reporter molecule, leading to greater signal enhancement.

To summarise the strength of the Raman spectroscopy techniques discussed, the following are listed in order of increasing sensitivity for analyte detection:

Raman < Resonance Raman < SERS < SERRS

2. Thesis Motivation & Overview

The long-term aim of this research was to develop a 'nano vehicle' targeted to inflamed cardiac tissue to deliver and subsequently release the statin payload. Initial investigations looked at solid gold nanoparticles as the core of the design with a focus on covalently attaching the statin to the nanoparticle surface, although electrostatic attachment was also investigated. Various linkers were proposed for this delivery role and the viability of each one was studied. Attachment of the statin to the nanoparticle surface was ideally facilitated through a biocompatible linker, possibly PEG or noncoding strands of DNA, which were studied first. However, keeping the statin liberation in mind, cleavable linkers were also investigated, with a pH responsive linker (acetal) being researched. It was later decided that environment-dependent release of the statin may not prove to be the most successful, and so focus was shifted to the various nanoparticle types that could provide an alternative release mechanism.

i. Chapter 3 explores the potential of iron oxide nanoparticles as the core of the design. Studies have shown drug release from these magnetic nanoparticles through the oscillation of a magnetic field.[72]

ii. Chapter 4 considers hollow gold nanoparticles as a potential candidate for the design. The synthesis of these particles was investigated, with a simple benchtop method and the ability to tune the LSPR. The photothermal properties of the HGNs were also explored, as studies have shown the intense local heating can release drugs from the surface and also reduce the volume of the atherosclerotic plaque.[73]

iii. Chapter 5 investigates the relationship between the Raman enhancement and the plasmonic heating. Multiple theories for the cause of the enhancement are discussed in this chapter, with the adatom hypothesis being the most probable.

3. Iron Oxide Nanoparticles

3.1 Chapter Introduction

As with most nanoscale materials, magnetic nanoparticles (MNPs) show different behaviours compared to their bulk relatives. Within a bulk magnetic material, multiple regions called magnetic domains exist, where the magnetic moments, or unpaired electrons, align. These domains of uniform magnetisation are separated by a domain wall which is energetically costly.[74-75] When the scale of the material is reduced to the nanoscale, to keep energy costs minimal, the magnetic order will not break into domains and instead it remains as a magnetic monodomain.[74] The critical MNP diameter is dependent on the material, but typically lies within the range of a few tens of nanometres.[76] This nanoscale behaviour is termed 'superparamagnetic' and a nanoparticle with this property acts like one giant paramagnetic atom and quickly responds to an externally applied magnetic field.[76] At high enough temperatures (e.g. room temperature), the thermal energy within each superparamagnetic nanoparticle is enough to allow spontaneous rotation of the magnetic moment. As a result, the net magnetic moment of a MNP system will be net zero, and appear as a nonmagnetic material.[74] This makes the use of superparamagnetic nanoparticles attractive for many biomedical applications since they are able to maintain colloidal stability and avoid agglomeration at room temperature. Figure 3.1 shows a schematic detailing how the magnetic moments align in a bulk material versus in a MNP.

Bulk Material
(Multiple Domains)

Individual
Nanoparticle

No Magnetic Field
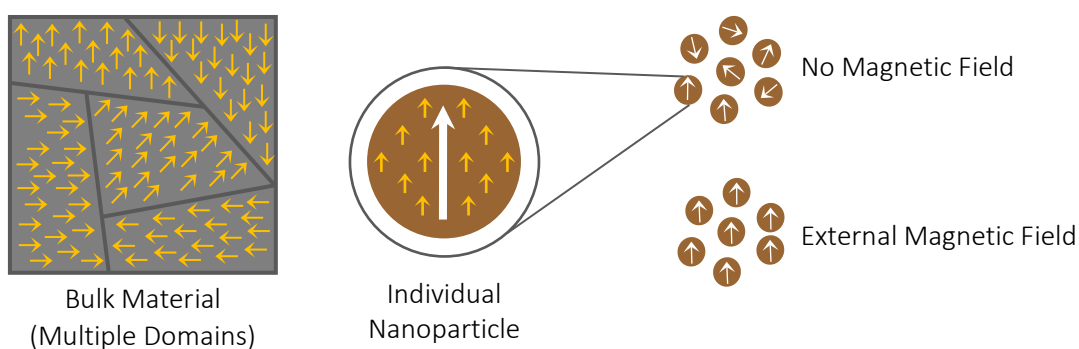
External Magnetic Field

Figure 3.1 - Schematic of magnetic domains in a bulk magnetic material compared to magnetic nanoparticles. Bulk materials have multiple magnetic domains, whereas nanoparticles exist as a monodomain. Applying an external magnetic field aligns the magnetic moments in a nanoparticle solution.

An additional benefit of employing MNPs in a medical application lies in the sample preparation. After the addition of any surface attaching molecule or mixing with a complex matrix, the sample can be easily cleaned by applying an external magnetic field to the side of the vial. This makes for simple wash steps, and can even be used to concentrate the sample for any further analysis.

The systemic distribution of therapeutic drugs can often lead to side effects as healthy tissues are adversely affected from the cytotoxic effects of the drug. This is very common in chemotherapy treatment, where the aggressive therapy has poor specificity for the tumour target. In the late 1970s, Widder *et al.* were the first to utilise the magnetic properties of iron oxide nanoparticles to selectively concentrate drug loaded nanoparticles in the tail of rats.[77] They employed MNPs into the synthesis of doxorubicin (an anticancer drug) loaded albumin microspheres. By applying an external magnet, they were able to concentrate the particles in the tail of the rats. The concept behind this delivery route was to guide the drug loaded MNPs by external magnets to the target site. Once on target, the nanoparticles could then be held in location until the therapy was complete or drug cargo had been released. This resulted in a high local concentration of the drug at the target site, reducing the adverse effects to other tissues.

More recently, Kheirkhah *et al.* magnetically guided and confined MNPs in the spinal cord of a rat model.[78] The subdermal placement of a neodymium magnet over the growing tumour site in the spinal cord localised the drug loaded MNPs after they were injected further down in the spinal canal. Their study indicated that combining MNP with drug delivery, could be a promising technique for targeting the spinal canal and treating diseases affecting the central nervous system.

As with all applications of nanoparticles in medicine, tailoring the colloidal parameters and functionalisation of the surface defines the success of the treatment. Common materials for MNPs are iron, cobalt and manganese with popular synthesis routes including co-precipitation, thermal decomposition, micelle synthesis, microemulsions and hydrothermal synthesis.[75-76] However, the majority of publications and medical

applications utilise iron oxide nanoparticles, due to their adaptable synthesis, good magnetic properties and colloidal stability. Iron oxide nanoparticles are often studied in the form of magnetite (Fe_3O_4), hematite (α-Fe_2O_3) and maghemite (γ-Fe_2O_3).[79]

The American Food and Drug Administration and the European Medicines Agency have approved the use of magnetic iron oxide nanoparticles for medical use.[75] They are being extensively employed for use as a contrast agent in magnetic resonance imagining (MRI), however research has been expanding into their use in molecular detection, as an agent in hyperthermia treatment and also as drug delivery vehicles.

Islamian *et al.* combatted breast cancer cells *in vitro* by combining MNP drug delivery with chemotherapy and radiotherapy.[80] They synthesised superparamagnetic hydroxyapatite coated iron oxide nanoparticles and conjugated doxorubicin and 2-Deoxy-D-Glucose, with the latter molecule improving tumour localisation. The nanocomposites showed promising results for enhancing the efficiency of chemotherapy and radiotherapy in the treatment of breast cancer.

The intrinsic magnetic properties of MNPs can also be utilised for assisting in drug release. Hua *et al.* used an oscillating magnetic field to trigger the release of doxorubicin from magnetic nanoparticles, resulting in a significant release of 70% of the drug load.[72] To confirm the oscillating field was the trigger for this release, the field was switched on and off in a cycle, with the % drug release shown in Figure 3.2(a).
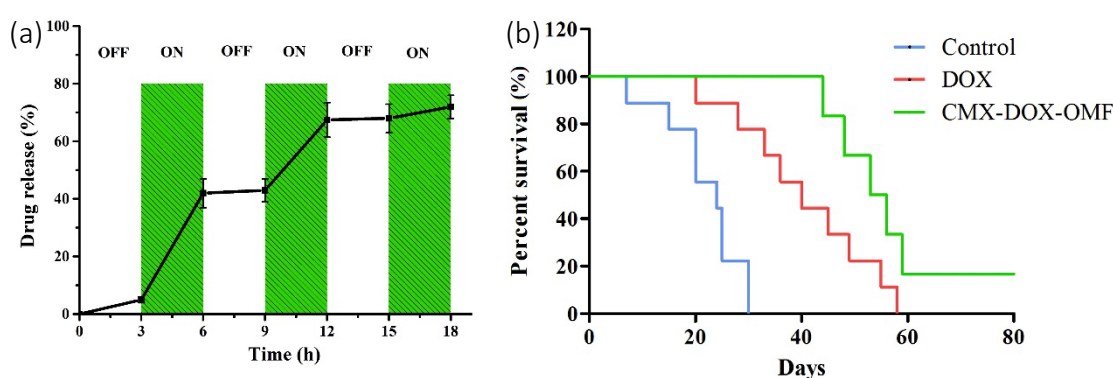

Figure 3.2 - An oscillating magnetic field was used to trigger the release of doxorubicin from the iron oxide nanoparticle surface. (a) shows the % drug release as the oscillating field was cycled through and on/off mode. (b) survival curves of mice in the 3 treatment groups: Control (saline), DOX (free drug), CMX-DOX-OMF (drug loaded MNP triggered by the oscillating magnetic field). Figures adapted from an open access publication. [72]

During the 'off' periods there is almost no increase in the drug release, indicating the oscillating magnetic field was responsible for the release. Figure 3.2(b) shows the survival curves of mice under three different treatments: just saline (Control group), free doxorubicin (DOX) and those treated with the drug loaded MNP (CMX-DOX-OMF) and subjected to the oscillating magnetic field. The control group only survived 24 days, whereas the group treated with MNP not only all survived until after day 40, but a few were still alive after 60 days. This study indicated magnetic nanoparticles were a promising vehicle for both delivering and releasing therapeutic agents *in vivo*.

For a given size, a hollowed or cage-like nanoparticle will have a higher surface area than a comparable solid nanoparticle. This is a favourable attribute for the drug delivery nanoparticle design as it allows for higher drug loading per nanoparticle. This in turn could lead to reduced dosages if the high localisation of a drug could be achieved. A study by Matsui *et al.* proposed iron oxide nanocages (IONCs) for the delivery of the drug Riluzole to treat metastatic osteosarcoma.[81] Their study focused on nanoparticle shape, and showed better drug efficacy compared to solid iron oxide nanoparticles.

3.2 Aims

The aim of this chapter was to explore the potential of using IONCs as the nanoparticle core of a drug-delivery design. To be considered as the nanoparticle vehicle, the target size was under 100 nm, since they were intended for future *in vivo* applications. Their synthesis and subsequently necessary phase transfer to an aqueous phase was investigated. The functionalisation with targeting and signalling molecules was also investigated. To facilitate this last step, gold coating of the IONCs was attempted to provide a facile metal surface for molecule attachment.

3.3   Results & Discussion

The large surface area of Fe_2O_3 nanocages (IONCs) is an attractive feature of the nanoparticles for drug delivery applications, and to explore their potential, they were synthesised through a galvanic replacement reaction.[82] The initial capping ligand was hydrophobic in nature which was problematic for the desired application, to combat this, a ligand exchange with 3,4-dihydroxyhydrocinnamic acid (DHCA) was carried out to transfer the nanocages to an aqueous phase. Au coating of the IONCs was carried out under mild conditions, using glucose as the reducing agent. The incorporation of gold to the drug delivery design would allow for the functionalisation with biological targeting molecules and Raman reporters. The synthesis steps to the final gold coated IONCs is summarised below in Figure 3.3.
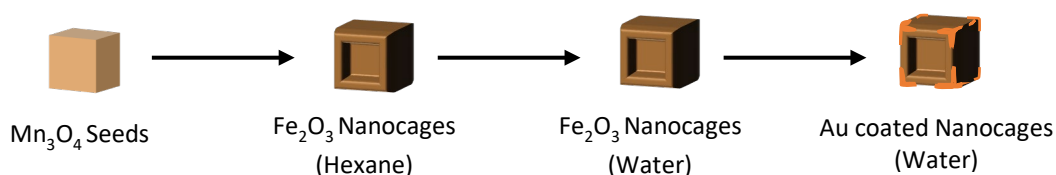

Mn_3O_4 Seeds Fe_2O_3 Nanocages Fe_2O_3 Nanocages   Au coated Nanocages
                                        (Hexane)   (Water)   (Water)

Figure 3.3 - Summary of the synthesis steps towards the gold coated iron oxide nanoparticles. First sacrificial Mn_3O_4 seeds are synthesised, then a galvanic reaction is initiated resulting in the iron oxide nanoparticles. The MNPs were next transferred into an aqueous phase to allow for future modifications. The final step was to gold coat the MNPs using a gentle glucose reduction method.

3.3.1   Nanocage Synthesis

Galvanic replacement reactions provide a route to synthesising nanoparticles with a hollow centre and a porous surface. Many hollow nanoparticle shapes have been demonstrated, including hollow triangular rings, cuboids, spheres and rods to name a few.[83] These surface features are controllable by altering the reagent ratios during synthesis. The reaction proceeds due to a difference in the electrochemical potential of the two metallic species present in the mixture. During synthesis, the metal with the higher reduction potential will be reduced while the metal with the lower reduction potential is oxidised. Essentially there is a redox reaction where electrons are donated from one metal species to the other as the reaction proceeds.

In the galvanic reaction carried out to synthesise the IONCs, the standard reduction potentials of Mn_3O_4/Mn^{2+} and Fe^{3+}/Fe^{2+} pairs were 1.82 V and 0.77 V, respectively.[82] Therefore the reaction proceeds with the reductive dissolution of Mn^{3+} and the oxidative precipitation of Fe^{2+} in the form of Fe_2O_3.

The first product of the synthesis is the manganese oxide (Mn_3O_4) seeds which act as the precursor to the IONCs. These act as a morphological template and dissolve upon reduction when iron (II) perchlorate is introduced to the reaction. During synthesis of the seeds, the manganese salt is dissolved in xylene, as well as oleylamine and oleic acid. The addition of water to the vessel triggers the reaction, and $Mn(OH)_2$ is formed as an intermediate species to the Mn_3O_4 seeds.[84] The transmission electron micrograph in Figure 3.4 shows the Mn_3O_4 precursor seeds, where almost all the nanoparticles lay flat on one face on top of the transmission electron microscopy (TEM) grid, this produced a very clear view of the face shape. The majority of the seeds had quadrilateral faces, presenting either as a square or a rhombus, both shapes having equal side length by definition. Therefore the seeds synthesised are a mixture
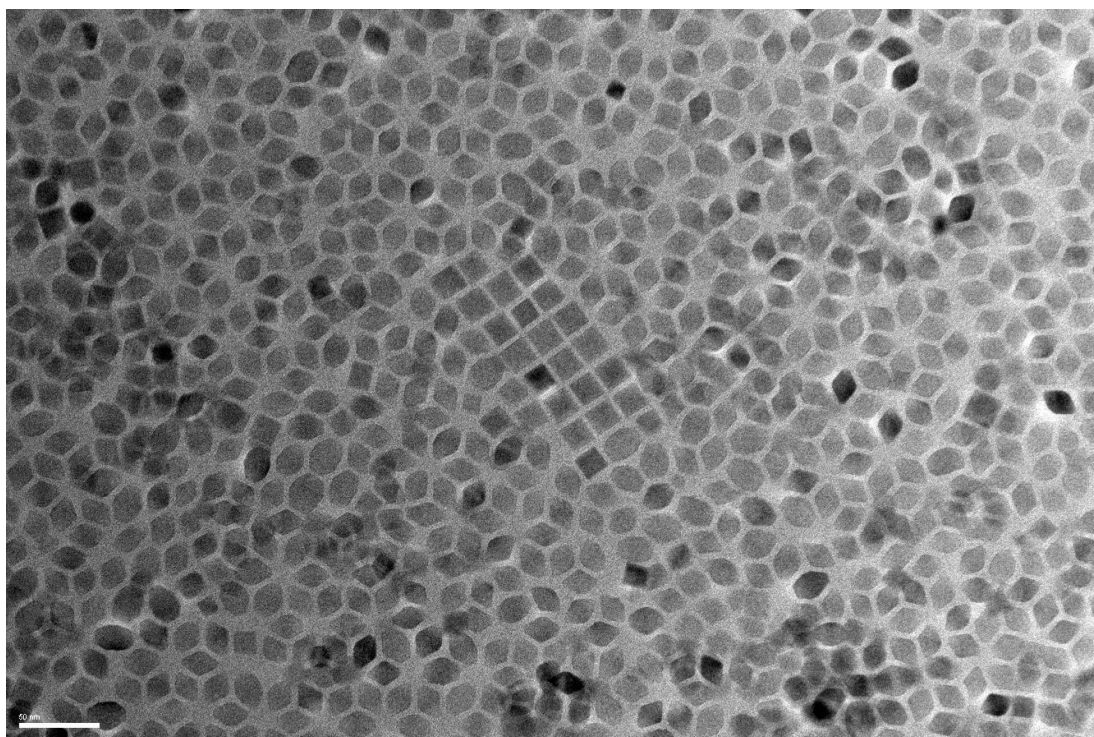

Figure 3.4 – TEM image of Mn_3O_4 seeds used as the template nanoparticle for the galvanic reaction. Sample was spotted onto carbon coated copper grids and left to air dry before imaging. Scale bar shows 50 nm.

of cuboids and rhombohedrons, with the majority of the sample population categorising as the latter. The image is representative of the sample population. Atomic force microscopy could also have been performed to further characterise the nanoparticle morphology in three-dimensions, an improvement on the two-dimensional data gained from TEM.

Once the iron (II) perchlorate had been introduced to the reaction, the galvanic reaction began instantaneously. The iron oxidises around the seeds, forming the cage-like structure that becomes the final frame of the IONC.[82] The preferential iron oxidation sites are at the corners and along the vertices of the Mn_3O_4 seeds, hence the final cage-like structure with a concave aspect on each face of the nanoparticle. The reaction is categorised as a redox reaction since the Mn_3O_4 seeds reduce while the iron simultaneously oxidises. Following literature examples the reaction should form maghemite nanoparticles (γ-Fe_2O_3), however for this synthesis further analysis would be needed to confirm the crystal structure. Figure 3.5 demonstrates the final form of the IONCs after the iron (II) perchlorate addition. Again, the image is representative of the sample population.
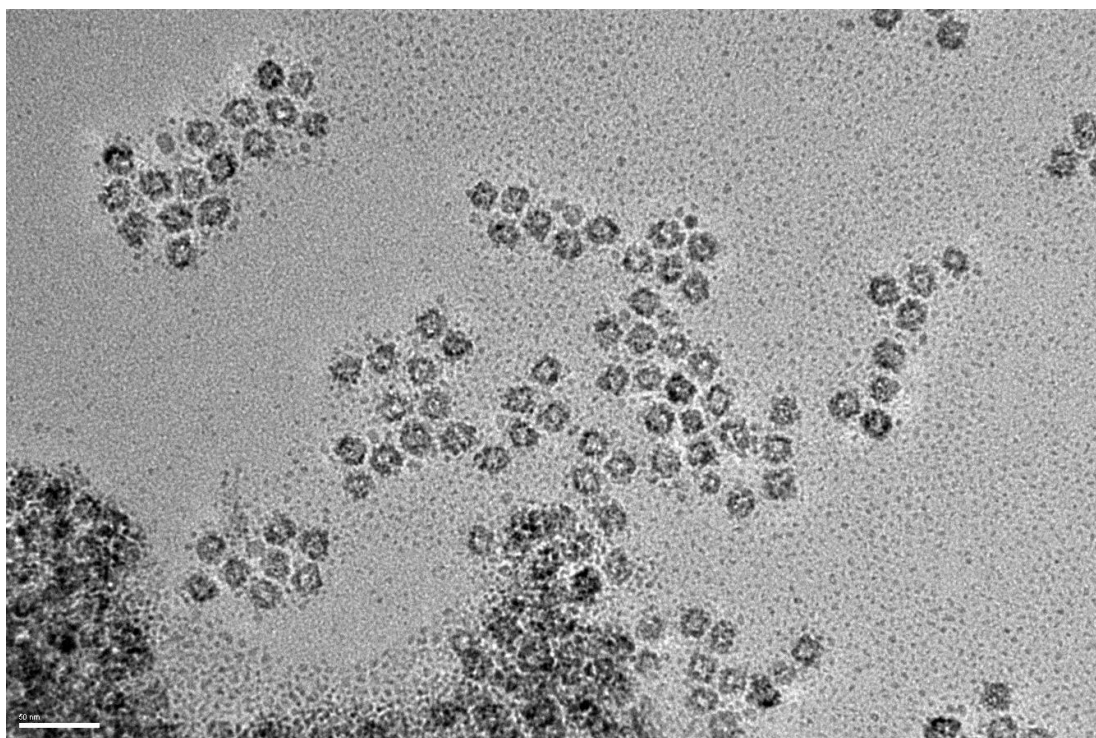

Figure 3.5 – TEM image of the product of the galvanic reaction, Fe_2O_3 nanocages. Sample was spotted onto carbon coated copper grids and left to air dry before imaging. Scale bar shown is 50 nm.

Comparing to the precursor nanoparticles in Figure 3.4 there is a clear change in the nanoparticle shape after the introduction of the iron (II) perchlorate. The faces of the nanoparticles are no longer uniform in density, indicated by the dark/light contrast of the nanoparticle faces in the image. This suggests there is a cavity or concave in the faces of the nanoparticles. The edges of some of the particles appear speckled, suggesting there could be additional pinholes along the edges of the nanocages. Examples of these surface features are reported in the literature using high resolution TEM.[82] Upon comparison to Figure 3.4, it can be noted that further purification steps could have been performed before imaging the IONCs, to produce a clearer image and reduced the background of excess reagents. However, the images are still in agreement with the literature regarding the nanoparticle synthesis methods.[82-84]

Using imageJ software, nanoparticle sizes were determined with the Mn_3O_4 seeds being 17.8 nm ± 3.0 nm on average and the IONCs were 16.3 nm ± 1.6 nm on average. These sizes are within error of each other, which is as expected given that the IONC form around the seed template. A histogram of the Mn_3O_4 seeds is shown in Figure 9.1 in the appendix. This broad distribution of sizes is expected given the mixture of cubic and rhombic faces of the Mn_3O_4 seeds, measuring from corner to corner in the case of the rhombic faces.

The concentration of the IONCs was determined by digesting the nanoparticles in a solution of hydrochloric acid (HCl) and analysing the absorbance of the digest using UV-Vis spectroscopy. A calibration curve was produced using $FeCl_3.6H_2O$ solutions that were also digested in the HCl solution. Figure 3.6 shows the average spectra obtained by analysing the digested solutions after 2 hours. The strong absorbance band at 335 nm corresponded to the Fe^{3+} ion in solution. This band was used to determine the concentration of the IONCs. Figure 3.7 shows the calibration plot (in purple) with the IONC sample (in teal) plotted on the linear response. By considering the dilutions made during sample preparation, the IONC stock solution had a calculated iron concentration of 41.3 mg/mL.
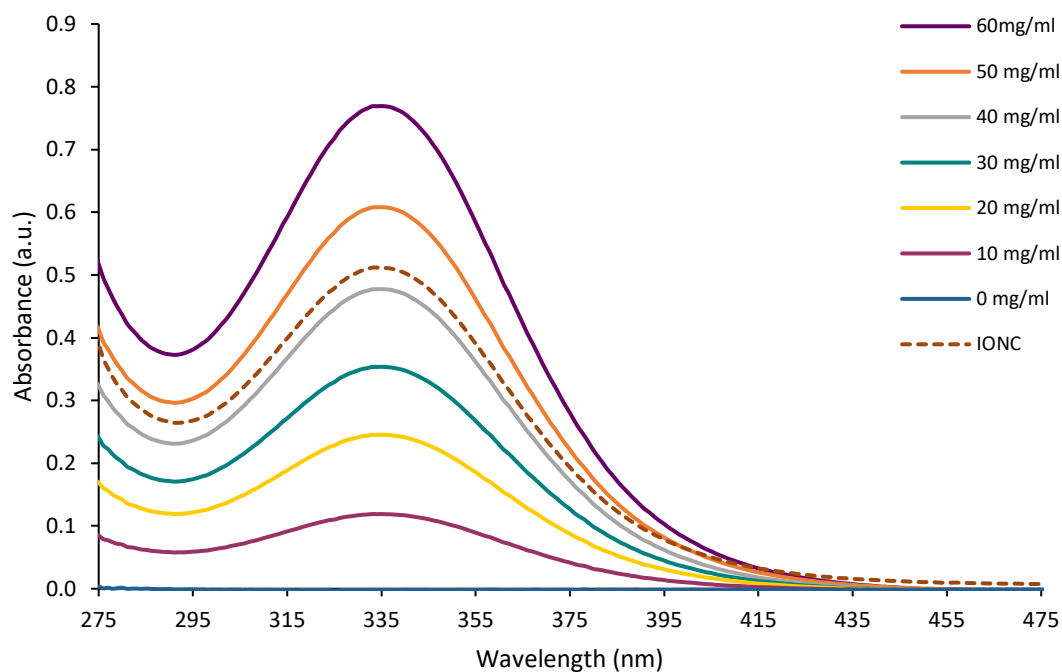
Figure 3.6 - Absorbance spectra of calibration curve samples and digested IONC sample. Samples were analysed at a 1 in 3 dilution in water. Spectra shown are the average of triplicate experiments with 3 measurements of each sample within each set. Measurements collected on a baselined fast scan rate (4800 nm/min, 1 nm intervals).
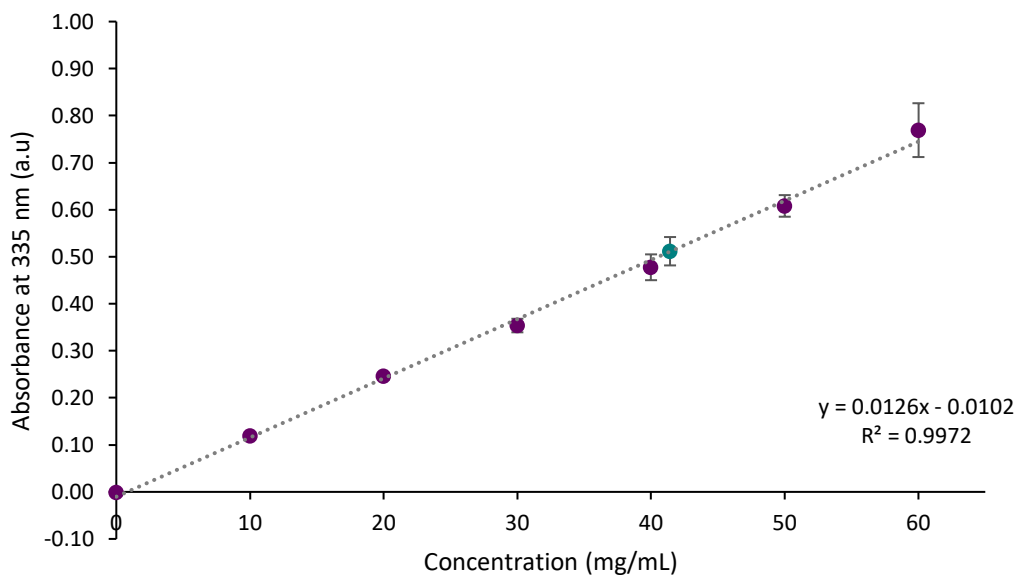

Figure 3.7 - Calibration plot of the digested $FeCl_3.6H_2O$ solutions (purple). Digested IONC shown in teal. Samples were analysed at a 1 in 3 dilution in water. Data obtained from an average of triplicate experiments with 3 measurements of each sample within each set. Measurements collected on a baselined fast scan rate (4800 nm/min, 1 nm intervals).

3.3.2 Phase Transfer of Nanocages

The nanocage synthesis was carried out in non-polar solvents, with the final wash step into hexane, this allows the hydrophobic IONCs to evenly disperse throughout the colloid and maintain stability. Oleic acid capped the IONC surface and contained a long fatty chain, resulting in the hydrophobic nature and the nanoparticles being immiscible in water. This caused issues for many further experiments and would be an issue long-term for any biocompatible application.

To resolve this issue, the IONCs were transferred into an aqueous phase. Surface molecule exchange with 3,4-dihydroxyhydrocinnamic acid (DHCA) was carried out to transfer the IONCs to an aqueous phase using a modified method from Liu *et al.*[85] Figure 3.8 illustrates the surface molecule exchange that results in a phase transfer of the IONCs.
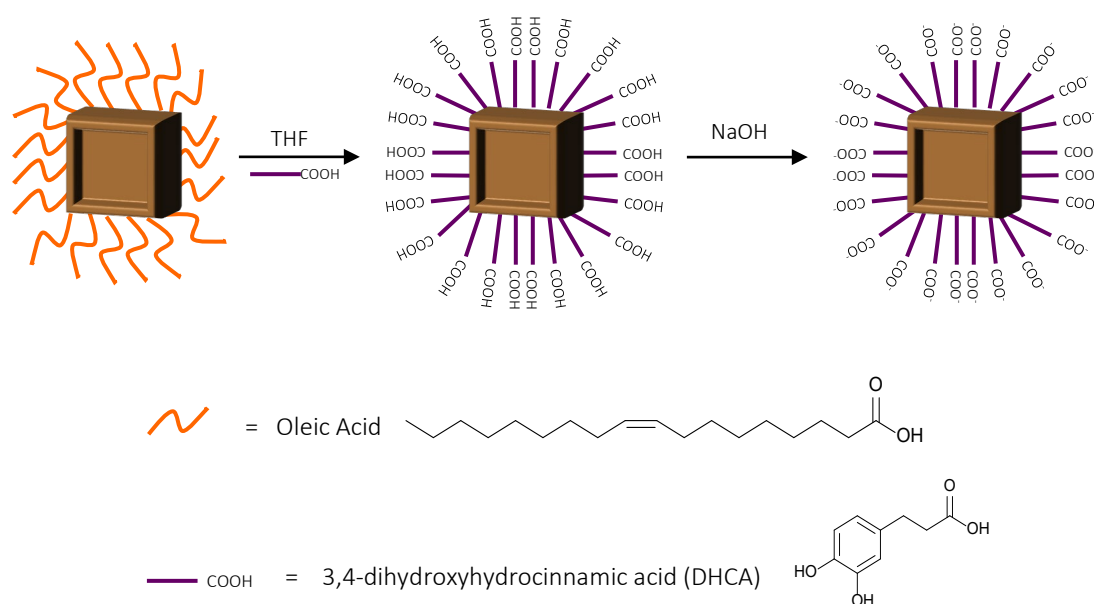

Figure 3.8 –Diagram illustrating the surface molecule exchange from oleic acid to 3,4-dihydroxyhydrocinnamic acid carried out in THF. NaOH is added to precipitate the particles, allowing collection and transfer from an organic phase to an aqueous phase. Molecular structure of each molecule shown in the key.

Oleic acid was replaced by DHCA on the IONC surface and conjugated through a five-membered metallocyclic chelate ring.[85] The catechol functionality of DHCA has a strong affinity for the iron oxide nanoparticle surface, ensuring an efficient exchange with the less strongly bound oleic acid. NaOH was added to neutralise the IONCs and

precipitate the resulting sodium salt which was collected due to its insolubility in THF. The DHCA-IONCs were then redispersed in water. As well as providing the hydrophilic nature of the nanocages, DHCA has a terminal carboxyl group which could provide an attachment point for any further modifications e.g. antibody conjugation.

3.3.3 Magnetic Properties of the Nanocages

It is common practice to investigate the effects of an applied magnetic field and temperature to the magnetisation of a sample, these results aid the categorisation of the magnetic behaviour. A superconducting quantum interference device (SQUID) is a highly sensitive magnetometer able to measure subtle changes in the magnetic moment of a sample. The basic magnetic properties of the IONCs were characterised on a Quantum Design MPMS-7 SQUID magnetometer at the University of Poland. All data was collected and processed by Marcin Witkowski. Both the dependence of the sample magnetisation (M) on an applied external magnetising field (H) and the temperature (T) were investigated. The oleic acid and DHCA coated IONCs were both characterised, resulting in very similar datasets. As such, only the DHCA-IONC data is presented since they were used in future experiments.

Magnetism curves were collected while applying a varying external magnetising field (H), Figure 3.9 shows the curve collected for the DHCA-IONCs at 300 K.
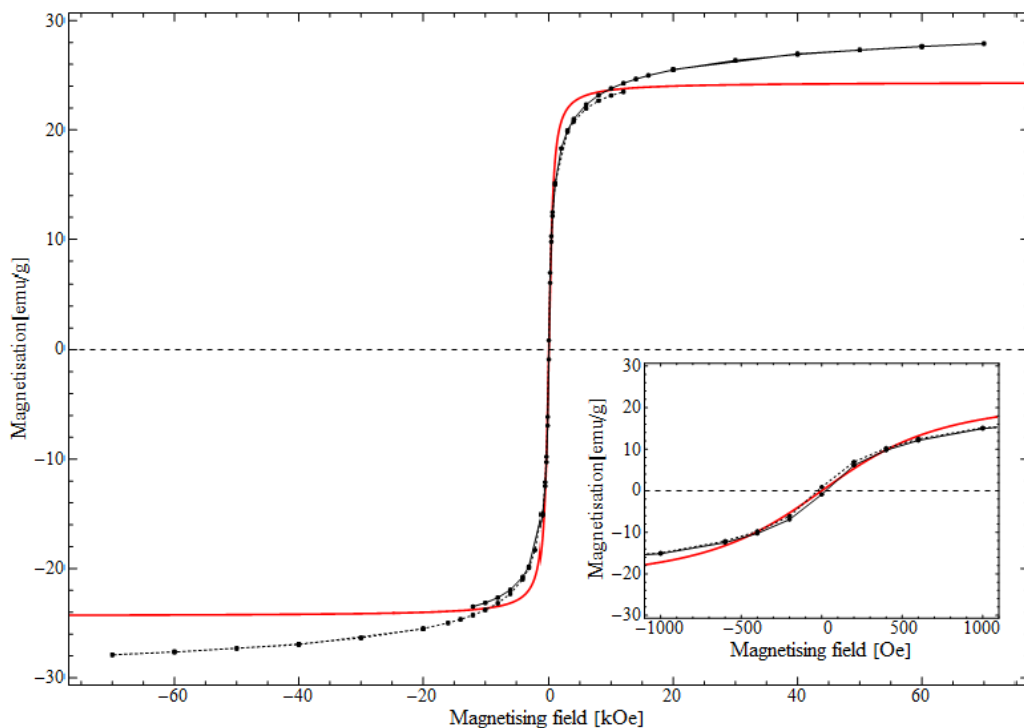
Figure 3.9 - Magnetisation curves for DHCA-IONCs at 300 K. In the inset: more detailed view of the low-field regime. Best fit of the Langevin function is presented in red.

When a high external magnetic field was applied (H, in kOe), characteristic saturation of the sample magnetisation was observed. Saturation occurs when the external field does not increase the magnetisation of the sample any further, and so the total magnetic flux density begins to plateau. At 300 K, the highest observed magnetisation was 27.89±0.15 emu/g. When an alternating magnetic field is applied to a sample, its magnetisation will trace out a loop termed a 'hysteresis loop'. If the reverse route does not retrace the forward path, then the sample is known to have hysteresis, a property relating the presence of many magnetic domains in the sample. However, since MNPs have a magnetic monodomain, the reverse trace almost perfectly lays over the forward direction. This lack of hysteresis is characteristic of superparamagnetic nanoparticles.[86]

Coercivity is a measure of the reverse field needed to drive the magnetisation to zero after being saturated. The DHCA-IONC sample had negligible coercivity at 300 K, estimated at 24.98±0.38 Oe. Some residual magnetic field known as the remanent field can become trapped in the instrument magnet when the field is set back to

zero.[87] This residual field is very small in comparison to the maximum field possible in the instrument, and typically lies up to about 20 Oe. Therefore the DHCA-IONC samples can confidently be categorised as superparamagnetic at 300 K due to the lack of significant hysteresis of M(H) dependence.

Figure 3.10 shows the magentism curve of DHCA-IONCs collected at 2 K. At 2 K the saturation of sample magnetisation is also observed at high external magnetic fields, with the highest observed magnetisation being 36.5±0.2 emu/g, a value higher than that recorded at 300 K. The inset in Figure 3.10 showed a hysteresis loop opened up with significant coercivity when the external field was reversed. It is estimated at 394.6±1.2 Oe, and this change in behaviour is typical for superparamagnetic nanoparticles as the superparamagnetism is reversibly destroyed by cooling. Langevin function fit and other fitting models were not appropriate for the dataset collected at 2 K due to the opening of the hysteresis loop, showing (H) dependence.
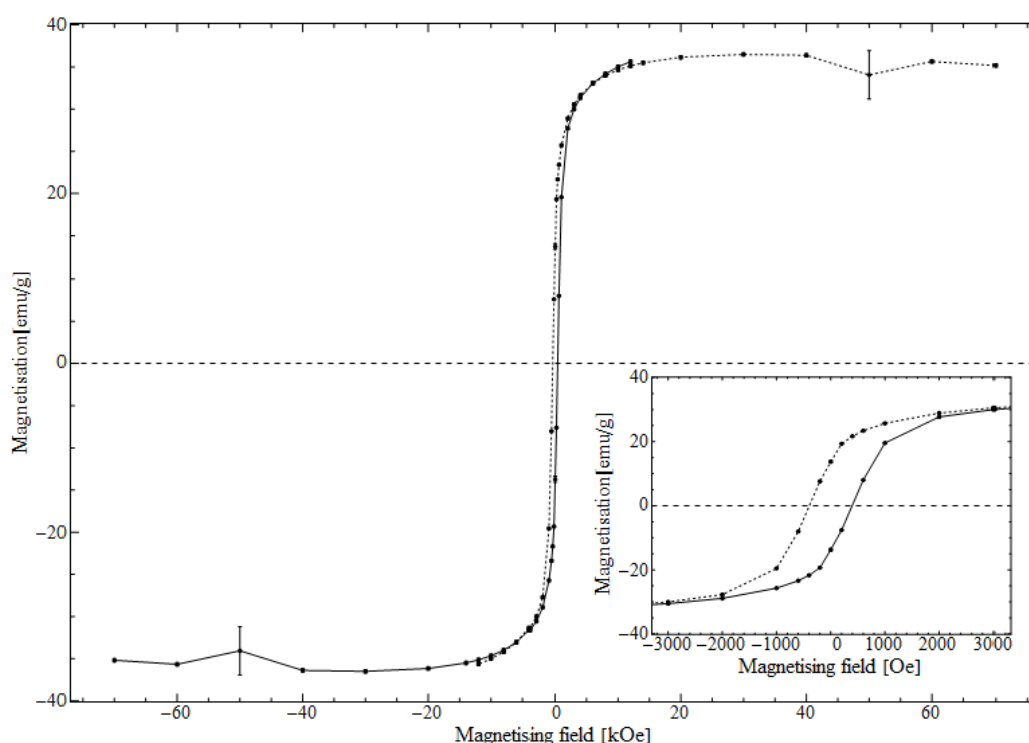

Figure 3.10 - Magnetisation curves for DHCA-IONCs at 2 K. In the inset: more detailed view of the low-field regime showing that the hysteresis loop opens up at the lower temperature. No Langevin function presented due to hysteresis.

Table 3.1 summarises the results from the investigation of M(H) dependence, with the DHCA-IONCs being classified as 'superparamagnetic' at room temperature. The saturation magnetisation and coercivity are negligible at 300 K, resulting in the superparamagnetic classification. This result is aligned with the literature, and is expected as the particle size decreases to the nanoscale, resulting in a single magnetic domain on each particle. At 2 K however, a hysteresis loop is present and the IONCs are categorised as ferromagnetic at this low temperature.

Table 3.1 - Summary of the magnetism studies carried out using the DHCA-IONCs, results shown at the two different temperatures investigated.

Property	At 300 K	At 2 K
Magnetic Behaviour	Superparamagnetic	Ferromagnetic
Saturation magnetisation (highest observed magnetisation method)	27.89 ± 0.15 emu/g	36.50 ± 0.20emu/g
Saturation magnetisation (Langevin function fit – red curve in Figure 3.9)	24.37 ± 0.51 emu/g	N/A
Coercivity	24.98 ± 0.38 Oe	394.6 ± 1.1 Oe

The second method of investigating the magnetic behaviour of the IONCs was to determine the magnetisation temperature dependence, M(T). Briefly, the sample is frozen to low temperatures, a very small magnetic field is applied, followed by the measurement of sample magnetisation at increasing temperatures. This step is called the zero field cooling (ZFC) curve. Next, the method is repeated, except also reducing the temperature in the presence of the applied low magnetic field. The slightly different data curve this method produces is called the field cooling (FC) curve.

In ZFC, the magnetic moments are essentially all frozen in place, as the temperature increases and thermal energy is added to the system, some magnetic moments will have the freedom to flip and follow the magnetic field orientation. The measured magnetisation of the sample will increase as the temperature increases, this is known as 'unblocking'. The temperature at which the majority of the magnetic moments are

unblocked is called the 'blocking temperature (T_B)'.[74] Figure 3.11 shows the ZFC (lower curve) and FC (upper curve) obtained from the DHCA-IONC sample.
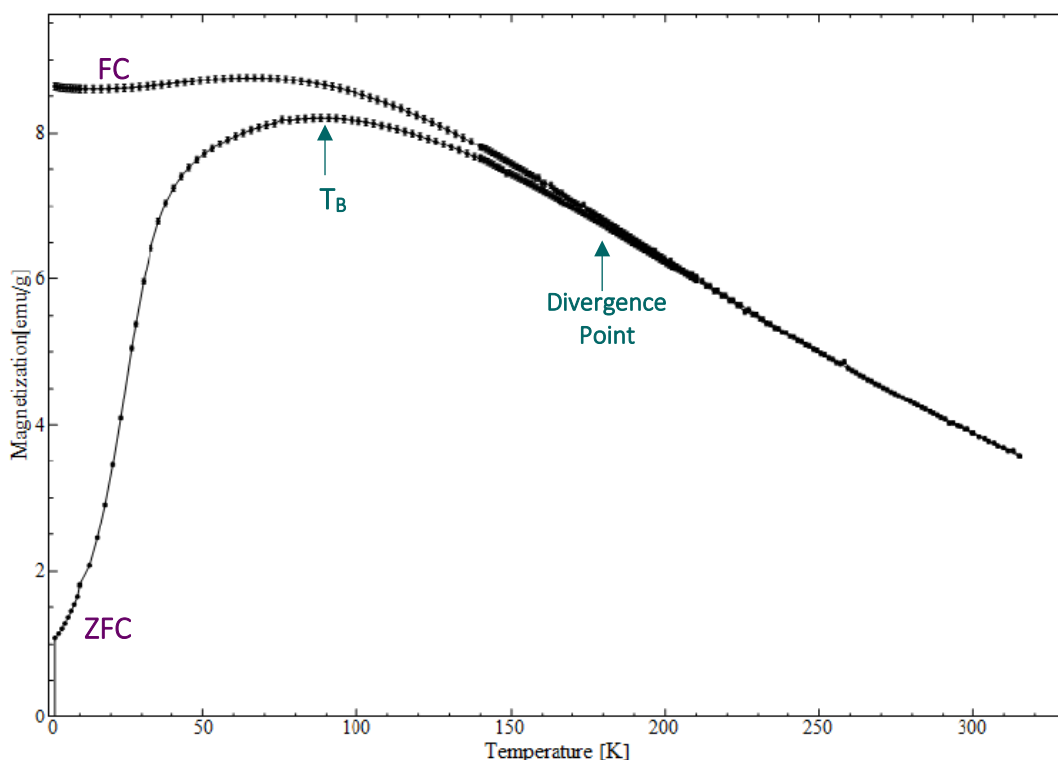

Figure 3.11 – Magnetisation temperature dependence at 100 Oe (external field) for the DHCA-IONCs. Lower curve is the ZFC and the upper curve is the FC. Blocking temperature (T_B) and the divergence point are both highlighted in the figure.

The peak in the ZFC curve indicates the blocking temperature, which in Figure 3.11 lies at around 100 K. Normally the divergence point of the two curves lies over this point in perfectly monodispersed samples. The divergence point is around 175 K in this data set. The lack of definition in the maximum of the ZFC curve suggests it is the sum of multiple maxima, also indicating a range of nanoparticle sizes. In summary, 175 K is the maximal blocking temperature of the sample, i.e. T_B of the largest IONCs in the sample, while 100 K is the mean blocking temperature of the IONC size population. Due to the lack of definition in the blocking temperature, it can be assumed that the IONCs were polydispersed.

Overall, the IONCs fit the criteria of superparamagnetic behaviour in that they show negligible coercivity at room temperature (300 K) and there exists a blocking temperature below which the effects of thermal energy are diminished and ferromagnetic order appears.[86]

3.3.4 Gold Coating of Nanocages

Gold coating of the MNPs not only increases biocompatibility and protects the magnetic core from oxidation, but it widens the choice of molecules able to functionalise the nanoparticles. The gold surface also has an LSPR and so generates an enhanced electromagnetic field when it interacts with light, and so can intensify the Raman signal from any Raman reporters on the nanoparticle surface. This is known as surface enhanced Raman scattering (SERS), a technique which is being increasingly investigated for use in medical applications. With the correct pairing of Raman reporter and interrogating laser, nanoparticles can be detected below the skin which is an attractive feature for any new medical treatment. Ideally, the gold coating would cover the IONC corners and vertices to give the maximum Raman signal, but leave the concave faces free to house the drug load. Both gold sputtering and a mild gold reduction in solution were investigated to incorporate gold to the IONCs.

3.3.4.1 Gold Sputter Coating

IONCs were spotted onto a glass slide and allowed to air dry before undergoing the gold sputter process. Various collection methods were attempted to free the nanoparticles from the slide surface. Gentle scraping and sonication in ethanol were tested, with the latter being more successful. However a large number of nanoparticles remained fixed to the glass slide, and were collectively visible to the naked eye. Spotting different concentrations of IONCs and a range of sputtering parameters were also investigated. However owing to the very poor recovery of the gold coated IONCs, other methods were investigated to incorporate gold to the nanoparticle design.

3.3.4.2 Gold Coating – Solution Reduction

Glucose is a mild reducing agent, and when in the presence of gold ions, it will reduce them to atoms, initiating the nucleation process that leads to gold coated nanoparticles. The mild conditions promote the controlled reduction of Au(I) onto the IONCs and avoids the formation of new gold nuclei.[88] With any nucleation process,

already established particles, defects in the glassware or even contaminants can act as a point of nucleation. This is the reason glassware is thoroughly cleaned prior to nanoparticle synthesis. However, in the case of gold incorporation to the IONCs, this can be used advantageously, and the gold should nucleate around the already formed IONCs, optimistically at the pointed vertices.

After the ligand exchange into an aqueous phase, the IONCs were cleaned by centrifugation and added to a round bottom flask along with the gold salt solution and glucose. After sonication, the solution was dark brown in colour, owing to the concentrated IONCs. Under rotation and heating in an oil bath, the solution changed to an opaque orange colour. This was an indicator that the gold ions had reduced in the presence of the glucose onto the IONCs.

An important feature of the system, was that the IONCs were magnetic and this property was used advantageously in the purification steps. Simply placing the samples into a magnetic rack separated the IONCs from the water suspension, with the particles held along the side of the eppendorf closest to the magnet. Removing the solution and replacing with fresh water removed any excess reagents and unattached gold nanoparticles.

Figure 3.12 shows the extinction spectra from the IONCs, Au-IONCs and a magnetic wash supernatant. The appearance of an extinction band at 534 nm in the Au coated sample (purple) indicates the reduction of the gold onto the surface of the IONCs had been successful, and is in alignment with the literature.[88] The initial magnetic wash step would have only recovered the magnetic IONCs and as such, any gold that was reduced to separate gold nanoparticles would have been removed in the supernatant. A small band present at around 560 nm in the magnetic was supernatant (grey) suggests some gold nanoparticles have been removed during the washing process. This was an important step, as any further SERS work in future experiments would have to be a result of the Au-IONCs and not from remaining AuNP in solution.
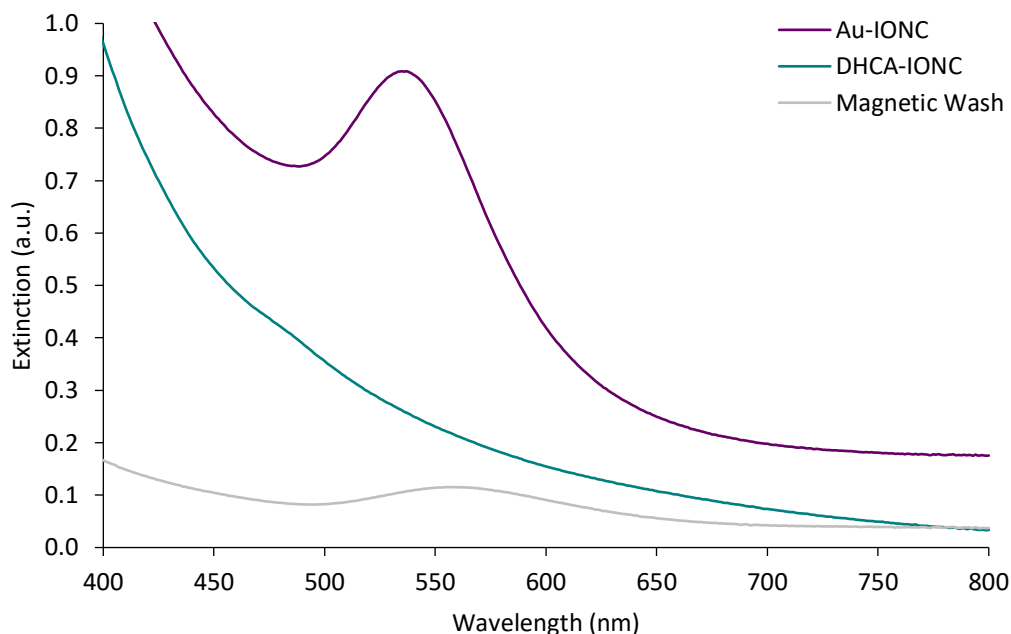
Figure 3.12 - Extinction spectra of the IONCs, Au coated IONCs, and the supernatant from the magnetic wash. Samples were diluted in water accordingly before analysis: DHCA-IONC 1 in 120 parts, Au-IONC 1 in 10 parts and wash supernatant was analysed neat. Spectra shown are the average of triplicate measurements collected on a baselined fast scan rate (4800 nm/min, 1 nm intervals).

3.3.5 SEM images of Au-IONCs

Controlling the gold coating process of the IONCs proved to be very difficult, various experimental parameters were explored including IONC concentration, Au concentration, reaction time and temperature. Previous attempts resulted in complete encapsulation of the IONCs, presenting as large gold clumps when viewed under SEM, indicating the Au salt concentration was too high for the concentration of IONCs used. However even with modifications to the gold reduction parameters, it remained extremely difficult to confirm if the Au coating was only at the corners and along the vertices of the IONCs given the resolution of the microscopes available at the time. A scanning electron microscopy (SEM) image of Au-IONCs is shown overleaf in Figure 3.13.

The bright white particles visible in the image are gold nanoparticles. Since the Au-IONCs were magnetically washed post synthesis, it can be concluded that these larger AuNPs must be attached to either an individual IONC or a cluster of them.

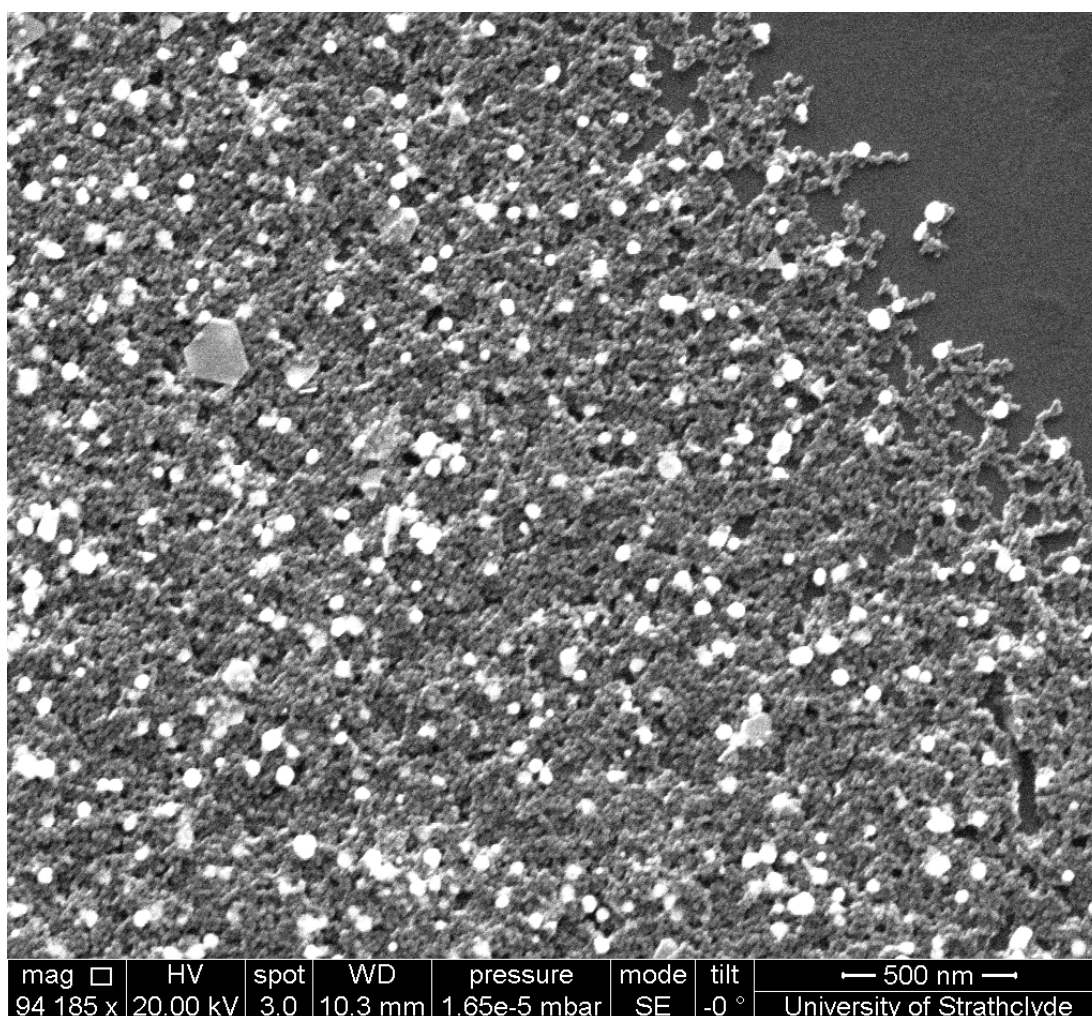| mag □	HV	spot	WD	pressure	mode	tilt	⟵ 500 nm ⟶
94 185 x	20.00 kV	3.0	10.3 mm	1.65e-5 mbar	SE	-0 °	University of Strathclyde

Figure 3.13 - SEM image of Au-IONCs. Scale bar shows 500 nm. Individual IONCs are visible at the edge of the cluster on the right hand side of the image. The bright white particles visible are most likely AuNPs that have formed and are attached to the IONC surface. Sample spotted onto a silica wafer and imaged using a field-emission environmental SEM (FEI Quanta 250 FEG-ESEM).

These could have formed from a large nucleation point on the IONC surface, or grown free in solution and merged with an IONC later in the synthesis. Elemental mapping of the sample could provide further analysis of the nanoparticle composition. It could conclude whether Au is present on the IONCs surface or just in the larger particles observed in Figure 3.13. There is still a possibility gold is present along the IONC edges, however the thickness of this layer could be too thin to contrast to the IONC surface under SEM resolution.

3.3.6 SERRS Response of Gold Coated Nanocages

Having a Raman reporter on the surface of the nanoparticles would allow them to be tracked for *in vitro* and *in* vivo studies. This would be an important feature of the drug delivery design to monitor the efficiency of the plaque targeting and also observe whether they accumulate in any other tissues. A proof of concept study used malachite green isothiocyanate (MGITC) as the Raman reporter. It is a commonly used molecule which contains a chromophore within its structure and has two main absorbance bands at around 460 nm and 620 nm. Figure 3.14 shows the absorbance spectrum and also the molecular structure of the Raman reporter.
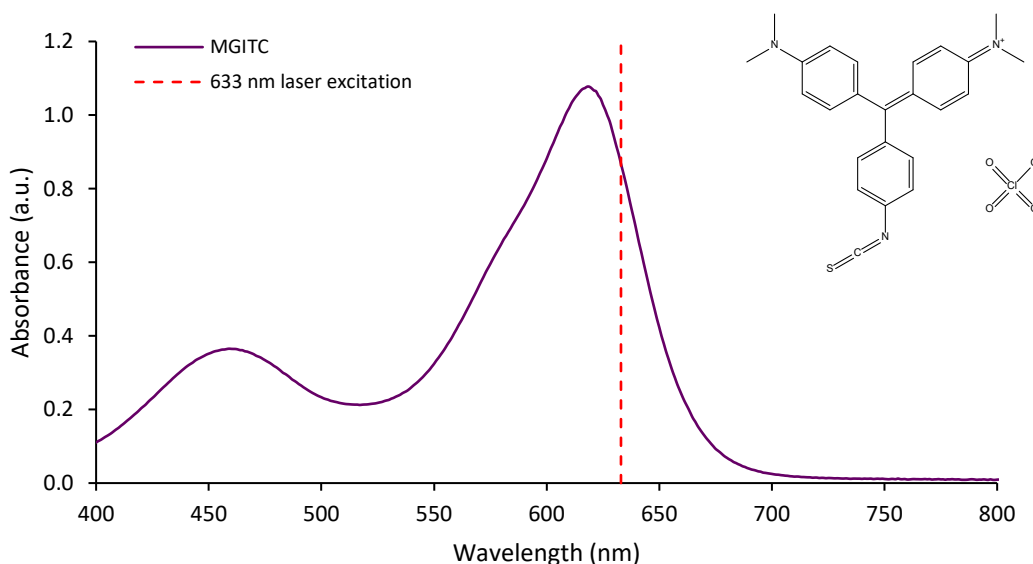

Figure 3.14 - Absorbance spectrum of 9.1 µM MGITC solution. Two main absorbance bands are present, one at ≈460 nm and a stronger one at ≈620 nm. The molecular structure of MGITC is shown in the upper right corner. The 633 nm laser excitation wavelength of the Raman spectrometer used in the following experiment is also shown (dashed red line). Spectrum shown is the average of triplicate measurements collected on a baselined fast scan rate (4800 nm/min, 1 nm intervals).

For collecting the Raman spectra of the functionalised Au-IONCs, an excitation laser wavelength of 633 nm was selected to induce resonance Raman scattering. The incoming laser wavelength overlapped with the main electronic transition within the MGITC molecule, and as such, lead to a greatly enhanced intensity of Raman scattering being observed in Figure 3.15. The control sample of IONCs with MGITC (Control B) showed no signal, indicating the gold coating was vital for the Raman reporter attachment and resultant SERS signal.
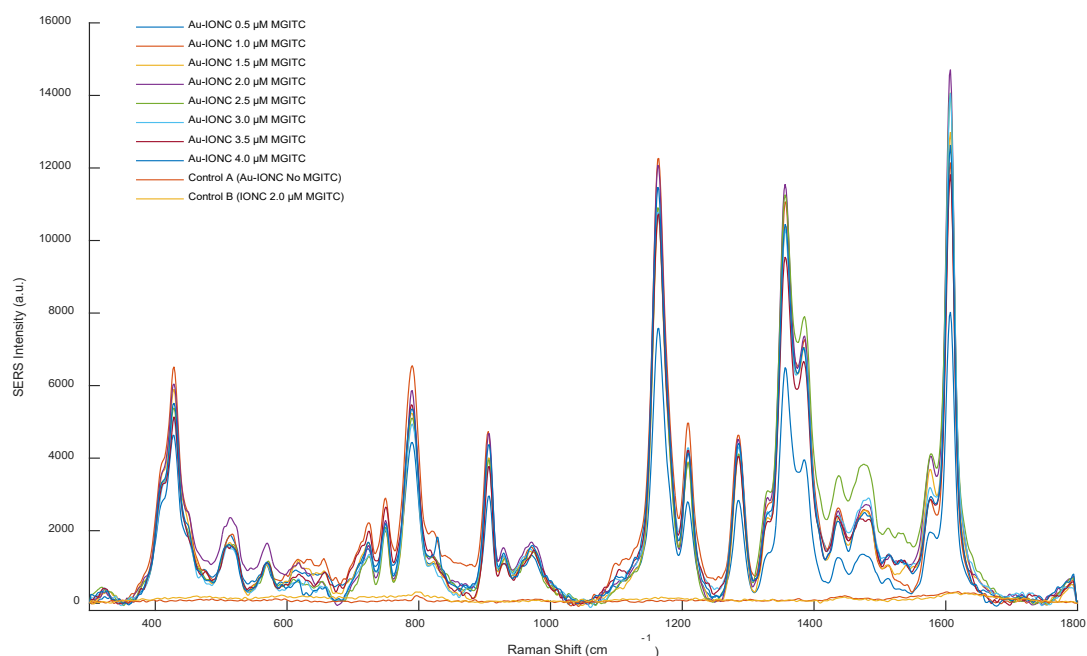
Figure 3.15 - SERRS spectra of MGITC-Au-IONC from 0 to 4 µM. Spectra obtained on a Renishaw Microscope set up, 633 nm excitation (100 mW) at 100% laser power, scanning from 300 to 1800 cm^{-1} for 30 seconds. Triplicate measurements were taken of each sample and averaged for plotting. All spectra underwent baseline subtraction prior to plotting using MATLAB software.

Each peak observed in the spectra corresponds to a molecular vibration or stretch within MGITC. The dominating peak at 1607 cm^{-1} corresponds to the N-Phenyl and C-C aromatic stretching modes of the molecule.[89] By focussing on this peak, the most intense spectrum was observed from the sample containing 2 µM MGITC, after which the peak height began to decrease. Initially it could be suggested, that this concentration of MGITC reporter is optimal for the Au-IONCs. However in order to suggest this, the extinction spectrum of each sample should be obtained to ensure the signal enhancement is not a result of nanoparticle aggregation, which would lead to an enhanced Raman scattering. Figure 3.16 shows the extinction spectra collected from each of the samples investigated in Figure 3.15.

The extinction spectra of samples containing more than 2 µM of MGITC show slight aggregation. This instability presents as a second band appearing around 625 nm. All the samples containing a final concentration between 0.5-2 µM MGITC show a slight broadening of the main plasmon compared to Control A with no MGITC. In which case it could be suggested that the lowest concentration of MGITC studied, 0.5 µM, would be optimal as it showed the least deviation from the control sample yet still exhibited
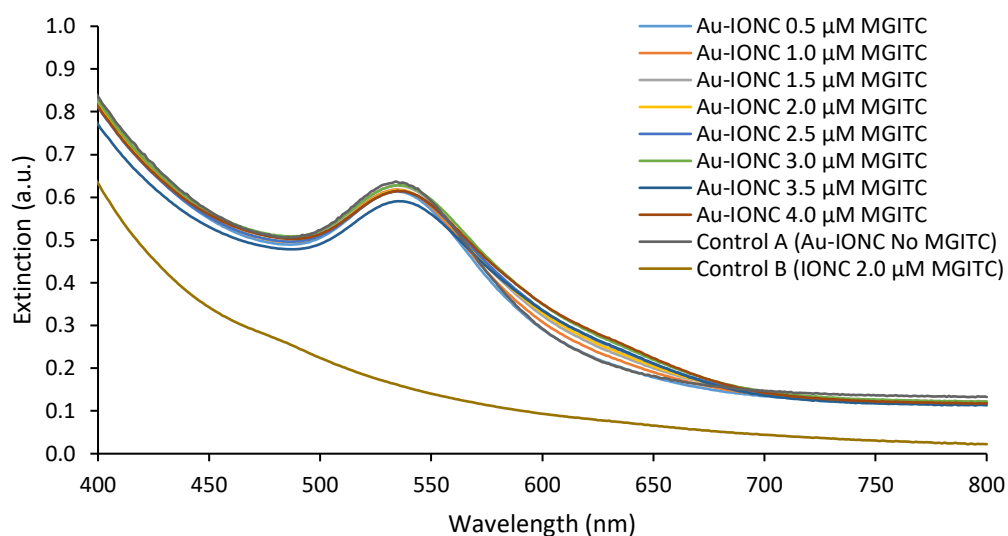
Figure 3.16 - Extinction spectra of Au-IONC with a range of MGITC concentrations 0.5-4.0 μM. Spectra shown are the average of triplicate measurements collected on a baselined fast scan rate (4800 nm/min, 1 nm intervals).

a strong Raman spectrum under the conditions tested. This proof of principle experiment showed that the Au-IONCs could facilitate SERRS, and by using a resonant Raman reporter, a further enhanced signal was achieved. This showed promise for the overall aim of the drug-delivery nanoparticle vehicle, as tracking *in vivo* would be useful for evaluating the accumulation at the target site.

3.3.7 Antibody Functionalisation of Gold Coated Nanocages

Noonan *et al.* reported the targeted *in vivo* SERS imaging of multiple vascular biomarkers using antibody-functionalised nanoparticles.[45] Their work was able to target intercellular adhesion molecule 1 (ICAM-1), vascular cell adhesion molecule 1 (VCAM-1) and P-selectin, all of which are overexpressed in atherosclerotic plaques in a humanised mouse model. Therefore, a biological targeting molecule (antibody) was included in the overall nanoparticle vehicle design for this delivery system.

Firstly, Au-IONCs were functionalised with MGITC and a thiolated polyethylene glycol (PEG) linker, CT(PEG)$_{5000}$. The PEG linker was modified with a thiol for nanoparticle attachment at one end and a carboxylic acid group at the other end. The latter functional group was utilised to conjugate the antibody (anti Human ICAM-1) to the

Au-IONCs. This antibody was chosen for the proof of principle experiment, to demonstrate the capability of the nanoparticle design to target a CVD biomarker. This type of chemistry joins a primary amine and a carboxylic acid through carbodiimide crosslinking chemistry. Carbodiimides are zero-length crosslinkers that are used to mediate the conjugation of a carboxylic acid and a primary amine, without being part of the resulting amide bond themselves.[90] A schematic of the reaction pathway used in the antibody and PEG conjugation is shown in Figure 3.17.
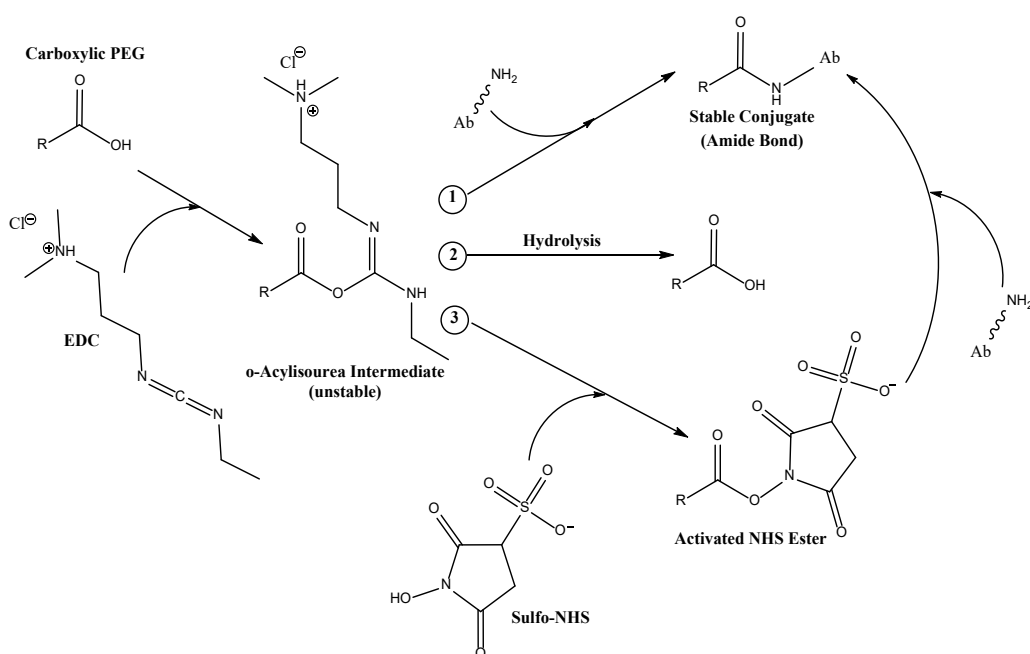

Figure 3.17 - Pathway of carbodiimide crosslinking reaction between the carboxylic acid terminated PEG and the primary amines found in the lysine residues of the Fc region of the antibody.

A popular carbodiimide often used is 1-ethyl-3-(3-dimethylaminopropyl)-carbodiimide (EDC), which converts the carboxylic acid group (on PEG) to an unstable intermediate, called an activated O-acylisourea intermediate. This intermediate becomes primed for nucleophilic attack from a primary amine and has three possible fates in the solution. It can conjugate with a primary amine (found on lysine residues in the Fc region of the antibody), it can hydrolyse back to the original carboxylic acid, or it can react with water soluble N-hydroxysulfosuccinimide (sNHS). The latter pathway forms another stable intermediate, which can then in turn react with the amine residues in the antibody (Ab). The primary amine forms the amide bond with the carboxylic acid and

a soluble EDC by-product is released. An advantage of using the additional sulfo-NHS reagent is that it increases the stability of the active intermediate, which in turn improves the efficiency of the reaction with the primary amine.

The first step of the EDC coupling is most efficient in an acidic environment, and so 4-morpholinoethanesulfonic acid (MES) buffer was used to optimise the reaction conditions. Additionally, a buffer free of any other amines and carboxylic acids was used to prevent competition with the target molecules. The second, more stable NHS ester intermediate allows for efficient conjugation at physiological pH, and so 4-(2-hydroxyethyl)piperazine-1-ethanesulfonic acid (HEPES) buffer was utilised at this stage. Once the antibody was conjugated to the PEG linker through the Fc region, the antibody is oriented so that the Fab region is available for the antigen binding.[90]

To test the success of the antibody conjugation, a lateral flow test was prepared in house. These are a simple cellulose based device which are primarily used to detect the presence of a target analyte within a liquid sample. A generic capture antibody was spotted halfway up the strip and allowed to air dry. The strip was then submerged in a running buffer containing the Ab functionalised gold coated IONCs sample. If the crosslinking chemistry was successful, the conjugates would be immobilised as they flow over the capture antibody. Visual comparison of the control (PEG-Au-IONC) and sample (Ab-PEG-Au-IONC) lateral flow strips was indicative that the carbodiimide crosslinking reaction had been successful. Figure 3.18 shows the dry lateral flow strips after a wash step.
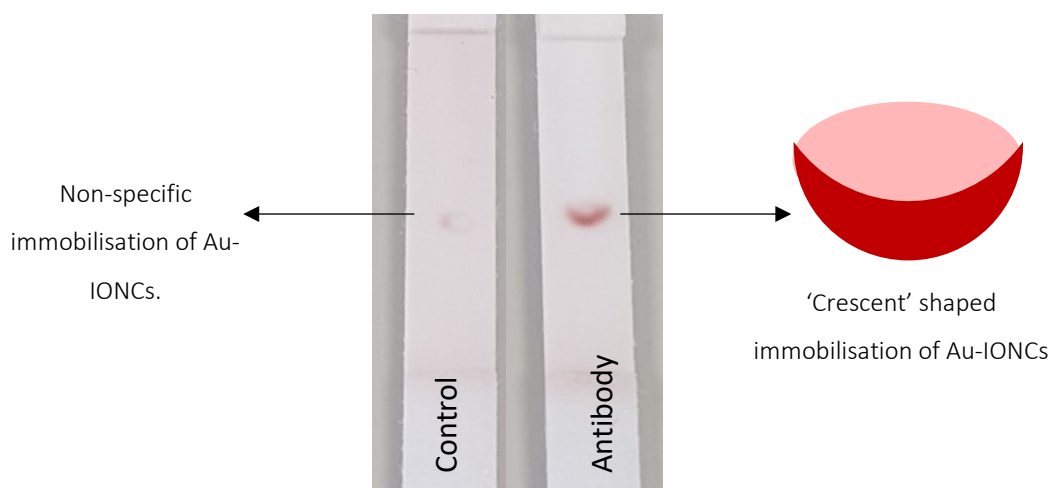

Figure 3.18 - Lateral flow strip of control and antibody containing sample. A dark red crescent shape is visible in the antibody containing sample, this is indicative of a greater level of nanoparticle immobilisation. This is a result of the affinity between the capture and target antibody.

A dark red crescent is visible in the antibody containing sample, this is indicative of the Au-IONCs being immobilised on the Ab spot. Although there is a slight spot in the control sample from non-specific binding, the presence of the dark spot in the sample strip suggests the carbodiimide crosslinking reaction had been successful and the ICAM antibody was conjugated to the CT-PEG$_{5000}$.

The area where the capture antibody was spotted was mapped using Raman spectroscopy, where the MGITC on the Au-IONCs surface provided a comparable Raman response. Peak intensity maps (based on the peak at 1614 cm^{-1}) were produced to illustrate the increased immobilisation of Au-IONCs in the antibody containing sample. Figure 3.19 shows the increased immobilisation of antibody functionalised Au-IONCs compared to the control.
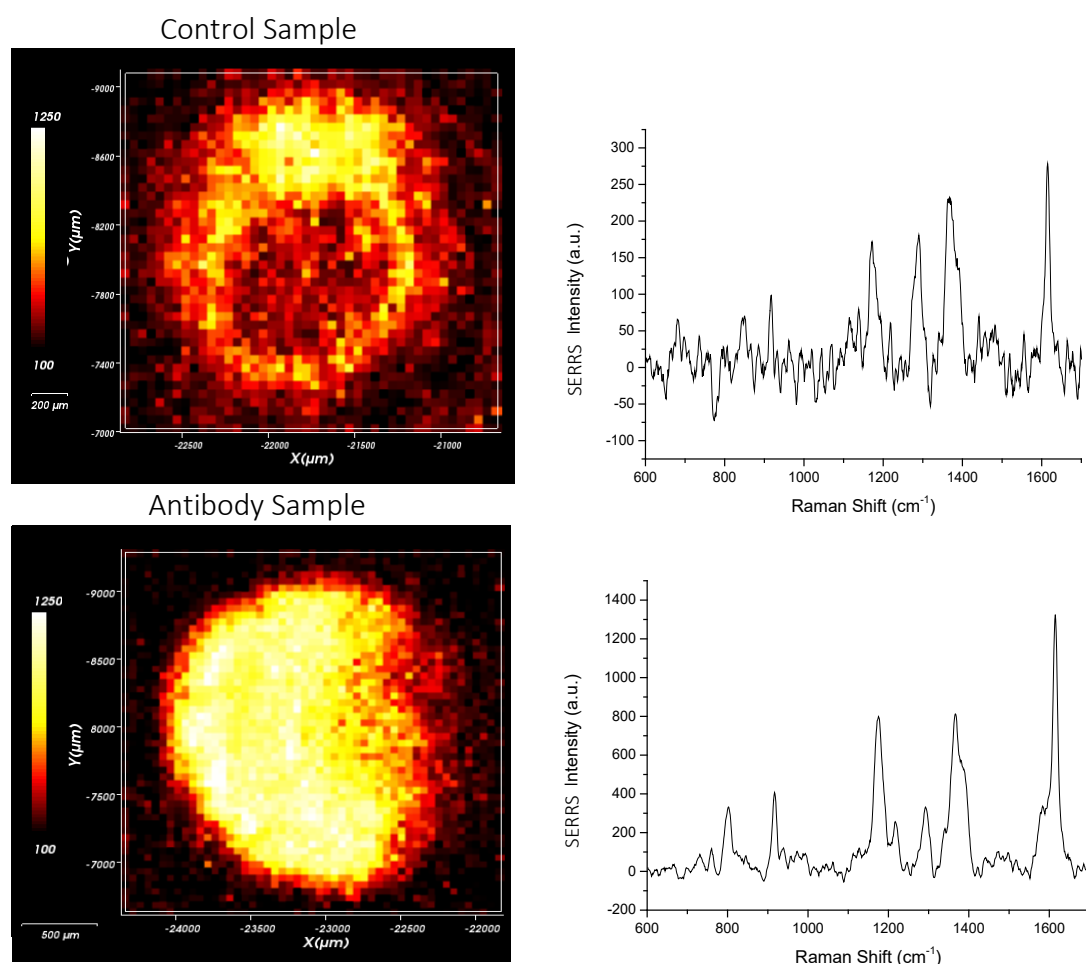

Figure 3.19 - Peak intensity maps (at 1614 cm^{-1}) of the spots shown on the lateral flow strips in Figure 3.18, spot orientation differs between maps and image of the lateral flow strips. Brighter white/yellow areas indicates higher MGITC Raman signal. Maps collected using a 633 nm excitation laser at 100% power, 1200 cm^{-1} centre, acquisition 1s and 50 μm steps. Spectra indicate signal obtained at the centre of each spot.

Some non-specific binding of the nanoparticles is present in the control sample. In future this could be reduced by increasing the number of wash steps to remove any trapped nanoparticles or even using lateral flow strips with different pore sizes in the cellulose component. Note the large increase in signal intensity in the SERRS spectra of the antibody containing sample, this enforces the result of the succesful crosslinking chemistry as these particles were selectively retained in higher concentrations compared to the control. The SERRS analysis offers advantages over the standard colourmetric observations, in that lower concentrations of immobilised nanoparticles can be detected. This could be used in future experiments in a quantitive manner to probe the specificity of the Ab binding.

3.4 Concluding Remarks

The synthesis of iron oxide nanocages from a sacrificial template was achieved via a galvanic reaction. To increase the biocompatibility of the IONCs, they were successfully transferred into an aqueous phase via surface molecule exchange. These particles were characterised, including a study into their magnetic behaviour. They were determined to be superparamagnetic, as is expected for iron oxide particles on the nanoscale, confirmed by their blocking temperature and lack of hysteresis. This could be a useful physical property of the nanoparticles in order to trigger drug release under the influence of an external magnetic stimulus.

The gold coating provided a plethora of functionalisation options, with both a Raman reporter (MGITC) and a PEG/antibody conjugation demonstrated. The successful addition of these to the IONC surface was a positive step towards identifying a suitable candidate for the core of the nanoparticle drug delivery system. The specificity of the antibody/antigen recognition could also have been investigated to understand whether any unwanted immobilisation of the Ab-Au-IONCs from other capture antibodies found in the body could interfere with the drug delivery system.

Under closer inspection using SEM it became apparent that the mild gold reduction process was not as controllable as first thought, with larger gold particles being present in the sample even after magnetic separation. The presence of these large gold particles was undesirable for this application and most likely gave rise to the good SERRS response shown in Figure 3.15. After numerous attempts to eliminate these from the sample and modifications to the experimental methods, it was decided that another nanoparticle core may be more suitable for the application.

Learning from the difficulty of the gold manipulation, the next nanoparticle type investigated was hollow gold nanoparticles (HGNs). A particle with similar attractive features for drug delivery, i.e. large surface area and a Raman active surface, but with the gold surface already in place. The potential of HGNs as the core of a drug delivery system will be explored in the subsequent chapters.

4. Hollow Gold Nanoparticles

4.1 Chapter Introduction

Nanoparticles with a hollow core and a gold shell are termed hollow gold nanoparticles (HGNs).[91] The aspect ratio of the shell thickness/diameter can be varied during synthesis, it is this variation of the aspect ratio that leads to their interesting optical properties. HGNs show enhanced LSPR properties as a result of their dual interface nature. The plasmon modes on the inner cavity surface and the outer surface of the HGNs couple, leading to a hybridisation of the plasmons, resulting in a bulk LSPR in the near-infrared (NIR) region.[91] The shell thickness controls the plasmon coupling efficiency, with a thinner shell resulting in the strongest interaction.

Sun *et al.* were one of the first groups to publish a method for synthesising hollow nanoparticles using a silver nanoparticle template and metal salt solution to initiate a replacement reaction.[83-92] Now a variety of hollow nanoparticle structures exist, where the precursor nanoparticle shape dictates the resultant hollow nanoparticle shape. Similarly, cobalt nanoparticles can be used as the template for HGNs, however these must be handled and synthesised in an inert atmosphere due to the susceptibility of cobalt to oxidation. Great control of the HGN size and shell thickness can be achieved using a Schlenk line to provide the protective atmosphere.[93]

The versatile synthesis of HGNs has gained a mass of interest within the field of nano-medicine, with applications in photothermal therapy and drug delivery. HGNs are an appealing nanoparticle choice for use in a drug delivery system as their cavity centre allows for a higher drug loading while their LSPR appears in the NIR region (typically 520-1000 nm).[91] You *et al.* found that the hollow interior of HGNs enabled a 3.5 fold increase in the loading of doxorubicin compared to solid AuNPs of the same size.[94] The gold surface also allows for a plethora of molecule functionalisation and also surface enhanced spectroscopies. These properties are an advantage over other popular drug

carrier nanoparticles such as liposomes or polymer nanoparticles that only serve as a drug reservoir.

Biological tissues impede the penetration of photons, however light in the NIR region can reach deeper in the biological tissue and thus this region provides a more accessible optical window. Scattering is the dominant light-tissue interaction within this window, which leads to an increase in the distance travelled by photons. The window exists in the region where water and haemoglobin have their lowest absorbance of light, around 650-900 nm.[95] Figure 4.1 shows the absorbance spectra of water, haemoglobin and oxygen bound haemoglobin, the lowest absorbance is between 650-900 nm, and as such this is the optimal wavelength of light to use for biological applications. The LSPR of HGNs can be tuned to fall within this biological window, which is another advantage of employing them in a biological application compared to their solid relatives.
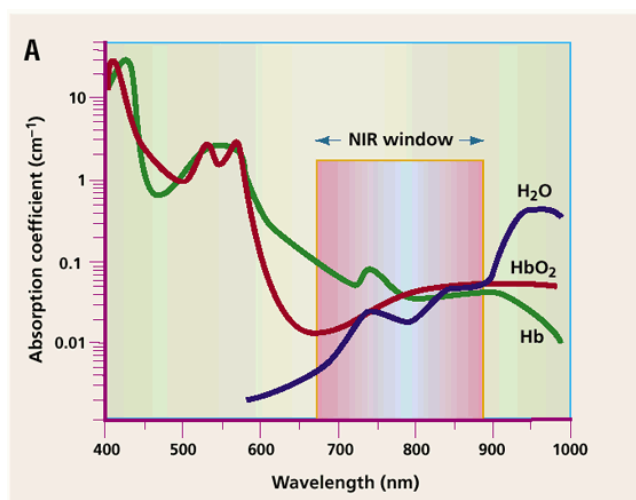

Figure 4.1 - The NIR window is ideally suited for in vivo imaging because of the minimal light absorption by haemoglobin (<650 nm) and water (>900 nm). Figure adapted with permission from Springer Nature. Nature Biotechnology, A Clearer Vision for in vivo Imaging, Ralph Weissleder, Copyright 2001.[95]

You *et al.* utilised HGNs for a dual treatment of melanoma, and showed that doxorubicin loaded HGNs were capable of photothermal ablation and drug release upon NIR light irradiation.[94] Their two fold approach showed superior cell killing and was attributed to the HGN mediated photothermal conversion and localised cytotoxicity of the released doxorubicin.

You *et al.* progressed this work further by synthesising doxorubicin loaded HGNs that could actively target EphB4, a receptor overexpressed on the cell membrane of tumours and blood vessels undergoing angiogenesis (growth of new vessels).[96] The active targeting of the receptors showed improved regression of the tumour volume in comparison to controls as shown in Figure 4.2.
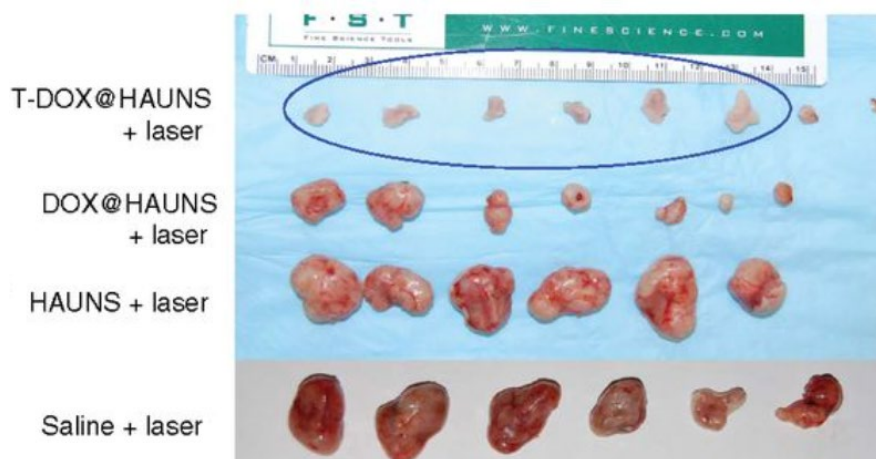

Figure 4.2 - Treatment with targeting doxorubicin loaded HGNs (called hollow gold nanoshells in this publication, T-DOX@HAuNS) followed by NIR laser irradiation resulted in significantly decreased tumour growth when compared with treatments with non-targeted DOX@HAuNS, HAuNS or the saline control. Tumours were removed on day 22, except for the saline control at day 9. Regression of the tumours to merely scar tissue was observed in the full treatment group highlighted by the blue circle. Adapted from the Cancer Res., 2012, 72, 4777–4786, J. You, R. Zhang, C. Xiong, M. Zhong, M. Melancon, S. Gupta, A. M. Nick, A. K. Sood and C. Li, Effective photothermal chemotherapy using doxorubicin-loaded gold nanospheres that target EphB4 receptors in tumours, with permission from AACR.[96]

4.2 Aims

The aim of this chapter was to investigate the potential of HGNs as the core of the drug delivery design. First, the synthesis was explored with focus on a simple benchtop method, aiming for particles below 100 nm in size. This size limit would allow for cellular penetration, bioclearance and efficient scattering and absorption of light. The parameters controlling the synthesis were explored in order to tune the LSPR between 518-850 nm. Functionalisation of the gold surface with Raman reporters and biorecognition molecules was also studied.

4.3 Results & Discussion

4.3.1 Synthesis of Hollow Gold Nanoparticles

This method of HGN synthesis was adapted from a paper by Goodman *et al.*[97], where the facile method is carried out on the benchtop, and not via a Schlenk line which is common practice for synthesising HGNs. The HGNs were synthesised through a galvanic replacement reaction between sacrificial silver nanoparticle (AgNP) cores and a gold salt. This type of reaction is a redox process and can be broken down to the oxidation of the silver template nanoparticle and the reduction of the gold salt to atomic gold.[98]

The galvanisation reaction proceeded due to the difference in the reduction potentials between the metals; the gold salt solution had a higher reduction potential than the AgNP, 1.002 V for $[AuCl_4]^-$/Au and 0.7996 V for Ag^+/Ag compared to the standard hydrogen electrode.[99] The silver ions had a higher diffusion rate and as such caused pinholes to form, it was the diffusion through these voids that lead to the hollow structure, this is known as the Kirkendall effect.[98]

As the Ag continued to oxidise, the core of the sacrificial template depleted, creating the vacant core of the HGNs. As the gold ions reduced to atoms, a critical concentration was reached and they nucleated and grew into small clusters forming the gold shell around the template. Figure 4.3 illustrates a cross-sectional view of the HGN formation and redox reaction occurring.

$$Anodic\ reaction\!: Ag \rightarrow Ag^+(aq) + e^-$$

$$Cathodic\ Reaction\!: AuCl_4^-(aq) + 3e^- \rightarrow Au(s) + 4Cl^-(aq)$$

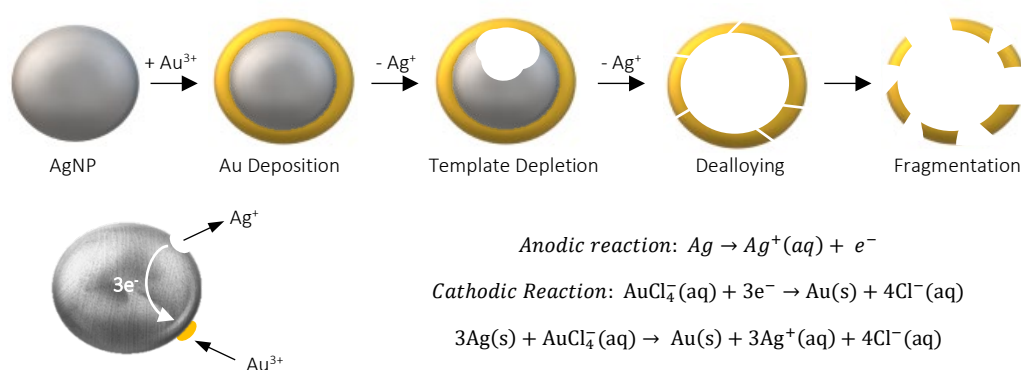$$3Ag(s) + AuCl_4^-(aq) \rightarrow Au(s) + 3Ag^+(aq) + 4Cl^-(aq)$$

Figure 4.3 – Cross-sectional schematic showing the mechanism of HGN formation involving the simultaneous oxidative dissolution of the silver nanoparticle and reductive precipitation of the gold salt around the template nanoparticle. During the dealloying stages, pinholes are formed on the surface of the nanoparticles and fragmentation can also occur. The redox half equations and overall balanced equation are also show for the galvanic reaction.

Citrate AgNPs, hydroxylamine AgNPs and ethylenediaminetetraacetic acid (EDTA) AgNPs were investigated for the galvanic reaction. The reaction proceeded at a much slower rate for EDTA AgNPs with the reaction completing overnight, in comparison the reaction using hydroxylamine AgNPs was almost instantaneous, with an immediate colour change from the yellow AgNPs to the characteristic royal blue HGNs. This suggests the capping agent greatly influences the rate of the redox reaction. When comparing citrate and hydroxylamine AgNPs, the latter are much simpler to synthesise and have greater inter-batch consistency, hence hydroxylamine AgNPs were chosen as the sacrificial core for the HGNs. In brief, the hydroxylamine AgNP synthesis consisted of mixing an aqueous solution of sodium hydroxide and hydroxylamine hydrochloride at room temperature before rapidly adding a solution of sodium nitrate. The reaction was stirred for only 15 minutes and required no heating. Following this synthesis method, AgNP were typically 65-75 nm in diameter, measured using DSL. Figure 4.4 shows a typical extinction spectrum for hydroxylamine AgNPs, with a λ_{max} of 410 nm and a narrow bandwidth of 78 nm, indicating the particles are monodispersed. The particular batch shown had a hydrodynamic diameter of 71.4 ± 1.9 nm.
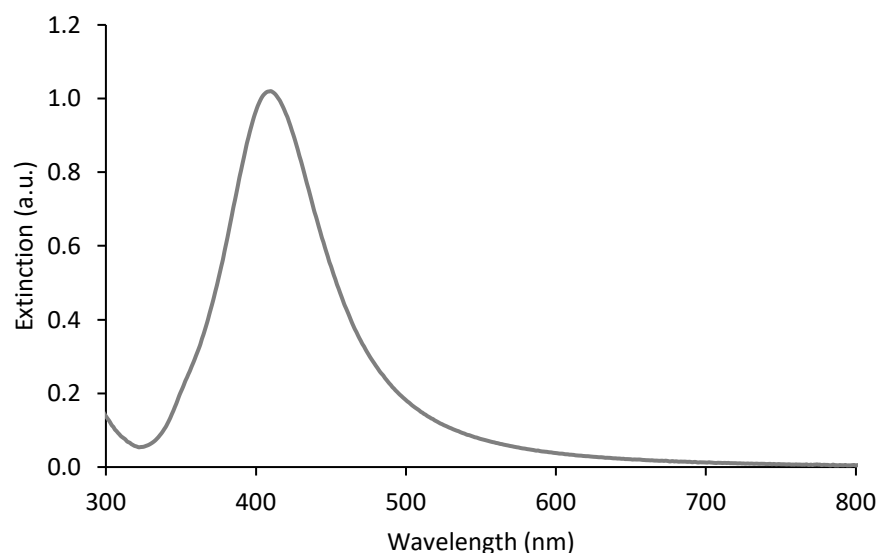

Figure 4.4 - Extinction spectrum for hydroxylamine AgNPs (1 in 10 dilution in water). Spectrum is the average of triplicate measurements collected on a baselined fast scan rate (4800 nm/min, 1 nm intervals).

Figure 4.5 shows a SEM image of HGNs synthesised using hydroxylamine AgNP as the sacrificial core. The resolution of the microscope used was not high enough to observe any surface features such as pinholes. However it can be seen that the nanoparticles are uniform in size and shape, with a small portion of the sample containing broken or toroidal nanoparticles. Figure 9.2 in the appendix shows the size distribution of the HGNs in the SEM image, with an average particle size of 54 nm ± 11 nm. This suggests the hydroxylamine AgNPs cores were uniform in size and shape to result in HGNs of similar characteristics. The difference in size between the AgNPs and HGNs can be attributed to the analysis method used to obtain the measurements. Measurements from electron microscopy represent the metallic core of the particles, whereas DLS considers the hydrodynamic diameter of the particles, therefore the latter measurement is often an over estimate of the actual size.

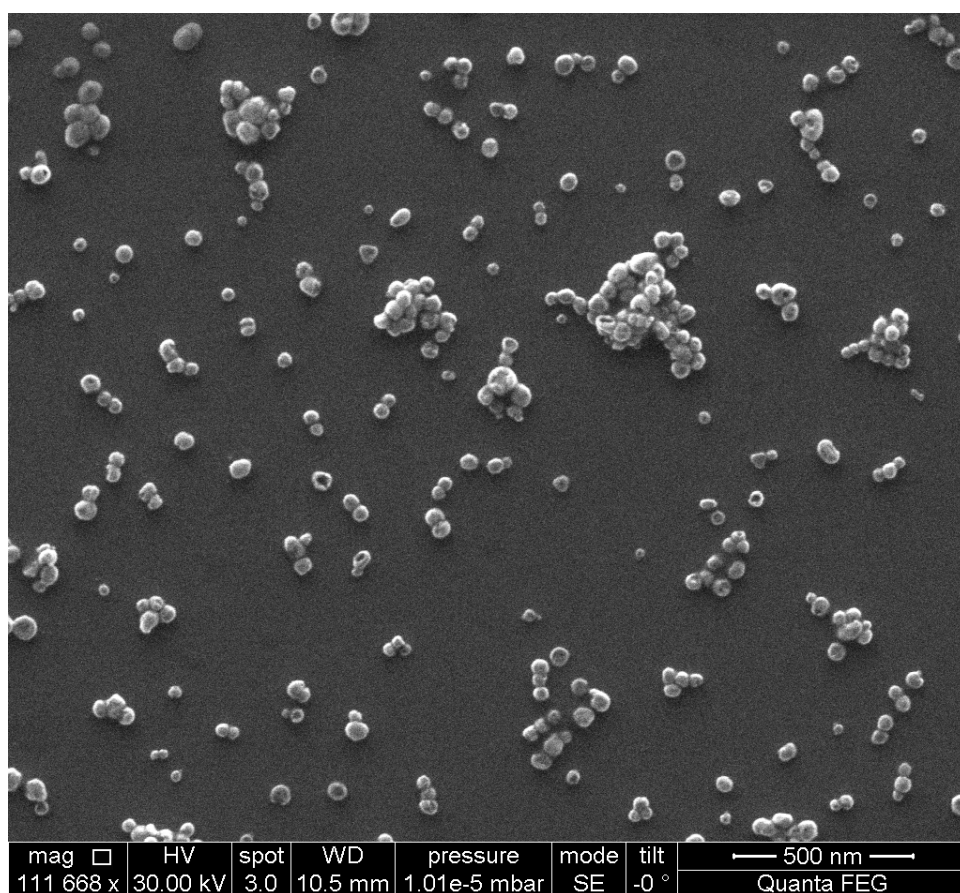| mag □	HV	spot	WD	pressure	mode	tilt	⊢— 500 nm —⊣
111 668 x	30.00 kV	3.0	10.5 mm	1.01e-5 mbar	SE	-0 °	Quanta FEG

Figure 4.5 - SEM image of HGNs synthesised using the galvanic replacement reaction. Scale bar shows 500 nm. Sample spotted onto a silica wafer and imaged using a field-emission environmental SEM (FEI Quanta 250 FEG-ESEM).

Figure 4.6 shows a transmission electron micrograph of HGNs used in a later experiment but synthesised using the same method as discussed above. This higher resolution imaging technique shows the hollow centres, uneven surface morphology and even some broken shells within the HGN sample.
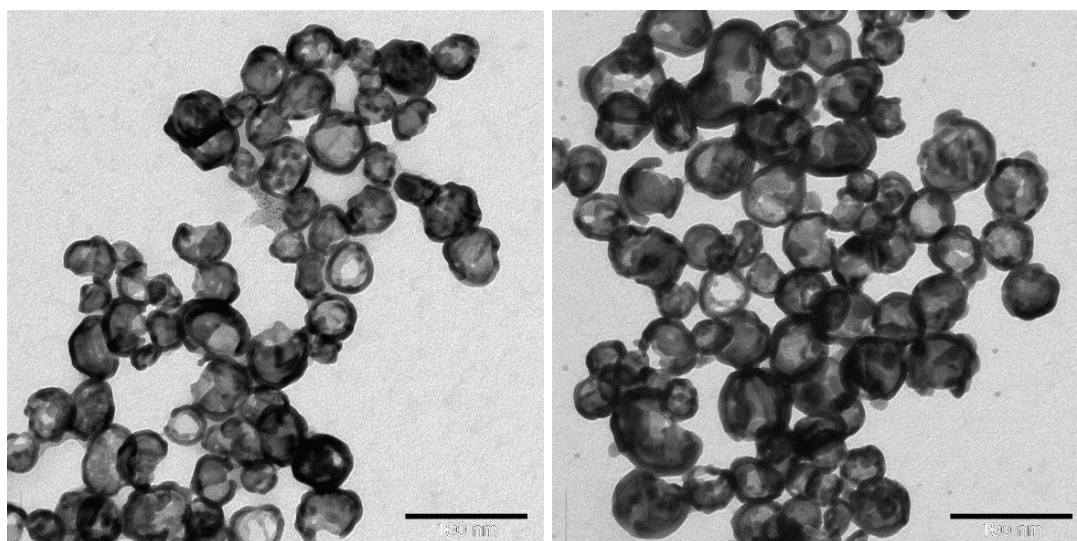

Figure 4.6 - Transmission electron micrographs of HGNs used for a later experiment. Synthesised using the same protocol as discussed above. Scale bar in each is 100 nm.

The stability of HGNs in any biological environment would need to be studied to better understand their potential as a drug delivery agent. Once in the bloodstream, a protein corona would form on the surface of the particles and could lead to degradation. Goodman *et al.* studied HGN stability in biological environments and found that the shells can degrade and fragment in low pH environments and also in human serum at physiological pH.[97] The complex nature of biological media make it difficult to pinpoint one cause of fragmentation. However Goodman suggested it is a combination of high ionic strengths, the presence of proteins, low pH environments and dissolved oxygen that lead to the breakdown of the shells. This degradation route could be advantageous for the desired application, and speed up clearance after drug delivery. However, the fate of the dissolved fragments and the time taken for the HGNs to degrade would need to be investigated further in biodistribution studies.

4.3.1.1 Shifting the LSPR of Hollow Gold Nanoparticles

An attractive feature of HGNs is the ability to tune the LSPR of the bulk colloid for a desired application. This can mean shifting it to coincide with the wavelength of an excitation laser or into the optical window (≈650-900 nm) if needed for a biological application.[95] The LSPR can be manipulated by changing the aspect ratio between the core and shell diameter. Multiple studies have shown as the aspect ratio increases, the HGN plasmon lies at longer, lower energy wavelengths of light.[100-93]

Two different experimental methods for controlling the LSPR were investigated, one where the Au concentration was varied and the other where the Ag concentration was varied, with all other components in the reaction mixture remaining constant. Figure 4.7 shows the extinction spectra of seven batches of HGNs, where each increasing batch number had more gold/potassium carbonate (Au/K_2CO_3) solution added to the reaction mixture. As the concentration of Au^{3+} ions was increased across the batches, the plasmon band showed a consistent bathochromic (red) shift to longer wavelengths, this trend is consistent with that reported in the literature.[101,102,103] The position of the plasmon of each batch of HGNs is denoted in the figure key, ranging from 702-850 nm. The systematic red shift and broadening of the plasmon is a result of the changing shape and coverage on the HGN shells.

Sun and Xia suggested that the synthesis proceeded through two main steps, the first being the formation of hollow structures with the shells being made from Au-Ag alloys. Then if a critical concentration of Au is present in the synthesis, this can lead to hollow structures with slightly reconstructed shapes and porous shells due to dealloying.[104] Other than overall size and shell thickness, the LSPR can be influenced by remaining Ag in the alloy shell. Additionally, any changes in porosity or surface morphology could influence the position of the LSPR.
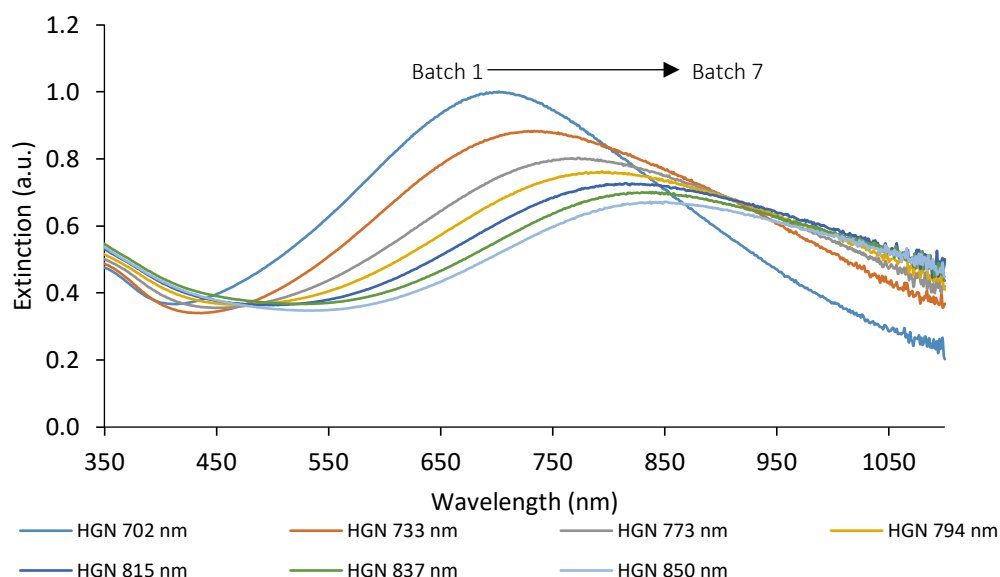
Figure 4.7 - Extinction spectra of seven batches of HGNs synthesised from the values in Table 7.2 in the experimental section. A bathochromic shift to longer wavelength was observed when the Au concentration was increased during synthesis. The legend indicates the LSPR of each batch. Spectra shown are the average of triplicate measurements collected on a baselined fast scan rate (4800 nm/min, 1 nm intervals).

Initially when a lower concentration of Au^{3+} is present in the reaction, pinholes form on the surface of the particles due to the oxidised Ag^+ diffusing into solution. As the Au^{3+} concentration increases, these holes grow larger and form cavities. If the concentration increases further, the openings can coalesce as a result of Ostwald ripening.[103] The ability to tune the LSPR in this direction is due to structural transformations from the AgNPs to the HGNs. The level of Au-Ag alloying and differences in the pore number and size contribute to this varying property.[97]

The AgNP template size (75 nm by DLS) and concentration were kept constant through each batch, and therefore it can be deduced that the extra gold ions would reduce onto the outer shell, resulting in HGNs with thicker shells and therefore a larger diameter overall. This correlates well with the size data shown in Figure 4.8, which shows an increasing hydrodynamic diameter as Au^{3+} concentration was increased across batches.
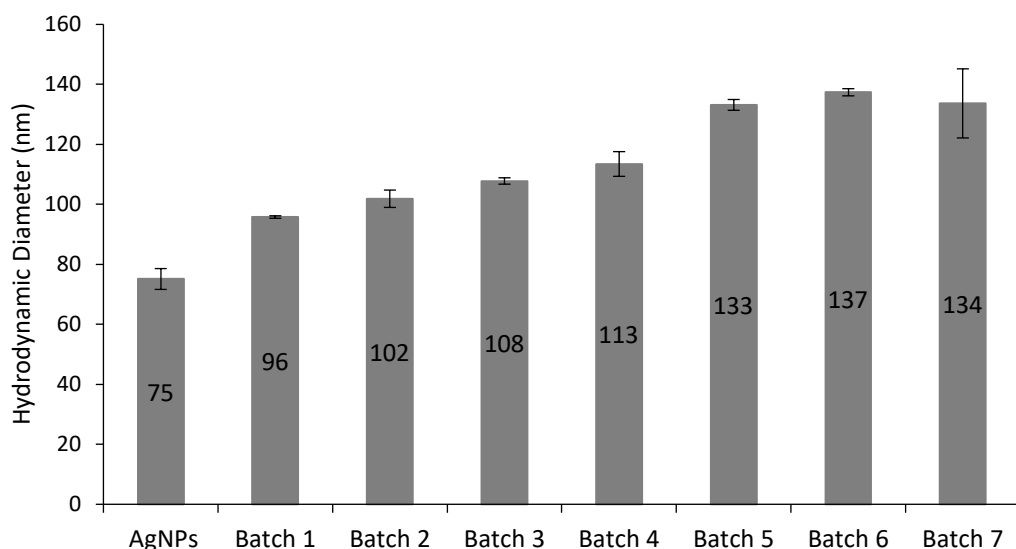
Figure 4.8 - Hydrodynamic diameters of the seven batches of HGNs as measured in triplicate by dynamic light scattering. Average diameter is shown inside the bars for each batch.

To push the LSPR in the opposite direction, the concentration of AgNPs was increased while keeping all other reagents constant. Figure 4.9 shows the extinction spectra of the batches with increasing AgNP concentration, where a hypsochromic (blue) shift trend was observed between batches with LSPRs ranging from 518-725 nm. Again, this trend is a result of the molar ratio of Ag and Au in the reaction and can be considered the reverse of the above explanation for the red shifted LSPR. Since only the AgNP concentration was increased, each batch produced should have a thinner shell than the preceding batch. This is due to more Ag surface being available for the redox reaction, but with a limited concentration of Au for the reaction.

The imbalance of reagents in the synthesis meant that for the batches with excess AgNPs, more silver remained alloyed in the HGNs. This was detected spectroscopically in the underlying band appearing at around 410 nm. To investigate this further, inductively coupled plasma mass spectrometry (ICP-MS) could have been performed to detect excess silver in the HGN core, since this is an elemental analysis technique. Alternatively, elemental mapping could have been performed on the HGNs to check for the presence of silver in the core.
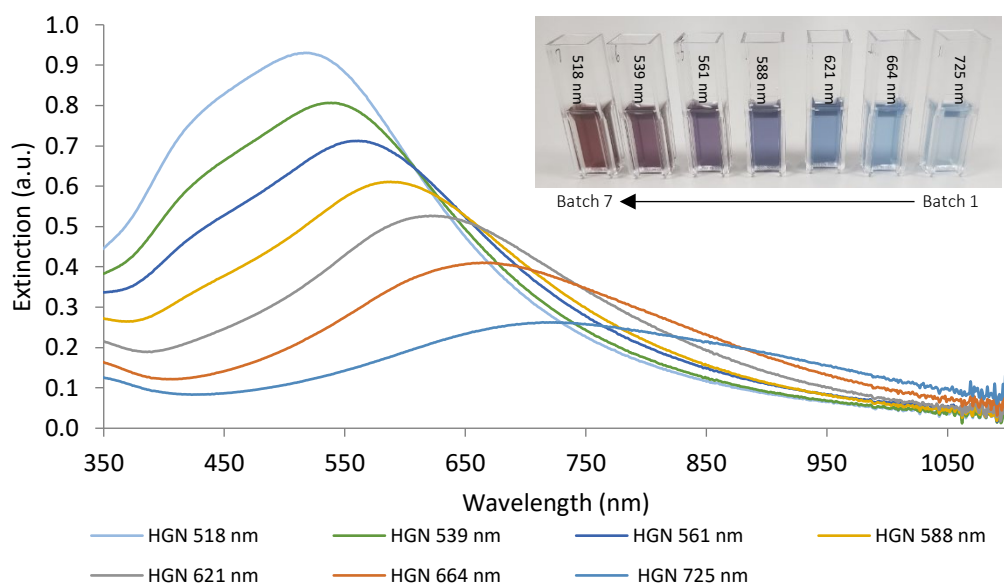
Figure 4.9 - Extinction spectra of Batches 1-7 synthesised from the values in Table 7.3. A hypsochromic shift to shorter wavelength was observed as the concentration of AgNP cores was increased during synthesis. The legend indicates the LSPR of each batch synthesised. Samples were analysed at a 1 in 4 dilution in water. Spectra shown are the average of triplicate measurements collected on a baselined fast scan rate (4800 nm/min, 1 nm intervals). Inset shows colour range of HGNs synthesised in the experiment.

Due to the difference in extinction spectra, the HGN batches were visibly different in colour. The inset in Figure 4.9 shows the range of HGN colours synthesised going from a deep burgundy to a light blue, with the corresponding λ_{max} of each batch shown above. As expected and in contrast to the previous experiment, the hydrodynamic diameter of the batches reduced as the concentration of Ag was increased across the batches synthesised, as shown in Figure 4.10.
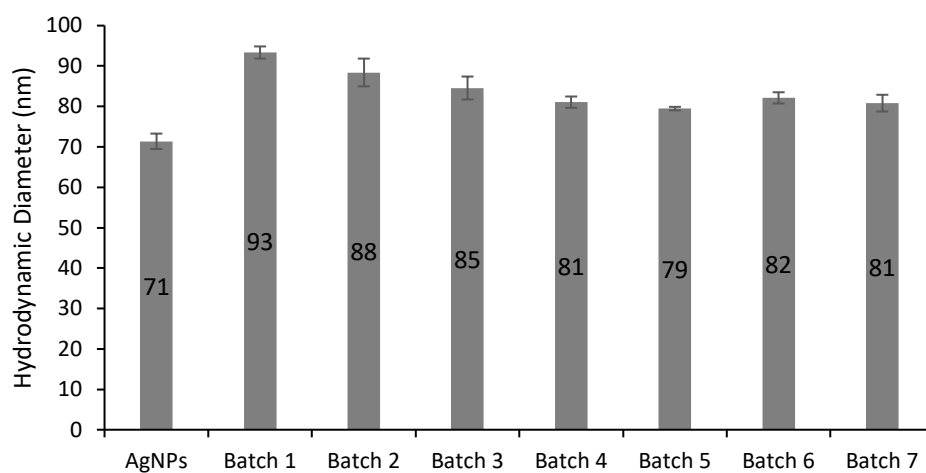

Figure 4.10 - Hydrodynamic diameters of the seven batches of HGNs as measured in triplicate by dynamic light scattering. Average diameter is shown inside the bars for each batch.

It should be noted that different AgNPs batches were used for these experiments and as such slightly different sizes and starting concentrations were used. As a comparison, Table 4.1 denotes the properties characterised from the two batches of AgNPs, both samples were diluted 1 in 10 parts in water prior to analysis. This does not affect the experimental observations made, and the shifting LSPR and increasing/decreasing shell thickness is independent of what AgNP stock was used. Both batches were characterised and were very similar, both showed a small bandwidth, or full width half maximum (FWHM) value, a property which indicates a narrow size distribution of the nanoparticles.

Table 4.1 - Characterisation of the two AgNP batches used in the previous experiments.

	Experiment 1 (Varying [Au])	Experiment 2 (Varying [Ag])
λmax (nm)	408	410
Max Extinction (a.u.)	0.922	1.020
FWHM (nm)	79	78
Hydrodynamic Diameter (nm)	75.1±3.5	71.4±1.9

These two studies showed that by altering the molar ratios of the AgNPs and Au solution in the synthesis, it was possible to synthesis HGNs with an LSPR ranging from 518-850 nm. It may be possible to push this range wider if different sized AgNPs sacrificial cores were used. Temperature and choice of metal precursor nanoparticle are also known to influence the tuning of the LSPR but were not investigated in this work.[91]

4.3.1.2 HGN Synthesis Reproducibility

The reproducibility of the HGN synthesis was investigated, while controlling as many parameters as possible. The same batch of AgNPs and Au/K_2CO_3 solution was used to eliminate variation in the inter-batch size or concentration and reduce the error introduced from preparing the growth solution. Figure 4.11 shows the extinction spectra of five replicate batches with λ_{max} occurring at 699, 691, 702, 693, 700 nm respectively. The average λ_{max} from the five batches is 697±4.7 nm, showing a small variation in the HGNs synthesised.
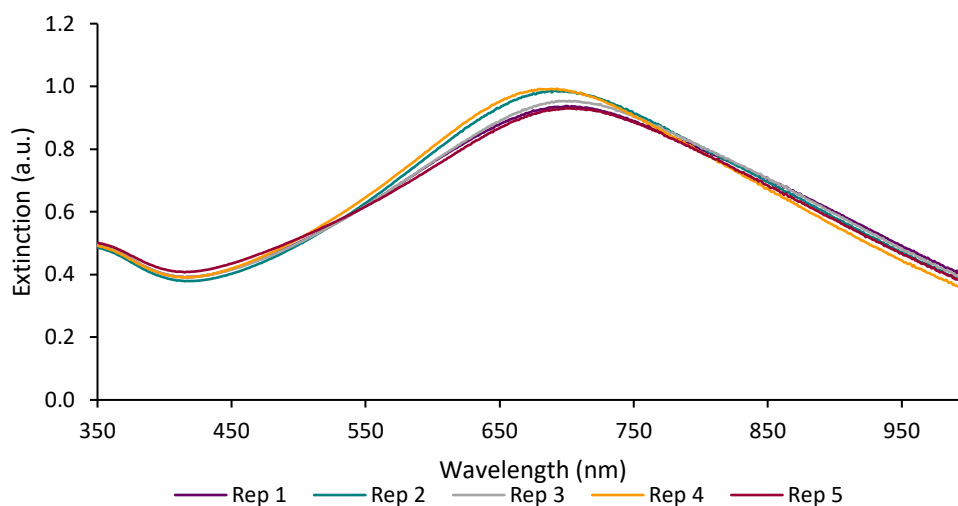
Figure 4.11 – Extinction spectra of the five replicate batches of the HGNs synthesised. Spectra shown are the average of triplicate measurements collected on a baselined fast scan rate (4800 nm/min, 1 nm intervals).

Each batch was then analysed by DLS to estimate the diameter of the HGNs. Figure 4.12 shows the sizes obtained, with an average of 88±4 nm, as shown by the purple dashed line in the figure. The synthesis method could be considered 'crude' in comparison to the traditional methods of synthesising HGNs using a Schlenk line, since the benchtop synthesis simply involved stirring solutions at room temperature. Measuring the solutions using a measuring cylinder and the rate at which they were poured into the reaction mixture was kept as consistent as possible, however there will inevitably be human error introduced during this synthesis, owing to the small variations seen between batches. Overall, this method of synthesising HGNs appears to be reproducible and appropriate for the intended application.
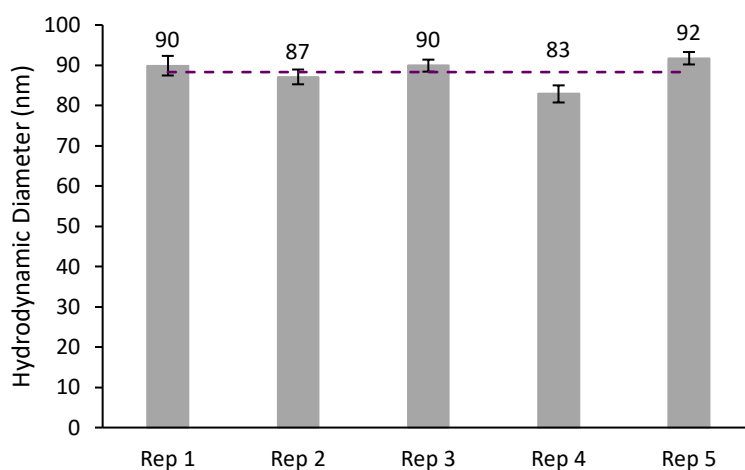

Figure 4.12 - Hydrodynamic diameters of the five replicate HGN batches. The average size of 88±4 nm is marked as the dashed purple line.

4.3.1.3 HGN Synthesis Scalability

As with all nanotechnologies with an application in medicine, scalability is a consideration if the method was to be used in a clinical setting. A preliminary experiment was conducted to investigate the scalability of the galvanic reaction. The lowest total volume studied was 10 mL, then scaled x5, x10, x20 and x50 to study total volumes of 50, 100, 200 and 500 mL respectively. This was the largest that the synthesis could be scaled with the apparatus and equipment available in the laboratory.
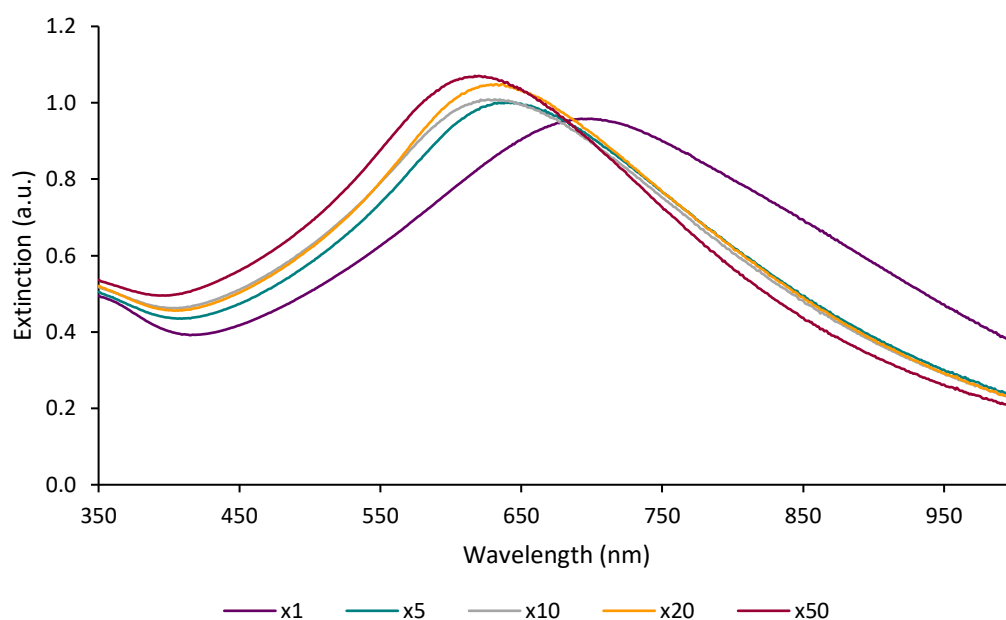

Figure 4.13 - Extinction spectra of the five batches with increasing total volumes to investigate scalability of the HGN synthesis. Spectra shown are the average of triplicate measurements collected on a baselined fast scan rate (4800 nm/min, 1 nm intervals).

Figure 4.13 shows the extinction spectra from each batch. It is evident that the HGNs synthesised varied in size and morphology between batches, suggested by the different λ_{max}. From the smallest to largest total volume, the LSPRs lie at 693, 639, 631, 637 and 618 nm respectively. As the total volume increases, a blue shift in the plasmon was observed, indicating smaller, thinner shelled particles were being synthesised. This hypothesis is supported by Figure 4.14, which shows the hydrodynamic sizes of the HGNs in each batch.
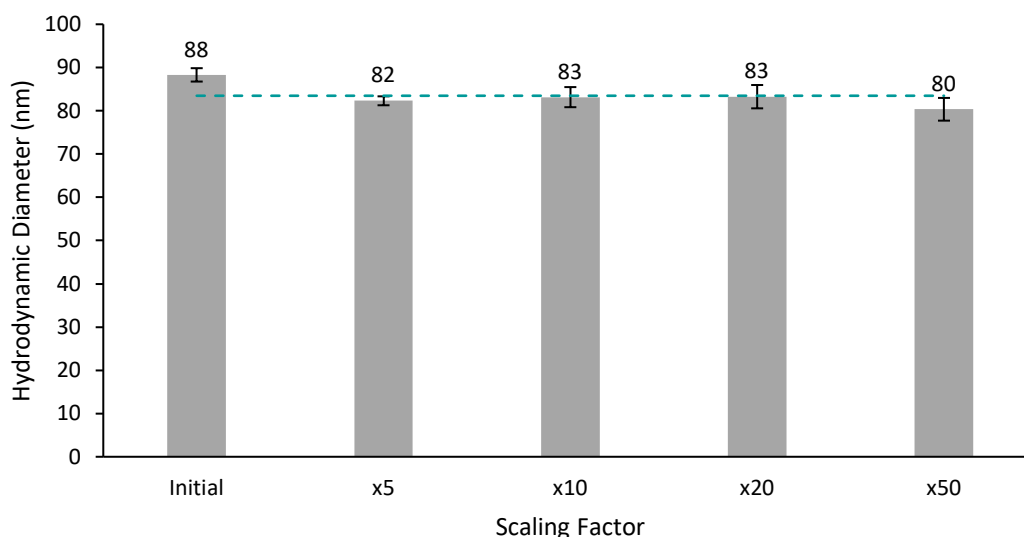
Figure 4.14 - Hydrodynamic diameters of the five HGN batches of varying total volume. The average size is shown as the dashed teal line.

The size of the flask and magnetic stirrer bar that were used for each batch were also scaled up in an attempt to keep the variables minimised. However, it is evident from the variation in LSPR and size, that the reaction conditions were not identical. It can be hypothesised that the mixing of the reaction was not kept constant between batches. This could have influenced the final HGNs synthesised since the relative reactant concentration would have been slightly different within the reaction mixture. These results suggest galvanic HGN synthesis is scalable, but would require more careful control of the parameters to ensure the quality of the final nanoparticles.

4.3.2 Functionalisation of HGNs with Bio-recognition Molecules

ICAM-1 was selected to demonstrate the ability of HGNs to carry bio-recognition molecules which could be used to target the inflamed atherosclerotic plaques. This is a membrane protein which is found in low concentrations in unstimulated vascular endothelial cells. Upon cytokine stimulation (part of the atherosclerotic progression pathway), the concentration of the ICAM-1 protein is greatly increased in the endothelial membrane.[45] Similar membrane proteins include VCAM-1 and P-selectin which behave in the same way upon stimulation in an inflamed artery. The increased

presence of these membrane proteins in inflamed cardiac walls is the reason for their use as a biological target for the drug delivery design. Section 3.3.6 discussed a similar experiment with IONCs instead of HGNs, the conjugation order was also slightly altered. An 'off-particle' conjugation method was used for the HGNs, this is in contrast to the 'on-particle' method used for IONCs. A schematic of the method is shown in Figure 4.15. It was found that the off-particle method, i.e. conjugating the PEG linker and antibody before the addition of nanoparticles, was more efficient than trying to carry out the crosslinking chemistry whilst the PEG was on the nanoparticle surface. This is likely due to less steric hindrance when carried out free in solution and without the presence of nanoparticles.
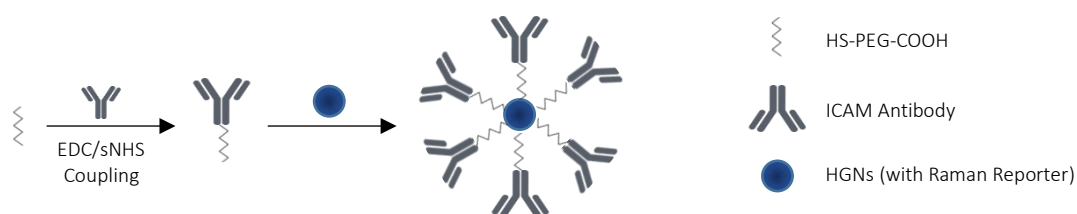

Figure 4.15 - Schematic of the off-particle antibody labelling approach via an EDC/sNHS coupling reaction. Coupling carried out in solution before the Raman reporter functionalised HGNs were introduced.

To prevent repetition, only the lateral flow strip of this conjugation method is presented. Figure 4.16 shows the results of the lateral flow test, with very clear discrimination between the control (PEG-HGNs) and antibody containing sample (Ab-PEG-HGNs).
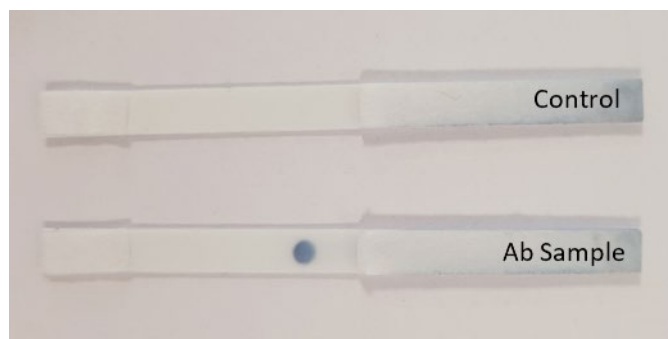

Figure 4.16 - Lateral flow strips were spotted with a generic capture antibody. The antibody containing sample was immobilised and presented as the dark blue spot on the right. The control showed no binding to the area where the capture antibody had been spotted.

This bio-recognition test confirmed the success of the antibody conjugation, as the presence of the anti-human ICAM-1 antibody on the surface immobilised the HGNs on the strip. Compared to the IONC samples in the previous chapter, there is better discrimination between samples and no non-specific binding in the control sample. The HGNs are much larger than the IONCs, and so it can be thought that they are too large to get trapped in the pores of the cellulose paper, leading to the clearer discrimination.

4.3.3 Functionalisation with a Raman Reporter

SERS has been used in numerous *in vivo* and *in vitro* studies as a non-invasive and non-destructive detection method.[105] The ability to sensitively detect biomarkers or biological binding interactions, often simultaneously in a multiplex system, has made SERS a popular area of research for future medicines. Raman measurements are made possible by functionalising the surface of a metallic nanoparticle with a Raman reporter label, often a dye. Also on the surface would be a biological molecule able to capture or bind with the target of interest, therefore if a Raman signal from the dye is detected, it infers a biological recognition event has occurred.

There exists a plethora of Raman reporters for this role, with some attaching electrostatically to the nanoparticle surface and others through a covalent bond. Each one has a 'signature' spectrum, which identifies the presence of the nanoparticles in the biological sample. Naturally, many biological tissues and cellular molecules also have a Raman signature which can overlap and dominate a signal, therefore interfering with the clarity and detection limits of the Raman reporter on the nanoparticles.

One way to navigate around this issue is to use a Raman reporter that contains an alkyne within its structure. This structure has a unique vibrational signature, with the distinct $C{\equiv}C$ stretching bands appearing in a Raman silent region. This region lies between 1800-2800 cm^{-1} and is also known as the 'cell silent region' since no endogenous biological molecules have a signal here, therefore producing a

background free window of detection.[106] Another attractive feature of the alkyne group is that it is small in comparison to many fluorophores which are currently employed in biological imaging. They therefore have a relatively minor influence on biological properties due to their small size.[107]

Hu *et al.* have synthesised an array of alkyne tags, each with a distinct alkyne Raman frequency ranging from 2017-2262 cm^{-1}.[108] By altering the conjugation length and end capping substitution, they were able to produce 20 distinguishable Raman signatures and termed this molecular range a 'carbow' (carbon rainbow). They modified these carbow molecules into organelle-specific imagining probes and were able to imagine multiple cellular structures simultaneously *in vitro*.

This paper strongly demonstrated the potential power of alkynes within biological imaging. If HGNs were to be used as part of a new medical treatment it would be desirable to track them *in vivo* in order to evaluate the target site accumulation. For this role, an alkyne containing Raman reporter would be ideal. As a proof of concept, phenylacetylene was chosen as the model Raman reporter to study due to its strong Raman signal.
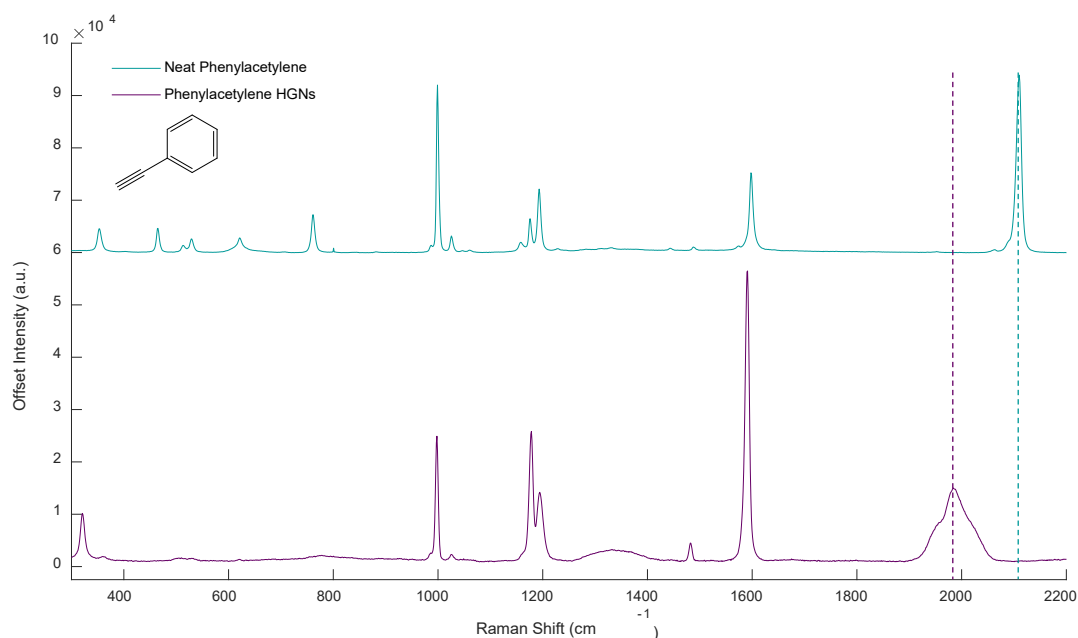

Figure 4.17 – Raman and SERS spectra of neat phenylacetylene (teal) and phenylacetylene on HGNs (purple). Collected on a Renishaw in via microscope, using a 785 nm 500 mW excitation laser, 300-2200 cm^{-1} scan range, 10 s acquisition, 50% laser power for the HGNs sample and 5% laser power for the reference spectrum. Triplicate measurements were averaged, baselined and offset before plotting using MATLAB software. The molecular structure of phenylacetylene is shown below the key.

Figure 4.17 shows a reference Raman spectrum of neat phenylacetylene (teal) and a SERS spectrum of the reporter molecule on the surface of the HGNs (purple). The alkyne peak of interest lies at 2110 cm^{-1} in the reference Raman spectrum and falls within the cell silent region of a Raman spectrum. Once conjugated to the nanoparticle surface, the peak significantly shifts by ≈125 cm^{-1}, this is in agreement with previous reports.[109-110] Multiple peaks are observed in the C≡C stretching region, it has been suggested that these are due to adsorption onto different crystal faces or the formation of different complexes.[111] Phenylacetylene is believed to adsorb via the terminal carbon in the alkyne moiety, and not through the phenyl ring. The peaks associated with the phenyl ring in the SERS spectrum do not significantly shift or broaden upon addition to the metal surface, indicating little or no interaction between the ring π-orbitals and the metal surface.[110] Table 4.2 shows the shift in peak positions from the Raman and SERS spectra of phenylacetylene shown in Figure 4.17.[111] The peaks highlighted in teal are assigned to the alkyne stretches and vibrations. The larger changes in frequency of these peaks indicate adsorption via this functional group.

Table 4.2 – Peak assignments of neat and nanoparticle bound phenylacetylene.

Reference Phenylacetylene (Raman) (cm^{-1})	Phenylacetylene HGNs (SERS) (cm^{-1})	Assignment
353	321	(C-CCH)
464		(C-C-C)
513		(C-C≡C)
529		Ring Vibrations ^{oop}
621		Ring Vibrations ^{in}
761		Ring Vibrations ^{in}
999	998	Ring Vibrations ^{in}
1026	1026	Ring Vibrations ^{in}
1158		
1175	1178	Ring Vibrations ^{in}
1193	1194	Ring Vibrations ^{in}
1488	1482	Ring Vibrations ^{in}
1599	1591	Ring Vibrations ^{in}
	1956	(C≡C)
	1985	(C≡C)
2110 region		(C≡C)
oop=Out-of-plane ring vibration	ip=In-plane ring vibration	

The characteristic shift between a bound and free alkyne molecule, could be exploited to study the release of an alkyne containing statin. Preliminary studies into the heating and Raman tracking of an alkyne on HGNs were attempted, however, instrument limitations meant that even the final concentration of Raman reporter added to the HGNs was not detectable when tested by Raman alone. Improvements to the system or even a different method for analysing the released Raman reporter after heating would need to be used to study this further.

Many Raman reporters were studied on the surface of the HGNs, with other examples shown later in the chapter. Chapter 5 focusses on a previously unseen phenomenon, where the SERS intensity of the adsorbed Raman reporter increased with plasmonic heating of the HGNs. Multiple Raman reporters were seen to follow this unusual behaviour and the possible reasoning behind the signal increase is discussed in the next chapter.

4.3.4 Photothermal Properties of Hollow Gold Nanoparticles

In addition to being a platform for enhancing Raman scattering, metallic nanoparticles can be utilised for photothermal therapy. If nanoparticles are plasmonically heated inside cells, the heat generated will dissipate to the surrounding environment, resulting in damage to the cell. This destructive effect can be used advantageously to target cells, such as macrophages, that promote atherosclerotic plaque progression. Kosuge *et al.* employed single walled carbon nanotubes and photothermal therapy to combat excessive macrophages in the atherosclerotic plaque.[112] Both *in vitro* and *in vivo* experiments showed the uptake of the nanoparticles by macrophages, with exposure to an 808 nm light source inducing apoptosis.

Photothermal therapy as an approach to regressing atherosclerosis has already been clinically tested in the Plasmonic Nanophotothermal Therapy of Atherosclerosis (NANOM-FIM) trial.[73] This trial studied the treatment of 180 patients with blood flow limiting arterial lesions. One third of the cohort were treated with an artery patch embedded with silica-gold nanoparticles, another third with silica-gold-iron

nanoparticles and the 60 control patients received a stent with no nanoparticles embedded. The photothermal conversion process was triggered either by intravascular or transcutaneous excitation by a NIR laser. The one year follow up saw no adverse effects, such as a site thrombosis, from the treatment. Both nanoparticle treatments saw a reduction in the volume of the atherosclerotic plaques, with the silica-gold nanoparticle cohort showing significantly lower risk of cardiovascular death when compared to the other groups. This promising clinical trial suggested that photothermal therapy significantly contributed to plaque regression.

Coupling the photothermal therapy potential of HGNs with their ability to carry drug loads and enhance Raman scattering, could make for a powerful multi-modal therapeutic agent for atherosclerosis. Many factors would need to be considered for translation to a clinical setting, however by initially investigating each one individually, it constructs a strong argument for their therapeutic potential.

To investigate the photothermal ability of HGNs, an in-house set-up was developed with initial experiments having the heating laser passing through a droplet of HGNs suspended between a needle tip and the thermocouple probe. However, the droplet was reducing in volume and evaporating as high temperatures were reached. Many configurations and sample holders were tried and tested, with the most efficient setup being shown below in Figure 4.18 which enabled the sample to be held in a small cylindrical vial (1.75 mL volume).
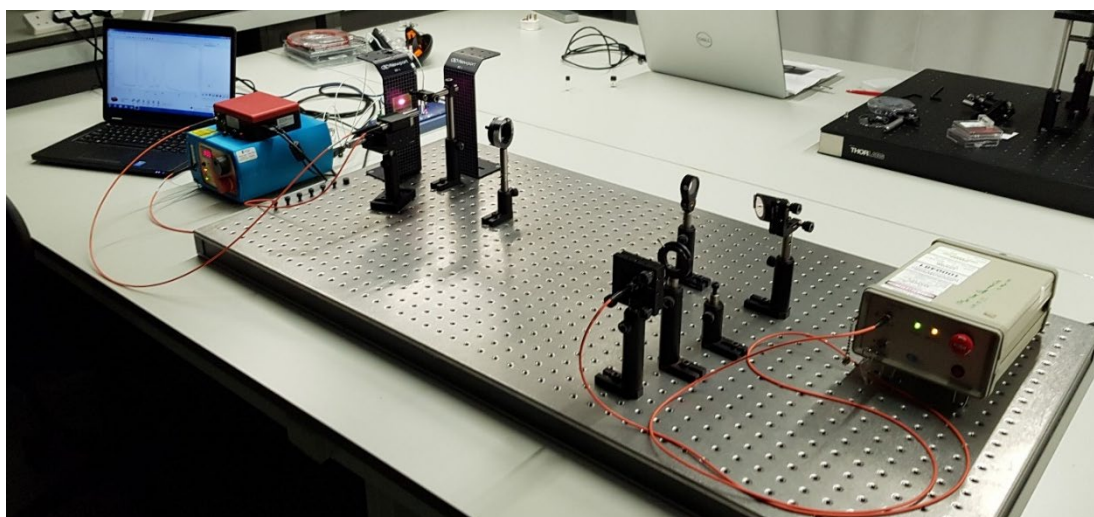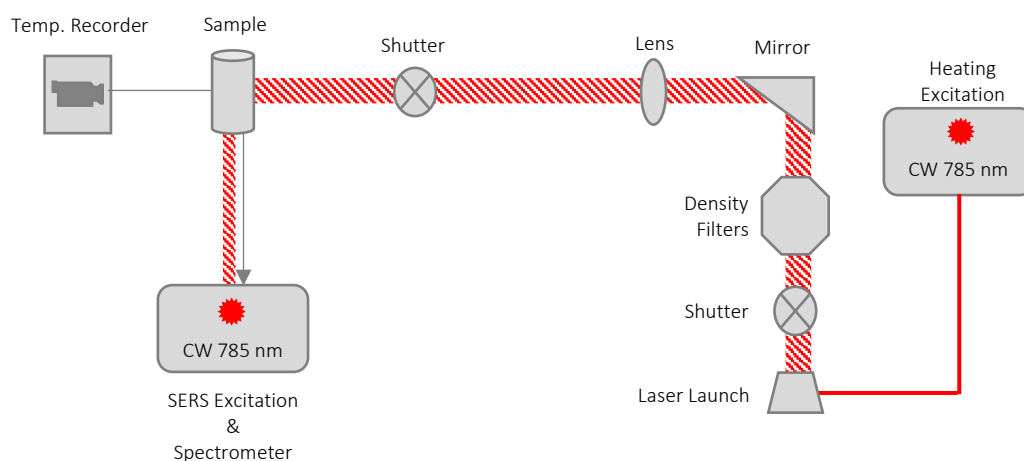
Figure 4.18 - Image of the in-house built set-up to investigate the photothermal properties of the HGNs. CW 785 nm lasers were used for both the heating of the HGNs and as the excitation source for the Raman spectroscopy experiments discussed in later sections.

4.3.4.1 Cycled Heating of the HGNs

Regardless of the experiment being carried out, the heating profile of the HGNs remained similar. An initial sharp increase in temperature, followed by a plateau when the maximum bulk temperature had been reached. The K-type thermocouple probe would be submerged in the samples (out of the path of the laser beam), passing through a small hole in the vial lid in an attempt to reduce a loss of sample volume, and connected to a Picologger for digitally recording the temperature. Figure 4.19 shows the heating and cooling curves of an HGN sample that was heated for 30 minutes, followed by a 10 minute cooling period before this process was cycled a further two times.
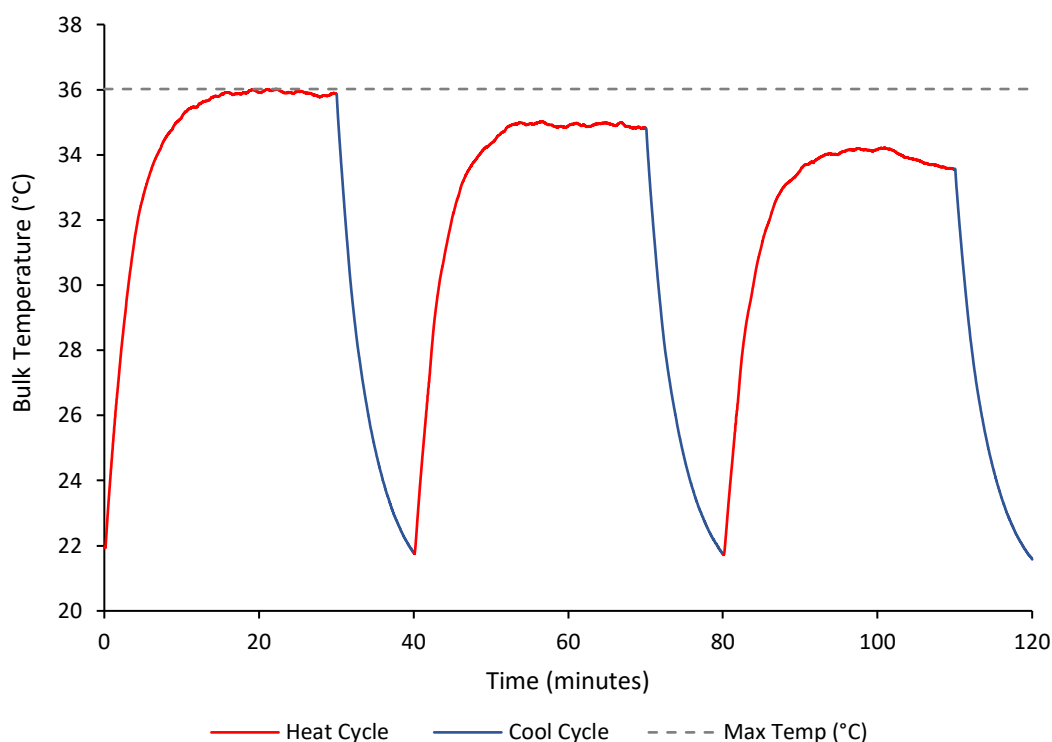
Figure 4.19 - Heating and cooling curves of HGNs interrogated with a 785 nm laser at 280 mW. Heated for 30 minutes, cooled for 10 minutes and this process was cycled 3 times with the same sample.

The heating laser was at full power, which at the point of the sample vial was measured at 280 mW. The 785 nm excitation laser lay within the absorption of the HGNs plasmon and as such excited the surface electrons. These then relaxed via electron-electron, electron-phonon and phonon-phonon interactions.[58,53,54] The thermal energy generated was then transferred to the surrounding water, resulting in an increase in the bulk solution temperature. The bulk temperature increase in the sample was ≈14°C, a comparative value to that observed by Harris-Birtill *et al.* when gold nanorods were heated with a CW laser.[113] It should be noted that as each cycle progressed, the maximum temperature the bulk solution reached dropped a degree. This could have been due to sample degradation, where the HGNs can no longer heat as efficiently as the first cycle.

To investigate the possibility of the HGNs changing, extinction spectra of a HGN sample with no heating (control) and the sample subjected to 3 cycles were collected and shown in Figure 4.20. All extinction spectra were collected once the samples had

cooled back to room temperature. There was also a visible colour change in the sample after heating, going from blue to purple.
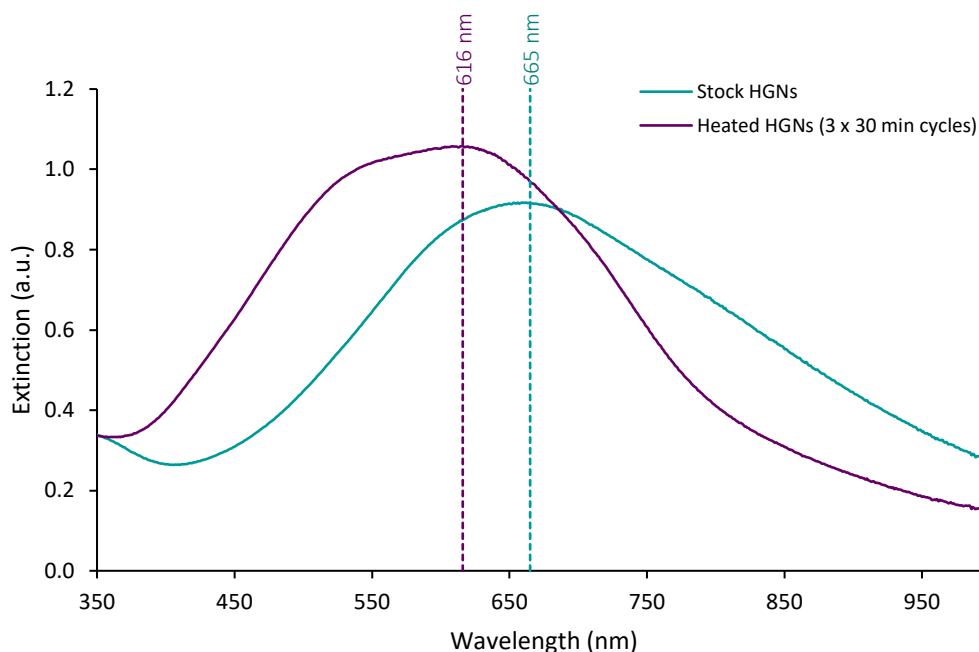

Figure 4.20 - Extinction spectra of HGNs with and without plasmonic heating applied. Spectra shown are the average of triplicate measurements collected on a baselined fast scan rate (4800 nm/min, 1 nm intervals).

The extinction profile of the sample interrogated with the laser shows a clear blue shift to shorter wavelengths and an increase in absorbance. The λ_{max} of the control HGNs was 665 nm and the heated HGNs shift by 49 nm to 616 nm. This substantial shift suggests there has been a morphological change to the HGNs or at the least, changes to the surface features of the HGNs. A second band can be seen on the shoulder of the main plasmon in the heated sample at ≈520 nm, another indication the heating has caused a change to the particle size/shape. It can be suggested from these results that the particles are becoming more 'solid like' since these types of particles characteristically have their LSPR at lower wavelengths. A study by Wheelar *et al.* found that a blue shift in HGN heating could be attributed to the fact that when HGNs are heated to a critical point, their mass is conserved and an increase in shell thickness is accompanied by a decrease in the outer diameter.[114] In another study Stagg *et al.* found that HGNs could exhibit a newly formed blue-shifted LSPR when in close spatial proximity, e.g. aggregates.[115]

This shift was dependant on the type of HGN contact, where a blue shift was observed for those interacting via surface-surface point contact.

Other than size, the LSPR could be influenced by any remaining Ag in the alloy shell, where the heating could cause further dealloying, therefore changing the Ag content of the HGNs. Additionally, any changes in porosity or the formation of dimers, trimers etc. could influence the position of the LSPR after heating. It is possible that a combination of these factors were contributing to the blue shift seen in the extinction spectra after plasmonic heating.

4.3.4.2 Concentration Dependence on HGN Heating

To better characterise the photothermal properties of HGNs, it was important to evaluate a number of factors, including nanoparticle concentration. HGN concentration also plays a vital role in the heating efficiency of the colloidal suspension. The bulk temperature increase as a function of concentration was investigated by comparing the stock solution to concentrated samples of the same HGN batch (≈90 nm), the heating profiles are shown in Figure 4.21.
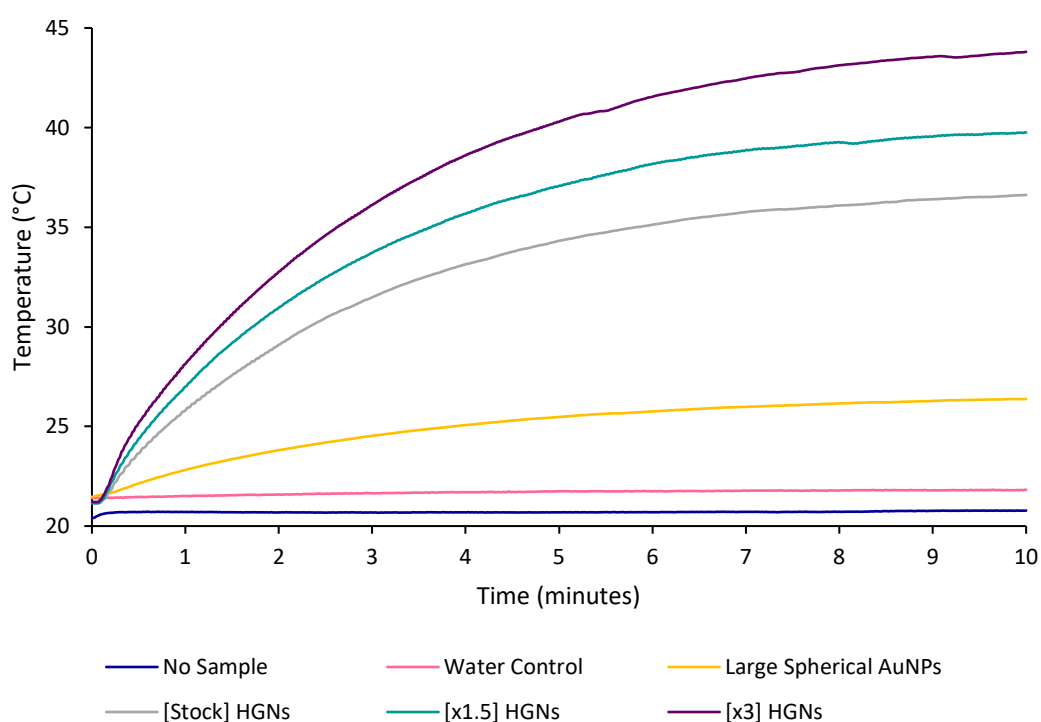

Figure 4.21 - Heating profiles of HGN samples at different nanoparticle concentrations. Samples interrogated with a 785 nm CW laser at 273 mW power for 10 minutes. Profiles are the average of triplicate experiments.

The continuous wave (CW) laser source used caused the nanoparticles to transfer the heat generated to the surrounding water through a conduction process at the metal surface.[116] The time taken for a system to equilibrate is dependent on the thermal conductivity and capacity of the surrounding medium. Studies have found that for HGNs, the heat generated dissipates within several nanoseconds through the surrounding water.[116]

The heating profiles show that the increase in HGN concentration correlated with an increase in bulk temperature. This was a result of more nanoparticles being present in the same sample volume, and so there was a larger contribution to the photothermal effect. In another experiment, the HGN concentration was estimated as 9.24×10^{10} nanoparticles/mL using a Nanosight microscope measuring the Brownian motion of nanoparticles. The particles studied in the other experiment were synthesised using the same method, so it can be assumed they would be of a similar concentration. Since the exact HGN concentration was not collected at the time of this experiment, the samples will be described as a factor fold of the stock concentration.

It should also be noted that there was a negligible temperature increase (0.4°C) from the two controls, a glass vial (no sample) and a vial with just water. This indicated that the water, which suspended the HGNs, had very little contribution to the overall temperature increase observed. It can also be confirmed that the laser beam was not hitting the thermocouple probe or the glass vial control would have dramatically increased in temperature. The solid AuNP sample (≈75 nm) was included to show that the HGN samples (≈90 nm) heated more efficiently in comparison to large solid particles. Figure 4.22 shows the starting and end temperatures of the large gold and HGN samples from the data shown in Figure 4.21.
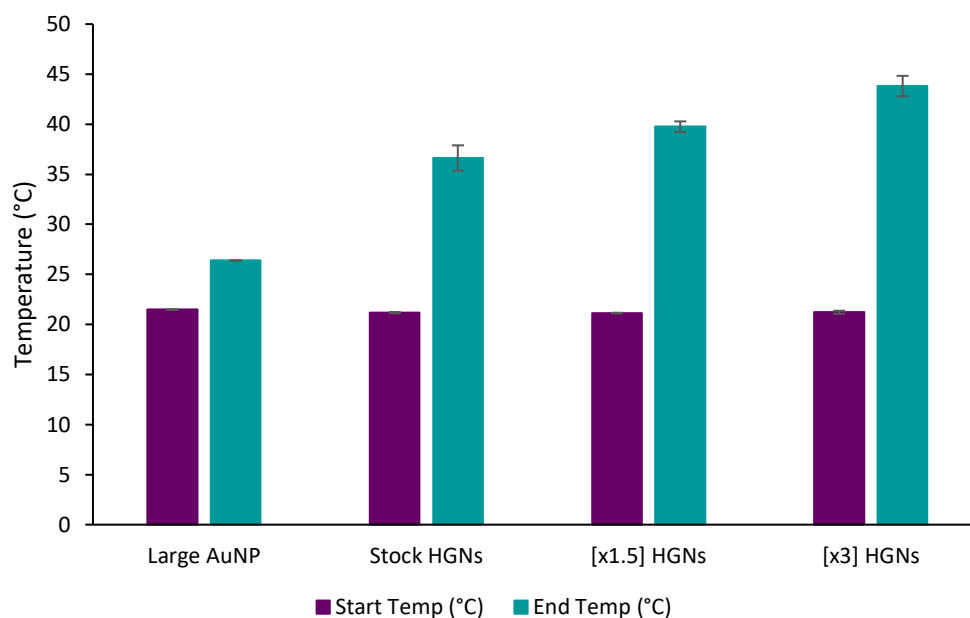
Figure 4.22 - Temperatures of samples before and after were heated for 10 minutes with a CW 785 nm laser at 273 mW power. Temperatures presented were the average of triplicate experiments.

The HGN concentration and maximum temperature reached followed the same increasing trend with the stock HGNs increasing by 15.4°C, the x1.5 HGNs by 18.6°C and x3 HGNs by 22.6°C. The large AuNPs only had a bulk increase of 4.9°C. This initial study into the relationship between HGN concentration and the photothermal process indicates there is a clear link between the two. Unsurprisingly, increasing HGN concentration leads to higher bulk temperatures being reached. This is important when considering any *in vivo* application of the HGNs, as this study shows that concentration is an influencing factor to account for when deciding the heating parameters.

4.3.4.3 Power Dependence on HGN Heating

Another factor that will influence the photothermal conversion process is the laser power. To investigate this variable, a range of lasers powers were used, maximising the instrumentation capabilities in the laboratory. Varying the laser power from 50 mW to 350 mW, the maximum power possible on the laser source, resulted in a steady increase in the maximum bulk temperature of the HGNs, as seen in Figure 4.23.
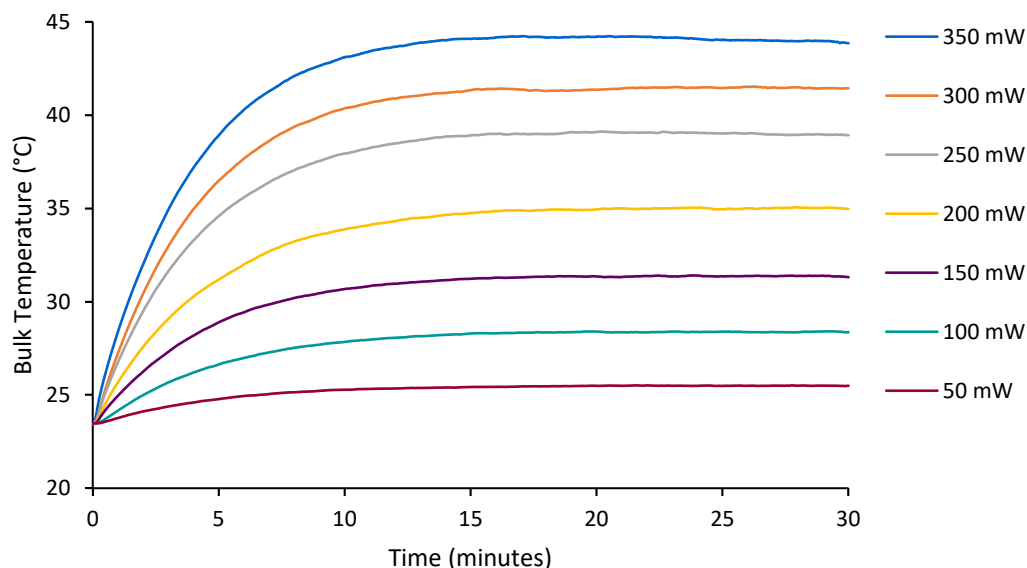
Figure 4.23 - Heating profiles of the same batch of HGNs interrogated using varying laser powers (50-350 mW) of a 785 nm excitation laser source for 30 minutes. Heating curves are the average of triplicate experiments.

The increase in bulk temperature is a direct consequence of the laser intensity used to interrogate the sample. The excitation source used was a CW laser, however it is generally believed a pulsed laser system is more efficient for inducing a photothermal effect.[91] The pause between pulses is said to allow for electron-phonon relaxation which results in better heat generation, a result of the competition between lattice cooling and nanoparticle absorption.

A study by Hatef *et al.* calculated the surface temperature increase of HGNs in relation to the CW laser beam intensity. Their study based calculations on HGNs with a diameter of 40 nm and a shell thickness of 3 nm. Although much smaller than the HGNs used in this work, the results are concordant. They found that the maximum temperature increase varied linearly with the laser intensity used as shown Figure 4.24. The inset figure shows the steady-state radial temperature increase around the HGN. The temperature drops dramatically as the distance from the HGN centre increases, where at around 200 nm from the centre, the temperature drops to 10% of its maximum value. This highlights that the heat affected zone is in close proximity to the nanoparticle surface, an ideal environment for releasing drug molecules from the surface of the particle. The possibility of long range heating

appears less likely as the temperature decreases with distance. Indicating damage to surrounding tissue in an *in vivo* application would be minimised.
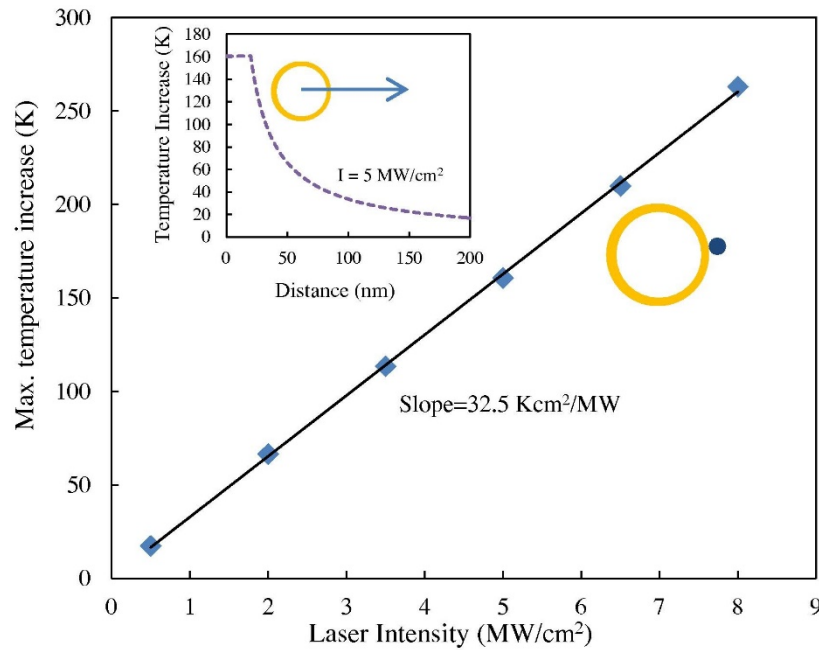

Figure 4.24 - Maximum temperatures increase at the surface of HGNs in water versus CW incident laser intensity. Inset shows the steady-state distribution of temperature increase as a function of the distance from the HGN centre for a laser intensity of I = 5 MW/cm^2. Reprinted from Int. J. Heat Mass Transf, 89, A. Hatef, S. Fortin-Deschênes, E. Boulais, F. Lesage and M. Meunier, Photothermal response of hollow gold nanoshell to laser irradiation: Continuous wave, short and ultrashort pulse, P.866-871, Copyright 2015, with permission from Elsevier.

From the data presented in Figure 4.23, the maximum temperature reached at each laser power and the change in bulk temperature is plotted overleaf in Figure 4.25. The trends in both plots are very linear, consistent with that calculation by Hatef *et al.* This also suggests the photothermal conversion process had not reached its maximum efficiency in respect to the laser input. 350 mW was the maximum laser power available in the laboratory for the experiment, however perhaps with a larger laser input power the maximum bulk temperature would have been reached.
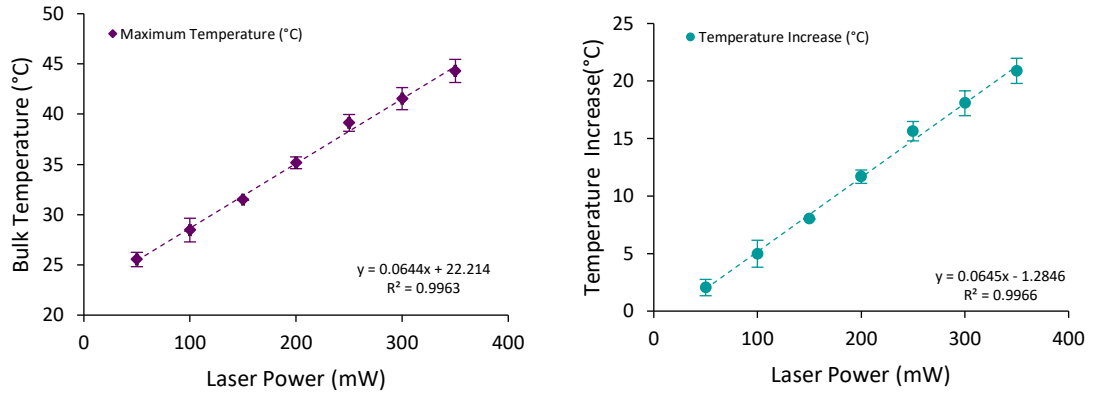
Figure 4.25 - The maximum bulk temperature reached at each laser power is plotted on the left hand figure. The increase in temperature from the initial temperature at each laser power is plotted on the right hand side. HGNs heated through a range of laser powers (50-350 mW), using a 785 nm excitation laser for 30 minutes. The plots are an average of triplicate experiments.

In any heating system, as the intensity of the laser source increases the temperature of the nanoparticle lattice will increase and can pass through the following stages: a threshold for acoustic vibrations, a melting threshold, a vaporisation threshold and finally a fragmentation threshold.[117] As a result of these increasing energy thresholds being reached, the surrounding medium can also pass through the stages depending on the temperature reached by the nanoparticles.

Reports in the literature have shown that when the laser power is high enough, the HGNs can anneal, collapse in on themselves or even fragment under the large power input.[53,58] However, often a high powered pulsed laser is required to induce this structural change. Prevo *et al.* found that even when HGNs with a plasmon far removed from the excitation wavelength were irradiated with a pulsed laser system, they annealed to solid spherical AuNPs.[118] However, it is not just laser intensity that influences the temperatures reached around a nanoparticle during heating. Equation 3.1 shows the contributing factors to the local temperature around a single nanoparticle in a steady state regime.[117]

Equation 3.1 - Local temperature around a single nanoparticle in the steady-state regime.

$$\Delta T(r) = \frac{q_{NP}}{4\pi K_m r} = \frac{\sigma_{Abs}(\omega)I(\omega)}{4\pi K_m r}$$

Where r is the distance from the centre of the nanoparticle, K_m is the thermal conductivity of the surrounding medium. The numerator expresses the heat generated by the nanoparticle, with $\sigma_{Abs}(\omega)$ denoting the nanoparticle absorption frequency and $I(\omega)$ the laser frequency. The nanoparticle absorption efficiency is an intrinsic property of the nanoparticle, dependent on the size, shape, state of aggregation and elemental composition. Therefore laser intensity is not the only factor influencing the maximum temperature reached during plasmonic heating. However the data presented in above figures was collected using the same batch of HGNs, it is therefore a direct investigation of the effect of laser power on plasmonic heating.

Wheelar *et al.* applied pulsed and CW excitation to the same batch of HGNs to compare the effect of the laser source with respect to any morphological changes.[114] Within their experiment they found the pulsed system induced the formation of solid AuNPs, whereas the CW system did not affect the HGN shape. This supports the theory that the additional relaxation time in the pulsed system leads to greater photothermal conversion and therefore morphological changes to the HGNs. The continuous wave laser source used in this research did not have the capacity to incite the dramatic shape changes observed in the above studies due to the comparably lower laser power. Extinction spectroscopy was also used to follow the effect of varying the laser power, Figure 4.26 shows that as the laser power was increased, it resulted in a further blue shift of the LSPR compared to the control (unheated) HGNs.
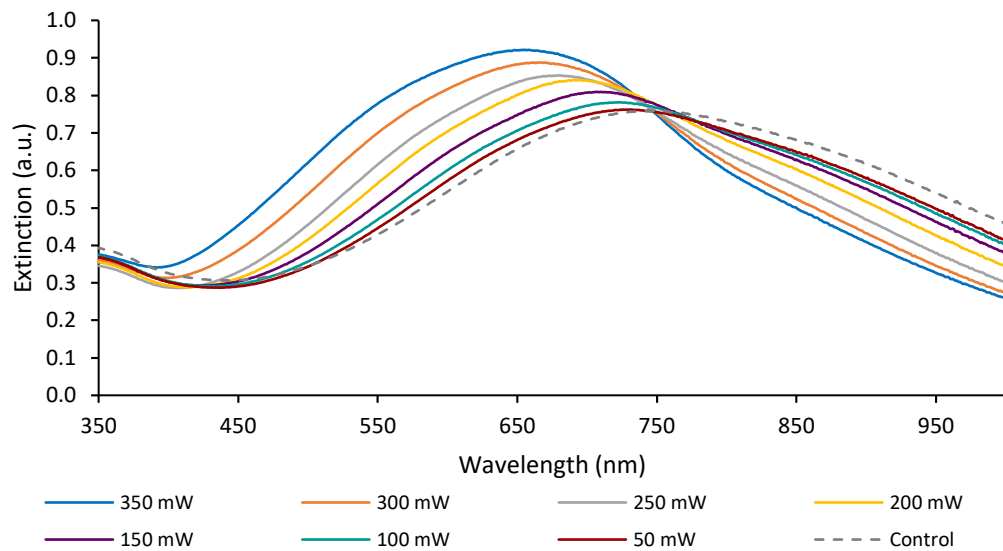

Figure 4.26 – Extinction spectra of the HGNs after 30 minutes heating at 50-350 mW. Spectra shown are the average of triplicate measurements collected on a baselined fast scan rate (4800 nm/min, 1 nm intervals).

The plasmon position of each sample after irradiation at each laser power is detailed in Table 4.3. The plasmon shift from the control sample is also noted, with all samples exhibiting a blue shift to lower, higher energy wavelengths. The largest plasmon shift post heating, was 95 nm and was observed when the highest laser power was used.

Table 4.3 - Average LSPR position of HGNs post heating at each laser power.

Power (mW)	350	300	250	200	150	100	50	0
λmax (nm)	655	667	679	690	707	723	731	750
Δ nm	95	83	71	60	43	27	19	-

Wheeler *et al.* saw no change in the extinction spectra when a CW laser source was used, indicating there was no morphological change post heating.[114] This conflicts with the results observed in the above experiment. Many factors may contribute to this, firstly, the HGNs were synthesised using different methods, where Wheeler used a cobalt template to produce much smaller HGNs at ≈50 nm. Secondly, the concentration and volume of HGNs studied differed as well as the instrument set up.

The blue shift however, can be attributed to a smaller morphological change in comparison to that seen with a pulsed laser system. As discussed previously, the blue shift could be a result of the particles shrinking to smaller HGNs with thicker shells. In experiments where an external voltage is applied to nanoparticles, an increase in electron density on the metal surface results in a blue-shift of the LSPR.[117] This comparison may partially explain the observed blue-shift, where after plasmonic heating, there is an increase in electron density on the nanoparticle surface and the electrons are more tightly bound. The shift in LSPR is linearly linked to the CW laser power used in the study. Overall, the experiment showed that the HGNs were changing morphologically with respect to the increasing laser power.

The standard laser power used in most of this work was 280 mW, this converted to a maximum power density of 4.5 W/cm^2 at the 4 mm focal point. In the literature, laser densities ranging from 2-32 W/cm^2 have been used for photothermal and drug release studies *in vivo*, therefore this work uses a realistic power density range for the application.[94,96,119,120,121]

4.3.4.4 Surface Temperature Measurements

There is an abundance of studies using nanoparticles for their photothermal response in application based papers, yet very few have investigated the surface temperature of the nanoparticles or their heating efficiency. This is likely due to the lack of robust analytical techniques available to measure these properties. Some groups have modelled and calculated the photothermal efficiency, however these are always carried out using spherical solid gold nanoparticles. Due to the obvious optical differences with HGNs, it was felt these calculations would not be transferable for this research.[57-122]

Effort has been made to answer the question surrounding surface temperature, with Baffou *et al.* creating a thermal microscopy technique which is sensitive to thermal-induced refractive index variation. However, it is limited by its diffraction resolution.[123] A modified atomic force microscope has also been used to map temperatures, however this was invasive due to the use of a tip and had a low spatial resolution of 50 nm. There also exist some spectroscopy techniques which have tried to elucidate the surface temperature of nanoparticles during heating. However these also have limitations of low resolution, slow readout times, the need for fluorescent tags or are often niche to a particular application.[123]

Hu *et al.* used SERS to measure temperature changes on plasmonic surfaces observing a sensitive frequency shift of a stretching band of phenyl isocyanide when the temperature increased (0.232 cm^{-1}/°C).[124] This technique although an improvement, used nanoparticles fixed on a glass slide and not free in solution. Our laboratory also did not have the facilities to recreate this method using the HGNs at the time of this research.

It can be assumed that a bulk temperature change from the photothermal conversion process is a result of even higher surface temperatures on the HGNs. The absorption of radiation into such a small quantity of gold and in a small volume, is likely to reach extremely high temperatures. As with most physical properties of nanoparticles, they differ from their bulk relatives. The melting point of gold nanoparticles has been

reported to only deviate from the bulk gold (1064 °C) if the particles are less than 10 nm.[125] If the difference in HGN shape is excluded, it can be assumed that the surface temperature does not reach the bulk melting temperature since there is no evidence of the HGNs melting with CW plasmonic heating in this research.

4.3.5 Excitation Wavelength Study

Raman spectroscopy systems are now available with excitation lasers ranging from the UV through to the NIR. Many factors need to be considered when choosing which wavelength to use as the excitation source, these can include cost, resonance enhancement, fluorescence background enhancement and appropriateness for the intended application. Referring back to the Equation 1.2 describing Raman intensity in the introduction section, it is known that the laser frequency is to the fourth power, and can greatly influence the scattering detected.

For this research a 785 nm excitation wavelength was chosen for both heating and Raman measurements as they fall within the biological optical window (650-950 nm) and were available for incorporation into the in-house built system. The longer excitation wavelength also reduces sample degradation, lowers photo bleaching and reduces background fluorescence. However, other excitation sources were available in portable/handheld spectrometers to study the performance of the HGNs as SERS substrates with laser wavelengths of 532, 638, 785 and 1064 nm.
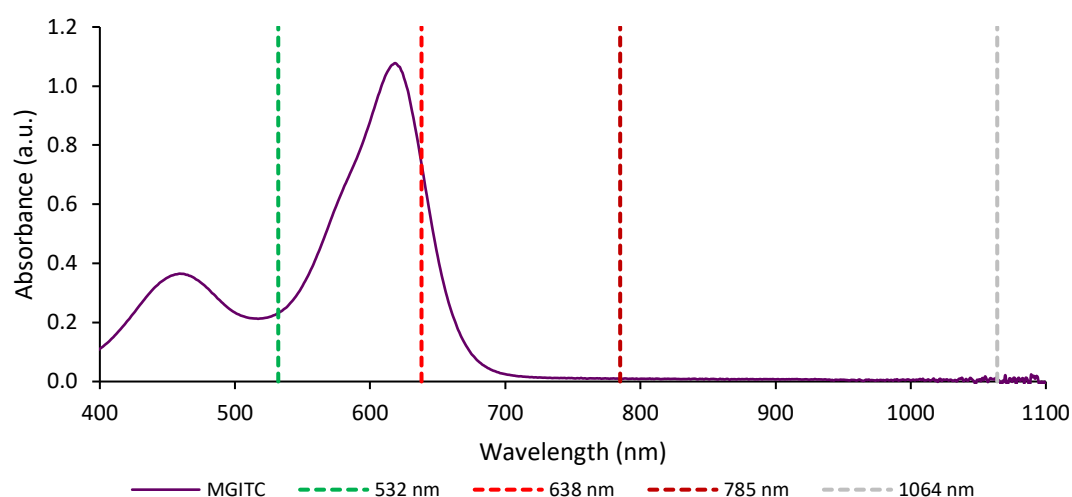

Figure 4.27 - Absorbance spectrum of 9.1 µM MGITC solution. Excitation laser wavelengths shown as dashed lines. Spectrum shown is the average of triplicate measurements collected on a baselined fast scan rate (4800 nm/min, 1 nm intervals).

Identical samples were prepared with MGITC (0.1 µM final concentration) adsorbed onto the surface of the HGNs. This Raman reporter is commonly described as non-fluorescent with a molecular absorbance at 460 and 620 nm as shown in the absorbance spectra in Figure 4.27. The excitation wavelengths of the spectrometers are shown as dashed lines.

It would be expected that the Raman intensity will be strongest for the excitation wavelength nearest the molecular absorbance, therefore the 532 and 638 nm excitation sources should induce a resonance effect, resulting in SERRS. The second consideration is the correlation between the HGN LSPR and the excitation wavelength. When nanoparticles are excited near their plasmon resonance wavelength, significant enhancement of the electromagnetic (EM) field around the metal surface arises. It is these enhanced EM fields that are the main contributor to the SERS effect. The extinction spectra of the MGITC-HGNs is shown in Figure 4.28.

The broad nature of the extinction profile of the HGNs, means all the investigated wavelengths should interact to an extent with the LSPR. Again, the spectrometers with an excitation at 532 and 638 nm should have the greatest enhancement due to the most overlap of the LSPR and excitation laser. Each spectrometer had a different laser power and spot size, and for some of the spectrometers these parameters were fixed.
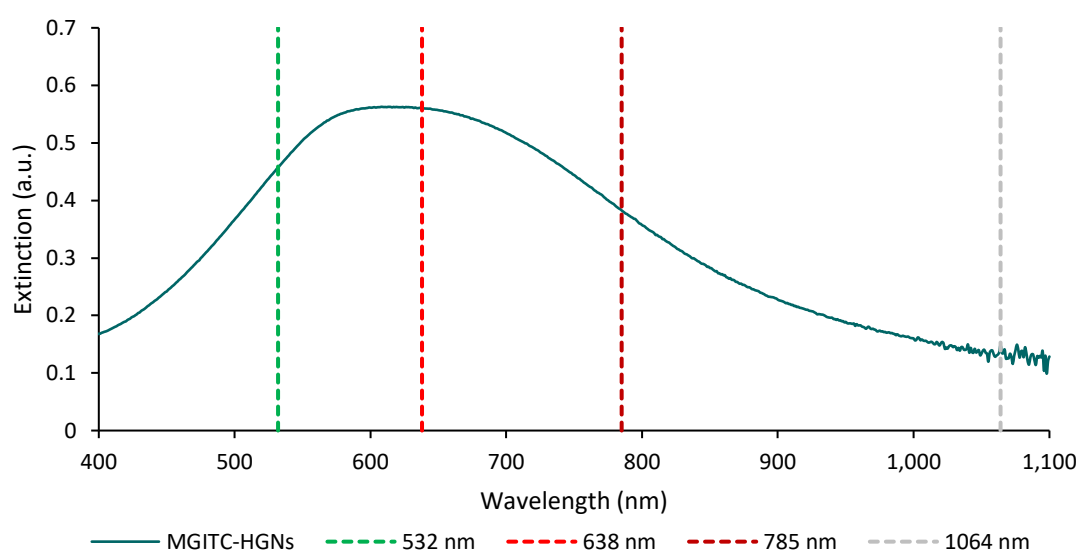

Figure 4.28 - Extinction spectra of MGITC-HGNs (50 nM). Excitation laser wavelengths shown as dashed lines. Samples were analysed at a 1 in 2 dilution in water. Spectrum shown is the average of triplicate measurements collected on a baselined fast scan rate (4800 nm/min, 1 nm intervals).

As such all spectra were normalised to an ethanol standard during processing. The resultant spectra are enlarged overleaf in Figure 4.29.

It was not possible to obtain a Raman spectrum of MGITC in solution at the same concentration as was added to the HGNs. Therefore, all the spectra collected are a result of an enhancement mechanism and not pure Raman.

When comparing the normalised SERS intensity of each excitation wavelength, the 532 and 638 nm spectra show the most enhanced signals. This is as expected since the Raman reporter has molecular absorbance close to these wavelengths, with the 532 nm spectra possibly gaining enhancement from two absorbance bands. Therefore, a resonance effect was induced and SERRS was collected at these wavelengths. Interestingly, the scaled intensity of the 1064 nm spectra is higher than the 785 nm spectra, even though the latter should have had better overlap of the LSPR and excitation wavelength. One explanation to this could be that the HGNs are self-absorbing the scattered light from the lower wavelength excitations. From previous heating experiments, it is evident that HGNs are efficient absorbers of incoming radiation, it would be plausible for some of the scattered light to be reabsorbed by neighbouring HGNs, and therefore the spectrometer doesn't detect the true Raman scattering.

Although not obvious in the extinction spectra, small dimers/multimers or clusters of HGNs could be responsible for the enhanced spectra obtained at 1064 nm excitation. If these hot spots had their plasmon maxima close to 1064 nm this could result in the enhanced spectra. Since there is little indication of this in the extinction spectra, it could be postulated that they are transient and not time stable. Even so, these could still result in the SERS spectra collected considering the Raman scattering is fast compared to the particle diffusion times.

Baia *et al.* saw a SERS signal at 1064 nm in their study of p-aminothiolphenol on gold nanoparticles, and attributed this unexpected enhanced signal to an aggregation process.[126]
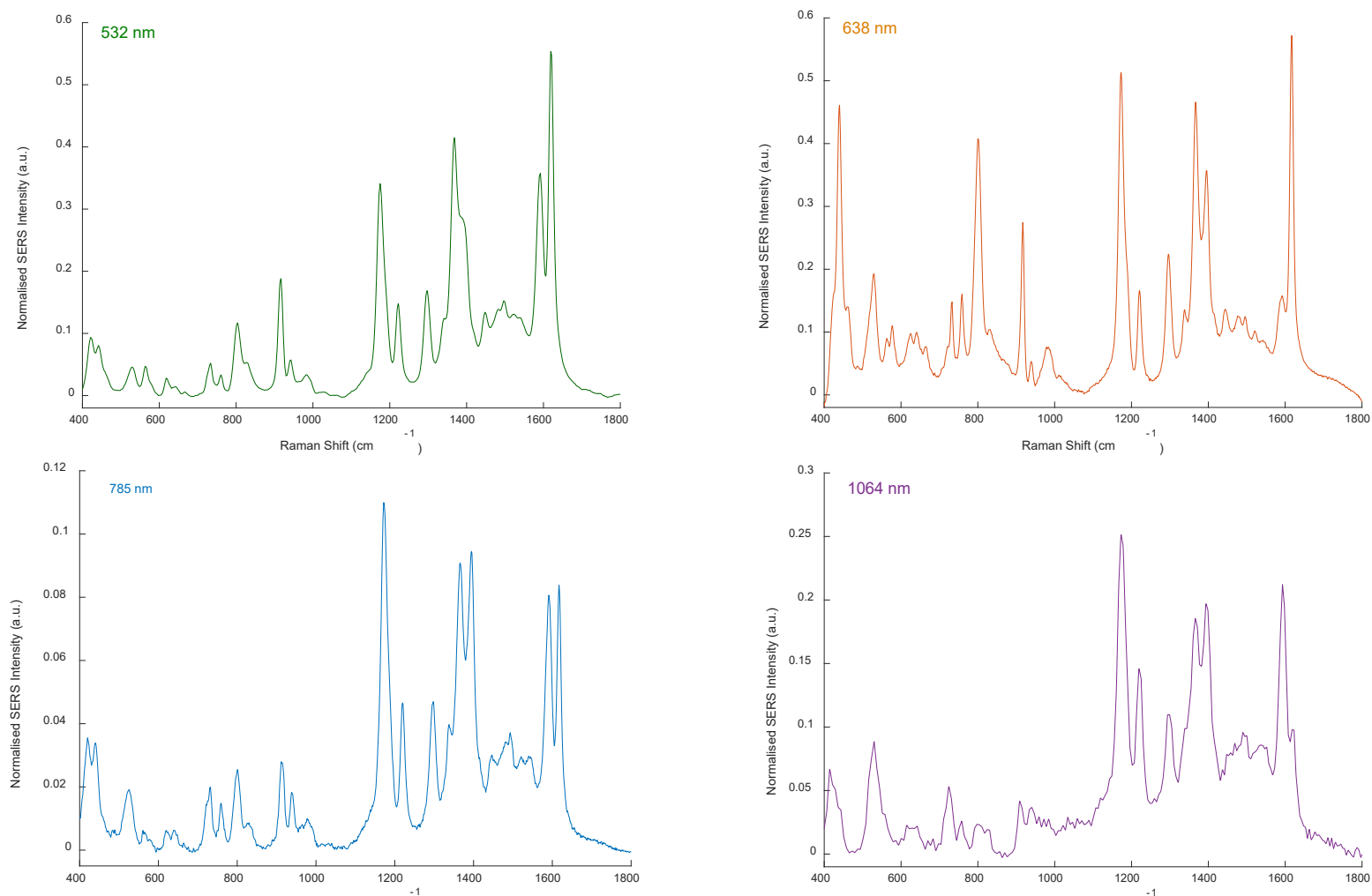
Figure 4.29 - Raman spectra of MGITC-HGNs (0.1 µM final concentration) at 532, 638, 785 and 1064 nm excitation wavelengths. All spectra were collected in triplicate at full laser power with a 1s acquisition. All spectra were processed before plotting – subtraction of a glass vial & bare HGN background, spectra cut to same wavelength range, baseline corrected, normalised to an ethanol standard and triplicate scans averaged.

Although the frequency of the peaks observed are the same for each excitation wavelength, the relative peak intensities differ between laser sources. This has already been reported in the literature with MGITC and other Raman reporters on metallic nanoparticles.[126,127,128] The main consensus for this observation is that the charge transfer (CT) mechanism of SERS can contribute to some bands more than others if the excitation matches the energy gap between the lowest and highest unoccupied molecular orbitals of a molecule. There exists an interplay of enhancement mechanisms at each of the excitation lines, and this is evident in the different peak ratios presented.

If other effects such as the CT or aggregates are involved, the enhancement mechanism becomes complex. However, this study showed that a spectra of the adsorbed molecule was attainable through all four wavelengths studied.

4.4 Concluding Remarks

The results presented in this chapter indicate HGNs would be an appropriate choice of nanoparticle for the delivery of statins to atherosclerotic plaques. Their synthesis can be modified to produce HGNs with LSPRS ranging from 518-850 nm. A property which is useful for biological applications given the optical window. Their synthesis was simple in comparison to most other HGN protocols using either air-sensitive cobalt or silica nanoparticles as the core. The pilot investigations into reproducibility and scalability suggested with better control of the experimental parameters, the HGNs could be synthesised reliably and on a larger scale.

Further to the LSPR shifting experiments, it would be interesting to characterise the heating and SERS behaviour of each batch to help select the best performing LSPR for these applications. It may be there is no one single LSPR that performs well both at heating and SERS, this is likely given that one event is based upon light absorbance and the other scattering. Most likely there will need to be a balance of performance with a nanoparticle that can sufficiently do both. It would also be worthwhile carrying out elemental analysis on the HGNs to evaluate how complete the dealloying step was during the galvanic reaction, as any leftover silver could be contributing to the heating and/or SERS reported.

When discussing the optimum LSPR of the HGNs for this application, it should be noted that an extinction spectrum is a combination of the nanoparticle absorbance and scattering, and does not always provide a correct indication to where the optimum Raman enhancement will be. Liu *et al.* developed a spectroscopic method to extract the scattering and absorbance factors simultaneously.[129] Their findings were in agreement with that simulated by discrete dipole approximations and an improvement on the current methods used to separate these contributions. Their study found that absorbing and scattering contribution can greatly differ between nanoparticles of the same shape/metal even with very similar extinction spectra. This has an effect on their intended application, and in their study they showed photothermal performance varied as a result of this differing absorbance factor. It

would be most interesting to analyse the HGNs using this technique to probe the scattering and absorbance contribution to the extinction spectra observed. This may give new information that could influence the synthesis of HGNs and thus indicate if a higher/lower LSPR would lead to better heating or SERS properties.

The HGNs show photothermal properties which were shown to be dependent on the concentration and power of the interrogating laser. These are both parameters that should be considered if this work was advanced to *in vitro* or *in vivo* studies. They were able to more efficiently convert the energy than solid gold nanoparticles of a similar size, which is another benefit to using HGNs as the drug carrier. Although the surface temperature was not concluded in this chapter, it would be of interest to see whether a modified version of the heating equations could estimate the temperatures reached during heating. More advanced modelling would be required to achieve this given the complex shape and surface of HGN in comparison to the simple spherical models used presently.

Finally, as a proof of concept, the HGNs were functionalised with an alkyne tag to demonstrate their ability to be tracked *in vivo* or *in vitro* given that this functional group has its spectroscopic bands in the cell silent region. Although this work was not taken further due to instrumentation limitations (limited spectral range and resolution on the heating set up), it would be interesting to use a set-up that combined the photothermal process and high range Raman spectroscopy to further probe the use of an alkyne tag as a Raman reporter in drug delivery.

5. Surface Enhanced Raman Spectroscopy with Hollow Gold Nanoparticles

5.1 Chapter Introduction

Hollow gold nanoparticles (HGNs) can be used as a substrate to enhance the Raman scattering of an adsorbed Raman reporter. The coupling of the outer shell and inner core LSPRs leads to a stronger electromagnetic field at the surface, owing to the SERS signal observed. Due to their red shifted LSPR, HGNs can be utilised in difficult imaging matrices such as biological tissues, due to the optical window at 650-900 nm.[95]

The first hyperpolarisability (β) is a measure of how easily a dipole will be induced under the influence of an electric field. HGNs have much higher β values when compared to similar sized solid gold nanoparticles, for example the β of ≈80 nm HGNs is three times that of solid AuNPs.[130] Hence they can be a much more effective substrate for SERS enhancement. Surface defects also contribute to the larger β values, due to the presence of pinholes known to generate hot spots.[130] Pinholes will form during the dealloying stages of HGN synthesis as detailed in Figure 4.3. This makes HGNs an interesting substrate for Raman spectroscopy since Raman scattering is the result of induced dipole oscillations interacting with an applied electromagnetic field.

Their use as a SERS substrate can be further enhanced by careful selection of the Raman reporter used. Extreme red shifted nanotags have been developed by Bedics *et al.* and consisted of HGNs with a chalcogenopyrylium dye on the surface.[131] These reporters outperformed the conventional Raman reporters under the same conditions, a result of having an absorption maxima at longer wavelengths to coincide with the HGN LSPR and excitation laser wavelength. This powerful pairing had picomolar range detection limits, showing promise for HGN use in deep tissue analysis.

The photothermal properties of HGNs can be used to enhanced the SERS response, and this was demonstrated by Kearns *et al.* who introduced the collapse of a

surrounding polymer coating with a Raman reporter embedded in the layer.[132] Upon heating, the polymer layer underwent a conformational change from a swollen disordered coil to a collapsed ordered globule. This pulled the trapped Raman reporter closer to the HGN surface, therefore 'switching on' the SERS. The SERS signal increases with proximity to the electromagnetic field, with the Raman reporter experiencing a higher field closer to the HGN surface.[133] Raman reporters must be in very close proximity to the nanoparticle surface (≈ a few nm) to be detected using SERS. The 'switching on and off' of the SERS was reversible, and purely induced by the 785 nm laser excitation and consequential distance displacement.

The work presented in this chapter uses HGNs in an unaggregated state to achieve SERS, and then the application of plasmonic heating to enhance the signal. However, the process is not reversible. An enhancement in the SERS intensity is observed only after irradiation with a 785 nm laser and suggests the HGNs are being modified somehow, giving rise to the superior optical properties observed. Figure 5.1 shows a schematic of the work presented in this chapter.
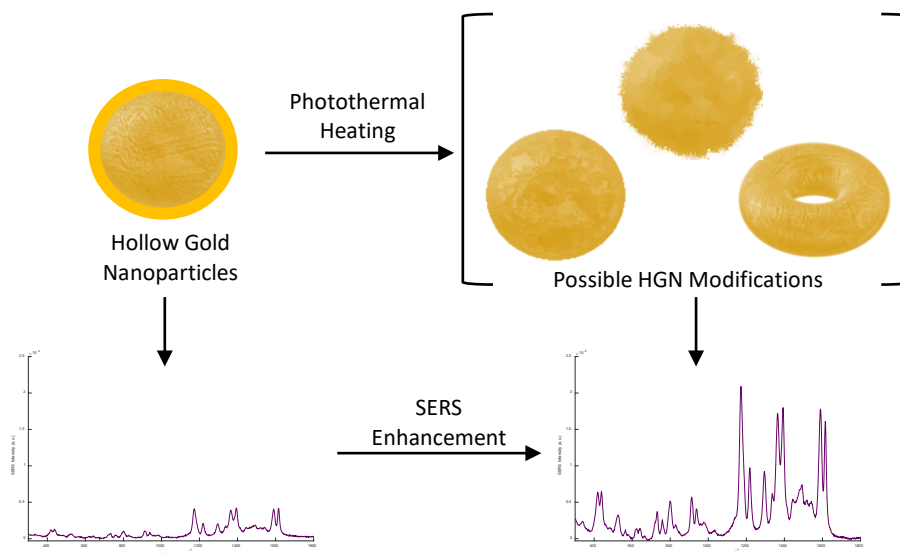

Figure 5.1 – Schematic showing the HGN modification as a result of photothermal heating. The intensity of the SERS signal obtained from the unheated HGNs is significantly lower than after they have been subjected to the photothermal conversion process.

5.2 Aims

The previous chapter showed that HGNs can be used to enhance the Raman signal of Raman reporter molecules. This chapter will investigate the effect of the photothermal effect with respect to the SERS signal observed. Four Raman reporters were studied: malachite green isothiocyanate (MGITC), 4-(1H-pyrazol-4-yl)pyridine (PPY), 2-mercaptopyridine (2-MPY) and benzenethiol (BT). Multiple hypotheses are proposed to explain the increase in SERS signal obtained, with the 'adatom' model being the probable cause.

5.3 Results & Discussion

5.3.1 Initial Observations of the SERRS and Photothermal Relationship

When investigating the release of molecules from the metal surface during plasmonic heating, an increase in the SERRS signal was instead observed as the HGNs were heated. At first considered an error, multiple repeats of the experiment confirmed it was a reproducible phenomenon. Figure 5.2 shows the observed increase in MGITC SERRS signal compared to the control (unheated) sample as the heating time was increased from 30 to 60 minutes.
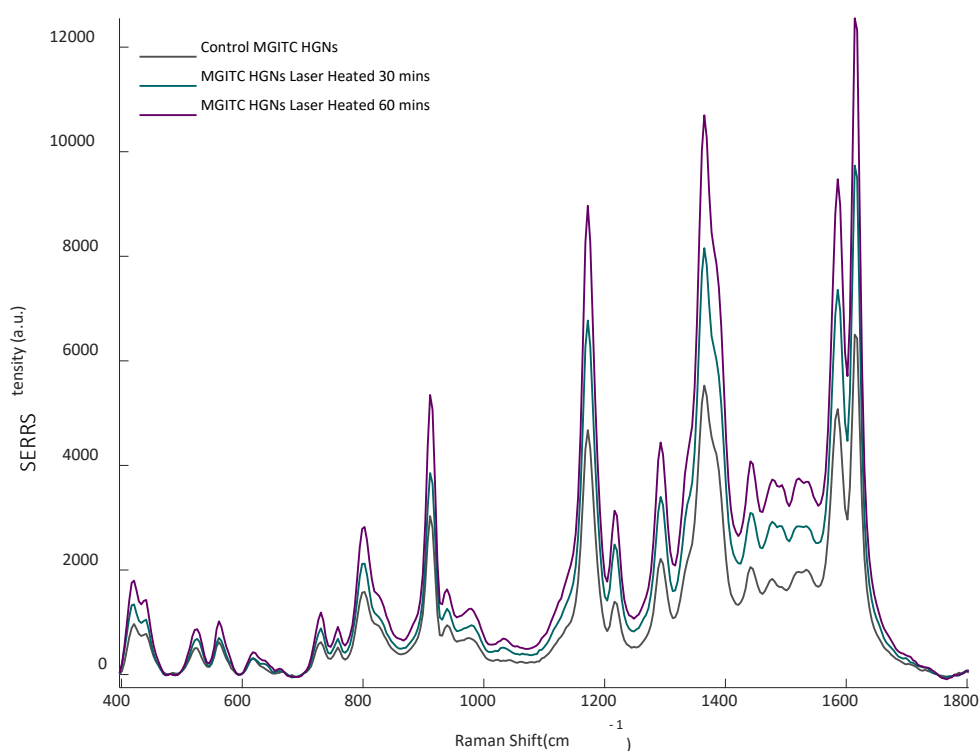

Figure 5.2 – SERRS spectra of MGITC-HGNs (0.1 μM final concentration) after 0, 30 and 60 minutes of laser interrogation. A CW 785 nm laser was used for inducing the photothermal conversion and a 532 nm (100 mW) excitation laser in a plate reader was used for collecting the SERRS spectra. Triplicate spectra were collected using 50% laser power for 0.5 second, 520 cm^{-1} centre with 150 μL of each sample in a 96 well plate.

Although interesting, this created a problem for the hypothesis being investigated at the time. The release of molecules from HGNs by heating has already been reported in many drug delivery studies[94-96], however, it was thought that Raman spectroscopy could be used to track their release from the surface. It was hypothesised that as

heating continued, the SERRS signal would decrease and if the supernatant was also analysed, the Raman reporter signal would increase in correlation. However, the previously unseen increase in SERRS signal obscured the expected results and if molecules were being released from the HGN surface, it was impossible to interpret this in the results.

5.3.2 Influence of Heat Source (Laser vs Heat block)

It was important to investigate whether the increase in SERRS signal was a direct consequence of the laser interrogation generating plasmonic heating or related to the bulk increase in temperature. To do this, MGITC-HGN samples were subjected to heating either by a 785 nm laser (280 mW) or a heat block. Figure 5.3 shows the average bulk heating profiles obtained when heated by the two sources.
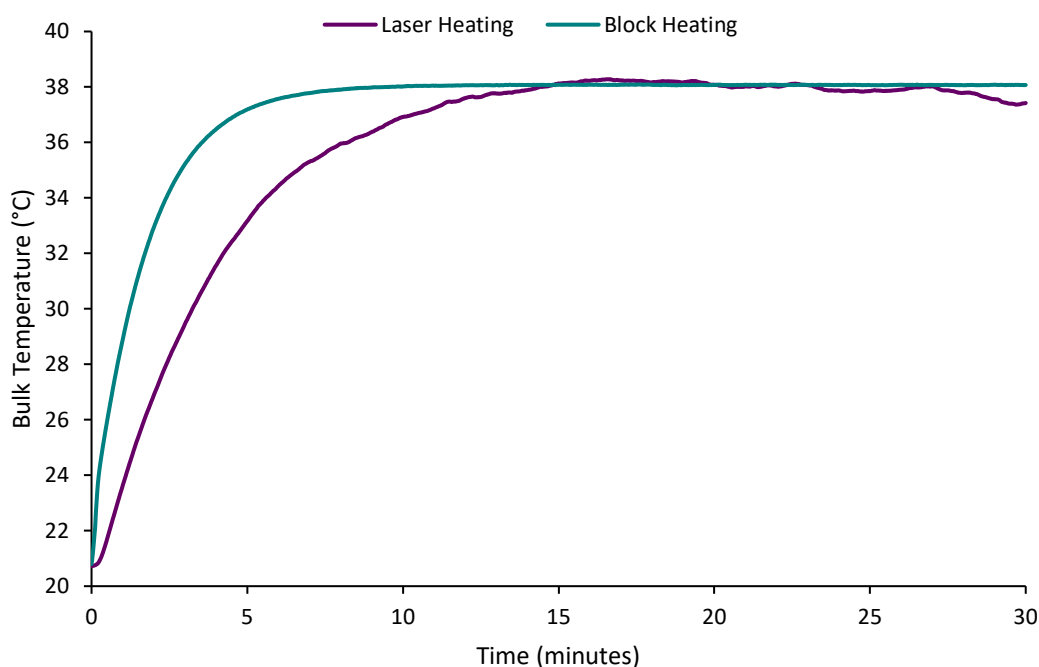

Figure 5.3 – Bulk heating profiles of bare HGNs using a 785 nm laser (purple) and a heat block set at 38°C (teal). The curves are the average of triplicate experiments.

As shown in the heating profile, by setting the heat block to 38°C, the bulk temperature of the HGNs was comparable to that of the samples interrogated with the laser for 30 minutes. Both samples reached a maximum bulk temperature of ≈38°C, with the heat block samples maintaining a steadier bulk temperature as seen

in the smoother heating profile. The maximum bulk temperature was also reached quicker in the heat block sample than in the laser heated sample. This is likely due to the more efficient heat transfer from the block through the glass vial to the sample in comparison to the heat dissipation from the HGN surface during the photothermal conversion process.

The extinction spectra after heating, shown in Figure 5.4, were interesting in that even though both samples reached a similar bulk temperature, their resulting extinction spectra differed. The samples heated by the block, showed a very similar extinction spectrum to the control samples which underwent no heat treatment. As expected, and as seen in the previous chapter, the HGNs heated with the laser experienced a blue shift of ≈45 nm compared to the control. This indicated that the plasmonic interaction with the laser was capable of changing the HGN extinction properties and that raising the bulk temperature of the sample does not lead to the same result.
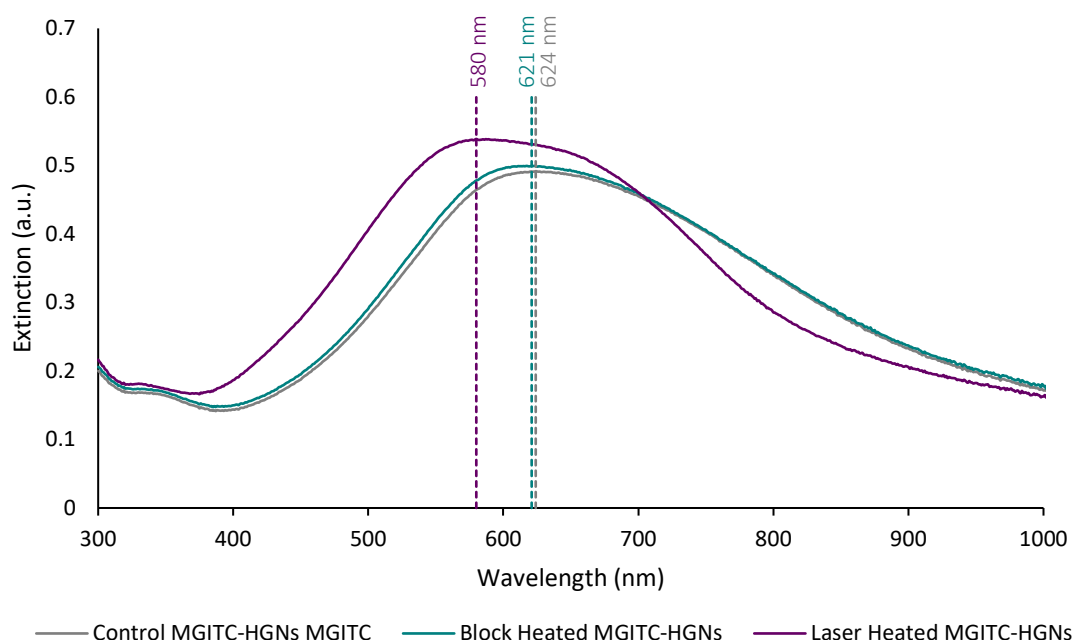

Figure 5.4 - Extinction spectra of control HGNs (grey), HGNs heated in the heat block (teal) and HGNs heated with a 785 nm laser at 278 mW, each for 30 minutes. Samples were analysed at a 1 in 2 dilution in water. Spectra shown are the average of triplicate experiments and triplicate measurements collected on a baselined fast scan rate (4800 nm/min, 1 nm intervals).

Since the extinction spectra has contribution from scattering and absorption, it would be expected that the SERS spectra would differ between the heat block and laser heated sample, given that Raman is a scattering event. Figure 5.5(a) shows the average SERS spectra before and after heating with each heat source.
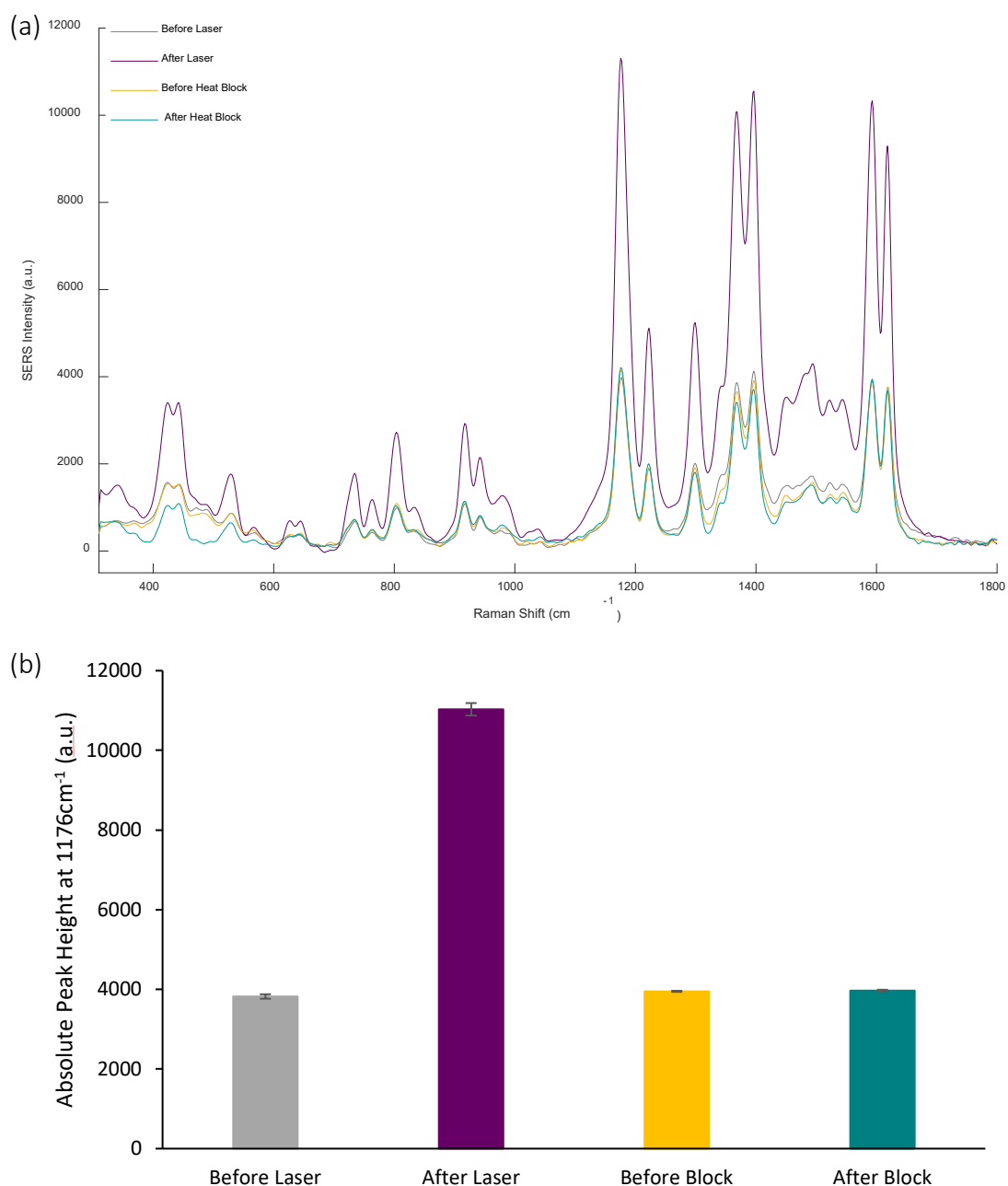

Figure 5.5 – (a) SERS spectra of MGITC-HGNs before and after heating with either the heat block or a 785 nm laser. Laser heating with a CW 785 nm excitation at 278 mW for 30 minutes. Triplicate spectra obtained with a 785 nm excitation laser (30 mW), 1s acquisition. Data processed using MATLAB: subtraction of a glass and bare HGNs background, baseline applied, smoothed, and 3 experimental reps were averaged before plotting. (b) Absolute peak height of the in-plane benzene bending peak seen at 1176 cm^{-1}. Peak height calculated by subtracting a baseline value at 1080 cm^{-1} from intensity at 1176 cm^{-1}. Error bars are the standard deviation of triplicate experiments.

The spectra from before laser heating, before block heating and after block heating overlay, indicating very little difference in the Raman scattering from the HGNs in these samples. However, the MGITC SERS spectra post heating with the laser source was significantly more intense than the other three spectra. Figure 5.5(b) highlights this by comparing the absolute peak height at 1176 cm^{-1}, a peak assigned to the in-plane bending of the benzene ring in MGITC.[89] The differences in spectral intensity indicated that the laser interrogation was the cause of the SERS increase and not the bulk temperature increase. An interaction existed between the laser and the HGNs causing a change in the optical properties, which lead to the different spectroscopic properties of the nanoparticles observed.

5.3.3 Time Interval Study with Malachite Green Isothiocyanate (MGITC)

As a well characterised Raman reporter, MGITC was used to study the relationship between the SERS signal observed and laser exposure. Characterisation of the HGNs after continuous laser interrogation for 60 minutes was compared to the control samples that underwent no heating.

5.3.3.1 Heating Profiles & Extinction Spectra

Figure 5.6 shows the heating profiles and extinction spectra collected before and after laser exposure. The heating profiles of each sample were as seen previously. Additional controls were included in experiment to show the effect of the two different laser systems. The grey heating curve shows the influence of the SERS laser only (CW 30mW, switched on for 10 seconds every 5 minutes), and there is no noticeable increase in bulk temperature. This constant bulk temperature indicates the SERS laser does not contribute to the photothermal process, a result of the low power and short acquisition time used.

The heating laser only (purple curve – CW 280 mW on for full 60 minutes) and SERS & heating laser (teal curve – both laser parameters described previously) follow the same profile and reach similar maximum temperatures. The difference is the steps observed every 5 minutes, this is a result of the heating laser shutter being closed

while the SERS measurement was taken. This method was investigated in another experiment, with Figure 9.3 in the appendix showing the interference of the heating laser to the detection of the Raman reporter. When only the heating laser is on, 90° Raman scattering can be collected by the detector positioned perpendicular to the heating laser beam. Hence the shutter was momentarily closed to record the Raman spectra without any contribution from the heating laser, resulting in the slight drop in temperature as seen in the step profile.
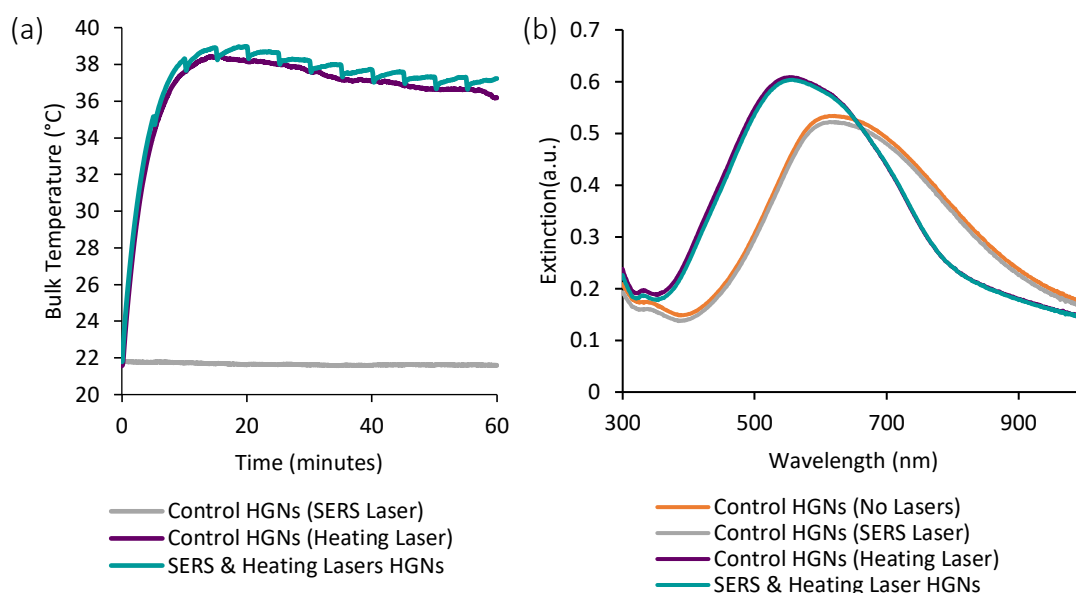

Figure 5.6 – (a) shows the average temperature profiles of each sample, when measured for 60 minutes. (b) shows the extinction spectra of HGNs each with a different laser treatment, measured at a 1 in 2 dilution in water. Spectra shown are the average of triplicate measurements collected on a baselined fast scan rate (4800 nm/min, 1 nm intervals).

The extinction spectra also supported the theory that the SERS laser had little contribution to the photothermal conversion process. The SERS laser only spectrum (grey) overlay the control spectrum (orange) which did not undergo any heating treatment. This confirmed the SERS laser was not at a high enough power or on for long enough to contribute to the photothermal process. The extinction spectra of the heating laser only (purple) and the SERS and heating laser (teal) also overlay. This was expected given the similar heating profiles, and indicated the shutter of the laser shutter did not influence the changes that occurred during the photothermal conversion process. The samples heated with the laser show a characteristic blue shift

of ≈75 nm, a larger shift than observed in Figure 5.4. However the HGNs were heated for an hour in this experiment, double the time previously studied, so it is not surprising they blue shifted further. Again it was observed that the samples changed colour from blue to light purple after plasmonic heating.

In a previous experiment, it was shown that the SERS laser had no effect on the spectral intensity over time. The spectra collected from the SERS laser only samples showed no changes in peak height over time as shown in Figure 9.4 in the appendix, again indicating no influence from the SERS laser to the photothermal process. Figure 5.7 shows the spectra collected from the SERS and heating laser samples, where spectra were collected every 5 minutes for 1 hour.
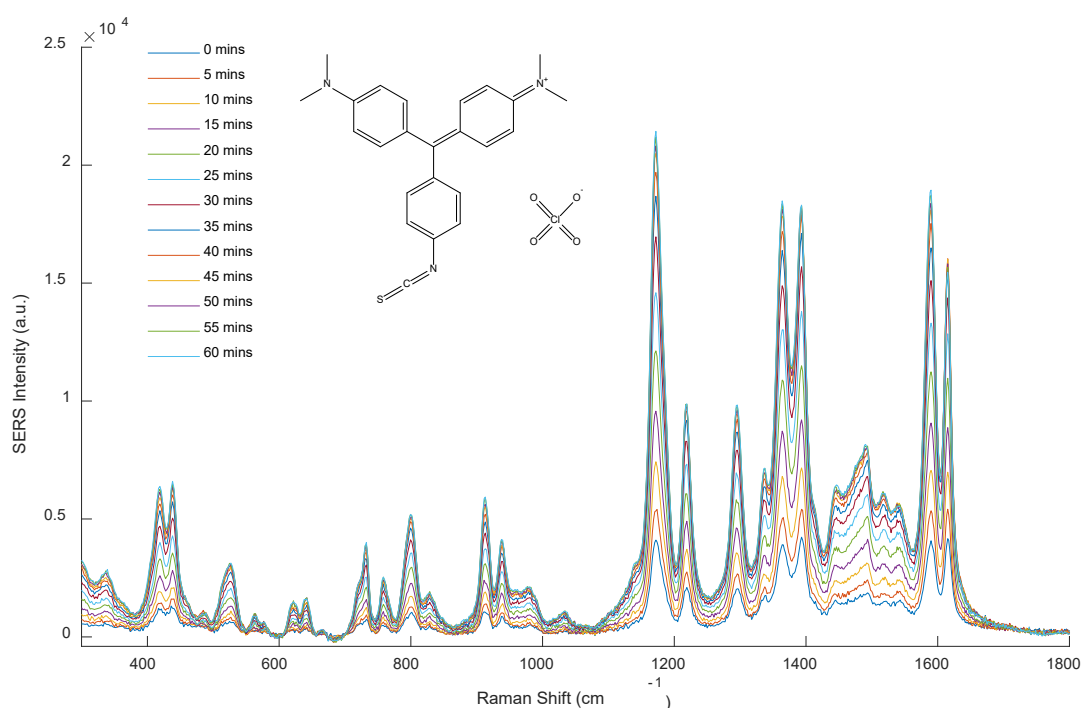

Figure 5.7 – SERS spectra of MGITC-HGNs collected every 5 minutes for 1 hour while interrogating with a 785 nm laser (278 mW). Spectra were collected using a 785 nm excitation (30 mW) source, 1s acquisition and 3 measurements at each time point. Data processing using MATLAB: subtraction of a glass and bare HGNs background, baseline applied, and 3 experimental reps were averaged before plotting.

There was a steady increase in all peak heights as the laser exposure time increased. The spectra collected at later time points showed less of an intensity increase compared to the previous time interval as shown in Figure 5.8, eventually leading to a plateau in peak height with the last few spectra overlaying. This suggested the change

that the laser induced on the nanoparticle surface had reach its maximum effect after 45 minutes, and further heating would not lead to more intense SERS spectra being observed. The intensity of the peak at 1172 cm^{-1}, which is assigned to the in-plane bending of the benzene rings within the MGITC structure, was plotted as a function of time in Figure 5.8, showing the increase in peak height as the heating time progressed. Intially the trend is linear, however after 45 minutes, the peak height begins to plateau. The factor by which the peak had increased is tabulated to the right of the figure. This value was calculated by dividing the absolute peak height at each time interval by that at time 0 before any heating was applied. After 1 hour of laser exposure the MGITC spectra had been enhanced over 5 fold.
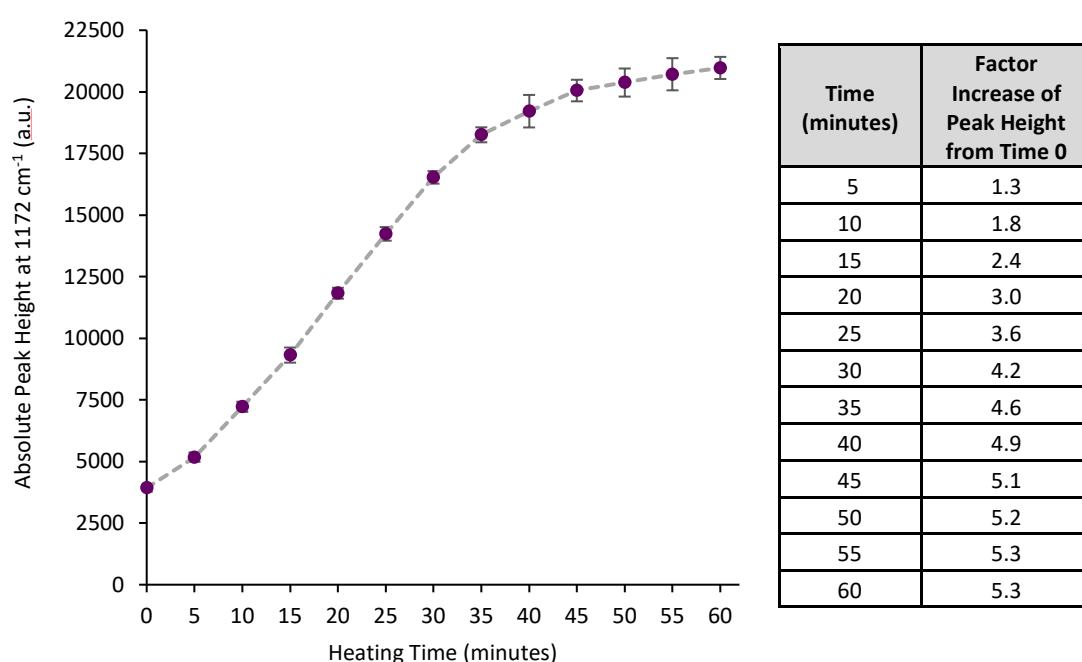

Time (minutes)	Factor Increase of Peak Height from Time 0
5	1.3
10	1.8
15	2.4
20	3.0
25	3.6
30	4.2
35	4.6
40	4.9
45	5.1
50	5.2
55	5.3
60	5.3

Figure 5.8 – Absolute height of the in-plane benzene bending peak seen at 1172 cm^{-1} at each time interval. Peak height calculated by subtracting a baseline value at 1080 cm^{-1} from the intensity at 1172 cm^{-1}. Error bars are the standard deviation of triplicate experiments. The table shows the factor increase in this peak at each time point in respect to the intensity at Time 0 before any plasmonic heated had been applied.

In the literature there are examples of using lasers to induce an increase in SERS of a Raman reporter molecule adsorbed onto a gold film.[134] However, the increase in signal is a result of the gold nanoparticles on the silicon substrate annealing under the influence of the high power pulsed lasers used. To date, no examples of increasing SERS with plasmonic heating in solution have been published.

It should also be noted that there is no correlation between bulk temperature and the SERS signal observed. Figure 5.9 overlays the data shown in previous figures, with the bulk temperature and SERS intensity of the 1172 cm^{-1} peak plotted against time.

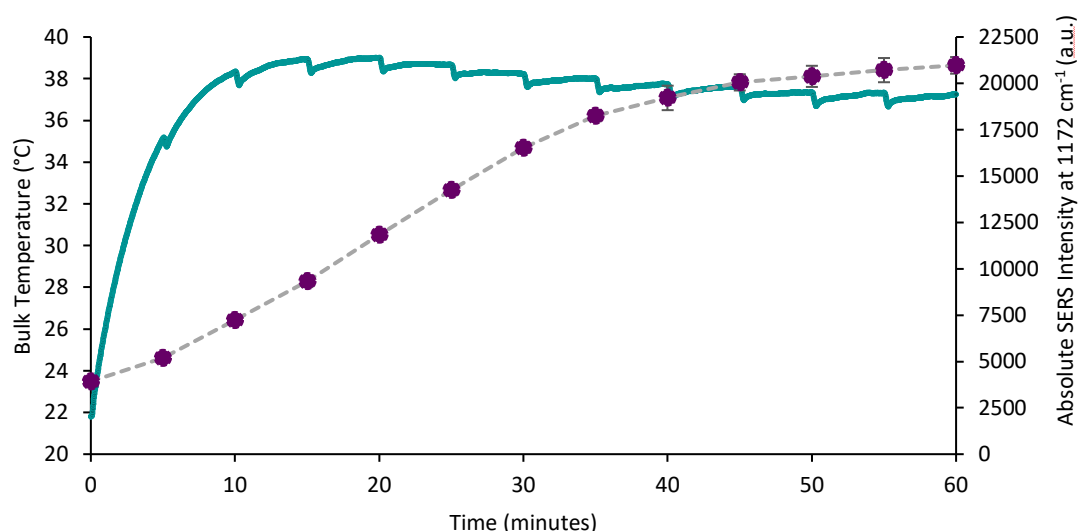Figure 5.9 - Overlay plot of the heating profile and the increase in SERS intensity of the peak at 1172 cm^{-1} against time. No correlation is observed between the increase in bulk temperature and increase in SERS response.

The lack of correlation between these two properties indicated that the bulk temperature did not influence the SERS signal observed, and is an independent property of the sample. To investigate this hypothesis further, the cooling of the samples post heating was investigated.

5.3.3.2 Temperature Dependence on the SERS Increase

The spectra collected at time 0 before any heating, after 60 minutes of heating and once the sample had returned to room temperature were compared to observe any spectral changes. Figure 5.10 shows the average spectra of each time point investigated, with the spectra collected after 60 minutes heating and at room temperature almost being identical. After cooling, the SERS spectra intensity did not return to that obtained before heating. This indicated that the phenomenon was not a reversible process and that there was a permanent physical change to the HGNs. It can be concluded that the bulk temperature of the sample did not affect the SERS signal observed since comparable spectra were collected when the sample was ≈38°C and when at room temperature.
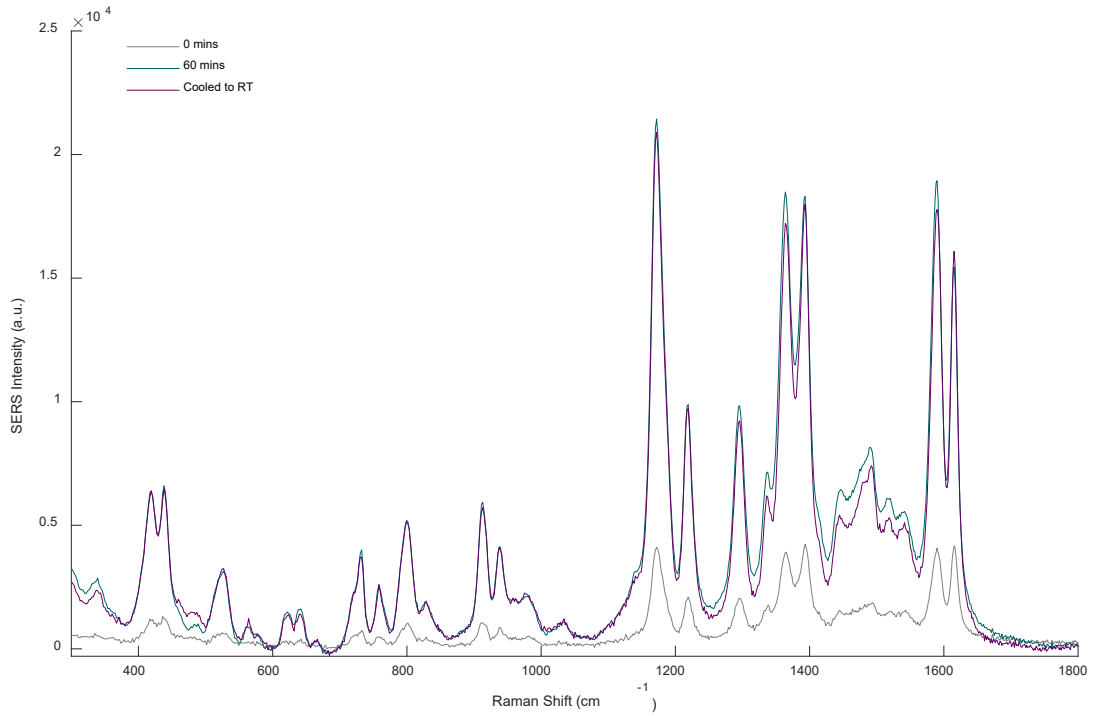
Figure 5.10 - SERS spectra of MGITC-HGNs collected at time 0, after 60 minutes of plasmonic heating and once cooled to room temperature. Spectra were collected using a 785 nm excitation (30 mW) source, acquisition 1s and 3 measurements at each time point. Data processing using MATLAB: subtraction of a glass and bare HGNs background, baseline applied, and 3 experimental reps were averaged before plotting.

5.3.3.3 Dynamic Light Scattering Measurements

Dynamic light scattering (DLS) measures Brownian motion and relates this to the size of the particles in the sample. It was originally thought that the laser interrogation may be shrinking the HGNs to smaller nanoparticles with thicker shells. If the size was changed after heating, this should be detectable using DLS. This is because the size and scattering ability of the nanoparticles are related. The intensity of the scattered light fluctuates over time, allowing the diffusion coefficient (D) to be obtained. Then using the Stokes-Einstein equation, the hydrodynamic radius (R_h) of the particles can be calculated. This relationship is shown in Equation 5.1, where k_b is the Boltzmann constant, T is the temperature and η is the viscosity of the medium.[135]

Equation 5.1 - Stokes-Einstein equation.

$$D = \frac{k_b\, T}{6\pi\, \eta\, R_h}$$

104

It is known that small particles diffuse faster, with larger particles diffusing more slowly. Larger particles also scatter more than smaller particles, and more in a forward angle, with small particles scattering more evenly in all directions. Therefore with the configuration of the DLS instrument used, larger particles are detected more at smaller angles. Figure 5.11 shows the average hydrodynamic size of the particles measured through a range of angles (50-140 θ) between the laser and the detector.
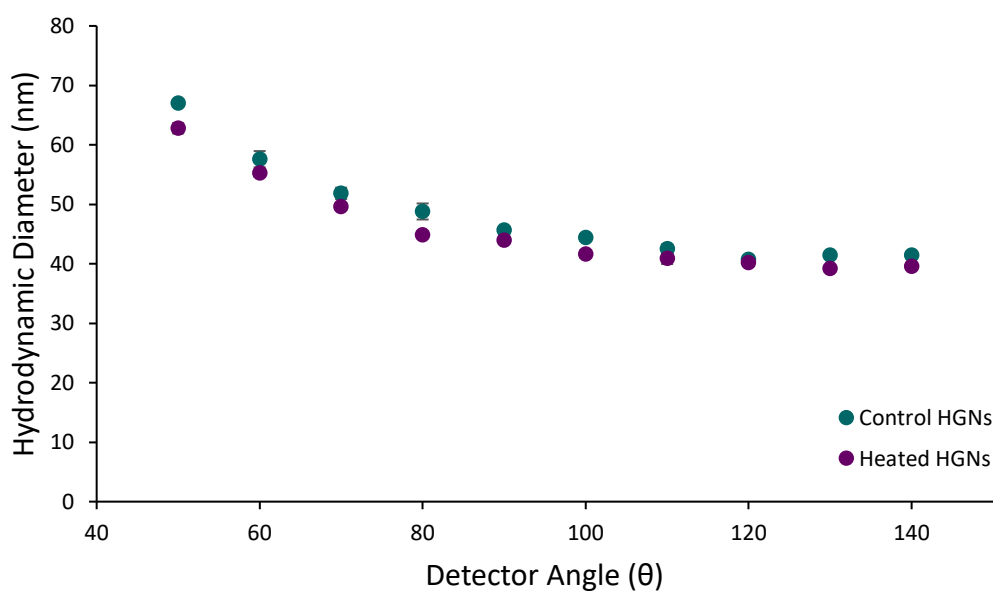

Figure 5.11 – Hydrodynamic sizes of the HGNs measured through 50-140 θ. Teal data points represent the control samples that underwent no heating treatment. The purple data set represents the average measurements of the laser interrogated MGITC-HGN samples presented previously in this chapter.

The sizes obtained from measuring through a range of detector angles, shows a distribution from ≈40-70 nm. It is known that that the HGN synthesis method is relatively crude compared to other methods and so it is not surprising there is slight polydispersity in the sample. Smaller particles with a calculated sizes of ≈2-5 nm were also detected, but not shown in the figure for clarity. These often appear in colloidal systems and do not tend to be an issue for SERS applications since particles this small are poor Raman scatters.

Through all detector angles, there is little change in the size between the control and heated samples, thus suggesting that even with laser interrogation, the overall size of the particles remains similar. This is unexpected given the blue shift observed in the

extinction spectra shown in Figure 5.6(b), it was expected that the heated HGNs would differ in size from the unheated nanoparticles. Therefore the proposed morphological change must be more subtle than a complete reshaping, and small surface features are changed instead. This hypothesis is discussed later in the chapter.

The light scattering detected at each angle is shown in Figure 5.12, and has been normalised with respect to the instrument diode. It can be seen that through all angles, the heated HGN samples showed a greater ability to scatter the laser light than the control samples. The curve profile of both datasets is unexpected since it is known that smaller particles are detected more at large detector angles and they are also inherently poorer Raman scatters. Therefore it could be suggested that they were present in the samples in large numbers to cause the increase in the normalised count rate obtained. However, the trend of interest is that the plasmon heated HGNs scatter more intensely than the control samples through all angles investigated. This correlates with the SERS data previously presented, as the more efficiently a nanoparticle can scatter light, the more intense the resulting Raman spectrum will be.
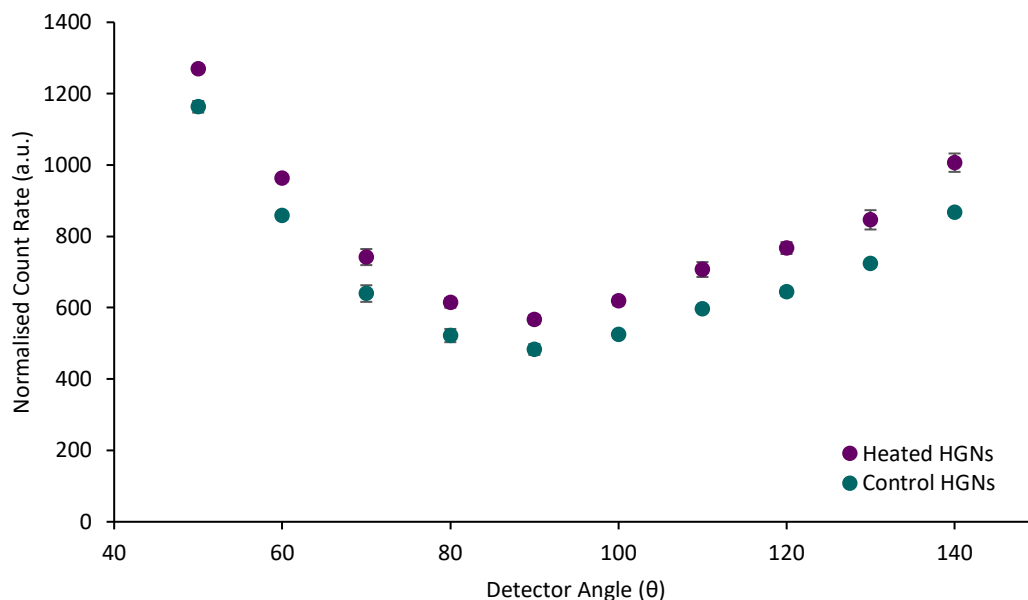

Figure 5.12 - Dynamic Light Scattering measurements showing the heated HGNs (purple) and untreated HGNs (teal). The light scattering of each sample was detected through a range of angles from 50-140 θ. The count rate at each angle was normalised with respect to the monitor diode.

Nanoparticle tracking analysis (NTA) is a similar technique that utilises the light scattering and Brownian motion of particles to obtain a size distribution of the sample. A video camera fixed to a microscope captures a video of the particles moving under Brownian motion. The NTA software is able to track the particles individually as they move around the video frame. Then using the Stokes-Einstein equation the hydrodynamic diameters are calculated. Figure 5.13 shows the output of the NTA analysis, with all three heated samples and the control showing very similar results.
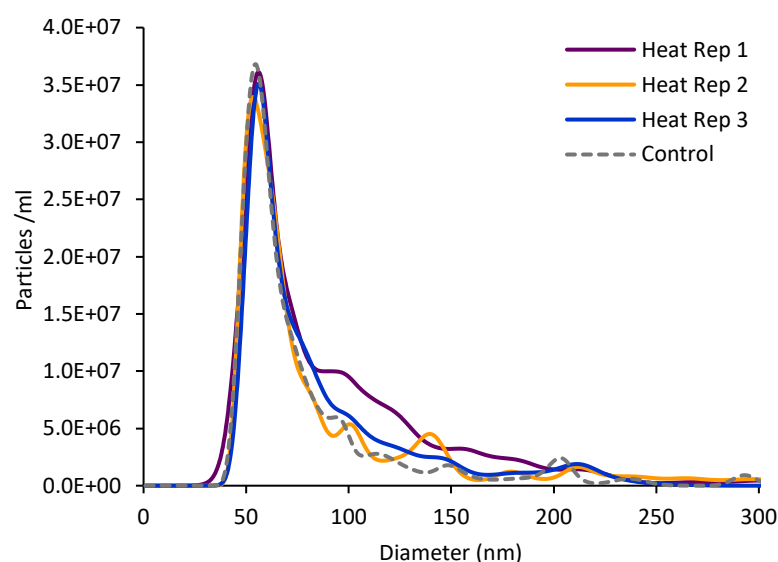

Figure 5.13 – Nanoparticle tracking analysis showing the nanoparticle diameter and correlating particle concentration.

The heated samples had an average hydrodynamic size of 72 nm with the control being 68 nm. The slight size increase could be caused by some larger aggregates in the samples of the heated samples, as is suggested in the longer tails after the main peak in the size distribution plot. Again, there is no large difference in average size between the control and heated samples, suggesting the changes induced by the photothermal effect are too subtle to be identified using DLS or NTA, therefore TEM analysis was implemented to provide a more definitive analysis of the morphology after heating.

5.3.3.4 Transmission Electron Microscopy

TEM was used to investigate the effect of the laser irradiation on the HGN morphology, Figure 5.14 overleaf shows representative images of each sample. The images show that the particles are hollow, indicated by the contrasting grey regions. This is a result of the different densities of the gold shell being bombarded with electrons during imaging. Both samples are heterogeneous and there exists some incomplete gold shells and some examples of toroidal HGNs. These are present in both the control and heated samples, and therefore most likely a product of the synthesis, not the laser.

No obvious differences were observable between the samples, which again suggests the effect of the laser interrogation is smaller and more subtle than can be observed with normal TEM. Perhaps high resolution TEM or small angle X-ray scattering (SAXS) would reveal more about the morphological change. The latter is a technique capable of extracting nanoscale data from a sample, e.g. nanoparticle size and shape and even pore sizes.

Characterisation of the MGITC-HGNs post heating showed a blue-shift in the LSPR to lower wavelengths but surprisingly very little observable morphological change in the TEM images were seen. At this stage, the effect of the photothermal conversion on the HGNs was not properly understood, therefore other Raman reporters were studied to decipher whether the effect was confined to changes in the MGTIC molecule or if the phenomena could be transferred to other Raman reporters. The investigation included Raman reporters with different structures and Au binding modes (isothiocyanate, thiol and pyridyl ring interaction), and all Raman reporters gave a similar increase in SERS trend with laser heating.

The studies also provided the characteristic blue shift of the LSPR after heating and no significant changes to the SERS intensity once the sample returned to room temperature. To keep these results concise, only the time interval SERS spectra and plot of the peak increase are shown for each of the Raman reporters. The additional investigations lead to a compilation of theories which are discussed after the subsequent datasets.
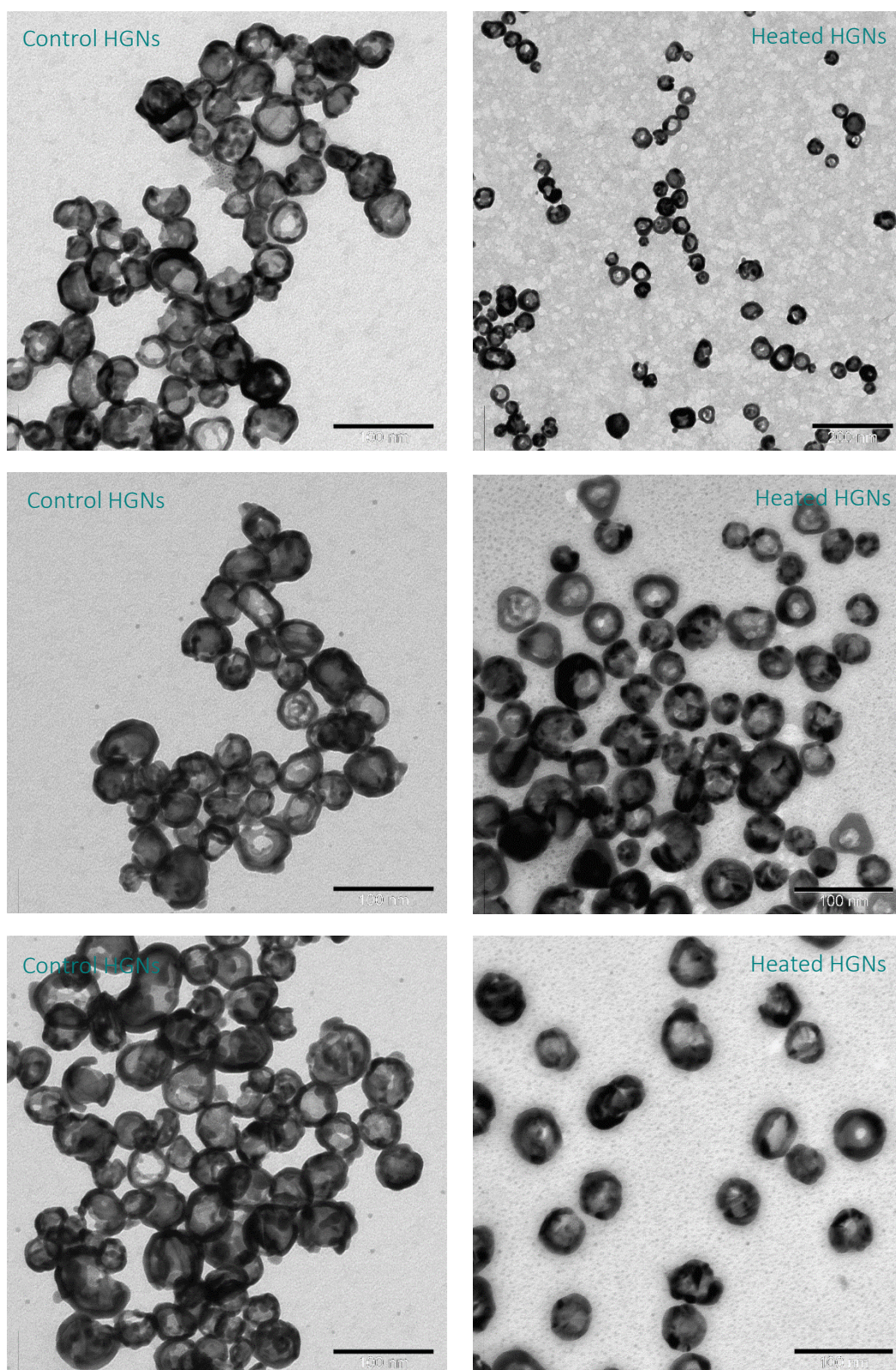
Figure 5.14 – Transmission electron micrographs of control (untreated) HGNs on the left and heated HGNs on the right. Scale bar in each is 100 nm except the top right image which is 200 nm.

5.3.4 Time Interval Study with 4-(1H-pyrazol-4-yl)pyridine (PPY)

4-(1H-pyrazol-4-yl)pyridine (PPY) is a non-resonant Raman reporter that is expected to bond to the HGN surface via the pyridyl ring N atom. Figure 5.15 shows the reference solid bulk Raman spectra of the reporter and the molecular structure.
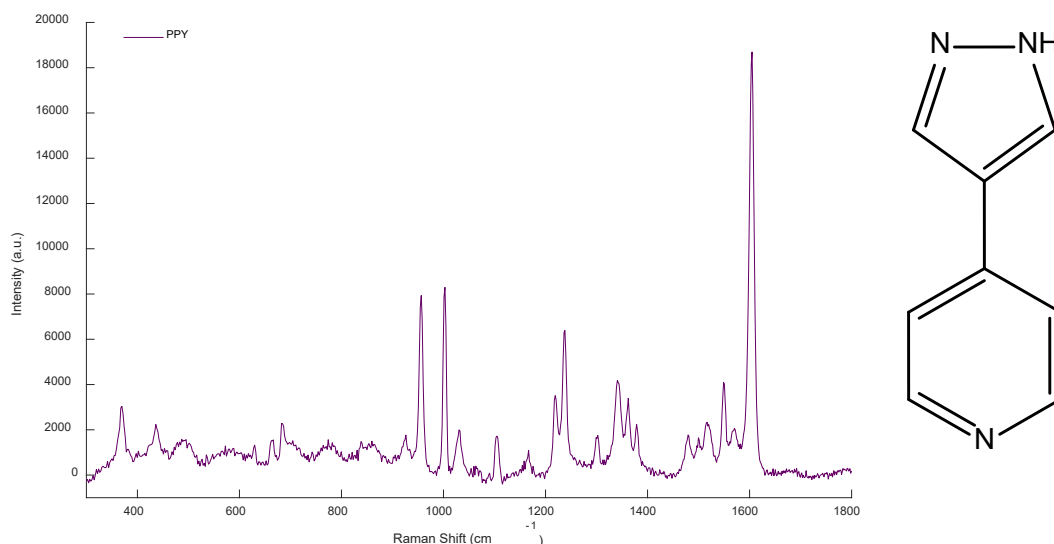

Figure 5.15 – Reference Raman spectra of solid PPY collected using a 785 nm excitation laser (30 mW for 50 ms). Molecular structure of PPY shown to the right of figure.

A time interval SERS study was carried out by heating PPY-HGNs under the same experimental parameters as for the MGITC study. From the results shown in Figure 5.16, it is noted that several peaks are shifted slightly from the reference spectrum, changes most likely due to the bonding interaction between the PPY and the nanoparticle surface. These small deviations indicate the structure of the PPY on the HGNs is different to when in the solid state. When a molecule is chemisorbed onto a metal surface, the molecular and metal orbitals overlap, changing the band positions and relative intensities.[136] If the peaks had been identical to the reference spectra, it would indicate the reporter was physisorbed instead. The peaks associated with the pyridyl group should be visible and enhanced in the SERS spectra if this mode of binding is correct. One of the associated peaks lies ≈1600 cm^{-1} and arises due to the aromatic C-C/N stretching, an intense peak in this position is visible in the SERS spectra.[136]
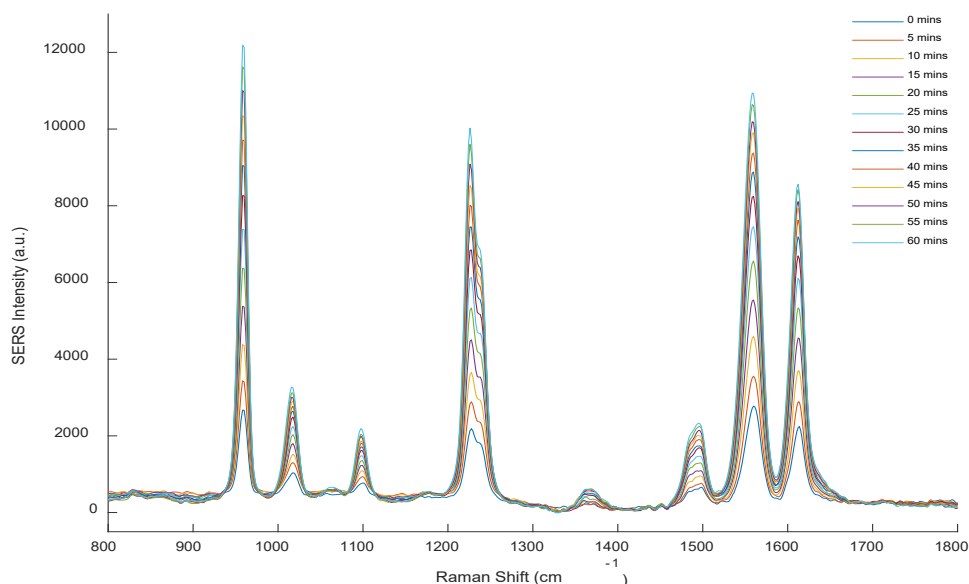
Figure 5.16 - SERS spectra of PPY-HGNs collected every 5 minutes for 1 hour while interrogating with a 785 nm laser (280 mW). Spectra were collected using a 785 nm excitation (30 mW) source, 1s acquisition and 3 measurements at each time point. Data processing using MATLAB: subtraction of a glass and bare HGNs background, spectral range cut, baseline applied, spectra smoothed and 3 experimental reps were averaged before plotting.

By focussing on a peak shifted away from where the glass background often interfered with the spectra ($\approx$1400 cm^{-1}), the increasing signal intensity was investigated. Figure 5.17 shows the increase in the peak at 959 cm^{-1} as a function of heating time. Similar to before, the trend is fairly linear, showing an increase in the SERS intensity as each time interval passed. Unlike MGITC-HGNs, the peak height had not plateaued after the 60 minutes of heating, suggesting further signal enhancement was possible. However for a comparable experiment, the heating time remained fixed at 60 minutes across all experiments. Reasons as to why the rate at which the SERS signal increases is discussed fully once all four Raman reporter studies have been presented.
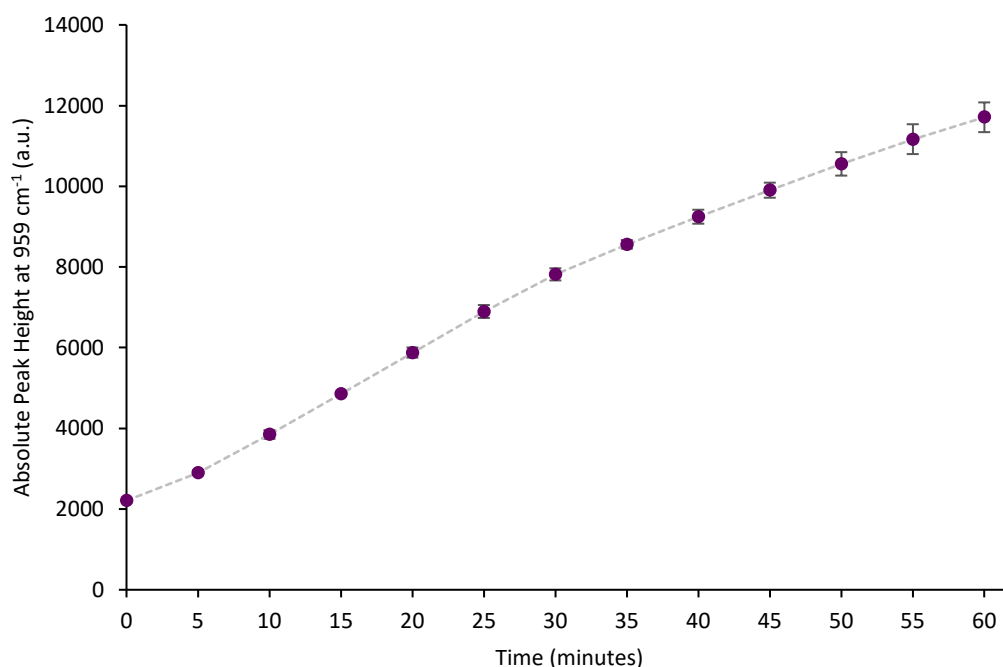
Figure 5.17 - Absolute height of the 959 cm^{-1} peak at each time interval. Peak height calculated by subtracting a baseline value at 930 cm^{-1} from the intensity at 959 cm^{-1}. Error bars are the standard deviation of triplicate experiments.

5.3.5 Time Interval Study with 2-Mercaptopyridine (2-MPY)

2-mercaptopyridine (2-MPY) is another non-resonant Raman reporter that is expected to bond to the HGN surface either via the thiol group or N atom. Figure 5.18 shows the reference Raman spectra of the reporter and the molecular structure.
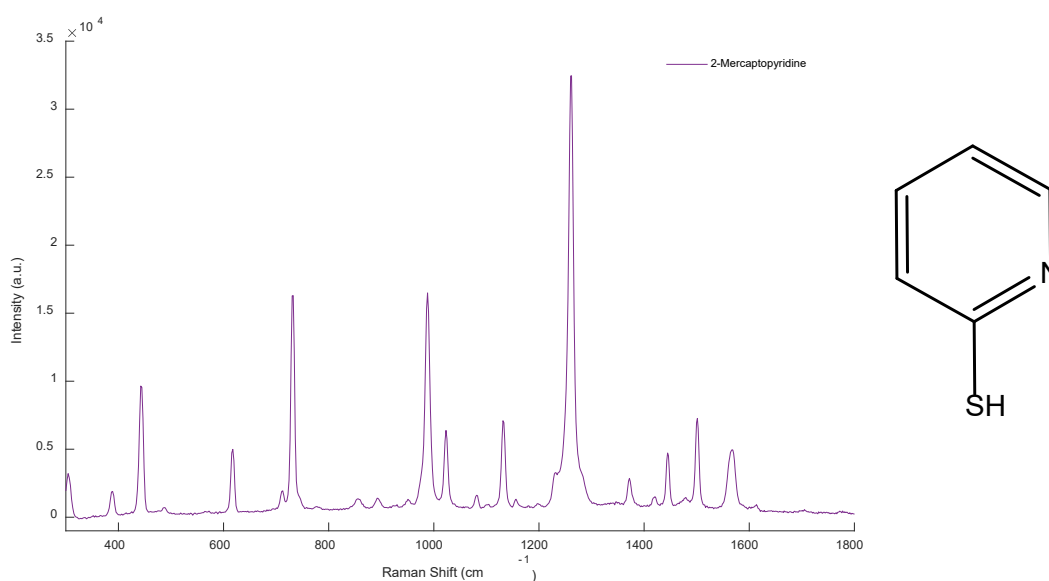

Figure 5.18 - Reference Raman spectra of solid 2-MPY collected using a 785 nm excitation laser (30 mW for 50 ms). Molecular structure of 2-MPY shown to the right of figure.

Theoretically, the Raman reporter could be adsorbed onto the metal surface by the sulfur or nitrogen atom or the π electrons of the ring. However if adsorption occurred through donation of the π-system, the plane of the aromatic ring would be parallel to the gold surface and therefore the peaks of the in-plane modes would be expected to show little enhancement. However, Figure 5.19 shows the time interval SERS spectra obtained from heating 2-MPY-HGNs, with the in-plane bending modes of the Raman reporter are enhanced. Do *et al.* assigned the in-plane bending modes of the ring (C-H) as 1050, 1083, 1117 and 1230 cm^{-1} when 2-MPY was on a silver substrate.[137] The spectra shown in Figure 5.19 have enhanced peaks at 1054, 1087, 1119 and 1233 cm^{-1} indicating 2-MPY does not adsorb through the ring structure. The enhanced peaks at 1007 and 1555 cm^{-1} can be assigned to the ring breathing and C-C/N stretching respectively, indicating these structures are also perpendicular to the metal surface.[137] These observations indicate that 2-MPY most likely adsorbed onto the HGN surface in a more upright orientation via the sulfur and/or nitrogen atoms.

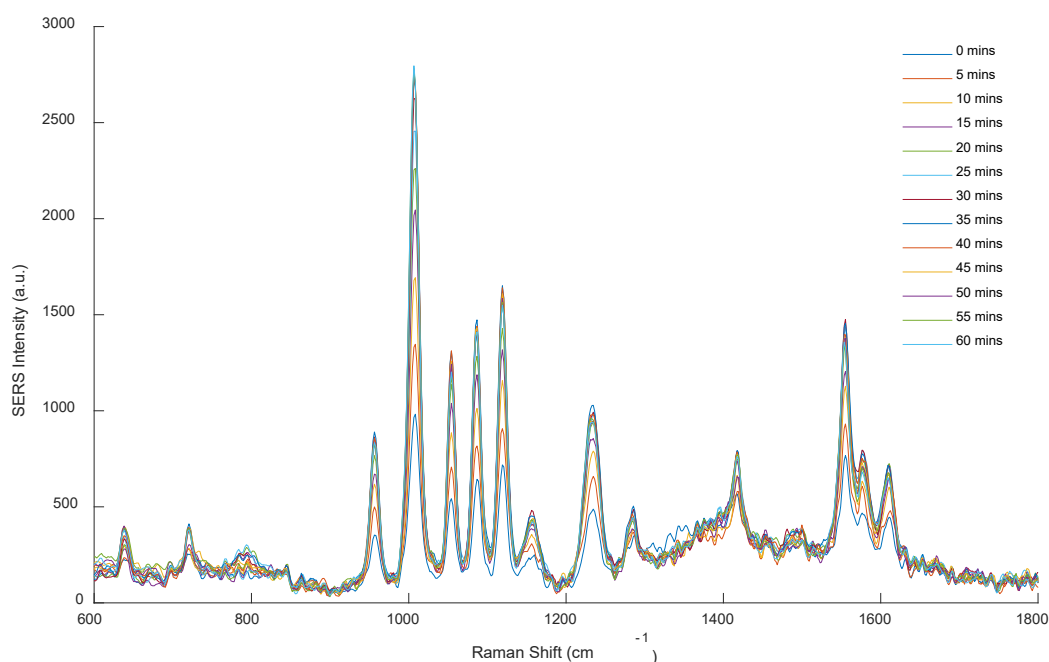Figure 5.19 - SERS spectra of 2-MPY-HGNs collected every 5 minutes for 1 hour while interrogating with a 785 nm laser (278 mW). Spectra were collected using a 785 nm excitation (30 mW) source, 1s acquisition and 3 measurements at each time point. Data processing using MATLAB: subtraction of a glass and bare HGNs background, spectral range cut, baseline applied, spectra smoothed and 3 experimental reps were averaged before plotting.

The increase in the peak at 1007 cm^{-1} as a function of heating time is shown in Figure 5.20. This time the trend begins linear, and then begins to plateau after 35 minutes of heating.
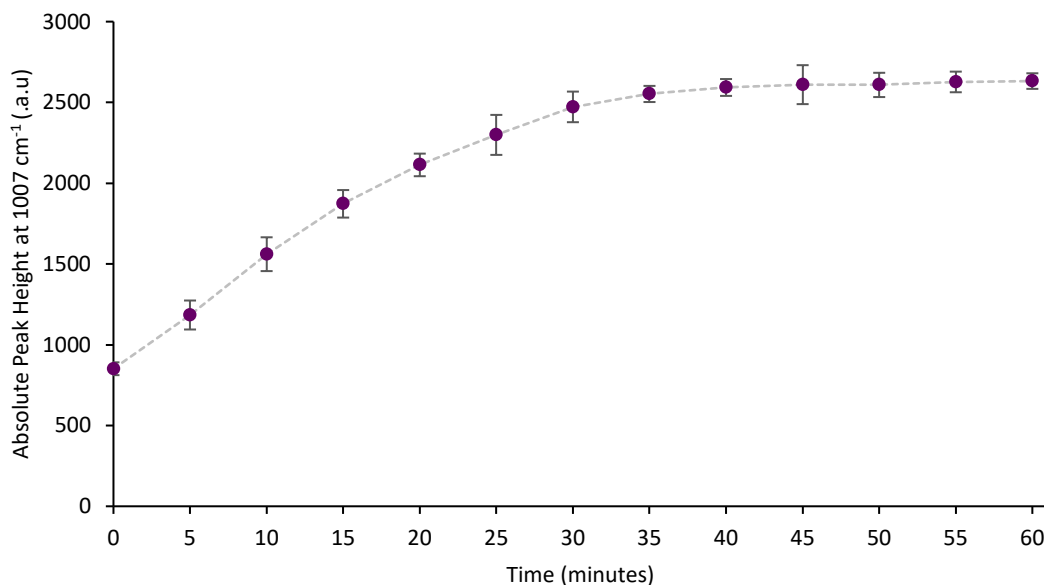
Figure 5.20 - Absolute height of the 1007 cm^{-1} peak at each time interval. Peak height calculated by subtracting a baseline value at 981 cm^{-1} from the intensity at 1007 cm^{-1}. Error bars are the standard deviation of triplicate experiments.

5.3.6 Time Interval Study with Benzenethiol (BT)

Benzenethiol (BT) is a non-resonant Raman reporter that is known to bond to a metal surface via the thiol group.[138] Figure 5.21 shows the reference Raman spectra of the reporter and the molecular structure.

Figure 5.21 - Reference Raman of neat benzenethiol collected using a 785 nm excitation laser (30 mW for 0.1 ms). Molecular structure of benzenethiol shown to the right of figure.

Fewer peaks are seen in the reference spectra than previous Raman reporters due to the small size and symmetry of the molecule. The peaks presen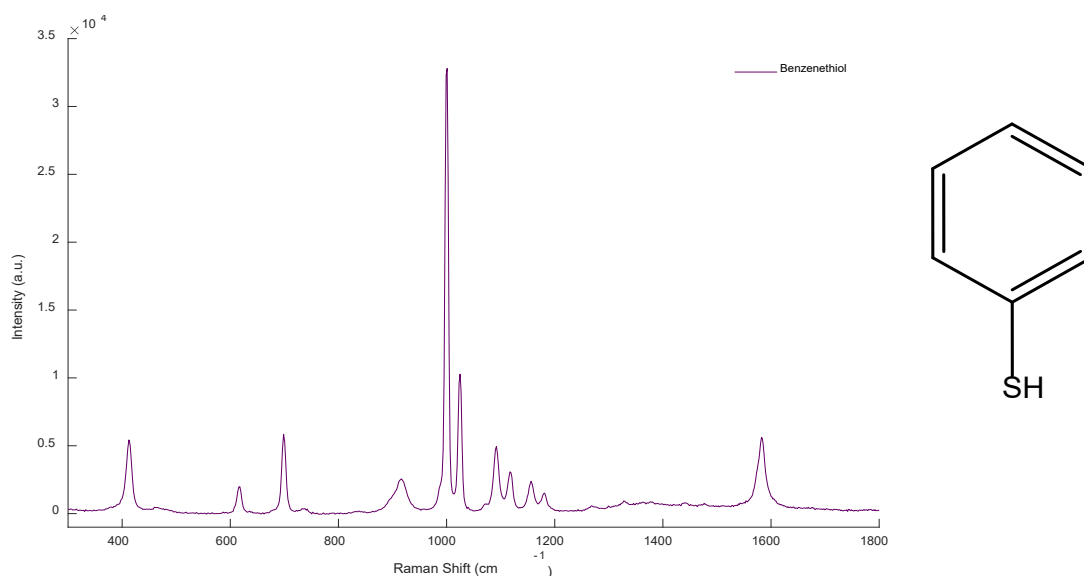t are in close alignment with those reported by Joo *et al.*, although a small number of peaks vary by a wavenumber or two, most likely due to differences in the spectral resolution of the spectrometers used.[138]

Figure 5.22 shows the SERS spectra obtained while heating the HGNs, with the peaks observed in close correlation with those previously reported.[138] There is a large enhancement of the peaks at 1074 and 1574 cm^{-1}, these have been assigned to the in-plane CCC bending/CS stretching and CC stretching modes respectively. This observation supports the binding method proposed. Upon binding, the S-H bond breaks, and the benzenethiolate anion adsorbs onto metal surface via the sulfur atom.
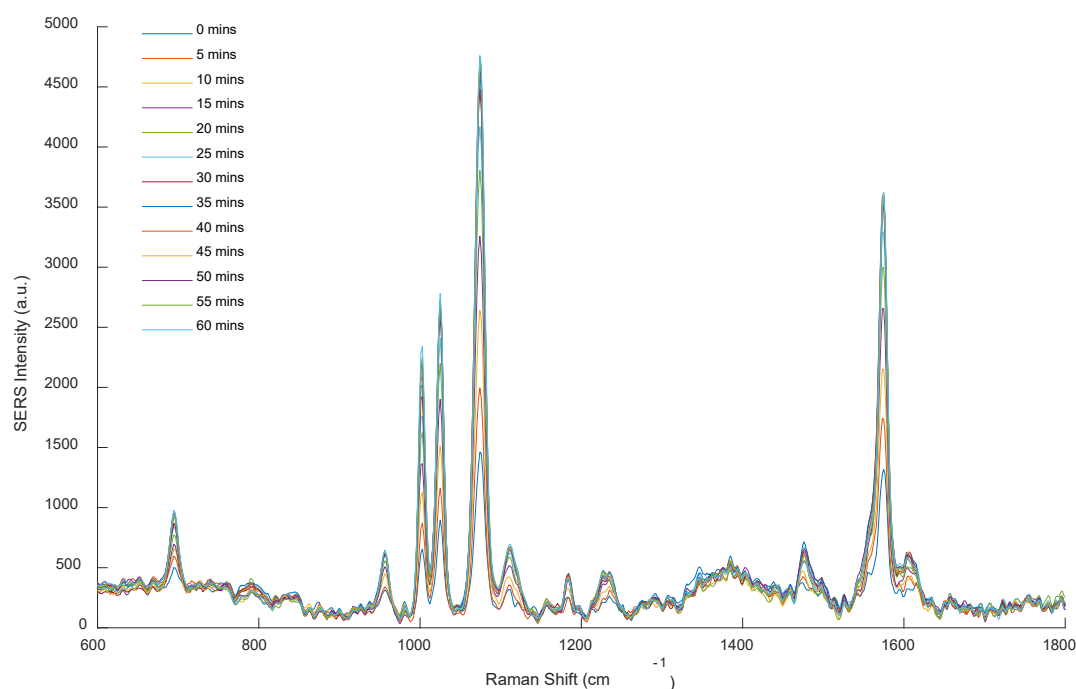
Figure 5.22 - SERS spectra of BT-HGNs collected every 5 minutes for 1 hour while interrogating with a 785 nm laser (279 mW). Spectra were collected using a 785 nm excitation (30 mW) source, 1s acquisition and 3 measurements at each time point. Data processing using MATLAB: subtraction of a glass and bare HGNs background, spectral range cut, baseline applied, spectra smoothed and 3 experimental reps were averaged before plotting.

Joo *et al* supported this binding mode by comparing the band frequencies of benzenethiol on AgNPs to that of the silver benzenethiolate salt.[138] The vibrational frequencies of the benzenethiol on AgNPs SERS spectra more closely correlated with those of silver benzenethiolate salt than of neat benzenethiol. The large enhancement

of the 1074 and 1574 cm^{-1} bands in Figure 5.22, indicate that these modes experienced a greater electromagnetic enhancement and therefore must have been perpendicular to the metal surface. Furthermore, the CS stretching mode at 1074 cm^{-1} was greatly enhanced compared to the reference Raman spectrum, indicating surface attachment through this group.

Similar to the other Raman reporters studied, the SERS intensity increases in correlation with increasing heating time. The absolute peak height of the intense peak at 1074 cm^{-1} was plotted with respect to heating time, as shown in Figure 5.23. A linear trend of increasing intensity was present, until around 30 minutes when the trend began to plateau and the peak height did not increase with further heating.
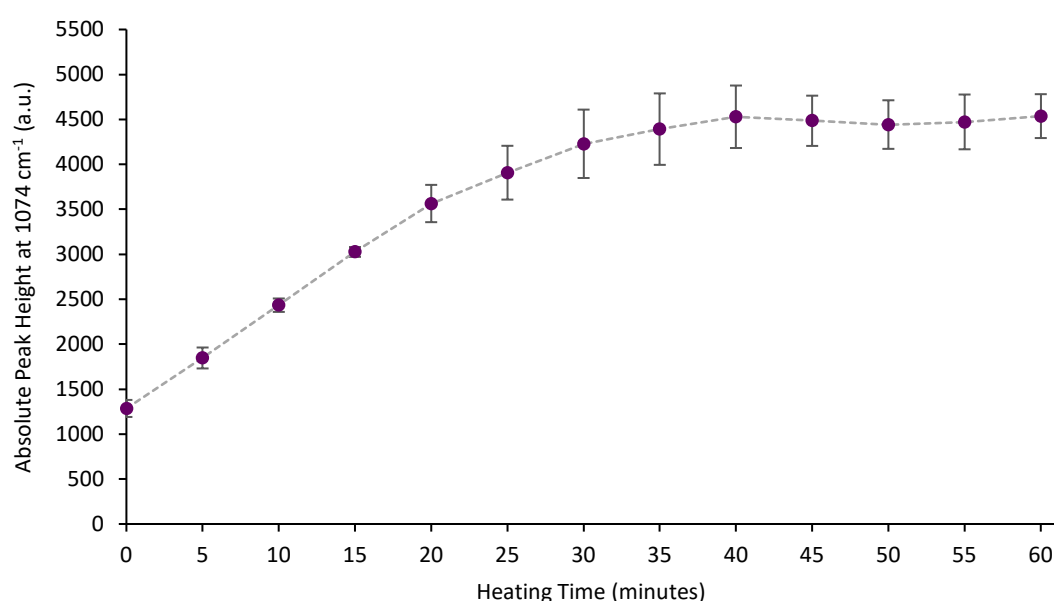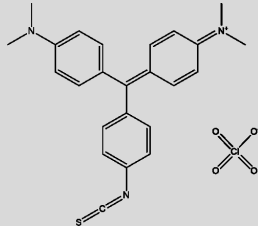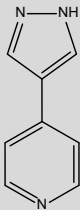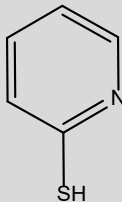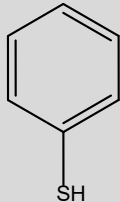
Figure 5.23 - Absolute height of the 1074 cm^{-1} peak at each time interval. Peak height calculated by subtracting a baseline value at 1050 cm^{-1} from the intensity at 1074 cm^{-1}. Error bars are the standard deviation of triplicate experiments.

Table 5.1 compares the increase in SERS and temperature of each Raman reporter during the plasmonic heating of the HGNs. The factor by which the peak of interest increased with respect to the intensity at time 0 is shown, as well as the temperature increase at each time point. All the Raman reporters gave rise to a similar increase in bulk temperature, with heating profiles shown in the appendix Figure 9.5. This table may be a useful reference point for the discussions that follow.

5.3.7   Summary of the Four Raman Reporters on HGNs

Table 5.1 – Summary of the factor increase of the main peak in respect to Time 0 and the bulk temperature at each time interval.

Heating Time (minutes)	MGITC (isothiocyanate)		PPY (pyridyl ring N)		2-MPY (thiol/pyridyl ring N)		BT (thiol)	
	Factor	Temp (°C)	Factor	Temp (°C)	Factor	Temp (°C)	Factor	Temp (°C)
5	1.3	35.1	1.3	35.2	1.4	34.4	1.4	34.4
10	1.8	38.3	1.7	38.6	1.8	37.7	1.9	37.8
15	2.4	38.9	2.2	39.5	2.2	38.3	2.4	38.4
20	3.0	39.0	2.7	39.3	2.5	38.2	2.8	38.5
25	3.6	38.6	3.1	38.9	2.7	38.0	3.0	38.4
30	4.2	38.2	3.5	38.4	2.9	37.7	3.3	38.3
35	4.6	38.0	3.9	38.0	3.0	37.5	3.4	38.1
40	4.9	37.7	4.2	37.7	3.0	37.4	3.5	38.1
45	5.1	37.6	4.5	37.5	3.1	37.1	3.5	38.0
50	5.2	37.3	4.8	37.4	3.1	37.1	3.5	37.9
55	5.3	37.3	5.1	37.2	3.1	36.9	3.5	37.9
60	5.3	37.2	5.3	37.2	3.1	36.9	3.5	37.8

5.3.8 Hypothesis behind SERS/Photothermal Observation

The increasing SERS response with plasmonic heating in solution has yet to be reported in the literature, and as such there is very little understanding of what may be causing the observation. Several hypothesises that could explain the signal enhancement are discussed next.

5.3.8.1 Modification of the Raman Reporter (Hot Electrons)

Surface plasmons can decay to 'hot electrons' which have a high kinetic energy and can move to molecules located near the metal surface. This transfer of energy can initiate polymerisation reactions or trigger a photocatalytic reaction.[139] Plasmonic nanostructures are therefore investigated for use in electronic devices, as they have been shown to induce the transport of 'hot electrons' into adsorbed molecules upon excitation. In brief, this mechanism is believed to proceed through the injection of an electron from the metal into an antibonding orbital of an adsorbed molecule.[140]

One molecule that can facilitate such events is 4-nitrothiolphenol (4-NTP). The fate of the molecule is different depending on the environment it experiences during the plasmonic excitation of the metal. Sun *et al.* used tip enhanced Raman spectroscopy to probe the hot electron transfer. They saw that 4-NTP could be converted to dimercaptoazobenzene through a plasmon-driven reaction by monitoring the change in Raman signal.[141] In another study Zhang *et al.* also saw this dimerization, however if the molecules were spaced far apart on the metal surface, they observed the nitro group cleaving instead, forming benzenethiol on the surface.[142] Cortes *et al.* reported the reduction of 4-NTP when the plasmon was excited in the presence of an acid halide. A six electron mediated reduction saw the formation of 4-aminothiolphenol from 4-NTP.[140] All of these transformations resulted in changes to the SERS spectra, with the appearance and/or disappearance of peaks.

To test the hypothesis that hot electrons were involved in increasing the SERS signal of the Raman reporters, 4-NTP was investigated for any spectral changes after heating. HGNs with 4-NTP on the surface were heated by the 785 nm laser, and the spectra increased in intensity as seen with the previous Raman reporters, the spectra are

shown in Figure 5.24. There were no large frequency shifts compared to those at time 0, or the appearance or disappearance of major peaks, this indicated the molecule was not undergoing any of the plasmon catalysed reactions described in the literature. From this experiment it can be concluded that under the laser powers and experimental conditions used, hot electrons were not ejected from the HGN plasmon as the Raman reporter molecular structure remained unchanged during heating.
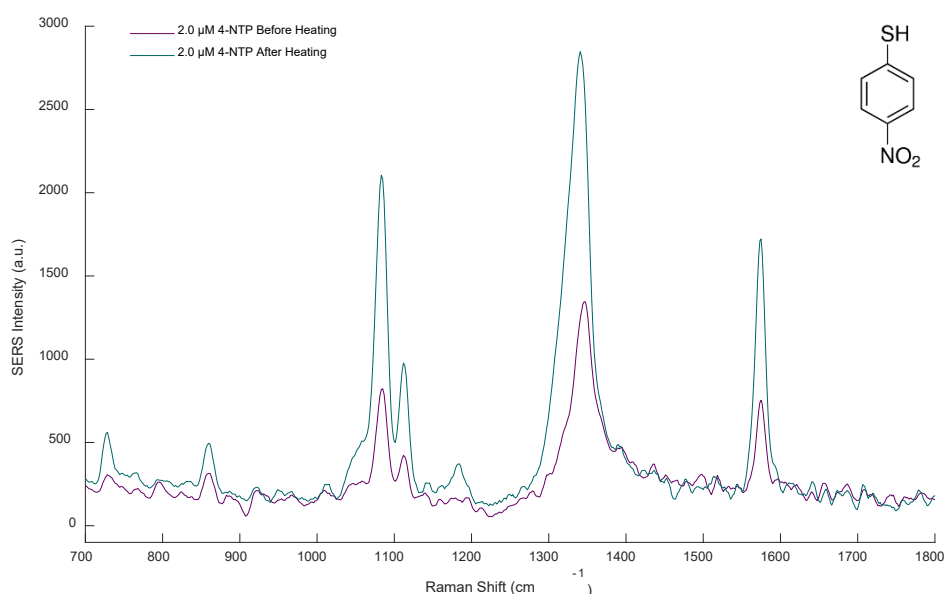
Figure 5.24 - Spectra collected before and after heating 4-NTP-HGNs with CW 785 nm laser (280 mW) for 30 minutes CW 785 nm SERS laser at 30 mW, 1s acquisition time, triplicate collection. Data processing using MATLAB: spectra averaged, subtraction of a glass and bare HGNs background, baseline applied and spectra smoothed. Molecular structure of 4-NTP shown in top right corner.

5.3.8.2 Raman Reporter Layer Rearrangement

It is well documented that the orientation of a Raman reporter on a plasmonic surface will influence which bands are enhanced in a Raman spectrum. Marshall *et al.* demonstrated the influence of molecule orientation on the SERS signal obtained from a single molecule in a plasmonic nano-gap.[143] The molecule orientation was determined using experimental SERS spectra and density functional theory calculations. It is therefore not unreasonable to suggest that Raman reporters could change orientation and repack on the metal surface, leading to the increased SERS signal.

For example, MGITC offers attachment points to the gold surface via the positively charged tertiary amine and the terminal sulfur atom. The N^+ atom can physisorb to the surface via an electrostatic interaction, while the sulfur atom will form a covalent bond. If the electrostatic attachment route is faster at forming, it could mean at time 0, many MGITC molecules are electrostatically bound in a disorganised layer, with some having diffused close enough to give effective SERS. Then as time passes, the favoured covalent link could prevail as molecules displace and reattach into an ordered packed layer with a more upright orientation, leading to the increased SERS signal observed.

When the relative peak heights in Figure 5.7 (spectra of MGITC-HGNs during heating) are compared, there are ratio changes in some peaks during the 30 minutes heating. With focus on the doublet at 1600 cm^{-1}, it can be seen that the ratio between the two peaks changes after 60 minutes of heating, this change is shown in Figure 5.25.
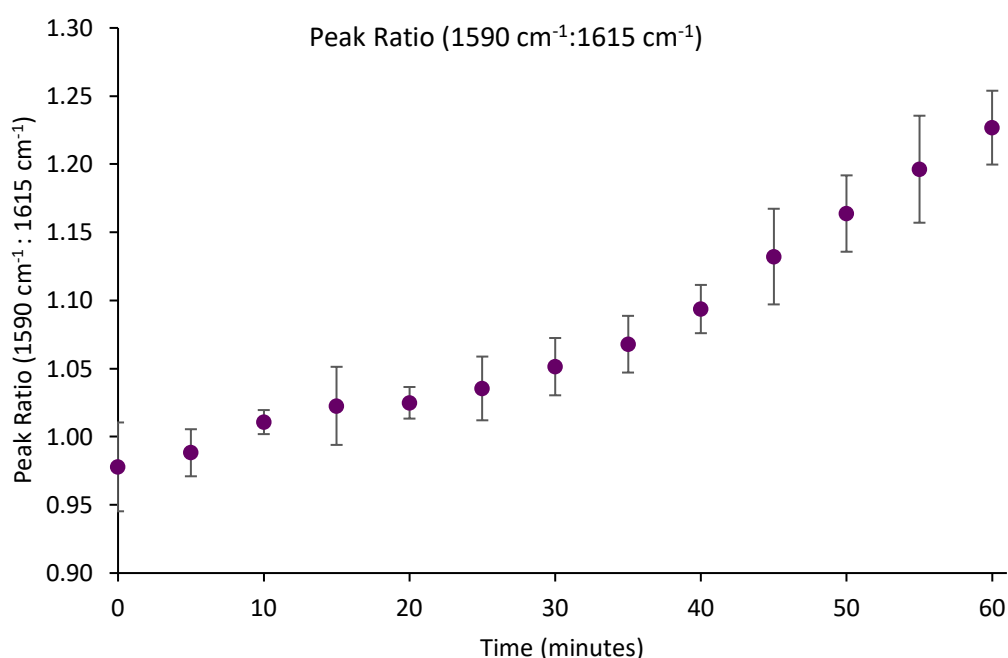
Figure 5.25 - Peak ratio of the doublet at 1590 cm^{-1} and 1615 cm^{-1} plotted as a function of heating time. Original MGITC-HGN spectra shown in Figure 5.7.

The 1590 cm^{-1} peak is assigned to the in-plane ring stretching and bending and the 1615 cm^{-1} peak to the N-PH ring and C-C stretch.[89] A change in intensity, but not frequency, indicates the molecule has changed orientation, or was packed differently on the HGN surface, supporting the rearrangement hypothesis. The SERS laser only

control from the MGITC-HGN heating experiment showed no changes to the double peak at 1600 cm^{-1} during the 60 minute data collection period. This indicated that the photothermal heating of the HGNs influenced the rearrangement of the Raman reporter on the nanoparticle surface.

If we hypothesise that MGITC can physisorb onto the HGN surface first, then rearrange, chemisorb and pack into an ordered layer, there should be evidence of this within the other Raman reporter studies too. Taking into account the structures and factor increases shown in Table 5.1, it should be noted that MGITC and PPY show similar factor increases, as do 2-MPY and BT respectively. Both MGITC and PPY have more than one possible binding site within their structure suggesting different orientations may be present when the molecule first encounters the HGN surface. Whereas 2-MPY and BT have one main binding route via the thiol. Even if 2-MPY bound through the N atom, it would result in a very similar orientation given its position in the ring with respect to the thiol substitute group.

When comparing the enhancement factors of all the Raman reporters, they all are similar after 5 minutes of heating, but 2-MPY and BT reach their maximum enhancement and plateau at a lower factor increase. This can be reasoned since their initial binding mode to the metal surface is limited to a covalent bond, and as such, at time 0 there already exists a fairly ordered layer. Over the heating time, this may pack further leading to the increase, but not to the same extent as observed with MGITC and PPY.

All the Raman reporters studied contained a conjugated ring system, so hypothetically they could also have induced reporter-reporter interactions (π-stacking) and formed a loosely bound secondary layer of reporter if the initial layer was laying flatter to the surface. This extra layer could have acted as a reservoir of Raman reporter molecules, providing more molecules as the original layer rearranged, forcing them into a more upright orientation. The resulting perpendicular orientation to the metal surface allows for a greater polarisability when the laser interacts with the HGNs, this in turn leads to an increase in the Raman scattering observed.

5.3.8.3 Morphological Changes in the HGNs

A characteristic blue shift in the LSPR was observed upon heating the HGNs and was due to a change in morphology. The shift indicated that smaller, more solid-like, particles were being formed, suggesting the HGNs were remodelling under the intense local temperatures. However, under closer inspection with TEM it can be seen this was not the case as no bulk change was present. Even though some toroidal particles were observed, they were also present in the control samples, indicating they do not form as a result of the laser interrogation. The images showed that a bulk change did not occur post heating, and therefore the shift in LSPR must be a result of a more subtle change to the HGN surface undetectable with low resolution TEM. A change in the elemental content of the HGN shells could contribute to the observed LSPR blue shift. If further dealloying had occurred as a result of heating, this could have changed the scattering contribution of the nanoparticles and in turn effect the SERS response. Further elemental analysis would be required to investigate this hypothesis.

5.3.8.4 Adatom Model

The surface of a crystal will be atomically smooth at zero temperature, then become rough as the temperature increases and a thermodynamic equilibrium is established.[144] This is due to the presence of 'adatoms', which are essentially additional metal atoms on top of the main crystal surface.

In the 1980s Otto and his colleagues proposed the 'adatom hypothesis' as a contribution to SERS.[145-146] They suggested that these adsorbed metal atoms facilitated the metal-molecule electronic transfer, therefore providing a pathway for the charge transfer mechanism of SERS. In line with this model, it would be expected that as the nanoparticle surface became rougher, then more SERS-active sites would be generated, leading to a greater SERS intensity of any adsorbed analyte.

This periodic displacement of atoms out of the surface plane can be stabilised by interacting with adsorbed molecules, with Feng *et al.* trapping charged gold adatoms with dimethyl sulfoxide (DMSO) on a gold surface.[147] It is known that gold adatoms

can diffuse along the metal surface and even be detached from the surface itself if involved in a bridging motif between adsorbed molecules. This results in the adatom being suspended above the gold surface.

As the temperature of a system increases, as does the entropy, and this results in a surface with atomic-scale roughness. Therefore it can be theorised that the increase in temperature that occurs during the plasmonic heating process causes an abundance of adatoms to 'pop out' from the nanoparticle surface, resulting in a much rougher surface due to the high density of adatoms. This extreme atomic-scale roughness would be expected to cause great enhancement to the Raman scattering, and would help explain the data presented previously.

To explore the adatom model further, more experiments were carried out. After HGN synthesis, citrate buffer was added as a preventative measure to increase stability. It is now thought that the citrate molecules not only increase inter-particle repulsions and therefore maintain colloidal stability, but actually aid in the stabilisation of the adatoms on the surface.[148] To probe this idea further, the role of citrate during heating and SERS analysis was investigated.

5.3.9 Influence of Citrate in the SERS/Temperature Relationship

To investigate the importance of citrate in the colloid, a fresh batch of HGNs was synthesised following the standard protocol. After the galvanic reaction had occurred, the batch was split into two, with citrate buffer (1 mL of 50 mg/mL) being added to one as normal and 1 mL of water to the other as a control, to keep concentrations comparable. As an initial study, both HGN types were subjected to heating with the 785 nm laser for 30 minutes. The control is referred to as 'bare HGNs' in all the following results. Figure 5.26 shows the average extinction spectra obtained from control (unheated) and heated samples.
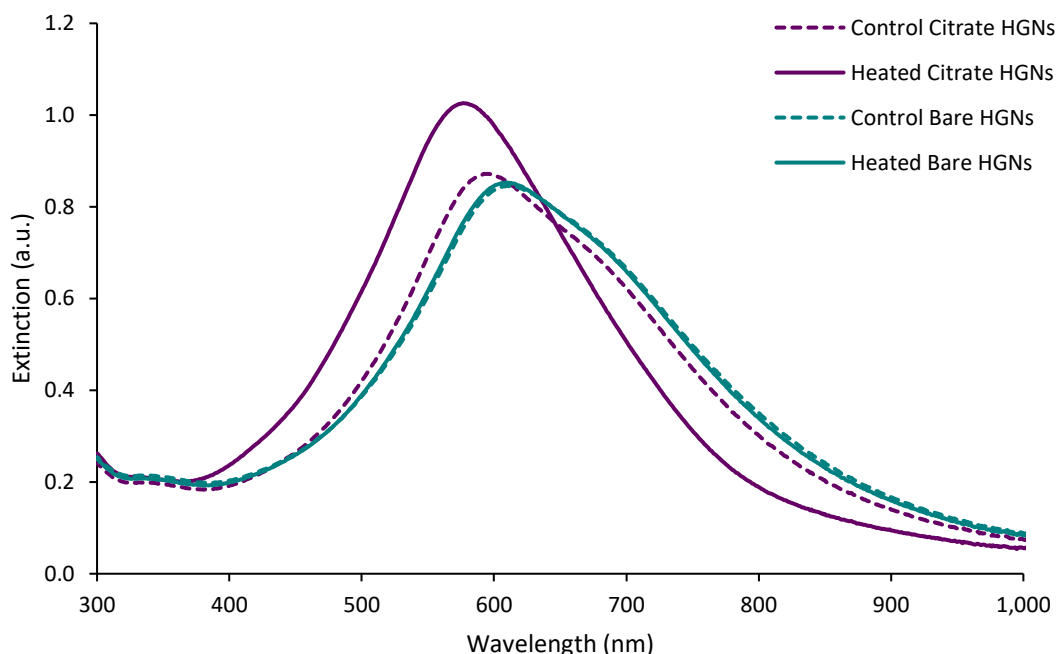
Figure 5.26 - Extinction spectra of bare and citrate capped HGNs. The dashed spectra represent the control (unheated) HGNs. The solid line spectra represent the HGNs after 30 minutes of heating with a 785 nm laser source. Samples were analysed at a 1 in 2 dilution in water. Spectra shown are the average of triplicate experiments and triplicate measurements collected on a baselined fast scan rate (4800 nm/min, 1 nm intervals).

The dashed spectra represent the unheated samples of both citrate and bare HGNs. When comparing each one to their corresponding heated samples, the citrate capped HGNs show the characteristic blue shift in the LSPR. Surprisingly, the bare HGNs do not show any deviation from the control spectra, suggesting no modification of the particles resulted from the plasmonic heating. This indicates that the citrate molecules capping the HGN surface play an additional role other than just electrostatic repulsion. Figure 5.27 shows the average heating profiles of each sample as well as the maximum temperature increase during the laser heating.

The bare HGNs heated the bulk solution an additional ≈3.4°C compared to citrate capped HGNs. The heating curves also differ in profile, with the bare HGNs showing a steady increase even at 30 minutes. The citrate capped HGNs peak at around 10 minutes, then the bulk temperature begins to decrease slightly. This suggests the photothermal conversion process is more efficient in the bare HGNs, and they are able to better dissipate their converted heat to the surrounding medium. It can be suggested that the surface bound citrate either blocks or absorbs the dissipating heat from the HGN lattice.
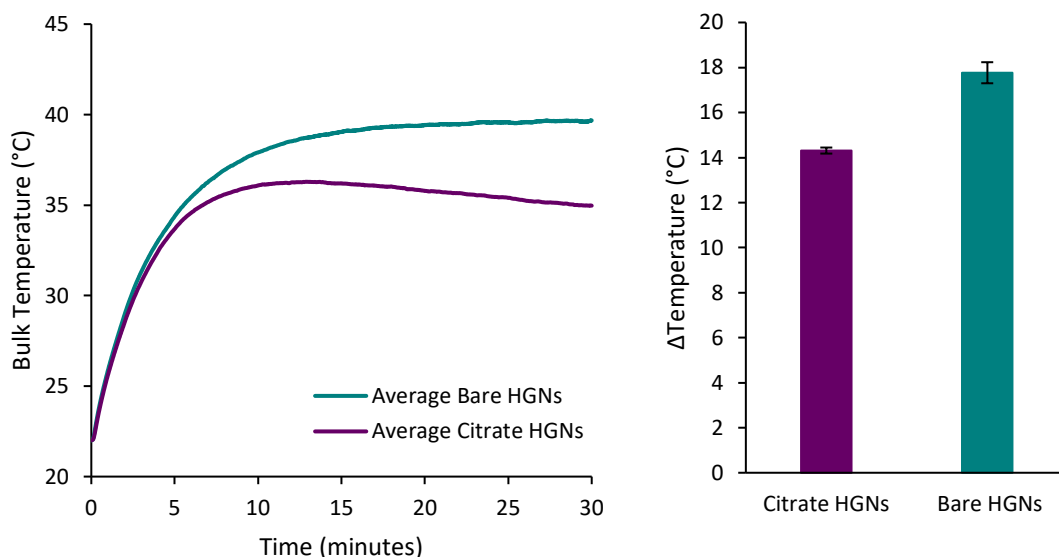
Figure 5.27 – Bulk temperature profiles and ΔTemperature of bare and citrate capped HGNs after being irradiated with a 785 nm laser for 30 minutes. Triplicate experiments were carried out and an average result taken for the figure.

A citrate molecule is comprised of three carboxylic acid groups as well as one hydroxyl group. Depending on the pH, many species can exist. For example, the molecule is sequentially deprotonated when moved to basic conditions. Figure 5.28 shows the deprotonation of citric acid, with the respective pKa values stated below each structure.
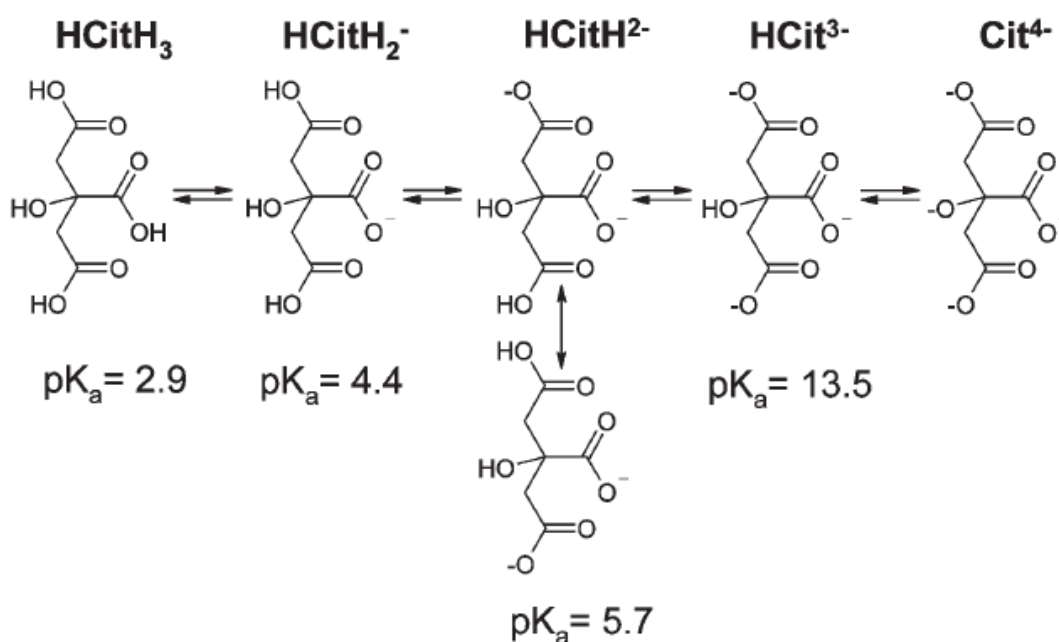
Figure 5.28 – Stepwise deprotonation of citric acid. The pKa is shown below each species to indicate the state of protonation at a variety of pH. Adapted from Heller *et al.* with permission from The Royal Society of Chemistry.[19]

The hydrogen on the central carboxyl group is the first to be deprotonated as the pH increases, then the terminal groups, before the central hydroxyl group is removed. This results in five separate species: citric acid ($HCitH_3$), dihydrogen citrate ($HCitH_2^-$), hydrogen citrate ($HCitH^{2-}$), citrate ($HCit^{3-}$) and a fully deprotonated citrate (Cit^{4-}).[149]

Park *et al.* used infrared and x-ray photoelectron spectroscopy to probe the binding modes of citrate on gold nanoparticles in acidic conditions.[148,150] In these studies, it was suggested that citrate anions adsorbed onto the gold surface through bridging coordination of the central COO^- group and the coordination of the terminal COO^- group.

The pH of both HGN batches was ≈7, indicating the batch with citrate buffer added would have had the molecules present in the triply deprotonated state as $HCit^{3-}$. In this state of protonation, it is suggested that the citrate binding can be monodentate or bridging bidentate depending on the density of Au adatoms on the surface.[148] Citrate can therefore act as a chelator, forming Au-O bonds and stabilising any surface reconstructions. The bond energy of this Au-carboxylate complex is expected to be in the range of chemisorption, owing to the positively charged low-coordinated Au adatom, with a bond energy similar to that of metal-oxygen bonds.[148]

Figure 5.29 illustrates a possible binding mode of a citrate anion with the adatoms. When citrate is present in the colloid, it can stabilise adatoms that are generated from heating. When no citrate is present, it is more likely the adatoms will return to the lattice plane given the lack of stability. It is believed the adatoms are in an Au(I) oxidation state, and are converted to neutral metal in the presence of a reducing agent. A molecule with excess electrons could donate to the adatom resulting in the reduction of Au^+ to Au^0.[151]
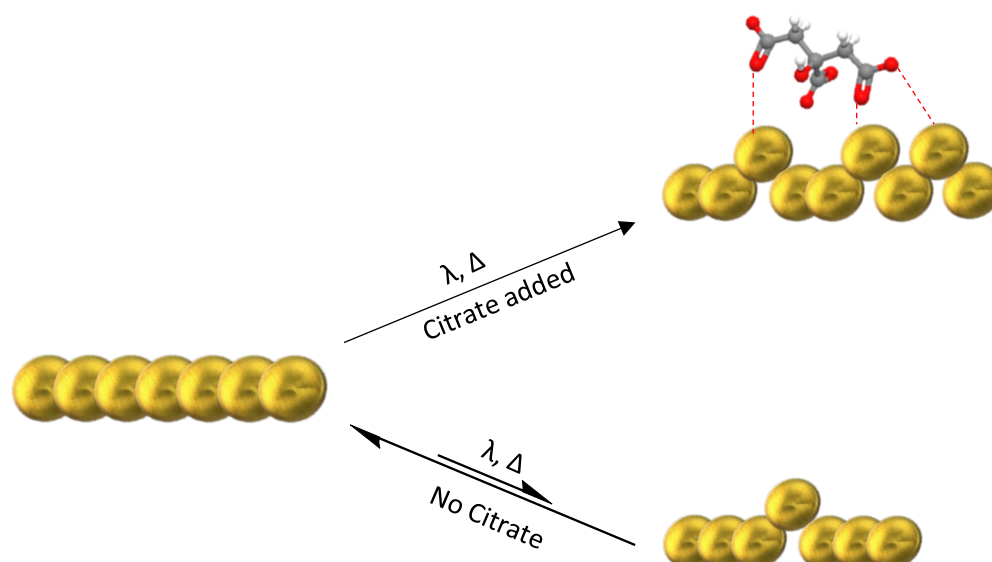
Figure 5.29 –Schematic showing one of the possible binding modes of the citrate anion with the adatoms. The top route shows the adatoms can be stabilised by a bridging bidentate or a monodentate mode when citrate is present. When no citrate is present, it is likely the adatoms will return to the lattice plane.

In this model, it is suggested that each carboxylate-binding mode of a citrate anion can either be monodentate or bridging bidentate depending on density and availability of neighbouring Au adatoms on the surface.[148] Many factors will influence how the citrate molecule binds to the gold surface, these include: number of adatoms present, position of the adatoms, strength of the adatom-carboxylate bond, extent of protonation of the carboxylate group (pH dependant) and any steric hindrance associated with the binding of multiple carboxylate groups in the one citrate molecule.[148] Within a sample of heated citrate-HGNs, it is most likely there is mixture of the binding modes possible.

The adatom-carboxylate complexation hypothesis provides an explanation for the puzzling experimental observations. This hypothesis is supported by the data shown previously, where the samples with citrate changed spectroscopically as seen in the extinction spectra, whereas the bare HGNs appeared to be the same as the control sample even after heating. This indicates that citrate is critical for stabilising the adatoms produced during heating.

A study by Tsuji *et al.* found that citrate could be decomposed and removed from the nanoparticle surface during laser irradiation.[152] At lower citrate coverage, they found that the removal of the stabilising molecule induced nanoparticle agglomeration, a factor leading to the formation of larger submicron particles. However, in this work, such larger particles were not observed after plasmonic heating as observed in the TEM images. This suggests that the particular laser parameters used in this work did not remove the citrate from the HGN surface. Supporting the theory that citrate molecules remained on the nanoparticle surface and were available to stabilise adatom formation during plasmonic heating.

5.3.9.1 Bare vs Citrate HGNs for SERS

As citrate was thought to affect the stability of adatoms generated during heating, it was logical to investigate its effect on the SERS response after heating. Figure 5.30 shows the average SERS spectra of MGITC on the surface of each batch of HGNs before and after heating.
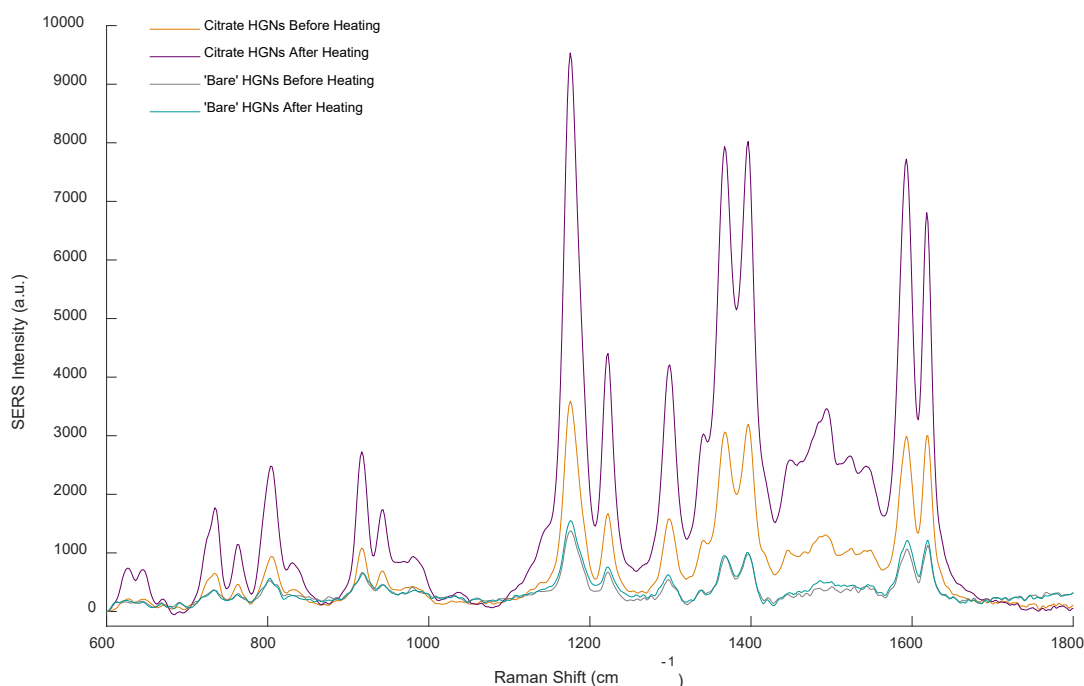
Figure 5.30 – SERS spectra of MGITC-HGNs before and after heating with a 785 nm laser (278 mW) for 30 minutes. The yellow (before) and purple (after) spectra are from the samples prepared with citrate capped HGNs. The grey (before) and teal (after) spectra are from the samples prepared with bare HGNs. Spectra were collected using a 785 nm excitation (30 mW) source, acquisition 1s and 3 measurements at each time point. Data processing using MATLAB: subtraction of a glass and bare HGNs background, spectral range cut, baseline applied, spectral smoothing and 3 experimental reps were averaged before plotting.

Each sample was prepared following the same protocol, therefore it is surprising that the spectra before any heating is different between the batches. The intensity of the citrate capped HGNs before heating is more than double that of the bare HGN sample. Linking back to the discussion about how MGITC adsorbs onto the surface, it can be suggested that without the initial electrostatic attraction between the negatively charged citrate and positively charged MGITC, less MGITC was able to adsorb onto the surface. After heating the two samples, very different trends were also observed with the citrate capped HGNs showing the expected trend of a large SERS increase. Whereas the bare HGNs showed minimal increase.

Figure 5.31 shows the absolute height of the peak at 1176 cm^{-1}, the citrate capped sample has a SERS increase of more than double its starting height, whereas the bare HGNs almost shows no increase at all. This suggests the adsorbed molecules, are vital for the stabilisation of the increasing adatom density on the metal surface.
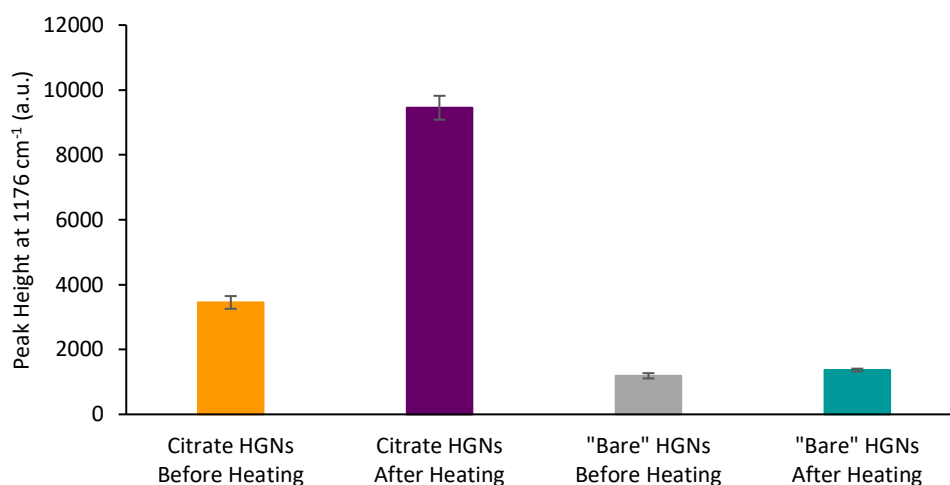
Figure 5.31 - Absolute peak height of the in-plane benzene bending peak seen at 1176 cm^{-1} for each sample. Peak height calculated by subtracting a baseline value at 1080 cm^{-1} from the intensity at 1176 cm^{-1}. Error bars are the standard deviation of triplicate experiments.

Studies on thiolated molecules and gold clusters are the most comparable to the system under investigation in this research. The current understanding of a gold-sulfur bond is that first, the thiol is deprotonated, which creates a radical. This then forms a thiolate-gold bond that has a strength close to that of the gold-gold bond.[153] As mentioned within the citrate discussion, adatoms can be suspended off the gold surface between binding molecules.[154] This results in a 'staple' motif, comprising of RS-Au-SR or RS-Au-RS-Au-SR as illustrated in Figure 5.32.
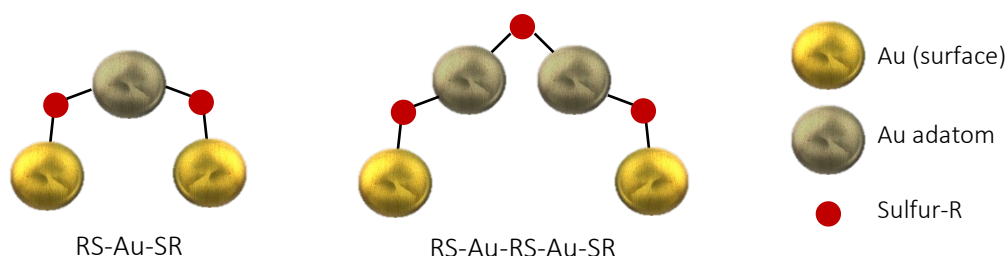
Figure 5.32 – Schematic showing the staple motifs formed between adatoms and the adsorbed thiolated molecule. R groups are omitted from the illustration for clarity.

The Au-S interface is not static, and the migration, desorption and readsorption of the thiolates is known to occur. Thiolates can move to different sites across a gold cluster, but this is a slow process at room temperature. However, the rate increases as the temperature elevates and migration is observed within tens of minutes at 70-90°C.[154] Entire staple motifs can also move on the surface, and it is reported that aromatic thiols can form gold islands of monoatomic height on the gold surface.[155]

The increase in SERS observed from citrate containing HGNs could be a combination of citrate/reporter molecules stabilising newly formed adatoms and the migration and clustering of adatoms on the gold surface as the temperature increases.

5.3.9.2 Order of addition of Malachite Green Isothiocyanate

The order of Raman reporter addition to the HGNs was investigated to probe their performance at stabilising the adatoms. Briefly, identical MGITC-HGN samples were prepared and the SERS spectra collected before and after heating. However one sample set had MGITC added prior to heating and the other after heating had occurred, this method is depicted in Figure 5.33.

Figure 5.33 –Cross-sectional schematic showing the two preparation routes, (a) where MGITC was added to the HGNs before plasmonic heating and (b) where the particles were plasmonically heated before MGITC addition.

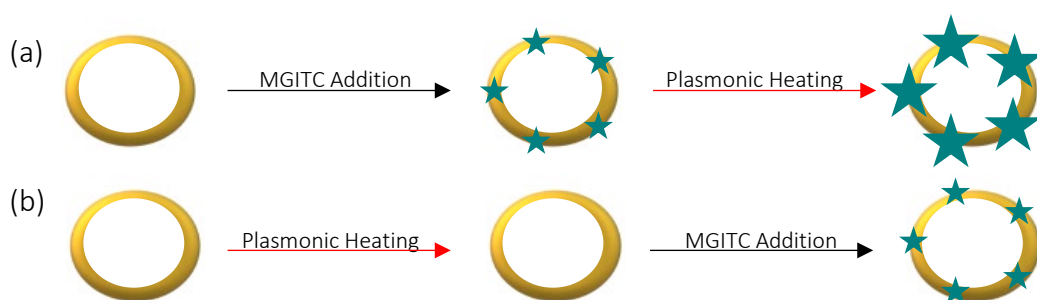Figure 5.34 shows the corresponding SERS spectra, from these it is interesting that the spectra was more intense when the MGITC was added after heating. The samples with the Raman reporter added before behave as expected. Figure 5.35 shows the absolute peak height at 1172 cm^{-1}, with the characteristic signal increase for the samples with MGITC added before.
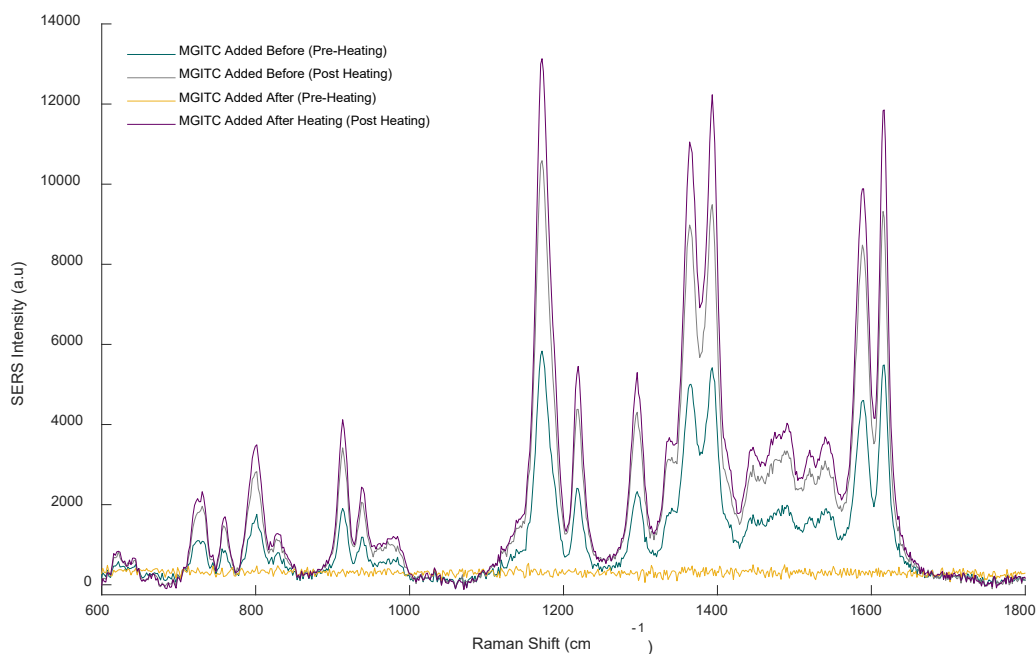
Figure 5.34 –SERS spectra of MGITC-HGNs before and after heating, and with the MGITC added before (teal and grey) or after heating (yellow and purple). Laser heating with a CW 785 nm excitation for 30 minutes. Triplicate spectra obtained with a 785 nm excitation laser (30 mW), 1s acquisition. Data processing using MATLAB: subtraction of a glass and bare HGNs background, baseline applied and 3 experimental reps were averaged before plotting.

The data suggests that either citrate is still present on the HGN surface after MGITC has been added and as such can support the generation of adatoms. Or that MGITC can also fulfil this role, but just not as efficiently as the citrate anion. The increase in signal when the MGITC is added after suggests that the citrate anion is more efficient at stabilising adatoms than the Raman reporter, due to the chelate effect. As the HGNs were heated and adatoms were generated on the surface, the citrate could stabilise these until the MGITC was added and the molecule exchange occurred. By adding the MGITC after heating, a larger density of adatoms existed and in turn gave rise to the more intense SERS spectra observed.

131
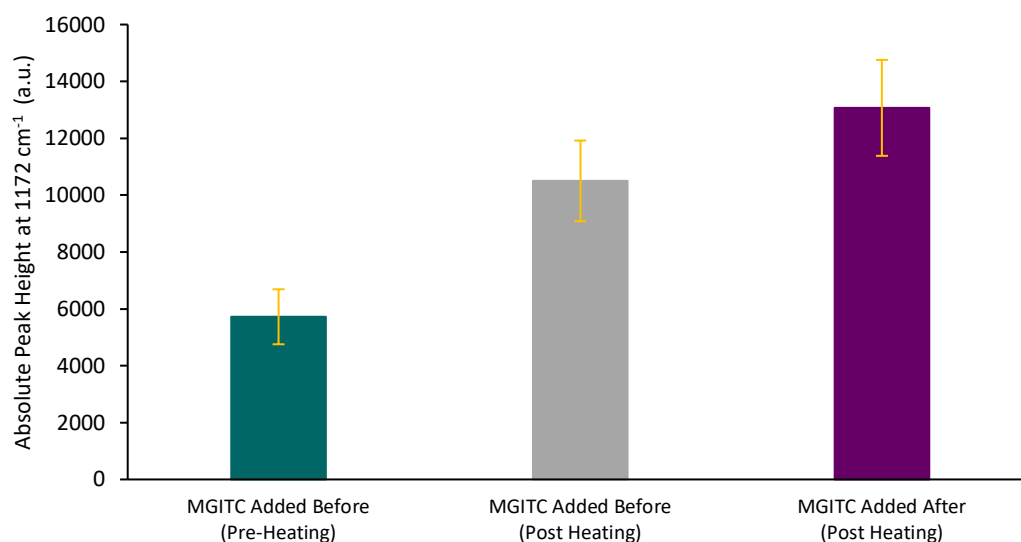
Figure 5.35 - Absolute height of the in-plane benzene bending peak seen at 1172 cm^{-1}. Peak height calculated by subtracting a baseline value at 1080 cm^{-1} from intensity at 1172 cm^{-1}. Error bars are the standard deviation of triplicate experiments.

A future study could be to investigate Raman reporters that have different chelating abilities. In turn, this should affect the efficiency of the molecule at stabilising adatoms generated during plasmonic heating. For example 1,2-bis(4-pyridyl)ethylene (BPE) and 1,2-bis(2-pyridyl)ethylene are similar molecules, and differ with the position of their N atom in the pyridyl rings. The former molecule has N in the 4- position and latter in the 2- position. This would affect the ability to chelate with adatoms, with the 2-postion more likely to support this bonding type, and stabilise increased adatom density during plasmonic heating. It would be expected that the SERS increase from this molecule after heating would be greater than that of the 4- related structure.

5.4 Concluding Remarks

The results within this chapter although perplexing at first, indicate a previously unexplored relationship between the photothermal effect and SERS. To date, there exist no examples of this in the literature, and although the understanding behind the process is still incomplete, the theories put forward help piece together the puzzle.

The most likely factors contributing to the increase in SERS are the reordering of the Raman reporter layer adsorbed to the HGN surface and the increasing density of adatoms. The latter is expected to be the dominating factor, with a change in the nanoparticle surface leading to an enhancement in the SERS signal observed. This could be the result of an increased electromagnetic field as adatoms cluster on the surface or from the enrichment of the charge transfer effect via Otto's adatom hypothesis.

The previous chapter showed that laser power had a linear effect on the maximum temperature reached by the HGNs and the resultant blue-shift of the LSPR. It can now be added that the LSPR shift could be due to an increased number of adatoms on the HGNs surface. Further work to investigate the relationship between laser power and surface changes should be carried out. One experiment could be to probe the SERS enhancement during plasmonic heating when varying laser powers are used. It would be expected that as the laser power of the heating laser increased, adatom density would also increase, and this could be observed by an enhancement in the Raman response from an adsorbed reporter.

These findings could be useful for future developments within nanotechnology as the ability to increase the SERS signal without inducing aggregation is desirable for many applications. Lower detection limits could be achievable using this enhancement method. In addition to the positive applications of these findings, it should be noted that researchers within this field should be aware of the possibility of a photothermal induced increase in SERS. Many groups use Raman reporter functionalised nanoparticles for tracking *in vivo*, or for quantifying the effects of photothermal therapy, and as such should take into consideration this possibility.

Current reports of plasmonic nanostructures being used for photothermal heating and SERS do not observe the behaviour discussed in this chapter. Therefore it would be important to carry out further experiments to see whether other nanoparticle types are capable of producing adatoms, and increasing the SERS response to the same degree, or whether this is only seen with these specific HGNs. Another future experiment could be to explore other capping agents for the nanoparticle synthesis and determine whether they can also stabilise the increase in adatoms on the nanoparticle surface during heating.

To better understand the cause of the SERS increase, it would be interesting to carry out investigations into the molecule-adatom binding, for example X-ray photoelectron spectroscopy which can probe the chemical and electronic states of atoms on a metal surface. This could help build the picture as to how the adatoms are stabilised on the surface. Molecular modelling and simulations may also shed light on the phenomenon, and could screen multiple molecules/reporters for their ability to support the adatom generation.

Many scientific discoveries are accidently found while pursuing something else. This chapter was serendipitously formed, and while it is a side step from the original path of the research, it is a fascinating finding which is yet to be fully understood. The results do have impact on the original aim however, as it is now evident that these HGNs are not suitable for simultaneous drug delivery, heating and Raman tracking.

6.Research Conclusions

This work investigated two nanoparticle candidates as the vector of a drug delivery design. First IONCs were investigated due to their large surface area and ability to release drug cargo under external magnetic simulation. They were successfully synthesised and their magnetic properties were determined as superparamagnetic. The IONC design appeared promising until it was realised that the gold coating step was less controlled that first thought. Efforts were then focussed on exploring an alternative nanoparticle type.

The prospect of using HGNs as the nanoparticle core was studied next, with variations in their synthesis producing HGNs with LSPRs into the NIR region. The ability to tune the LSPR was an attractive feature considering their intended biological use. The effect of the LSPR position on the photothermal capabilities of the HGNs could be explored further, as this might improve the choice of LSPR for the most efficient heat conversion. A more efficient conversion of the light to heat, could more efficiently release any drug cargo and allow for lower laser powers or interrogation times to be used.

The HGNs were successfully functionalised with a Raman reporter and antibody as a proof of concept for tracking and bio-recognition respectively. A pilot study was performed in biological samples (macrophages) and showed that a MGITC signal was detectable, this showed promise for the tracking application of the HGNs (data not shown). Another small biological study was carried out to observe any cellular changes after the incubation of macrophages with statins. Using Raman mapping, the treated samples were distinguishable from the control samples and were separated spectroscopically using principal component analysis. Their main spectral differences were in a peak at 1000 cm^{-1} most likely assigned to phenylalanine and another at 1447 cm^{-1} relating to either a protein/lipid band. Repeat studies and further work would need to be carried out to draw any conclusions, but these initial studies showed the statins did have an effect on one of the target cell lines.

The LSPR position may also influence the increasing SERS observed when the nanoparticles are subjected to plasmonic heating. This relationship between plasmonic heating and increasing SERS has currently not been published in the literature, therefore explaining the phenomena fully remains challenging. Theories such as hot electron injection and bulk morphological changes were experimentally negated, as there was no evidence of these happening as a result of the heating.

Decades ago, Otto and his colleagues proposed the adatom hypothesis as a cause of the enhanced Raman scattering observed when a molecule was extremely close to a plasmonic surface. Reviving this theory and hypothesising that the plasmonic heating creates a high density of adatoms on the HGN surface fits well with the data presented in this thesis. There exist some papers that have modelled the stabilisation of adatoms through adsorbed molecules on the metal surface. It is known that citrate plays a vital role in ensuring colloidal stability due to the charge repulsions, however the data shown in Chapter 5 indicates it has an additional role. The ability of citrate to bridge and bind to gold atoms that are on or above the surface plane is key to allowing the newly formed adatom sites to remain. This is seen in the final data sets presented, where the citrate capped HGNs had a superior SERS response compared to a batch with no citrate. In addition, the plasmonic heating did not significantly affect the SERS signal of the bare HGN sample, signifying the importance of citrate in the phenomena.

If the photothermal effect of HGNs was able to be computationally modelled and supported by experimental data, it could add weight to the adatom hypothesis. However, the expertise required to achieve this are outside the group skillset, therefore an external collaboration would have to be established to reach this goal.

More direct experimental evidence is needed to confirm that the growing adatom density causes the increase in SERS. However, if achieved, this could create an exciting new path in Raman scattering research, allowing for the increase in SERS response without the need for colloidal aggregation. It could offer an alternative platform to creating highly sensitive Raman based detection assays for the detection of disease or other molecules of interest.

7. Experimental

Anhydrous p-xylene 99%, oleylamine 70%, oleic acid 99%, manganese (II) acetate 98%, iron (II) perchlorate 98%, 3,4-dihydroxyhydrocinnamic acid 98%, sodium hydroxide 98%, hydroxylamine hydrochloride 99.9% , silver nitrate 99.9%, sodium citrate tribasic dehydrate 99%, potassium carbonate 99%, methanol 99.8%, phenylacetylene 98%, 2-mercaptopyridine (2-MPY) 99% and benzenethiol (BT) 99% and 4-nitrothiolphenol 80% were all purchased from Sigma Aldrich. Hydrogen tetrachloroaurate (III) hydrate 99.9% was purchased from Alfa Aesar. 4-(1H-pyrazol-4-yl)pyridine (PPY) 99% was purchased from Fluorochem. Malachite green isothiocyanate 99% was purchased from Thermo Fisher Scientific. The thiolated polyethylene glycol (HS-PEG$_{5000}$-COOH) was purchased from Laysan Bio Inc. All materials were used as received. Water was deionised and filtered by a Milli-Q® water system. Any glassware used was soaked in aqua regia, consisting of 1 part HNO$_3$ to 3 parts HCl.

All extinction spectra were collected using an Agilent Cary 60 UV-Vis Spectrophotometer set on a baselined fast scan rate (4800 nm/min, 1 nm intervals). Other instrumentation specifications are stated in the appropriate sections discussing the methods/results related to their use.

For centrifugation steps, a rotor with a 7.5 cm radius was used for most samples. Where a different centrifuge was used, the relative centrifugal force was stated.

7.1 Iron Oxide Nanocages

7.1.1 Iron Oxide Nanocage Synthesis

Prof Hiroshi Matsui kindly welcomed me to complete a short visit to his laboratory at the City University New York, where I learned the following synthesis.[81]

A 100 mL 3–neck round bottom flask and magnetic stirrer bar was cleaned in hydrochloric acid (38%) overnight. After rinsing and drying, the following reagents (neat) were added sequentially.

i. 15 mL ρ-xylene
ii. 824 µL oleylamine
iii. 157 µL oleic acid
iv. 170 mg manganese (II) acetate

The mixture was briefly sonicated for 10 seconds, where the solution changed from light brown to dark brown. The flask was then heated in an oil bath to 90°C while under magnetic stirring and reflux. 1 mL of water was added, before the mixture was refluxed for 90 minutes. Iron (II) perchlorate (610 mg in 1 mL water) was then added and refluxed for a further 90 minutes. The flask was lifted out the oil bath and allowed to cool to room temperature.

The colloid was purified through a series of centrifugation steps. The initial step was for 5 minutes at 3000 rcf, where the supernatant was kept and the pellet was discarded. An equal volume of ethanol was then added to the supernatant and the mixture was shaken. A second centrifugation step under the same conditions was completed, this time discarding the supernatant and keeping the pellet. 4 mL of hexane was then used to resuspend the nanocages that were then transferred to glass vials for storage.

7.1.2 Phase Transfer of Nanocages

Modified protocol from a publication by Liu *et al*.[85] To allow a phase transfer from organic to aqueous medium, 3,4-dihydroxyhydrocinnamic acid (DHCA) was used to functionalise the surface of the iron oxide nanocages (IONCs).

50 mg of DHCA in 6 mL of tetrahydrofuran (THF) was added to a 25 mL round bottom flask and fitted with a rubber septum. The flask was heated in an oil bath to 70°C under nitrogen flow. 500 µL of IONCs were centrifuged for 15 minutes at 13000 rpm and the pellet was resuspended in 1 mL of THF. This solution was then added dropwise to the flask and left to heat for 3 hours. A nitrogen filled balloon was used to help balance the vessel pressure while the IONCs were added. The mixture was cooled to room temperature and NaOH solution (500 mL, 0.5 M) was added to force precipitation of

the IONCs in solution. The mixture was then centrifuged for 10 minutes at 3000 rpm, and the pellet was resuspended in 2 mL of water.

7.1.3 Magnetic Properties of the Nanocages

IONCs samples were freeze dried and submitted for analysis using a Quantum Design MPMS-7 SQUID magnetometer. All data was collected and processed by Marcin Witkowski at the University of Poland.

The freeze dried nanoparticle sample was encapsulated in an envelope of Parafilm in order to prevent contamination and to localise the sample in the sample coil of the instrument. The magnetisation was determined at 300 K and 2 K as a function of external magnetic field up to 70'000 Oe (7 T). Hysteresis loops were measured by reversing the direction of the magnetic field down to -12'000 Oe (1.2 T).

Zero-field cooling (ZFC) and field cooling (FC) experiments were also performed in order to determine the blocking temperature of samples.

- ZFC - Cooling the sample from high temperature 315 K down to 2.0 K without external magnetic field. Followed by heating the sample back up from 2.0 K to 315.0 K under 100 Oe external magnetic field.
- FC - Cooling the sample down from room temperature to 2.0 K under 100 Oe external magnetic field.

7.1.4 Gold Coating of Nanocages

The main method for gold coating the IONCs was through the glucose reduction method.[88] Many variations of the synthesis, in terms of reagent concentration, IONC dilution, temperature and reaction times were investigated. However, for conciseness of this section, one version of the synthesis has been reported.

In a 50 mL round bottom flask, the following was added sequentially,

i.   1 mL IONC (Diluted 500 μL IONCs in 500 μL water)
ii.   4 mL water
iii. 1 mL Au sol (2.5 mg $HAuCl_4$ in 1 mL water)
iv.   30 mg Glucose

The mixture was sonicated for 2 minutes, before being lowered into an oil bath at 45°C and rapidly rotated for 10 minutes. The colloid was then aliquoted into eppendorfs and left on a magnetic rack until separated. The rack was 3D printed using a publically available template (https://www.thingiverse.com/thing:79424) on an Ultimaker 2+ 3D printer using a polylactic acid filament. Small rectangular magnets (1/2" x 1/4" x 1/8"), NdFeB (N42 Grade), were superglued into position to align parallel to the eppendorfs. This method of washing was followed by a centrifugation step of 5000 rpm for 20 minutes.

7.1.5 SERS Response of Gold Coated Nanocages

MGITC was studied at final concentrations of 0.5-4.0 μM with the Au-IONCs. The Au-IONCs were first diluted 10 fold, in water, then each sample contained 285 μL of this diluted stock solution. To make the desired MGITC concentrations, Table 7.1 was followed.

Table 7.1 - Volumes of 0.1 mM MGITC stock and water added to Au-IONCs to give a final MGITC concentration range of 0-4 μM.

[MGITC] (μM)	0.1 mM MGITC (μL)	water (μL)
Control	0	15
0.5	1.5	13.5
1.0	3.0	12.0
1.5	4.5	10.5
2.0	6.0	9.0
2.5	7.5	7.5
3.0	9.0	6.0
3.5	10.5	4.5
4.0	12.0	3.0

Samples were shaken for 30 minutes, then centrifuged for 20 minutes at 5000 rpm, before the pellet was resuspended in 300 μL water for further analysis.

7.1.6 Antibody Functionalisation of Gold Coated Nanocages

In preparation for the functionalisation of an antibody to the Au-IONCs, 2 mL of particles were first functionalised with MGITC (final solution concentration 2 µM) and carboxylic-thiol-PEG$_{5000}$ (final solution concentration 50 µM). After the final centrifugation step, the samples were resuspended in 70.9 µL MES buffer (pH6), 74 µL freshly prepared 1-ethyl-3-(3-dimethylaminopropyl)-carbodiimide (EDC) (1 mg/mL in MES buffer) and 217 µL N-hydroxysulfosuccinimide (NHS) (1 mg/mL in MES buffer). These samples were shaken for 20 minutes before centrifuging at 5000 rpm for 10 minutes. As a control, one sample was resuspended in 1000 µL HEPES buffer (no antibody). While the other was resuspended in 980 µL HEPES buffer and 20 µL of the antibody solution (R&D Systems, Human ICAM-1/CD54 Ab at 0.5 mg/mL). These samples were left to shake overnight, before a final centrifugation step.

To check for successful antibody conjugation to the CT-PEG$_{5000}$, a lateral flow strip was spotted with 0.5 µL mouse anti IgG$_2$ (R&D Systems, 1 mg/mL), to act as a generic capture antibody for the ICAM functionalised Au-IONCs. The Ab-PEG-Au-IONCs sample was concentrated (centrifuged and resuspended in 60 µL HEPES buffer) and 20 µL added to a 1.75 mL glass vial with an additional 30 µL HEPES buffer to make up the running solution. The lateral flow strip was then inserted, so the sample pad was immersed in the running solution. The strip was rinsed in a further 50 µL HEPES buffer and allowed to dry overnight. An identical protocol was followed for the control PEG-Au-IONC sample.

7.1.7 Nanoparticle imaging

TEM - Samples were spotted (2 µL) onto a carbon coated copper grid and allowed to air dry. They were then kindly imaged at the TEM facility at Hunter College, New York with the help of Dr Kristina Fabijanic.

SEM – Samples were spotted (2 µL) onto a silica wafer and allowed to air dry. They were then imaged using a field-emission environmental SEM (FEI Quanta 250 FEG-ESEM). An electron beam diameter of 'Spot size 3' was selected from the preset options and an accelerating voltage of 20 kV was used to capture the images.

7.2 Hollow Gold Nanoparticles

7.2.1 Synthesis of Hollow Gold Nanoparticles

Firstly, AgNPs were synthesised using a modified method by Leopold and Lendl.[156] In a large glass flask, sodium hydroxide (47 mg in 360 mL of water) and hydroxylamine hydrochloride (42 mg in 4 mL water) were mixed before silver nitrate (67 mg in 40 mL water) was rapidly added. The reaction proceeded quickly under rapid magnetic stirring. The mixture was allowed to stir for 15 minutes.

A modified protocol by Goodman *et al.* was used to synthesise the HGNs.[97] A gold stock solution (Au/K_2CO_3) was first prepared containing hydrogen tetrachloroaurate (III) hydrate (20 mg in 2 mL water) and potassium carbonate (25 mg in 100 mL water). This yellow solution was left for 30 minutes, until colourless, before use. A 50 mg/mL citrate buffer was also prepared as 1 g of sodium citrate tribasic dihydrate in 20 mL of water.

As a general method, 3 parts of the as prepared AgNPs and 6 parts water were magnetically stirred before 1 part of the Au/K_2CO_3 solution was rapidly added to the mixture, e.g. 30 mL AgNPs, 60 mL water and 10 mL Au/K_2CO_3 solution. After 5 minutes, sodium citrate buffer (2 mL) was added and left to stir for a further 10 minutes. These volumes were scaled and changed for different experiments and stated accordingly. Across the years of research, multiple batches of HGNs were synthesised and used in experiments, however the ratios stated above were used as the 'standard' HGN protocol.

7.2.2 Shifting the LSPR of Hollow Gold Nanoparticles

The LSPR of the HGNs can be controlled by altering the ratios of the three main components of the synthesis; AgNPs, water and Au/K_2CO_3 solution. Following the standard method stated above, a bathochromic shift was induced by altering the volume of Au/K_2CO_3 solution added. Table 7.2 states the reagent volumes used.

Table 7.2 –Reagent volumes used to synthesise red shifted HGNs.

Batch	AgNP (mL) [As synthesised]	Water (mL)	Au/K$_2$CO$_3$ Solution (mL) Au [0.196 mg/mL] K$_2$CO$_3$ [0.245 mg/mL]
1	3	6.2	0.8
2	3	6.0	1.0
3	3	5.8	1.2
4	3	5.6	1.4
5	3	5.4	1.6
6	3	5.2	1.8
7	3	5.0	2.0

To produce a hypsochromic shift, the silver content was varied while keeping all other reagents constant. Table 7.3 states the volumes used.

Table 7.3 - Reagent volumes used to synthesise blue shifted HGNs.

Batch	AgNP (mL) [As synthesised]	Water (mL)	Au/K$_2$CO$_3$ Solution (mL) Au [196 mg/L] K$_2$CO$_3$ [245 mg/L]
1	3	6	1
2	4	5	1
3	5	4	1
4	6	3	1
5	7	2	1
6	8	1	1
7	9	0	1

7.2.3 HGN Synthesis Reproducibility

Five batches of HGNs were synthesised following the same protocol; 6 mL water, 3 mL AgNPs and 1 mL Au solution. All batches were magnetically stirred in a small plastic vial. After 5 minutes, citrate buffer (200 µL of 5%) was added and allowed to stir for a further 2 minutes.

7.2.4 HGN Synthesis Scalability

To investigate the scalability of the HGN synthesis, batches were synthesised following the volumes in Table 7.4, while mixed in increasingly larger vials/flasks. The magnetic stirrer bars used were also proportionally increased in size as well as possible.

Table 7.4 - Reagent volumes used to investigate the galvanic reaction scalability.

Factor	Total Volume (mL)	AgNP (mL)	Water (mL)	Au Solution (mL)	5% Citrate Buffer (mL)
x1	10	3	6	1	0.2
x5	50	15	30	5	1
x10	100	30	60	10	2
x20	200	60	120	20	4
x50	500	150	300	50	10

7.2.5 Functionalisation of HGNs with Bio-recognition Molecules

An 'off-particle' conjugation method was used for the HGNs, this is in contrast to the 'on-particle' method used for the data presented in Chapter 3. Stocks of each reagent were freshly prepared before use, 1-Ethyl-3-(3-dimethylaminopropyl) carbodiimide (EDC) and N-hydroxysulfosuccinimide (sNHS) at 1mg/mL in 10 mM HEPES at pH 7.4. A solution of thiolated PEG (HS-PEG$_{5000}$-COOH; 12.5 µM) was also prepared in water (2.5 mg/500 µL). Anti-human ICAM-1/CD54 antibody (Monoclonal mouse IgG$_1$ purchased form R&D Systems) was reconstituted to a stock solution of 1mg/mL in PBS before being aliquoted and frozen for storage.

Table 7.5 - Volumes of reagents used in the carbodiimide coupling of the antibody and PEG linker.

Ab-Sample	Control Sample
[1] ICAM Ab (20 µL) + sNHS (217 µL)	[1] HEPES buffer (20 µL) + sNHS (217 µL)
[2] CTPEG (40 µL) + EDC (74 µL)	[2] CTPEG (40 µL) + EDC (74 µL)

Table 7.5 shows the volumes of each reagent required for the carbodiimide coupling reaction. Each eppendorf was incubated for 2 minutes before eppendorfs [1] and [2] were combined along with 649 µL HEPES buffer and left to shake overnight.

Meanwhile 1 mL of MGITC functionalised HGNs were prepared as before with a final solution concentration of 0.1 μM. The antibody samples were then split equally and 500 μL of MGITC-HGNs were added to each eppendorf and left to shake for 2 hours. These were centrifuged at 4500 rpm for 20 minutes, before the supernatant was removed and one pellet of each sample resuspended in 500 μL water and the other in 50 μL water for further analysis.

7.2.6 Lateral Flow Strip Analysis

Polyclonal Goat Ab IgG (1 mg/mL) was used as the secondary capture antibody and 0.5 μL was spotted onto the lateral flow strip and allowed to air dry. A running buffer was prepared consisting of 0.1 g bovine serum albumin (BSA), 34.4 mg phosphate buffer and 10 μL Tween 20 in 20 mL water. In a small glass vial, 20 μL of the concentrated HGN sample was mixed with 30 μL of the running buffer before the lateral flow strip was placed vertically in the vial. Once the solution had absorbed up the strip, two wash steps were carried out with 50 μL of the running buffer.

7.2.7 Functionalisation of HGNs with a Raman Reporter

Stock HGNs were concentrated 5 fold (via centrifugation) before functionalisation with phenylacetylene. 200 μL of concentrated HGNs were added to an eppendorf containing 42.5 μL water and 7.5 μL of a phenylacetylene stock (0.1 mM in ethanol). The samples had a final phenylacetylene solution concentration of 0.017mM. Samples were shaken for 60 minutes before a centrifugation step, where the supernatant was removed and the pellet was resuspended in water.

7.2.8 Photothermal Properties of Hollow Gold Nanoparticles

A system was built in-house to measure the photothermal properties of the HGNs, modelled on a publication by Richardson *et al.*[57] Briefly, a 1.75 mL glass vial was clamped in pathway of two laser systems. The vial contained 500 μL of HGNs with a K-Type thermocouple probe (from TC Direct) through the cap, with the tip of the probe positioned out of the path of the laser beam. The temperature probe was linked to a Picologger, which digitally recorded the temperature of the sample every second. An Ocean Optics CW 785 nm excitation laser was fibre optically coupled to a laser launch

and optically steered to pass through the sample vial. Perpendicular to the heating laser path was a Raman spectroscopy system consisting of a CW 785 nm excitation laser (Innovative Photonic Systems) and a spectrometer (Wasatch Photonics S-00142).

7.2.8.1 Cycled Heating of the HGNs

The heating set up described above was used, where 500 μL of HGNs were heated for 30 minutes using the 785 nm laser at full power (≈280 mW). Leaving the sample in the set up, it was allowed to cool for 10 minutes, then heated again for 30 minutes. This was repeated once more to record 3 consecutive heating/cooling cycles.

7.2.8.2 Concentration Dependence on HGN Heating

The standard heating set up was used for this experiment. Four eppendorfs containing 1500 μL of as prepared HGNs were centrifuged and the pellets resuspended in the following volumes of water to create a range of concentrations: 1500 μL for stock HGNs, 1000 μL for x1.5 HGNs, 500 μL for x3 HGNs. Citrate capped large spherical AuNPs (≈75 nm) were gifted from Fay Nicolson. 500 μL of each sample was added to a vial and allowed to equilibrate to room temperature before heating for 10 minutes. Typical laser power was 271 mW and the experiment was completed in triplicate.

7.2.8.3 Power Dependence on HGN Heating

The standard heating set up was also used to examine the power dependent HGN heating, except a CW 785 nm laser with a controllable power output was used as the heating source. 500 μL of HGNs were heated for 30 minutes at each laser power studied (50, 100, 150, 200, 250, 300 and 350 mW). The experiment was completed in triplicate.

7.2.9 Excitation Wavelength Study

500 μL MGITC-HGNs samples were prepared with a final solution concentration of 0.1 μM and the experiment carried out in triplicate. The spectrometers used were all in the Snowy range and operated using the same Peak software. Due to the safety overrides and closed nature of the spectrometers, it was not possible to reliably

measure the laser power at the sample, and as such only the maximum laser power is noted in Table 7.6. All spectra were acquired for 1s and collected in triplicate.

Table 7.6 - Details of the spectrometers used.

Excitation Wavelength (nm)	Instrument	Max Laser Power (mW)	Acquisition Time (s)
532	Snowy Portable	50	1
638	Snowy Portable	40	1
785	Snowy Portable	100	1
1064	Snowy Handheld	450	1

7.2.10 Heat block vs Laser Investigation

Nine MGITC-HGN samples were prepared with a final concentration of 0.1 µM, 500 µL of HGNs were added to an eppendorf containing 44.5 µL of water and 5.5 µL of 10 µM MGITC stock solution. Samples were shaken for 30 minutes, then centrifuged at 3000 rpm for 30 minutes. The supernatant was removed and the pellets resuspended in 500 µL of water. All the samples were pooled together and then aliquoted for analysis. This was to reduce any variation introduced in the sample preparation steps, e.g. pipetting errors, meaning if any discrepancies were observed in results, it could be concluded that they were related to the heating process only.

The heat block was set to 38°C and allowed to equilibrate before any samples were added. Foil was used to cover the samples during heating to prevent any heat loss.

7.2.11 Time Interval Studies

Four different Raman reporters were studied, malachite green isothiocyanate, 4-(1H-pyrazol-4-yl)pyridine, 2-mercaptobeneze and benzenethiol. The same batch of HGNs was used for all experiments to reduce variation in the photothermal conversion process/SERS response. All experiments were carried out in triplicate, and sample preparation and experimental parameters were kept as over the four studies.

7.2.11.1 Sample Preparation – Raman Reporter on HGNs

MGITC (0.1 µM final concentration) - 500 µL of HGNs were added to an eppendorf containing 44.5 µL of water and 5.5 µL of 10 µM MGITC stock solution.

PPY (0.2 µM final concentration) - 500 µL of HGNs were added to an eppendorf containing 39 µL of water and 11 µL of 10 µM PPY stock solution.

2-MPY (0.1 µM final concentration) - 500 µL of HGNs were added to an eppendorf containing 44.5 µL of water and 5.5 µL of 10 µM 2-MPY stock solution.

BT (0.5 µM final concentration) - 500 µL of HGNs were added to an eppendorf containing 22.5 µL of water and 27.5 µL of 10 µM BT stock solution.

Samples were shaken for 30 minutes, then centrifuged at 3000 rpm for 30 minutes. The supernatant was removed and the pellets resuspended in 500 µL of water. Once resuspended, the reporter-HGN samples were pooled together and then aliquoted for analysis.

All studies were carried out on the in-house built set up using the same CW 785 nm excitation laser for heating (≈280 mW) and CW 785 nm excitation laser for SERS measurements (30 mW). 500 µL of a sample was placed in a 1.75 mL glass vial and secured in position at the crossover of the two perpendicular laser systems. Temperature was recorded using a K-Type thermocouple probe inserted through the cap and linked to a digital data logger.

7.2.11.2 Dynamic Light Scattering & Nanoparticle Tracking Analysis

The samples from the above experiment with MGTIC-HGNs were used to determine nanoparticle sizes. Samples were analysed using an ALV/Compact Goniometer System-3 and a Malvern Nanosight instrument. Samples were recovered from the vials used in the SERS study and diluted prior to analysis. All measurements and data processing was carried out by Dr Georgina Zimbitas from the Chemical Engineering Department at the University of Strathclyde.

7.2.11.3 Transmission Electron Microscopy

Carbon coated copper grids were prepared with a plasma cleaner (20 mA for 30 s). Then samples were spotted (2 µL) onto a grid, covered and allowed to air dry. They were imaged at the University of Glasgow by Margaret Mullin on a JEOL 1200 TEM.

7.2.12 Citrate HGNs vs Bare HGNs

The standard method for preparing HGNs was followed as detailed in section 6.2.1 with one small modification. 5 minutes after the Au/K_2CO_3 solution had been added, the batch was split in two. To one half citrate buffer was added as normal, 1 mL of 5% citrate buffer. To the other half, 1 mL of water was added to keep the concentrations comparable. All samples were cleaned by centrifugation prior to use or analysis to remove any excess reagents in the colloid.

For the study with MGITC, a slightly lower final concentration was chosen as the bare HGNs were thought to have been less stable in solution due to the lack of citrate capping the surface. A final concentration of 50 nM was used, 500 µL of HGNs (either bare or citrate capped) was added to eppendorfs containing 47.25 µL water and 2.75 µL of 10 µM MGITC stock solution. The samples were then mixed for 30 minutes, centrifuged at 3000 rpm for 30 minutes and resuspended in 500 µL water for analysis.

7.2.13 Data Processing of SERS

All data was processed using MATLAB software (R2018a) and often followed a series of operations,

- Average the three measurements collected at each time interval.
- Subtraction of a spectrum of the glass vial containing bare HGNs. The glass gave an unavoidable large background at 785 nm, and so by subtracting this, any remaining peaks could be attributed to the Raman reporters. Figure 9.6 in the appendix shows the raw spectrum of a sample of MGITC-HGNs and the background spectrum which was subtracted to produce the corrected spectrum.

- If necessary, the spectral range was cut to just include the bands of interest.

- A baseline was applied using a function based on an asymmetric least square algorithm (Paul Eilers, 2002).

- If particularly noisy, a smoothing function was applied with a small factor e.g. 3, therefore avoiding the loss of data by over smoothing.

- The results from three experimental repeats were averaged before plotting.

8. References

1   World Health Organisation, http://www.who.int/mediacentre/factsheets/fs317/en/, Accessed Jan 2019. .

2   M. A. Seidman, R. N. Mitchell and J. R. Stone, in *Cellular and Molecular Pathobiology of Cardiovascular Disease*, eds. M. Willis, J. W. Homeister and J. R. Stone, Academic Press, London, 2013, pp. 221–237.

3   S. Xu, M. Bendeck and A. I. Gotlieb, in *Cardiovascular Pathology*, eds. L. M. Buja and J. Butany, Academic Press, London, 4th edn., 2015, pp. 85–124.

4   The British Heart Foundation, *CVD STATISTICS – BHF UK FACTSHEET*, 2017.

5   C. W. Tsao and R. S. Vasan, *Int. J. Epidemiol.*, 2015, **44**, 1800–1813.

6   J. K. Liao and U. Laufs, *Annu Rev Pharmacol Toxicol*, 2005, **45**, 89–118.

7   Natl. Heart Lung Blood Inst. Natl. Inst. Health, *Third Report of the National Cholesterol Education Program (NCEP) Expert Panel on Detection, Evaluation, and Treatment of High Blood cholesterol in Adults (Adult Treatment Panel III)*, 2002.

8   A. Endo, *J. Lipid Res.*, 1992, **33**, 1569–1582.

9   C.-Y. Wang, P.-Y. Liu and J. K. Liao, *Trends Mol. Med.*, 2008, **14**, 37–44.

10   D. Pella, R. Rybar and V. Mechirova, *Acta Cardiol. Sin.*, 2005, **21**, 190–198.

11   S. I. McFarlane, R. Muniyappa, R. Francisco and J. R. Sowers, *J. Clin. Endocrinol. Metab.*, 2002, **87**, 1451–1458.

12   A. Oesterle, U. Laufs and J. K. Liao, *Circ. Res.*, 2017, **120**, 229–243.

13   M. A. Albert, E. Danielson, N. Rifai and P. M. Ridker, *JAMA*, 2001, **286**, 64–74.

14   P. M. Ridker, *Circ Cardiovasc Qual Outcomes*, 2009, **2**, 279–285.

15   J. Davignon, *Circulation*, 2004, **109**, 39–43.

16   A. S. Antonopoulos, M. Margaritis, R. Lee, K. Channon and C. Antoniades, *Curr. Pharm. Des.*, 2012, **18**, 1519–1530.

17   T. E. Commission, *Recommendation on the definition of a nanomaterial (2011/696/EU)*, 2011.

18   B. Romana, M. Batger, C. A. Prestidge, G. Colombo and F. Sonvico, *Curr. Top. Med. Chem.*, 2014, **14**, 1182–1193.

19   A. Soni, A. Gadad, P. Dandagi and V. Mastiholimath, *Asian J. Pharm.*, 2011, **5**, 57–64.

20   S. Katsuki, T. Matoba, S. Nakashiro, K. Sato, J. I. Koga, K. Nakano, Y. Nakano, S. Egusa, K. Sunagawa and K. Egashira, *Circulation*, 2014, **129**, 896–906.

21   R. Duivenvoorden, J. Tang, D. P. Cormode, A. J. Mieszawska, D. Izquierdo-Garcia, C. Ozcan, M. J. Otten, N. Zaidi, M. E. Lobatto, S. M. van Rijs, B. Priem, E. L. Kuan, C. Martel, B. Hewing, H. Sager, M. Nahrendorf, G. J. Randolph, E. S. G. Stroes, V. Fuster, E. A. Fisher, Z. A. Fayad and W. J. M. Mulder, *Nat. Commun.*, 2014, **5**, 1-12.

22   N. Tsukie, K. Nakano, T. Matoba, S. Masuda, E. Iwata, M. Miyagawa, G. Zhao, W. Meng, J. Kishimoto, K. Sunagawa and K. Egashira, *J. Atheroscler. Thromb.*, 2012, **20**, 32–45.

23   R. P. Feynman, *Plenty of Room at the Bottom*, Pasadena, 1959.

24   D. M. Eigler and E. K. Schweizer, *Nature*, 1990, **344**, 524–526.

25   C. Toumey, *Techné Res. Philos. Technol.*, 2008, **12**, 133–168.

26   C. Binns, in *Introduction to nanoscience and nanotechnology*, ed. E. Desurvire, John Wiley & Sons, Hoboken, New Jersey, 1st Editio., 2010, p. xiii.

27   P. Hanks, T. Hill Long and L. Urdang, Eds., *Collins English Dictionary*, William Collins Sons & Co. Ltd., United States of America, 1st Editio., 1979.

28   F. J. Heiligtag and M. Niederberger, *Mater. Today*, 2013, **16**, 262–271.

29   R. R. Arvizo, S. Bhattacharyya, R. a Kudgus, K. Giri, R. Bhattacharya and P. Mukherjee, *Chem. Soc. Rev.*, 2012, **41**, 2943–2970.

30   M. Faraday, *Phil. Trans. R. Soc. Lond.*, 1857, **147**, 145–181.

31   J. Turkevich, P. C. Stevenson and J. Hillier, *Discuss. Faraday Soc.*, 1951, **11**, 55-75.

32   G. Frens, *Nat. Phys. Sci.*, 1973, **241**, 20–22.

33   X. Ji, X. Song, J. Li, Y. Bai, W. Yang and X. Peng, *J. Am. Chem. Soc.*, 2007, **129**, 13939–13948.

34   K. M. Mayer, J. H. Hafner and A. À. Antigen, *Chem. Rev.*, 2011, **111**, 3828–3857.

35   E. Petryayeva and U. J. Krull, *Anal. Chim. Acta*, 2011, **706**, 8–24.

36   C. A. Mirkin, R. L. Letsinger, R. C. Mucic and J. J. Storhoff, *Nature*, 1996, **382**, 607–609.

37   D. Pissuwan, T. Niidome and M. B. Cortie, *J. Control. Release*, 2011, **149**, 65–71.

38   B. Kumar, K. Jalodia, P. Kumar and H. K. Gautam, *J. Drug Deliv. Sci. Technol.*, 2017, **41**, 260–268.

39   B. Duncan, C. Kim and V. M. Rotello, *J. Control. Release*, 2010, **148**, 122–127.

40   K. Greish, in *Cancer Nanotechnology - Methods & Protocols*, eds. S. R. Grobmyer and B. M. Moudgil, Humana Press, 2010, pp. 25–37.

41   M. Y. Spivak, R. V Bubnov, I. M. Yemets, L. M. Lazarenko, N. O. Tymoshok and Z. R. Ulberg, *EPMA J.*, 2013, **4**, 1–23.

42   W. H. De Jong, W. I. Hagens, P. Krystek, M. C. Burger, A. J. A. M. Sips and R. E. Geertsma, *Biomaterials*, 2008, **29**, 1912–1919.

43   G. Sonavane, K. Tomoda and K. Makino, *Colloids Surfaces B Biointerfaces*, 2008, **66**, 274–280.

44   D. J. Lundy, K. Chen, E. K. Toh and P. C. Hsieh, *Nat. Sci. Reports*, 2016, **6**, 1–10.

45   J. Noonan, S. M. Asiala, G. Grassia, N. Macritchie, K. Gracie, J. Carson, M. Moores, M. Girolami, A. C. Bradshaw, T. J. Guzik, G. R. Meehan, H. E. Scales, J. M. Brewer, I. B. McInnes, N. Sattar, K. Faulds, P. Garside, D. Graham and P. Maffia, *Theranostics*, 2018, **8**, 6195–6209.

46   J. Zhang, A. Ma and L. Shang, *Front. Physiol.*, 2018, **9**, 1–5.

47   E. C. Dreaden, A. M. Alkilany, X. Huang, C. J. Murphy and M. a El-Sayed, *Chem. Soc. Rev.*, 2012, **41**, 2740–2779.

48   S. Rana, A. Bajaj, R. Mout and V. M. Rotello, *Adv. Drug Deliv. Rev.*, 2012, **64**, 200–216.

49   L. Grislain, P. Couvreur, V. Lenaerts, M. Roland, D. Deprez-Decampeneere and P. Speiser, *Int. J. Pharm.*, 1983, **15**, 335–345.

50   G. Storm, S. Belliot, T. Daemenb and D. D. Lasic, *Adv. Drug Deliv. Rev.*, 1995, **17**, 31–48.

51   T. Cedervall, I. Lynch, S. Lindman, T. Berggård, E. Thulin, H. Nilsson, K. A. Dawson and S. Linse, *Proc. Natl. Acad. Sci. U. S. A.*, 2007, **104**, 2050–2055.

52   K. Jiang, D. A. Smith and A. Pinchuk, *J. Phys. Chem. C*, 2013, **117**, 27073–27080.

53   S. Link and M. A. El-Sayed, *Int. Rev. Phys. Chem.*, 2000, **19**, 409–453.

54   X. Huang and M. A. El-Sayed, *J. Adv. Res.*, 2010, **1**, 13–28.

55   X. Huang, P. K. Jain, I. H. El-Sayed and M. a El-Sayed, *Lasers Med Sci*, 2008, **23**, 217–228.

56   Encyclopaedia Britannica, https://www.britannica.com/science/phonon, Accessed Feb 2019.

57   H. H. Richardson, M. T. Carlson, P. J. Tandler, P. Hernandez and A. O. Govorov, *Nano Lett.*, 2009, **9**, 1139–1146.

58   S. Link, C. Burda, M. B. Mohamed, B. Nikoobakht and M. A. El-Sayed, *J. Phys. Chem. A*, 1999, **103**, 1165–1170.

59   G. González-Rubio, A. Guerrero-Martínez and L. M. Liz-Marzán, *Acc. Chem. Res.*, 2016, **49**, 678–686.

60   A. Smekal, *Naturwissenschaften*, 1923, **11**, 873–875.

61   C. V. Raman and K. S. Krishnan, *Nature*, 1928, 501–502.

62   D. I. Ellis, D. P. Cowcher, L. Ashton, S. O'Hagan and R. Goodacre, *Analyst*, 2013, **138**, 3871–3884.

63   E. Smith and G. Dent, *Modern Raman Spectroscopy – A Practical Approach*, Wiley, First Edit., 2005.

64   M. Fleischmann, P. J. Hendra and A. J. McQuillan, *Chem. Phys. Lett.*, 1974, **26**, 163–166.

65   D. L. Jeanmaire and R. P. Van Duyne, *J. Electroanal. Chem. Interfacial Electrochem.*, 1977, **84**, 1–20.

66   M. G. Albrecht and J. A. Creighton, *J. Am. Chem. Soc.*, 1977, **99**, 5215–5217.

67   G. McNay, D. Eustace, E. W. Smith, K. Faulds and D. Graham, *Appl. Spectrosc.*, 2011, **65**, 825–837.

68   A. Campion and P. Kambhampati, *Chem. Soc. Rev.*, 1998, **27**, 241–250.

69 E. Le Ru and P. Etchegoin, *Principles of Surface Enhanced Raman Spectroscopy and Related Plasmonic Effects*, Elsevier B.V., Oxford, First Edit., 2009.

70 A. M. Stacy and R. P. Van Duyne, *Chem. Phys. Lett.*, 1983, **102**, 365–370.

71 S. Yang, X. Dai, B. B. Stogin and T. S. Wong, *Proc. Natl. Acad. Sci. U. S. A.*, 2016, **113**, 268–273.

72 X. Hua, Q. Yang, Z. Dong, J. Zhang, W. Zhang, Q. Wang, S. Tan and H. D. C. Smyth, *Drug Deliv.*, 2017, **24**, 511–518.

73 A. N. Kharlamov, A. E. Tyurnina, V. S. Veselova, O. P. Kovtun, V. Y. Shur and J. L. Gabinsky, *Nanoscale*, 2015, **7**, 8003–8015.

74 L. M. Socolovsky and O. M. Londono, in *Complex Magnetic Nanostructures*, ed. S. K. Sharma, Springer International Publishing AG, Switzerland, 1st Editio., 2017, pp. 1–38.

75 M. Colombo, S. Carregal-Romero, M. F. Casula, L. Gutierrez, M. P. Morales, I. B. Bohm, J. T. Heverhagen, D. Prosperi and W. J. Parak, *Chem. Soc. Rev.*, 2012, **41**, 4306–4334.

76 A. H. Lu, E. L. Salabas and F. Schüth, *Angew. Chemie - Int. Ed.*, 2007, **46**, 1222-1244.

77 K. J. Widder, A. E. Senyei and D. G. Scarpelli, *Proc. Soc. Exp. Biol. Med.*, 1978, **58**, 141–146.

78 P. Kheirkhah, S. Denyer, A. D. Bhimani, G. D. Arnone, D. R. Esfahani, T. Aguilar, J. Zakrzewski, I. Venugopal, N. Habib, G. L. Gallia, A. Linninger, F. T. Charbel and A. I. Mehta, *Sci. Rep.*, 2018, **8**, 1–9.

79 N. V. S. Vallabani and S. Singh, *3 Biotech*, 2018, **8**, 1–23.

80 J. Pirayesh Islamian, M. Hatamian, N. A. Aval, M. R. Rashidi, A. Mesbahi, M. Mohammadzadeh and M. Asghari Jafarabadi, *Breast*, 2017, **33**, 97–103.

81 S. Rampersaud, J. Fang, Z. Wei, K. Fabijanic, S. Silver, T. Jaikaran, Y. Ruiz, M. Houssou, Z. Yin, S. Zheng, A. Hashimoto, A. Hoshino, D. Lyden, S. Mahajan and H. Matsui, *Nano Lett.*, 2016, **16**, 7357–7363.

82 M. H. Oh, T. Yu, S.-H. Yu, B. Lim, K.-T. Ko, M.-G. Willinger, D.-H. Seo, B. H. Kim, M. G. Cho, J.-H. Park, K. Kang, Y.-E. Sung, N. Pinna and T. Hyeon, *Science.*, 2013, **340**, 964–968.

83 Y. Sun, B. Mayers and Y. Xia, *Adv. Mater.*, 2003, **15**, 641–646.

84 T. Yu, J. Moon, J. Park, Y. Il Park, H. Bin Na, B. H. Kim, I. C. Song, W. K. Moon and T. Hyeon, *Chem. Mater.*, 2009, **21**, 2272–2279.

85 Y. Liu, T. Chen, C. Wu, L. Qiu, R. Hu, J. Li, S. Cansiz, L. Zhang, C. Cui, G. Zhu, M. You, T. Zhang and W. Tan, *J. Am. Chem. Soc.*, 2014, **136**, 12552–12555.

86 M. J. Bonder, Y. Huang and G. C. Hadjipanayis, in *Advanced Magnetic Nanostructures*, eds. D. Sellmyer and R. Skomski, Springer Science & Business Media, New York, 1st Editio., 2006, pp. 183–206.

87 M. McElfresh, *Fundamentals of Magnetism and Magnetic Measurements: Featuring Quantum Design's Magnetic Property Measurement System*, 1994.

88 E. Iglesias-Silva, J. L. Vilas-Vilela, M. A. López-Quintela, J. Rivas, M. Rodríguez and L. M. León, *J. Non. Cryst. Solids*, 2010, **356**, 1233–1235.

89 H. B. Lueck, D. C. Daniel and J. L. Mchale, *J. Raman Spectrosc.*, 1993, **24**, 363-370.

90 Thermo Scientific, *Crosslinking Technical Handbook*, Rockford, 2009.

91 S. Adams and J. Z. Zhang, *Coord. Chem. Rev.*, 2016, **320–321**, 18–37.

92 Y. Sun, B. T. Mayers and Y. Xia, *Nano Lett.*, 2002, **2**, 481–485.

93 A. M. Schwartzberg, T. Y. Olson, C. E. Talley and J. Z. Zhang, *J. Phys. Chem. B*, 2006, **110**, 19935–19944.

94 J. You, G. Zhang and C. Li, *ACS Nano*, 2010, **4**, 1033–1041.

95 R. Weissleder, *Nat. Biotechnol.*, 2001, **19**, 316–317.

96 J. You, R. Zhang, C. Xiong, M. Zhong, M. Melancon, S. Gupta, A. M. Nick, A. K. Sood and C. Li, *Cancer Res.*, 2012, **72**, 4777–4786.

97 A. M. Goodman, Y. Cao, C. Urban, O. Neumann, C. Ayala-orozco, M. W. Knight, A. Joshi, P. Nordlander and N. J. Halas, *ACS Nano*, 2014, **8**, 3222–3231.

98 X. Xia, Y. Wang, A. Ruditskiy and Y. Xia, *Adv. Mater.*, 2013, **25**, 6313–6332.

99   P. Vanysek, in *CRC Handbook of Chemistry and Physics, Internet Version*, ed. D. R. Lide, CRC Press, Boca Raton, FL, 2005, pp. 23–33.

100   J. B. Jackson, S. L. Westcott, L. R. Hirsch, J. L. West and N. J. Halas, *Appl. Phys. Lett.*, 2003, **82**, 257–259.

101   V. Vongsavat, B. M. Vittur, W. W. Bryan, J. H. Kim and T. R. Lee, *ACS Appl. Mater. Interfaces*, 2011, **3**, 3616–3624.

102   R. A. Alvarez-Puebla, D. J. Ross, G. A. Nazri and R. F. Aroca, *Langmuir*, 2005, **21**, 10504–10508.

103   M. H. Kim, X. Lu, B. Wiley, E. P. Lee and Y. Xia, *J. Phys. Chem. C*, 2008, **112**, 7872-7876.

104   Y. Sun and Y. Xia, *J. Am. Chem. Soc.*, 2004, **126**, 3892–3901.

105   L. E. Jamieson, S. M. Asiala, K. Gracie, K. Faulds and D. Graham, *Annu. Rev. Anal. Chem.*, 2017, **10**, 415–437.

106   S. Hong, T. Chen, Y. Zhu, A. Li, Y. Huang and X. Chen, *Angew. Chemie - Int. Ed.*, 2014, **53**, 5827–5831.

107   H. Yamakoshi, K. Dodo, A. Palonpon, J. Ando, K. Fujita, S. Kawata and M. Sodeoka, *J. Am. Chem. Soc.*, 2012, **134**, 20681–20689.

108   F. Hu, C. Zeng, R. Long, Y. Miao, L. Wei, Q. Xu and W. Min, *Nat. Methods*, 2018, **15**, 194–200.

109   L. . Abrantes, M. Fleischmann, I. . Hill, L. . Peter, M. Mengoli and G. Zotti, *J Electroanal Chem*, 1984, **164**, 177–187.

110   H. Feilchenfeld and M. J. Weaver, *J. Phys. Chem*, 1989, **93**, 4276–4282.

111   S. W. Joo and K. Kim, *J. Raman Spectrosc.*, 2004, **35**, 549–554.

112   H. Kosuge, S. P. Sherlock, T. Kitagawa, R. Dash, J. T. Robinson, H. Dai and M. V. McConnell, *J. Am. Heart Assoc.*, 2012, **1**, 1–10.

113   D. Harris-Birtill, M. Singh, Y. Zhou, A. Shah, P. Ruenraroengsak, M. E. Gallina, G. B. Hanna, A. E. G. Cass, A. E. Porter, J. Bamber and D. S. Elson, *PLoS One*, 2017, **12**, 1–21.

114   D. A. Wheeler, R. J. Newhouse, H. Wang, S. Zou and J. Z. Zhang, *J. Phys. Chem. C*, 2010, **114**, 18126–18133.

115   S. M. Stagg, K. L. Knappenberger, A. M. Dowgiallo and M. Chandra, *J. Phys. Chem. Lett.*, 2011, **2**, 2946–2950.

116   A. Hatef, S. Fortin-Deschênes, E. Boulais, F. Lesage and M. Meunier, *Int. J. Heat Mass Transf.*, 2015, **89**, 866–871.

117   V. Amendola, R. Pilot, M. Frasconi, O. M. Maragò and M. A. Iatì, *J. Phys. Condens. Matter*, 2017, **29**.

118   B. G. Prevo, S. A. Esakoff, A. Mikhailovsky and J. A. Zasadzinski, *Small*, 2008, **4**, 1183–1195.

119   J. Park, J. Park, E. J. Ju, S. S. Park, J. Choi, J. H. Lee, K. J. Lee, S. H. Shin, E. J. Ko, I. Park, C. Kim, J. J. Hwang, J. S. Lee, S. Y. Song, S. Y. Jeong and E. K. Choi, *J. Control. Release*, 2015, **207**, 77–85.

120   J. You, R. Zhang, G. Zhang, M. Zhong, Y. Liu, C. S. Van Pelt, D. Liang, W. Wei, A. K. Sood and C. Li, *J. Control. Release*, 2012, **158**, 319–328.

121   W. Lu, C. Xiong, G. Zhang, Q. Huang, R. Zhang, J. Z. Zhang and C. Li, *Clin*, 2009, **15**, 876–886.

122   K. Jiang, D. A. Smith and A. Pinchuk, *J. Phys. Chem. C*, 2013, **117**, 27073–27080.

123   G. Baffou, P. Bon, J. Savatier, J. Polleux, M. Zhu, M. Merlin, H. Rigneault and S. Monneret, *ACS Nano*, 2012, **6**, 2452–2458.

124   S. Hu, B. J. Liu, J. M. Feng, C. Zong, K. Q. Lin, X. Wang, D. Y. Wu and B. Ren, *J. Am. Chem. Soc.*, 2018, **140**, 13680–13686.

125   G. Schmid and B. Corain, *Eur. J. Inorg. Chem.*, 2003, 3081–3098.

126   M. Baia, F. Toderas, L. Baia, J. Popp and S. Astilean, *Chem. Phys. Lett.*, 2006, **422**, 127–132.

127   W. Leng and P. J. Vikesland, *Langmuir*, 2014, **30**, 8342–8349.

128   J. Ye, J. A. Hutchison, H. Uji-i, J. Hofkens, L. Lagae, G. Maes, G. Borghs and P. Van Dorpe, *Nanoscale*, 2012, **4**, 1606.

129   B. J. Liu, K. Q. Lin, S. Hu, X. Wang, Z. C. Lei, H. X. Lin and B. Ren, *Anal. Chem.*, 2015, **87**, 1058–1065.

130   M. Chandra, A. M. Dowgiallo and K. L. Knappenberger, *J. Phys. Chem. C*, 2010, **114**, 19971–19978.

131 M. A. Bedics, H. Kearns, J. M. Cox, S. Mabbott, F. Ali, N. C. Shand, K. Faulds, J. B. Benedict, D. Graham and M. R. Detty, *Chem. Sci.*, 2015, **6**, 2302–2306.

132 H. Kearns, N. C. Shand, K. Faulds and D. Graham, *Chem. Commun.*, 2015, **51**, 8138–8141.

133 S. S. Masango, R. A. Hackler, N. Large, A. I. Henry, M. O. McAnally, G. C. Schatz, P. C. Stair and R. P. Van Duyne, *Nano Lett.*, 2016, **16**, 4251–4259.

134 C. Lin, L. Jiang, J. Zhou, H. Xiao, S. Chen and H. Tsai, *Opt. Lett.*, 2010, **35**, 941-943.

135 X. M. Miao, C. Xiong, W. W. Wang, L. S. Ling and X. T. Shuai, *Chem. - A Eur. J.*, 2011, **17**, 11230–11236.

136 Z. Zhuang, J. Cheng, X. Wang, Y. Yin, G. Chen, B. Zhao, H. Zhang and G. Zhang, *J. Mol. Struct.*, 2006, **794**, 77–82.

137 W. H. Do, C. J. Lee, D. Y. Kim and M. J. Jung, *J. Ind. Eng. Chem.*, 2012, **18**, 2141-2146.

138 T. H. Joo, M. S. Kim and K. Kim, *J. Raman Spectrosc.*, 1987, **18**, 57–60.

139 J. J. Baumberg, *Faraday Discuss.*, 2019, **214**, 501–511.

140 E. Cortés, W. Xie, J. Cambiasso, A. S. Jermyn, R. Sundararaman, P. Narang, S. Schlücker and S. A. Maier, *Nat. Commun.*, 2017, **8**, 1–10.

141 M. Sun, Z. Zhang, H. Zheng and H. Xu, *Sci. Rep.*, 2012, **2**, 1–4.

142 Z. Zhang, T. Deckert-Gaudig, P. Singh and V. Deckert, *Chem. Commun.*, 2015, **51**, 3069–3072.

143 A. R. L. Marshall, J. Stokes, F. N. Viscomi, J. E. Proctor, J. Gierschner, J. S. G. Bouillard and A. M. Adawi, *Nanoscale*, 2017, **9**, 17415–17421.

144 Y. Kajikawa, in *Thin Film Growth: Physics, Materials Science and Applications*, Woodhead Publishing Limited, First Edit., 2011, pp. 60–82.

145 A. Otto, *Appl. Surf. Sci.*, 1980, **6**, 309–355.

146 J. Billmann, G. Kovacs and A. Otto, *Surf. Sci.*, 1980, **92**, 153–173.

147 Z. Feng, S. Velari, A. Cossaro, C. Castellarin-Cudia, A. Verdini, E. Vesselli, C. Dri, M. Peressi, A. De Vita and G. Comelli, *ACS Nano*, 2015, **9**, 8697–8709.

148 J. W. Park, *Part. Part. Syst. Charact.*, 2019, **36**, 1800329.

149   A. Heller, A. Barkleit, H. Foerstendorf, S. Tsushima, K. Heim and G. Bernhard, *Dalt. Trans.*, 2012, **41**, 13969–13983.

150   J. W. Park and J. S. Shumaker-Parry, *J. Am. Chem. Soc.*, 2014, **136**, 1907–1921.

151   C. J. Sandroff and D. R. Herschbach, *Langmuir*, 1985, **1**, 131–135.

152   T. Tsuji, T. Yahata, M. Yasutomo, K. Igawa, M. Tsuji, Y. Ishikawa and N. Koshizaki, *Phys. Chem. Chem. Phys.*, 2013, **15**, 3099–3107.

153   H. Häkkinen, *Nat. Chem.*, 2012, **4**, 443–455.

154   T. Bürgi, *Nanoscale*, 2015, **7**, 15553–15567.

155   E. Pensa, E. Corte, G. Corthey, P. Carro, C. Vericat, M. H. Fonticelli, G. Benítez, A. A. Rubert and R. C. Salvarezza, *Acc. Chem. Res.*, 2012, **45**, 1183–1192.

156   N. Leopold and B. Lendl, *J. Phys. Chem. B*, 2003, **107**, 5723–5727.

9. Appendices

Appendix I

Figure 9.1 - Histogram of Mn$_3$O$_4$ seed sizes in Figure 3.4 (n=100). Lengths measured show in corner of plot, depending on shape of seed face.
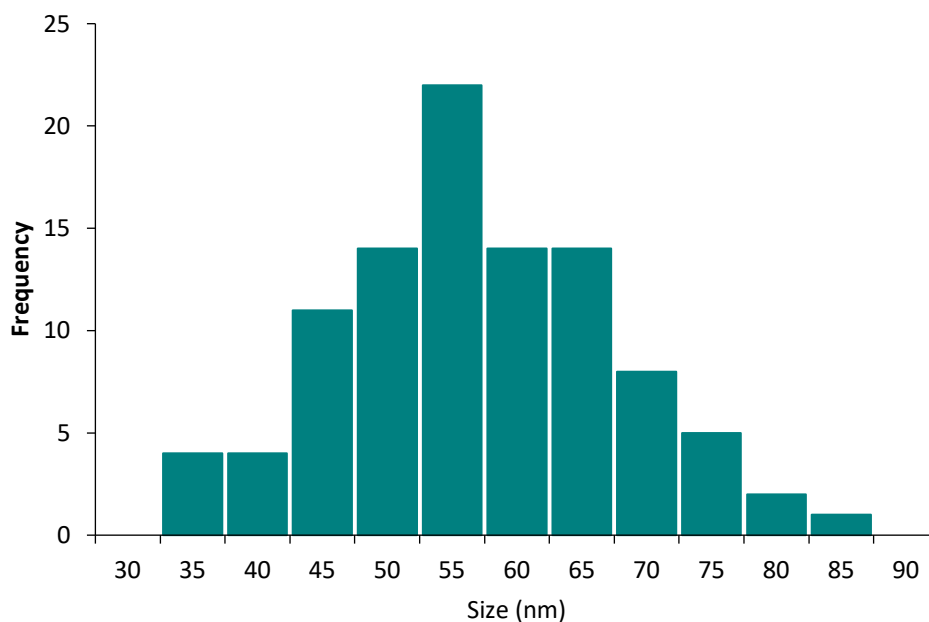
Figure 9.2 - Histogram of hollow gold nanoparticles (n=100) shown in the SEM image in Figure 4.5.
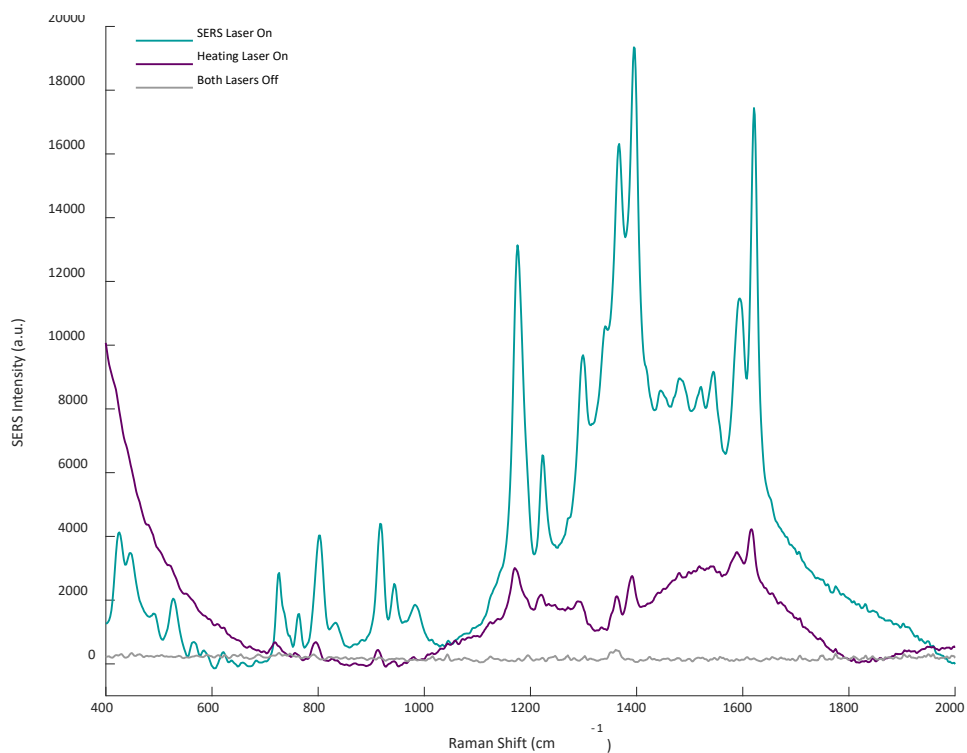
Appendix III

Figure 9.3 – Raw spectra of heated MGITC-HGNs in the three different laser configurations – SERS laser on (teal), heating laser on (purple), and both lasers off (grey). Notice the 90° Raman scattering detected from the spectrometer sitting perpendicular to the heating laser. Hence the heating laser shutter was closed while SERS spectra were collected to prevent additional contribution to the signal.
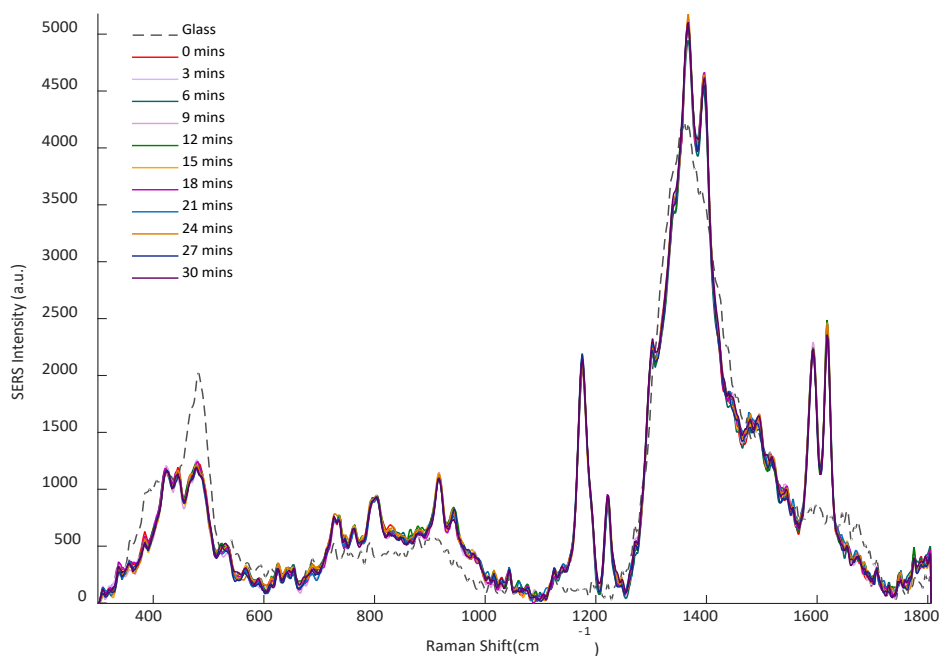
Figure 9.4 - SERS spectra of MGITC-HGNs collected with only exposure to the SERS laser (CW 30mW, 1s integration time, 5 minute intervals for 30 minutes). Data processing using MATLAB: spectral range cut, baseline applied, smoothed and 3 experimental reps were averaged before plotting.
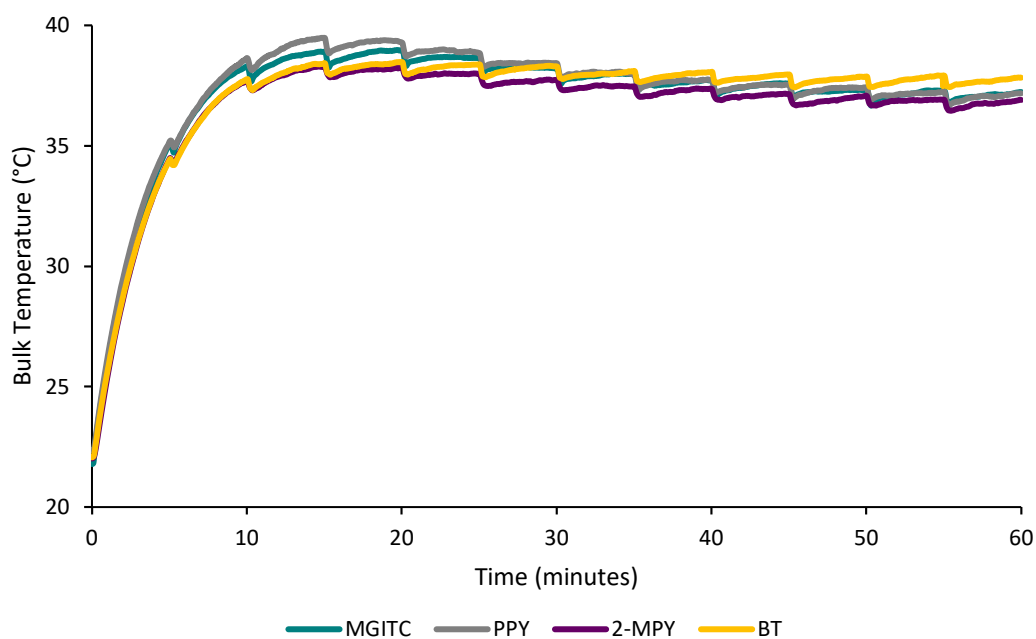
Appendix V

Figure 9.5 - Heating profiles of each Raman reporter on the same batch of HGNs. Average heating profile of triplicate experiments shown. Each sample was irradiated for 60 minutes with a CW 785 nm laser (280 mW).
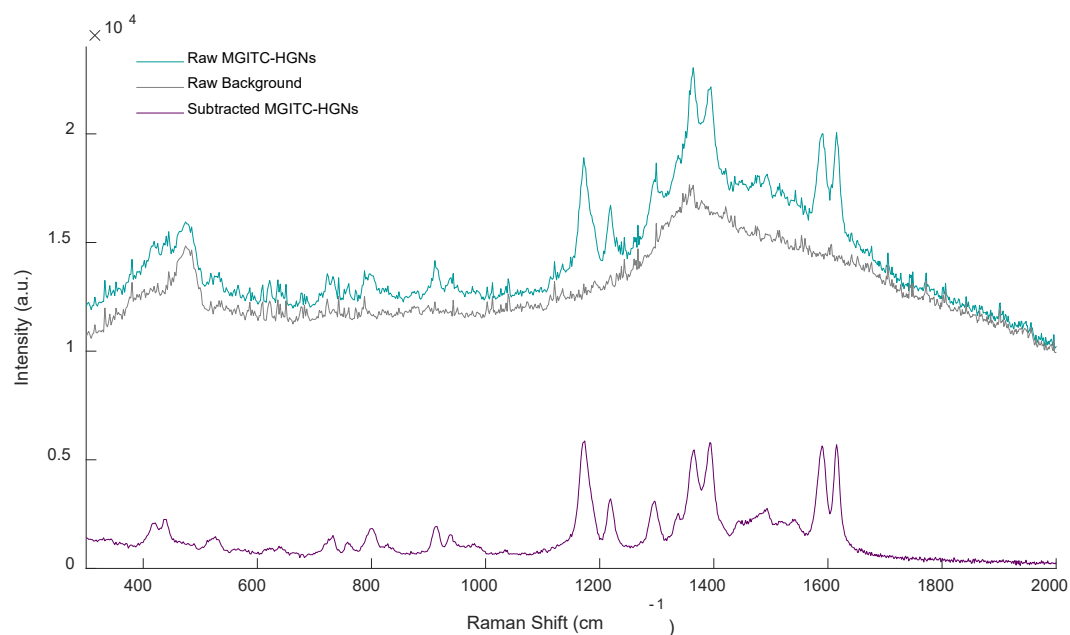
Figure 9.6 – Raw spectra of MGITC-HGNs (teal) and glass vial with bare HGN background (grey). Subtracting the background spectrum leads to the corrected MGITC-HGN spectrum (purple). Spectra collected using a 785 nm (30 mW) excitation laser with a 1s acquisition, triplicate measurements collected.

"Yes, indeed," they repeated together; "but if we'd told you then, you might not have gone—and, as you've discovered, so many things are possible just as long as you don't know they're impossible."

Norton Juster (The Phantom Tollbooth)